FINITE ELEMENT MODELLING OF STIFFENED

STEEL BOX GIRDERS WITH IMPERFECTIONS

by

MOHAMED ABDEL KADER EL AGHOURY, B.SC., M.SC.

A THESIS

Submitted to the School of Graduate Studies

in Partial Fulfilment of the Requirements

for the Degree

Doctor of Philosophy

McMaster University

 JUNE 1986

ISBN 0-315-33457-6

FINITE ELEMENT MODELLING OF STIFFENED STEEL BOX GIRDERS WITH IMPERFECTIONS

TO MY DEAR WIFE

NORMAN

DOCTOR OF PHILOSOPHY (1986)
(Civil Engineering and Engineering Mechanics)

McMASTER UNIVERSITY
Hamilton, Ontario
Canada

TITLE: Finite Element Modelling of Stiffened Steel Box Girders with Imperfections

AUTHOR: Mohamed Abdel Kader El Aghoury, B.Sc. (Ain Shams University)
M.Sc. (Ain Shams University)

SUPERVISORS: Dr. R.M. Korol and Dr. F.A. Mirza

NUMBER OF PAGES: xix, 190

ABSTRACT

An elasto-plastic large displacement finite element model has been developed to analyse stiffened steel plated box girders. It is capable of predicting inelastic buckling behaviour and ultimate strength under static loads. Both geometric imperfections and residual stresses are included to account for inherent flaws due to fabrication processes.

The model is formulated through a three-dimensional assemblage of rectangular plate elements for the webs, flanges and diaphragms, and eccentric beam elements for stiffeners. Plate and beam elements employed in the model incorporate both bending and in-plane actions. The non-conforming rectangular plate elements used utilize special provisions for displacement continuity along junctions between components of the box. To reduce computational time and half band width requirements, diaphragms are treated as substructures and then coupled with the rest of the box.

For material nonlinearity, yielding is described by the Von Mises criterion and the associated Prandtl-Reuss equations of plasticity. Subsequent yielding is governed by the isotropic hardening rule.

Finite element formulation for large deflection is based upon a total Lagrangian description. In the solution to problems, the analysis involves the Newton-Raphson iterative method for the nonlinear analysis using an incremental load procedure.

The formulation is first verified using a variety of beams, plates and three-dimensional plate assemblage problems. The present predictions compare favourably with other theoretical and experimental results already published in the technical literature.

The proposed model is then applied to a symmetrical overhanging stiffened steel box girder recently tested to simulate a typical pier girder of a continuous bridge. A series of numerical simulations were made both for the perfect box and its imperfect equivalent, in which imperfections are confined to the compression flange. Attention was focused on initial plate panel imperfections, longitudinal stiffener out-of-straightness, and idealized residual stresses.

Analytical results to be presented include ultimate load, failure mode, state of longitudinal stress distribution, and spread of plasticity. A comparison with results from the physical model shows excellent agreement. The imperfections postulated for the theoretical model are shown to somewhat reduce the predicted strength of box girders. Any analysis neglecting this effect overestimates the buckling strength.

ACKNOWLEDGEMENTS

I would like to express my sincere appreciation to my research supervisors, Dr. R.M. Korol and Dr. F.A. Mirza, for their valuable guidance, advice, criticism and encouragement throughout the course of this study. It has been a privilege to work under their supervision.

I am very grateful to the other members of my supervisory committee, Dr. M. Dokainish, Dr. A. Ghobarah, Dr. T. Aziz for their valuable comments and suggestions.

My personal involvement with the study would not have been possible without the financial support of McMaster University for which I am most grateful.

I would like to express special thanks to my friend and colleague Dr. Mohamed El Sobki for his great help in preparation of the figures, Mrs. Janet Ryding for assistance in editing this thesis, and also to express my appreciation for the help offered by the staff of Academic Computing Services during the development of the computer models.

The remarkable speed and accuracy of typing by Mrs. Z. Unelli, and the staff in the Burke Sciences Word Processing Centre, to whom I am indebted.

Finally, to my father's memory and my mother, from whom their guidance and moral support made this work possible, my very special thanks.

This work is dedicated to my wife, Norhan, and my children Ihab and Raabia, in recognition of their sacrifices during the period of this study.

TABLE OF CONTENTS

TABLE OF CONTENTS (cont'd.)

LIST OF FIGURES

LIST OF FIGURES (cont'd.)

LIST OF FIGURES (cont'd.)

LIST OF TABLES

LIST OF SYMBOLS

A_s	- cross sectional area of the stiffener
A_w	- area of weld deposit
a,b,t	- length, width and thickness of plate element
$\bar{b}$	- spacing between longitudinal stiffeners in the compression flange
B, D, ℓ	- width, depth and length of the beam element
c	- width of tension block on each side of the weld
e	- eccentricity of the beam element
E	- modulus of elasticity
E_T	- tangent modulus
E, $\bar{E}$ or E_T	- depending on stress level
F	- yield function
H'	- hardening modulus
L^p	- length of the stiffened panel
ℓ or L	- length or span of the stiffener
t or t_p	- plate thickness
N_p, N_b	- in-plane and out-of-plane shape functions for the rectangular elements
N_p^s, N_b^s	- in-plane and out-of-plane shape functions for the stiffener elements
P	- applied load
P_{ult}	- ultimate load
ℓ/r	- slenderness ratio

u, v, w – displacement fields

V – volume of the plate element

V^s – volume of the stiffener element

w_o – initial imperfection displacement field

$\bar{w}_o^{st}$ – maximum amplitude of the stiffener mode

$\bar{w}_o^{pl}$ – maximum amplitude of the plate panel mode

$\bar{w}_o^*$ – equivalent amplitude of initial imperfection

w^p – width of the stiffened compression flange

u^{sc}, w^{sc} – axial and out-of-plane displacements for the centre line of the stiffener

u^{st}, w^{st} – axial and out-of-plane displacement for the top edge of the stiffener

$u_i, v_i, \theta_{zi}, w_i, \theta_{xi}, \theta_{yi}$ – plate element degrees of freedom at node i

X, Y, Z – global coorodinates

$\varepsilon_x, \varepsilon_y, \gamma$ – strain components

$\sigma_{xx}, \sigma_{yy}, \sigma_{xy}$ – stress components

σ_y – yield stress

σ^1 – devatoric stress

$\bar{\sigma}$ – effective stress

δ – deflection

δ_o – initial deflection

ν – Poisson's ratio

λ – plastic strain multiplier

ξ, η, z – nondimensional coordinates of rectangular element

LIST OF MATRICES

$\{A\}$	- vector of polynomial coefficients (Equation 2.75)
$[B_L]$	- linear strain matrix for rectangular elements
$[B_L^s]$	- linear strain matrix for stiffener elements
$[B_{NL}]$	- nonlinear strain matrix for rectangular elements
$[B_{NL}^s]$	- nonlinear strain matrix for stiffener elements
$[B]$	- total strain matrix for rectangular elements
$[B^s]$	- total strain matrix for stiffener elements
$[C]$	- matrix defined by Equation 2.76
$[D]$	- elastic compliance matrix
$[D_{ep}]$	- elasto-plastic compliance matrix
$[\bar{D}]$	- elastic or elasto-plastic compliance matrix, depending on the stress level
$\{F\}$	- external load vector
$\{F_B\}_d$	- global condensed load vector for the diaphragm
$\{F_I\}$, $\{F_B\}$	- load vectors corresponding to interior and exterior nodes of the diaphragm
$[G]$	- matrix of first derivatives of shape functions for plate elements
$[G^s]$	- matrix of first derivative of shape functions for stiffener elements
$[k_L]$	- small displacement stiffness matrix for plate elements
$[k_L^s]$	- small displacement stiffness matrix for stiffener elements
$[k_{NL}]$	- initial displacement stiffness matrix for plate elements
$[k_{NL}^s]$	- initial displacement stiffness matrix for stiffener elements

LIST OF MATRICES (cont'd.)

$[\bar{k}] = [k_L] + [k_{NL}]$

$[\bar{k}^s] = [k_L^s] + [k_{NL}^s]$

$[k_\sigma]$ - initial stress stiffness matrix for plate elements

$[k_\sigma^s]$ - initial stress stiffness matrix for stiffeners elements

$[k_T]$ - total stiffness matrix for plate element

$[k_T^s]$ - total stiffness matrix for stiffener element

$[K_T\ (\underline{\delta}_n^m,\ \underline{\sigma}_n^m)]$ - global tangential stiffness matrix after n^{th} load increment and m^{th} iteration

$[K_{II}], [K_{BB}], [K_{IB}]$ - global sub-matrices related to diaphragm substructuring (Equation 2.105)

$[ST]_d$ - global condensed stiffness matrix of the diaphragm

$[M]$ - matrix which depends on stress level (Equation 2.40)

$[N]$ - matrix of shape functions for plate elements

$[Q], [S], [S_o]$ - matrices related to the plate elements and defined by Equations 2.17 to 2.19

$\{Q^s\}, \{S^s\}, \{S_o^s\}$ - matrices related to the stiffener elements and defined by Equations 2.89 to 2.91.

$\{R\}$ - vector of internal loads

$[T]$ - transformation matrix for plate elements

$[T^s]$ - transformation matrix for stiffener elements

$\{\omega\}$ - vector of weight factors

$\{\varepsilon_o\}$ - initial strain vector

LIST OF MATRICES (cont'd.)

$\{\varepsilon^L\}$, $\{\varepsilon^{NL}\}$	- linear and nonlinear strain vectors for plate elements
$\{\varepsilon_s^L\}$, $\{\varepsilon_s^{NL}\}$	- linear and nonlinear strain vectors for stiffener
$\{\varepsilon\}$	- total strain vector for plate elements
$\{\varepsilon_s\}$	- total strain vector for stiffener elements
$\{\sigma_o\}$	- initial stress vector
$\{\sigma\}$	- stress vector for plate elements
$\{\sigma^s\}$	- stress vector for stiffener elements
$\{\delta\}$	- displacements vector
$\{\delta_e\}$	- element nodal displacements vector
$\{\delta^s\}$	- nodal displacements vector for stiffener elements
$\{\delta_p^s\}$	- in-plane nodal displacements vector for stiffener elements
$\{\delta_b^s\}$	- out-of-plane nodal displacements vector for stiffener elements
$\{\delta_I\}$, $\{\delta_B\}$	- displacement vectors corresponding to interior and exterior nodes of the diaphragm
$\{\delta_o\}$	- initial displacement vector for plate elements
$\{\delta_o^s\}$	- initial displacement vector for the stiffener elements
$\{\psi\}$	- vector of residual forces

CHAPTER ONE

INTRODUCTION

1.1 Introduction

The application of thin-walled steel box girders as principal load carrying members in bridge structures has gained considerable popularity since the Second World War due to major developments in material and welding technologies, and the tendency towards new and more slender steel structures.

The box girder is a complex structural member comprised of stiffened horizontal flange plates, and vertical or inclined web plates. In addition, it is typically provided with transverse diaphragms over the supports, together with some intermediate diaphragms or cross frames, if necessary. Plate reinforcement of the box's components is generally accomplished by weldment of longitudinal and transverse structural elements such as angles or Tees.

The composition of a box girder gives the designer considerable freedom to place material in the most efficient manner with respect to

strength and stiffness requirements. As such, there can be significant reductions in weight as compared to other structural types, so that longer spans can be achieved.

In effect, box girders are designed to function three dimensionally to resist bending, shear, and substantial torsional loadings. Consequently, the use of box girder construction in bridges leads to superior structural performance over truss or plate girder bridges, and often constitutes an economical solution in the intermediate to long span range.

Steel box girders are much more complicated than the commonly used compact section beam members. In terms of their influencing behaviour, such phenomena as: shear lag, torsional warping, and cross sectional distortion, have been the subject of many investigations [1-4]. Another aspect related to nonlinear behaviour is the post-buckling strength of the plate panels which is affected by the stress distribution within the box girder's components, and the existence of initial imperfections.

1.2 Background to the problem

It is known that the compression flange is the most critical of a box girder's components since its buckling can initiate failure of the entire structure [5]. Unfortunately, in many practical cases, the plate width-to-thickness ratios used in the design are in the range of 30 to 70 where post-buckling reserve strength is negligible; while the

weakening effect of imperfections is not. The reason for the absence of post-buckling strength of the compression flange is that plasticity is usually encountered at stress levels close to the buckling stress. Besides, the boundary edges of the flange are free to pull-in at the junctions of the webs.

The collapse during erection of four large steel box girder bridges [6, 7] in the late 1960's and early 70's, taught structural designers lessons about the behaviour of these girders and resulted in several simple rules for design and detailing [8]. Theoretical and experimental studies have been mainly performed in the three countries affected by the accidents, namely the United Kingdom [9,10], Australia [11], and West Germany [12, 13]. Some conclusions were tentatively made at that time [14], e.g.

"The linear plate buckling theory appears to be sufficiently on the unsafe side for sections that are wide, in comparison with their length, so that consideration of the ultimate strength theory of initially deformed stiffened panels needs to be used in design."

The above statement, indicates the importance of imperfections on the buckling strength of steel box girder bridges, and underscores the need for a rigorous buckling investigation, both analytical and experimental.

Theoretical determinations of the collapse behaviour of box girders have been largely restricted to individual components such as

flanges [15-18], webs [19, 20], and diaphragms [21, 22]. Few theoretical studies have been done on the behaviour of the whole box as an integral structure [23-25].

The problem of investigating the behaviour of a whole steel box girder is very complex because it is influenced simultaneously by: a) the interaction between all walls composing the box girder, b) the presence of numerous longitudinal and transverse stiffeners, c) the material nonlinearity, due to yielding of certain portions of the girder, and d) geometric nonlinearity (change of geometry effect).

A mathematical formulation of the behaviour of a steel box girder is very complex; while, on the other hand, experimental tests tend to be unduly expensive. However, both kinds of investigation are required to achieve further understanding of the behaviour of box girders.

1.3 Imperfections and their effects

In the fabrication industry, steel box girders are constructed from stiffened steel plate components that include the flanges, webs and diaphragms. The reinforcement of these components is achieved through welding of longitudinal and transverse stiffeners in the form of flats, Tees or angles. Due to the fabrication processes that involve flame cutting, welding, and assembly of the components, two major types of imperfection are incurred. One type is geometric, and includes the deviation from flatness in the plate components which comprise the box

girder, out-of-straightness, and lateral deflection of the stiffeners as shown in Figure 1.1. The second is known as a structural imperfection and exhibits itself as a residual stress equilibrated system that results from shrinkage due to welding at sections remote from the free ends [18, 26]. The residual stress distribution is characterized by localized tensile yielding stresses at the welds (in the heat affected zones), which is balanced by compressive stresses in the rest of the cross section. A typical welding residual stress distribution in an open or "bathtub" type box girder is shown in Figure 1.2.

An additional complication arises due to geometrical deviations from out-of-planeness of the flange and web plates, and out-of-straightness of the stiffeners and cross girders, either by curvature, or by not being in line, (especially near the joints or splices). These imperfections introduce secondary eccentricities which exacerbate those induced by the applied loading, and reduce the strength of steel plated structures [27]. Not only the amplitude of initial imperfection but also the mode of imperfection may affect the strength, especially in stiffened panels. In fact, the factor which controls the critical mode of failure is the net eccentricity at the centre of the stiffened panel [28]. Since the magnitude and the mode of imperfection affect the strength of stiffened panels, the importance of geometrical imperfections then becomes apparent.

Up to the early 1970's very little information was available concerning the role of imperfections on box girder behaviour. To shed light on this aspect of the problem, measurements of imperfections on

panels, subpanels and stiffeners of steel bridges were made in several European countries [29-31] and, recently in Canada [32]. Some distortional tolerances given by national codes are displayed in Table 1.1. The diversity of the tolerance levels indicates the uncertainty of the role played by, and the extend to which, imperfections affect the strength of these structures.

The principle cause of residual stresses stems from the welding of stiffeners to the plate elements comprising the webs and flanges. These stresses are dependent on a number of parameters including plate and stiffener geometries, rate of weldment deposition, the number of passes and their application sequencing. The consequences of such a fabrication procedure is to incur further residual stresses in both the stiffeners and the plate elements. Fortunately, it appears reasonable [18] to assume that uniform compressive residual stresses are balanced by a block of tensile yield on each side of the weld.

The magnitude of compressive stresses induced in plated structures due to welding, can be considerable when compared to the critical buckling stresses of the plate sub-panels. Consequently, they should not be ignored when they are combined with those induced by subsequent loading.

1.4 Literature Review

The first systematic studies in the field of thin-walled beam theory were done by Vlasov [33, 34] and by Timoshenko [35, 36], who

worked on open or single cell section beams. This was later generalized for beams of any section by Karman and Christensen [37]. Capurso [38] developed a more general theory of thin-walled beams which even takes shear lag into account.

Buckling behaviour of complicated box girders has been addressed by examining separately the plate panels constituting each component, i.e the compression flange has been frequently distinguished separately from the webs and diaphragms. As a result, simplifications can be made that have led to three different approaches, namely; the strut approach, the orthotropic plate approach, and the discretely stiffened plate method.

In the strut approach, the membrane effect in the plate is disregarded, and the stiffened plate is replaced by a series of unconnected struts consisting of a stiffener and an associated effective width of the plate. Such width is normally based on empirical formulae [39]. Systematic studies employing that concept have been carried out by Little [40], Horne [41], Murray [16] and Smith [42].

In the orthotropic plate approach, the stiffened plate is treated as an equivalent orthotropic plate. Massonnet and Maquoi [43] used such an approach in which large deflection is considered together with a failure criterion which limits the mean longitudinal stresses along the unloaded edges of the orthotropic panel to the yield stress value. Recently, this theory has been modified and simplified by Jetteur [44] to account for the shear lag effect. The approach, however, did not account for the effect of residual stresses.

The discretely stiffened plate approach is considered to be the most accurate evaluation of the ultimate strength since it accounts for the possibility of the local behaviour of plate panels between stiffeners, and the overall behaviour of a stiffened plate to be interactive. The discretely stiffened plate approach can be derived by utilizing finite difference or finite element methods. Moolani and Dowling [45] adopted the finite difference method to investigate the collapse behaviour of stiffened panels. Because the finite element technique is particularly versatile, it has been used for predicting the collapse behaviour of stiffened steel panels or cylinders. Papers grouped under this heading have been presented by many authors such as Crisfield [46, 47], Soreide et al. [48, 49], Nordsve and Moan [50], Fujita et al. [51], and Ueda and Yao [52]. The above researchers only investigated the behaviour of isolated stiffened panels under different boundary conditions and edge loadings. They accounted for elasto-plastic large deflection behaviour. However the differences between their aproaches lie in the continuum formulation, material representation, type of finite elements and solution method adopted.

Crisfield [46] considered the effect of residual stresses in unstiffened panels, while Ueda and Yao [52] studied simply supported steel panels stiffened with uneccentric flat stiffeners, including the effect of residual stresses. More recently, Nordsve and Moan [50] modelled the residual stresses for eccentrically stiffened plate panels.

Although much work has been done to investigate the behaviour of stiffened plates, relatively little has been accomplished concerning the

investigation of the behaviour of the whole box. In 1972, Graves Smith [53] investigated the response of unstiffened box beams under pure bending. Yilamz [21] analysed the behaviour of prismatic straight unstiffened steel box girders loaded up to failure. He excluded buckling of the box's components. Puthli et al. [22] investigated modelling of an unstiffened box girder, where the nonlinear behaviour of the box's components at an intermediate support was considered. However, the effect of residual stresses was excluded in their analysis. Lee [54] developed a three-dimensional plate assemblage nonlinear finite element program to study the collapse behaviour of cold-formed thin-walled beams under different loadings. More recently, Jetteur et al. [23] simulated the behaviour of stiffened steel box girders with, and without, shear lag using the finite element method. However, his model was incomplete, since it excluded diaphragm modelling and the effect of residual stresses. As yet, to the author's knowledge, there has not been a comprehensive model that embraces all the components of a stiffened box girder and accounts for both geometric and structural imperfections.

With respect to the experimental investigations into the behaviour of box girder, few tests have been conducted. Parr and Maggard [55] reported on the ultimate strength of an unstiffened box beam having stocky plate components and subjected to flexural loads only. Corrado [56], and Corrado and Yen [57] conducted experiments on two box girder models to failure in bending and torsion. Eight box girders were tested by Dowling et al. [58], and their results highlight the fact that collapse may also arise from buckling of the web plates or by a complex interaction of buckling of the flanges, webs, and other

components. Massonnet and Maquoi [43] tested stiffened box girder models under pure bending. Roderick and Skaloud [59] reported on a stiffened box girder tested as a cantilever and compared the experimental collapse load with other theories available in the literature. Models of box girder bridges were tested by Dubas [60] and subsequently by Steinhardt [61, 62]. Six box girders, measuring 8.6 m in span, 1.5 m in height and 1.0 m in width, were tested to failure by Mikami, Dogaki and Yonezawa [63]. In Canada, Tupula [64] tested three stiffened box girder models up to collapse. Korol and Thimmhardy [65, 66] tested a symmetrical overhanging rectangular stiffened steel box girder that consisted of thin plates with width-to-thickness ratios which are commonly used in Canada. The model was to simulate the behaviour of a pier girder for a continuous bridge structure over the Rideau River in Ottawa, Canada.

1.5 Objective and scope

The literature has revealed that previous finite element models did not consider all the components that comprise a typical stiffened steel box girder as acting integrally. In addition, these models considered only geometric imperfections or residual stresses due to welding. To this end, then, a rigorous elasto-plastic large displacement, finite element model is developed [67]. This incorporates the components within the framework of an entire structure in an efficient way. A major contribution of the work is the inclusion of geometric and structural imperfections which arise during the girder manufacturing processes. The model represented in this thesis is capable of predict-

ing inelastic buckling behaviour of the entire girder and its ultimate strength under statically applied loading. It is also applicable to other types of three dimensional structures.

Although the box girder's plate panels were assumed to deform with large displacements prior to failure, the associated strains would be expected to remain small. Consequently, the problem of large strains is beyond the scope of the present study. Plate panel out-of-plane deviations, and out-of-straightness of stiffeners are the geometric imperfections that are taken into account. Residual stresses due to shrinkage of the weldment are also considered and represent the type of structural imperfection included. The choice of the finite element method used for this study permits the handling of arbitrary loading, boundary conditions and material properties.

From theoretical and experimental data available in the literature, validation tests were performed on the model developed. Thus confirmed, the present finite element model was applied to a symmetrical overhanging stiffened steel box girder model recently tested at McMaster University, to check the degree to which the model is capable of predicting the box behaviour and strength.

Moreover, the present versatile theoretical model can be used extensively in future research to account for all parameters typical to stiffened steel box girders, and to provide insight into the structural behaviour of such a complex structure.

The finite element modelling of stiffened steel box girders is represented in Chapter 2. The basic type of elements used in the modelling process are formulated considering both bending and in-plane actions. The non-conforming rectangular plate elements are used to model the plate components of the box, while eccentric beam elements are applied to represent the stiffeners. Diaphragms are treated as substructures and then coupled with the rest of the box. Geometric and material nonlinearities have been treated separately and were incorporated with strain-displacement equations and stress-strain equations in matrix notation. With the application of the principle of virtual work, nonlinearities were subsequently combined and the tangent stiffness matrix is developed.

In Chapter 3, the method of solution is discussed, and the finite element model which is based on the mathematical formulation of Chapter 2, is tested. Test examples include simple structural components such as beams, plates, and 3-D thin-walled structures such as a single chord hollow section T-joint and an unstiffened steel box girder. These examples, which cover different loading configurations and boundary conditions, are compared with published values of other researchers who used analytical approaches or experiments.

Applications of the finite element model to a symmetrical overhanging stiffened steel box girder model tested at McMaster University is investigated in Chapter 4. A series of analytical simulations is performed to study the effects of failure load sensitivity to imperfections. These tests were made for perfect box and imperfect girders with

different types of imperfection confined to the compression flange. These types included out-of-planeness of plate panels, stiffener out-of-straightness, residual stresses, and a superimposed imperfection mode. One simulation is carried out to investigate the effect of shear lag on strength reduction of the girder. Comparison of results with experiments and other sources is made, wherever possible.

The work is concluded in Chapter 5. Recommendations are made for possible future work using the present model.

TABLE 1.1

Some Distortional Tolerances Given by National Codes [68]

CODE	COUNTRY	TYPE OF DISTORTION	
		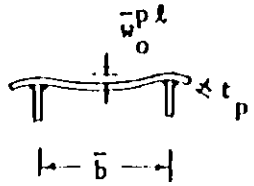	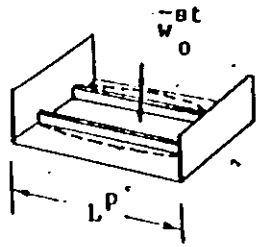
Merrison rule (1973)	United Kingdom	$\bar{w}_o^{pl} < \min \begin{cases} t_p/6.0+2 \\ t_p/3 \end{cases}$	$\bar{w}_o^{st} = L^p/1200$ towards the plate $= L^p/900$ towards the stiffener $\bar{w}_o^{st} > 2.0$ mm
BS 5400 (1982)	United Kingdom	$\frac{\bar{b}}{165}\sqrt{\frac{\sigma_y}{355}}$	$L^p/750$
NBN BS1-001	Belgium	$\bar{b}/250$: max 4 mm	$L^p/500$: max 8 mm
DAST 012	West Germany	$\bar{b}/250$	$L^p/400$
CN2	Italy	$\bar{b}/400$	$L^p/500$
NS 3472	Norway	$\bar{b}/133$	$L^p/1000$
St. BK-N1	Sweden	$\bar{b}/150$	$L^p/600$
AASHTO (1975)	U.S.A.	$\frac{0.159\ L^p}{144\sqrt{t_p}}$: max 4.8 mm	$L^p/480$

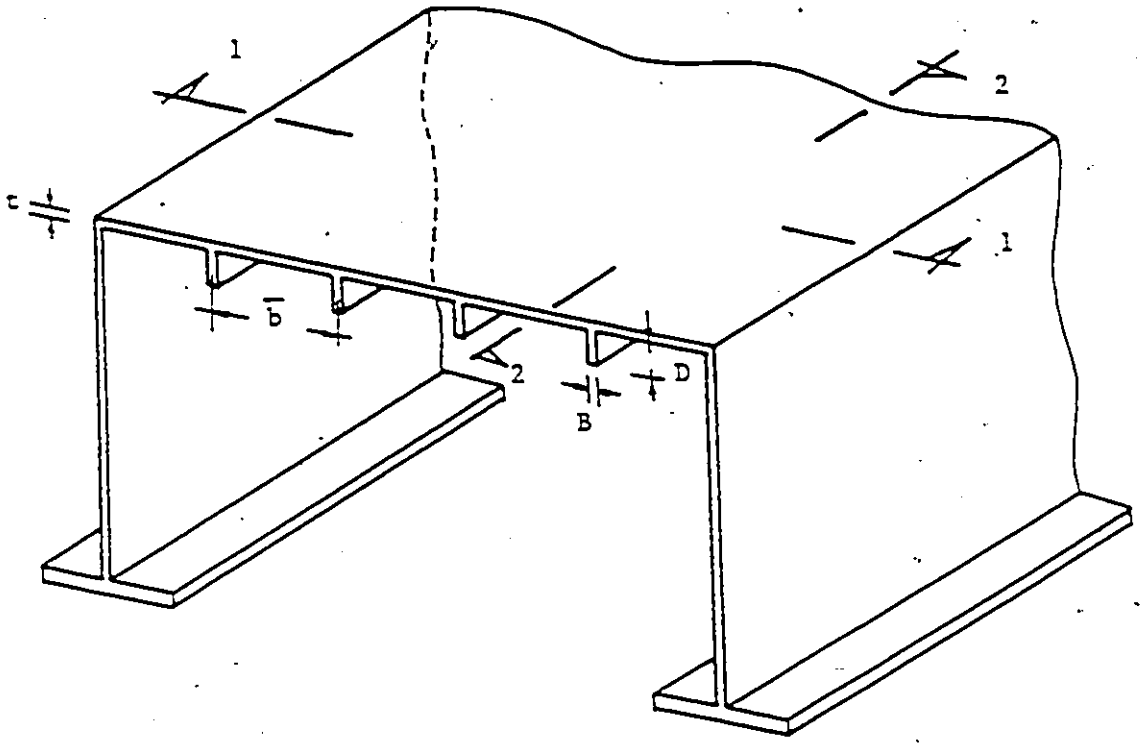

a) Typical stiffened steel box girder

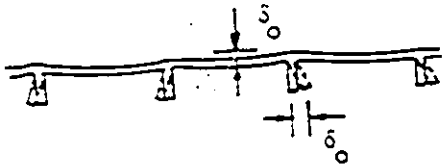

Sec. 1-1

b) Plate imperfection and lateral deflection of the stiffeners

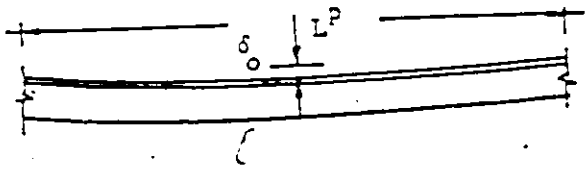

Sec. 2-2

c) Out-of-straightness of the stiffeners

Figure 1.1 : An example of Geometric Imperfections Confined to Compression Flange of Stiffened Box Girder

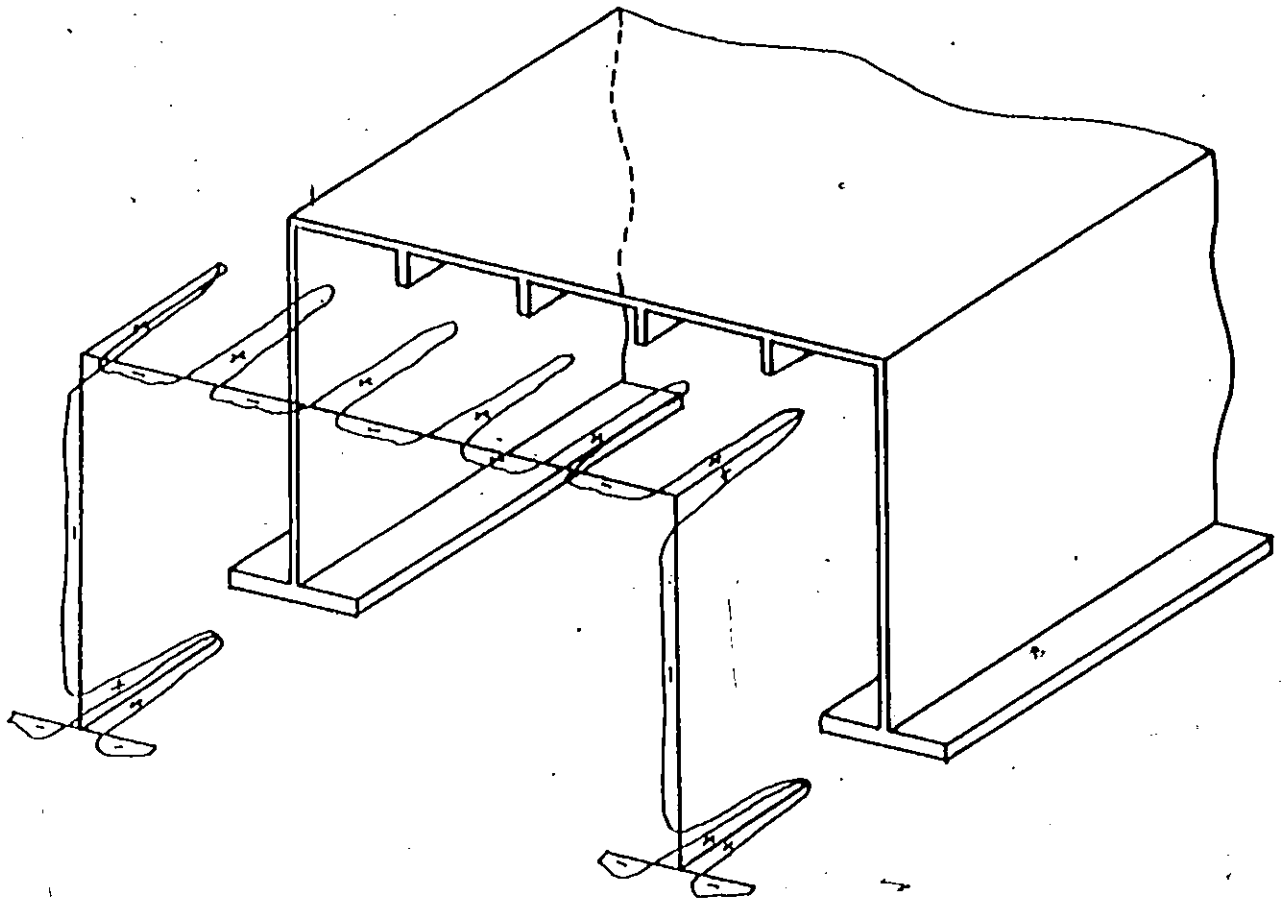

Figure 1.2 : Typical Distribution of Longitudinal Residual Stresses in Steel Box Girder

CHAPTER TWO

FINITE ELEMENT MODELLING OF STIFFENED STEEL BOX GIRDER

2.1 Introduction

The objective of this chapter is to develop a realistic analytical model for predicting the behaviour of stiffened steel box girders under static loads. A typical configuration of a stiffened box girder is shown in Figure 2.1. It is intended to include in this model all components comprising a stiffened box girder (flanges, webs, diaphragms, longitudinal and transverse stiffeners, etc.) as separate entities modelled individually as different finite elements. Both geometric and material nonlinearities are included so that the inelastic buckling behaviour and the ultimate strength of a box girder can be predicted. Geometric imperfections and locked-in stresses due to welding are also to be accounted for.

The following points have been considered in the finite element modelling.

- In computing the element stiffness matrices, it is assumed that the girder is made of thin-walled members so that Kirchhoff's hypothesis for plate bending is valid.

- The deflections and initial imperfections of the box girder's components can be large enough to alter the geometry of the structure significantly. Hence, Marguerre's large deflection theory for shallow thin shells has been adopted [69]. Consequently, the nonlinear strain-displacement relationships include the second order terms due to large deflection and those terms corresponding to the initial imperfections of the mid-surface of the box's skin.

- The approximation used for initial imperfections is the same as that used for the plate bending element's displacement field. However, the nodal degrees of freedom (D.O.F.) for the former are prescribed in accordance with the initial imperfect shape of the box girder's plate components.

- The residual stresses, due to welding, are incorporated via an idealized pattern [18, 50] in self-equilibrium.

- Lagrangian formulation is adopted in which stresses and strains are referred to the orginal configuration while the displacements are described with respect to the initial position.

Since a box girder is essentially a spatial plate structure and often strengthened by beam stiffeners, in-plane and out-of-plane actions

should be included in the finite element modelling. At the present time, it is intended to model straight box girders with rectangular box section. For bending action, the twelve degrees of freedom, non-conforming rectangular plate element is used [70]. Although, Abu Ghazeleh [71] had developed the rectangular element to achieve displacement compatibility between the in-plane and out-of-plane displacements for the flanges and webs or diaphragms at the junctions of the box girder's components, a modified and more economical version of this element is employed in the model to be presented.

An eccentric beam-column element is used to model the longitudinal stiffeners as well as the transverse stiffeners of the box girder. Only symmetric stiffeners (i.e. flats and Tees) have been considered.

Three-dimensional assemblage is achieved through proper transformation of the element stiffness matrices from local to the global coordinate system for various elements involved. The sub-global stiffness matrices for a diaphragm is first assembled. This is then subjected to static condensation so as to eliminate the degrees of freedom for the nodes not lying on the perimeter of the diaphragm. This helps to reduce the size of the overall global stiffness matrix and hence renders a more efficient numerical scheme.

2.2 Rectangular Plate Element Formulation

2.2.1 Displacement Fields

The use of Abu-Ghazeleh's element [71], that provides inter-element displacement compatibility for rectangular elements which are normal to each other, leads to six D.O.F. per node i.e. u, v, w, θ_x, θ_y, and θ_z. However, a modified version of this element has been adopted in the present modelling in such a way as to achieve both, displacement continuity along the edges of the box, and minimal total number of unknowns for the overall box structure. Hence, three different plate elements have been used. These elements are different from each other only in terms of the in-plane displacement fields. Referring to Figure 2.1, element type A, which lies at the junctions between flanges and webs or flanges and diaphragms, has a cubic field for in-plane displacement normal to the edge (i.e. edge 1-2 in Figure 2.2 (a)) at a junction. All other in-plane displacements are linear along the element edges. Element type B (Figure 2.1), at the corner of mutually perpendicular elements, (flange-web-diaphragm) provides a cubic field for in-plane displacements normal to its two intersecting edges (i.e. edges 1-2, and 1-4 in Figure 2.2(a)). Again, all other in-plane displacements are linear along the element edges. The interior elements (element type C) have linear in-plane displacements along all edges.

The displacement field corresponding to the twelve D.O.F non-conforming rectangular plate bending element (a × b) is given by

$$w(\xi, \eta) = a_1 + a_2 \xi + a_3 \eta + a_4 \xi^2 + a_5 \xi \eta + a_6 \eta^2$$

$$+ a_7 \xi^3 + a_8 \xi^2 \eta + a_9 \xi \eta^2 + a_{10} \eta^3$$

$$+ a_{11} \xi^3 \eta + a_{12} \xi \eta^3 \qquad (2.1)$$

where $\xi = \frac{x}{a}$, and $\eta = \frac{y}{b}$ are the dimensionless coordinates as shown in Fig. 2.3.

For in-plane action, the following displacement fields are used for element type A;

$$u(\xi, \eta) = a_{13} + a_{14} \xi + a_{15} \eta + a_{16} \xi \eta \qquad (2.2)$$

$$v(\xi, \eta) = a_{17} + a_{18} \xi + a_{19} \eta + a_{20} \xi \eta + a_{21} (1-\eta) \xi^2$$

$$+ a_{22} (1-\eta) \xi^3 \qquad (2.3)$$

and for element type B;

$$u(\xi, \eta) = a_{13} + a_{14} \eta + a_{15} \xi + a_{16} \xi \eta + a_{17} (1-\xi) \eta^2$$

$$+ a_{18} (1-\xi) \eta^3 \qquad (2.4)$$

$$v(\xi, \eta) = a_{19} + a_{20} \xi + a_{21} \eta + a_{22} \xi \eta + a_{23} (1-\eta) \xi^2$$

$$+ a_{24} (1-\eta) \xi^3 \qquad (2.5)$$

However, the interior elements (type C) employ the following simple bilinear displacements fields:

$$u(\xi,\eta) = a_{13} + a_{14}\,\xi + a_{15}\,\eta + a_{16}\,\xi\,\eta \tag{2.6}$$

$$v(\xi,\eta) = a_{17} + a_{18}\,\xi + a_{19}\,\eta + a_{20}\,\xi\,\eta \tag{2.7}$$

These polynomials lead to different degrees of freedom per node for different elements. After solving for the generalized parameters for the in-plane and out-of-plane displacement polynomials in terms of the nodal D.O.F., the following equations result:

$$u(\xi,\eta) = \sum_{i=1}^{n} N_{pi}(\xi,\eta)\,\delta_{ui} \tag{2.8a}$$

$$v(\xi,\eta) = \sum_{i=1}^{n} N_{pi}(\xi,\eta)\,\delta_{vi} \tag{2.8b}$$

$$w(\xi,\eta) = \sum_{i=1}^{12} N_{bi}(\xi,\eta)\,\delta_{wi} \tag{2.8c}$$

where $N_{pi}(\xi,\eta)$ and $N_{bi}(\xi,\eta)$ are the shape functions for in-plane and out-of-plane displacements and are listed in Appendix A.1. In addition, n depends on the type of element and takes a value of 4 or 6. δ_{ui} and δ_{vi} are the in-plane degrees of freedom for u, and v displacement fields, respectively. It should be noted that, the in-plane displacements have been used to obtain the in-plane rotation degree of freedom as $\theta_z = (\frac{\partial v}{\partial x} - \frac{\partial u}{\partial y})/2$ and have been accommodated through a

transformation matrix. Moreover, δ_{wi} represents the out-of-plane degrees of freedom w, $\theta_x = \frac{\partial w}{\partial y}$, and $\theta_y = -\frac{\partial w}{\partial x}$.

The elements considered in the modelling have different degrees of freedom per node. Therefore, an added degree of freedom θ_z has been introduced at each node to streamline the process. If the node does not have that degree of freedom it is suppressed to zero during assemblage.

The full displacement vector for a rectangular plate element is then given by;

$$\{\delta_e\}^T = < u_1, v_1, \theta_{z1}, w_1, \theta_{x1}, \theta_{y1}, u_2, v_2, \theta_{z2}, w_2,$$

$$\theta_{x2}, \theta_{y2}, \ldots \theta_{y4} > \qquad (2.9)$$

Equations 2.8 may now be combined into a single equation as

$$\begin{Bmatrix} u \\ v \\ w \end{Bmatrix} = [N] \{\delta_e\} \qquad (2.10)$$

where the matrix [N] of shape functions differs according to the element type in use.

2.2.2 Strain-Displacement Relationship

By adopting Marguerre's shallow shell theory, the strain (including membrane and flexure) - displacement equations of plates can be written in the following form:

$$\varepsilon_{xx} = \frac{\partial u}{\partial x} - z\frac{\partial^2 w}{\partial x^2} + \frac{1}{2}\left(\frac{\partial w}{\partial x}\right)^2 + \frac{\partial w_o}{\partial x}\frac{\partial w}{\partial x}$$

$$\varepsilon_{yy} = \frac{\partial v}{\partial y} - z\frac{\partial^2 w}{\partial y^2} + \frac{1}{2}\left(\frac{\partial w}{\partial y}\right)^2 + \frac{\partial w_o}{\partial y}\frac{\partial w}{\partial y}$$

$$\gamma_{xy} = \frac{\partial v}{\partial x} + \frac{\partial u}{\partial y} - 2z\frac{\partial^2 w}{\partial x\,\partial y} + \left(\frac{\partial w}{\partial x}\right)\left(\frac{\partial w}{\partial y}\right) + \frac{\partial w_o}{\partial y}\frac{\partial w}{\partial x} + \frac{\partial w_o}{\partial x}\frac{\partial w}{\partial y} \qquad (2.11)$$

where w_o denotes the initial deflection displacement field of the plate due to imperfections. u, v and w are displacements in the x, y and z directions, respectively, and $\{\varepsilon\}^T = < \varepsilon_{xx} \;\; \varepsilon_{yy} \;\; \gamma_{xy} >$ are the strain components.

The strains $\{\varepsilon\}$ can be separated into linear $\{\varepsilon^L\}$ and nonlinear $\{\varepsilon^{NL}\}$ parts for convenience as

$$\{\varepsilon\} = \{\varepsilon^L\} + \{\varepsilon^{NL}\} \qquad (2.12)$$

where the individual parts are given by

$$\{\varepsilon^L\} = \begin{bmatrix} \frac{\partial}{\partial x} & 0 & -z\frac{\partial^2}{\partial x^2} \\ 0 & \frac{\partial}{\partial y} & -z\frac{\partial^2}{\partial y^2} \\ \frac{\partial}{\partial y} & \frac{\partial}{\partial x} & -2z\frac{\partial^2}{\partial x\,\partial y} \end{bmatrix} \begin{Bmatrix} u \\ v \\ w \end{Bmatrix} \qquad (2.13)$$

and

$$\{\epsilon^{NL}\} = \frac{1}{2} \begin{Bmatrix} (\frac{\partial w}{\partial x})^2 \\ (\frac{\partial w}{\partial y})^2 \\ 2\,(\frac{\partial w}{\partial x})\,(\frac{\partial w}{\partial y}) \end{Bmatrix} + \begin{Bmatrix} (\frac{\partial w}{\partial x}\frac{\partial w_o}{\partial x}) \\ (\frac{\partial w}{\partial y}\frac{\partial w_o}{\partial y}) \\ (\frac{\partial w}{\partial x}\frac{\partial w_o}{\partial y}) + (\frac{\partial w}{\partial y}\frac{\partial w_o}{\partial x}) \end{Bmatrix} \qquad (2.14)$$

First consider the linear terms of the strain vector. Equation 2.13. can be rewritten as

$$\{\epsilon^L\} = [B_L]\ \{\delta_e\} = \begin{bmatrix} \frac{\partial N_{pi}}{\partial x} & 0 & -z\frac{\partial^2 N_{bi}}{\partial x^2} \\ 0 & \frac{\partial N_{pi}}{\partial y} & -z\frac{\partial^2 N_{bi}}{\partial y^2} \\ \frac{\partial N_{pi}}{\partial y} & \frac{\partial N_{pi}}{\partial x} & -2z\frac{\partial^2 N_{bi}}{\partial x\,\partial y} \end{bmatrix} \{\delta_e\} \qquad (2.15)$$

where the linear matrix $[B_L]$ depends on geometry of the element.

It is well known that the bilinear in-plane element gives particularly poor results for analysis of in-plane bending problems unless a large number of elements are employed [72, 73]. This is due to the parasitic shear strains associated with bending strains when the element is subjected to in-plane bending. Instead of using reduced numerical integration technique [46], only terms corresponding to in-plane displacement in the last row of the B-matrix in Equation 2.15 are modified to get rid of the parasitic shear strain. This is

accomplished in such a way to achieve constant shear strain; as an average value at the centroid of a rectangular element.

Now consider the nonlinear terms. Equation 2.14 can be written as

$$\underset{3\times1}{\{\epsilon^{NL}\}} = \frac{1}{2}\underset{3\times2}{[S]}\underset{2\times1}{\{Q\}} + \underset{3\times2}{[S_o]}\underset{2\times1}{\{Q\}} \tag{2.16}$$

where

$$[S]^T = \begin{bmatrix} \frac{\partial w}{\partial x} & 0 & \frac{\partial w}{\partial y} \\ 0 & \frac{\partial w}{\partial y} & \frac{\partial w}{\partial x} \end{bmatrix} \tag{2.17}$$

$$[S_o]^T = \begin{bmatrix} \frac{\partial w_o}{\partial x} & 0 & \frac{\partial w_o}{\partial y} \\ 0 & \frac{\partial w_o}{\partial y} & \frac{\partial w_o}{\partial x} \end{bmatrix} \tag{2.18}$$

and vector $\{Q\}$ is then given by

$$\underset{2\times1}{\{Q\}} = \begin{bmatrix} \underset{1\times24}{G_1} \\ \underset{1\times24}{G_2} \end{bmatrix} \underset{24\times1}{\{\delta_e\}} = \underset{2\times24}{[G]}\underset{24\times1}{\{\delta_e^*\}}. \tag{2.19}$$

Using Equations 2.8(c), matrix [G] in Equation 2.19 can be expanded as

$$[G] = \begin{bmatrix} 0 & 0 & 0 & \frac{\partial N_{b1}}{\partial x} & \frac{\partial N_{b2}}{\partial x} & \frac{\partial N_{b3}}{\partial x} & 0 & 0 & 0 & \frac{\partial N_{b4}}{\partial x} & \frac{\partial N_{b5}}{\partial x} & \frac{\partial N_{b6}}{\partial x} \\ 0 & 0 & 0 & \frac{\partial N_{b1}}{\partial y} & \frac{\partial N_{b2}}{\partial y} & \frac{\partial N_{b3}}{\partial y} & 0 & 0 & 0 & \frac{\partial N_{b4}}{\partial y} & \frac{\partial N_{b5}}{\partial y} & \frac{\partial N_{b6}}{\partial y} \end{bmatrix}$$

$$\begin{bmatrix} 0 & 0 & 0 & \frac{\partial N_{b7}}{\partial x} & \frac{\partial N_{b8}}{\partial x} & \frac{\partial N_{b9}}{\partial x} & 0 & 0 & 0 & \frac{\partial N_{b10}}{\partial x} & \frac{\partial N_{b11}}{\partial x} & \frac{\partial N_{b12}}{\partial x} \\ 0 & 0 & 0 & \frac{\partial N_{b7}}{\partial y} & \frac{\partial N_{b8}}{\partial y} & \frac{\partial N_{b9}}{\partial y} & 0 & 0 & 0 & \frac{\partial N_{b10}}{\partial y} & \frac{\partial N_{b11}}{\partial y} & \frac{\partial N_{b12}}{\partial y} \end{bmatrix} \qquad (2.20)$$

Now look at the incremental form of Equation 2.16

$$d\{\varepsilon^{NL}\} = \frac{1}{2}\, d[S]\ \{Q\} + \frac{1}{2}\,[S]\ d\{Q\} + [S_o]\ d\{Q\} \qquad (2.21)$$

Owing to the linearity of matrices [S] and {Q} in terms of displacement, one can write [70];

$$\frac{1}{2}\,[S]\ d\{Q\} = \frac{1}{2}\, d[S]\ \{Q\} \qquad (2.22)$$

and after substitutions, Equation 2.21 can be rewritten as

$$d\{\varepsilon^{NL}\} = [S]\ d\{Q\} + [S_o]\ d\{Q\} = [\underline{S} + \underline{S_o}]\ d\{Q\} \qquad (2.23a)$$

The incremental form of Equation 2.19 substituted into Equation 2.23(a), leads to the following:

$$d\{\varepsilon^{NL}\} = [\underline{S} + \underline{S_o}]\ [G]\ d\{\delta_e\} \qquad (2.23b)$$

Since the strain matrix due to large deflection $[B_{NL}]$ is sought, which relates the incremental strains to incremental displacements via Equation 2.23(b), it is obtained as

$$[B_{NL}]_{3\times24} = [\underset{3\times2}{S} + \underset{3\times2}{S_o}]\ \underset{2\times24}{[G]}. \tag{2.24}$$

Using the definition expressed in Equation 2.17 to 2.19, and based on the assumption that the initial imperfection displacement field within each element is expressed by the conventional finite element shape functions, one can write;

$$[B_{NL}] = \begin{bmatrix} G_1 & 0 \\ 0 & G_2 \\ G_2 & G_1 \end{bmatrix} \{\delta_e\} \begin{bmatrix} G_1 \\ G_2 \end{bmatrix} + \begin{bmatrix} G_1 & 0 \\ 0 & G_2 \\ G_2 & G_1 \end{bmatrix} \{\delta_o\} \begin{bmatrix} G_1 \\ G_2 \end{bmatrix} \tag{2.25}$$

where $\{\delta_o\}$ is the prescribed nodal displacement vector for a plate element accounting for initial imperfections according to its orientation. Finally, $[B_{NL}]$ takes the following form.

$$\underset{3\times24}{\{B_{NL}\}} = \begin{bmatrix} \underset{1\times24}{G_1}\ \underset{24\times1}{\{\delta_o + \delta_e\}}\ \underset{24\times1}{G_1}\ \underset{1\times24}{} \\ \\ \underset{1\times24}{G_2}\ \underset{24\times1}{\{\delta_o + \delta_e\}}\ \underset{24\times1}{G_2}\ \underset{1\times24}{} \\ \\ \underset{1\times24}{G_2}\ \underset{24\times1}{\{\delta_o + \delta_e\}}\ \underset{24\times1}{G_1}\ \underset{1\times24}{} + \underset{1\times24}{G_1}\ \underset{24\times1}{\{\delta_o + \delta_e\}}\ \underset{24\times1}{G_2}\ \underset{1\times24}{} \end{bmatrix} \tag{2.26}$$

Combining the linear and nonlinear parts together, the final incremental strains are then given by

$$d\{\varepsilon\} = [B_L + B_{NL}]\ d\{\delta_e\} = [B]\ d\{\delta_e\} \tag{2.27}$$

where the total strain matrix is given by

$$[B] = [B_L] + [B_{NL}]. \qquad (2.28)$$
$$3\times24 \quad 3\times24 \quad 3\times24$$

The strain matrix [B] is a function of position within an element and displacements. However, only the $[B_{NL}]$ component needs to be evaluated each time during the incremental nonlinear analysis since it depends on the element nodal displacement $\{\delta_e\}$.

2.2.3 Tangent Stiffness Matrix

Using the virtual work principle, the equilibrium equation for a finite element at any time can be written as

$$\{\psi\ \{\delta_e\}\} = \int_V [B]^T \{\sigma\}\, dV + \{f\} = \{\underline{0}\}. \qquad (2.29)$$

The integral term in Equation 2.29 represents the resisting load vector due to internal stresses and $\{f\}$ represents the load vector due to the externally applied loads. For incremental load analysis, the incremental form of Equation 2.29 can be expressed as

$$d\{\psi\} = \int_V d[B]^T \{\sigma\}\, dV + \int_V [B]^T \{d\sigma\}\, dV + d\{f\} = \{\underline{0}\}. \qquad (2.30)$$

In the elastic range the stress vector $\{\sigma\}$ can be computed from

$$\{\sigma\} = [\tilde{D}]\,(\{\varepsilon\} - \{\varepsilon_o\}) + \{\sigma_o\} \tag{2.31}$$

where $\{\sigma_o\}$ is the initial stress vector, $\{\varepsilon_o\}$ is the initial strain vector and $[\tilde{D}]$ is the elastic compliance matrix [D] given by

$$[D] = \frac{E}{1-\nu^2}\begin{bmatrix} 1 & \nu & 0 \\ \nu & 1 & 0 \\ 0 & 0 & \frac{1-\nu}{2} \end{bmatrix}. \tag{2.32}$$

However, $[\tilde{D}]$ can be an elasto-plastic compliance matrix $[D_{ep}]$ depending on the stress level and is presented in the next Section.

The incremental form of Equation 2.31, relating incremental strains to incremental stresses, takes the following form:

$$\{d\sigma\} = [\tilde{D}][B]\{d\delta_e\} \tag{2.33}$$

Also note that

$$d[B]^T = d[B_{NL}]^T \tag{2.34}$$

because

$$d[B_L] = [\underline{0}] \tag{2.35}$$

The substitution of Equations 2.33 to 2.35 into Equation 2.30, leads to

$$d\{\psi\} = \int_V d[B_{NL}]^T \{\sigma\}\, dV + \int_V [B]^T [\tilde{D}]\ [B]\ \{d\delta_e\}\, dV \qquad (2.36)$$

The first term on the right hand side, after some manipulations, yields the initial stress matrix $[k_\sigma]$.

$$\int_V d[B_{NL}]^T \{\sigma\}\, dV = [k_\sigma]\ \{d\delta_e\} \qquad (2.37)$$

The substitution of $[B_{NL}]$ from Equation 2.24 into the equation above, the following results:

$$[k_\sigma]\ \{d\delta_e\} = \int_V [G]^T d[\underline{S} + \underline{S}_o]^T \{\sigma\}\, dV \qquad (2.38)$$

The product $d[\underline{S} + \underline{S}_o]^T \{\sigma\}$ is evaluated separately using Equation 2.23(b) to obtain

$$d[\underline{S} + \underline{S}_o]^T \{\sigma\} = d \begin{bmatrix} \underline{G}_1\{\delta_o+\delta_e\} & \underline{0} & \underline{G}_2\{\delta_o+\delta_e\} \\ \underline{0} & \underline{G}_2\{\delta_o+\delta_e\} & \underline{G}_1\{\delta_o+\delta_e\} \end{bmatrix} \begin{Bmatrix} \sigma_{xx} \\ \sigma_{yy} \\ \sigma_{xy} \end{Bmatrix}$$

$$= \begin{bmatrix} \sigma_{xx} & \sigma_{xy} \\ \sigma_{yx} & \sigma_{yy} \end{bmatrix} \begin{bmatrix} \underline{G}_1 \\ \underline{G}_2 \end{bmatrix} d\{\delta_e\} \qquad (2.39)$$

The further use of Equation 2.20 reduces Equation 2.39 to

$$d[\underline{S} + \underline{S}_o]^T \{\sigma\} = [M]\ [G]\ d\{\delta_e\} \qquad (2.40)$$

where matrix [M] depends on the current stress level. Substituting Equation 2.40 into Equation 2.38 leads to the initial stress matrix required, i.e.

$$[k_\sigma] = \int_V [G]^T [M] [G] \, dV \tag{2.41}$$

Using Equation 2.28, the second term on the right hand side of Equation 2.36 can be expanded as

$$\int_V \left([\underline{B}_L + \underline{B}_{NL}]^T [\tilde{D}] [\underline{B}_L + \underline{B}_{NL}] \, d\{\delta_e\} \right) dV =$$

$$[\underline{k}_L + \underline{k}_{NL}] \, d\{\delta_e\} = [\bar{k}] \, d\{\delta_e\} \tag{2.42}$$

where $[k_L]$ is the small displacement stiffness matrix, and $[k_{NL}]$ represents the initial displacement stiffness matrix. Both $[k_L]$ and $[k_{NL}]$ matrices can be expressed as

$$[k_L] = \int_V [B_L]^T [\tilde{D}] [B_L] \, dV \tag{2.43}$$

$$[k_{NL}] = \int_V \left([B_L]^T [\tilde{D}] [B_{NL}] + [B_{NL}]^T [\tilde{D}] [B_{NL}] \right.$$

$$\left. + [B_{NL}]^T [\tilde{D}] [B_L] \right) dV. \tag{2.44}$$

However, these are usually computed together as $[\bar{k}]$.

Now, the elemental discretized equilibrium equation is written as

$$d\{\psi\} = \left([k_L] + [k_{NL}] + [k_\sigma]\right) d\{\delta_e\} + d\{f\}$$

$$= \left([\bar{k}] + [k_\sigma]\right) d\{\delta_e\} + d\{f\} = [k_T]\, d\{\delta_e\} + d\{f\}$$

$$= \{\underline{0}\} \qquad (2.45)$$

Matrix $[k_T]$ is the total tangential element stiffness matrix and has to be updated during each load increment. The total stiffness matrix $[k_T]$ is evaluated via numerical integration. Twenty seven Gaussian integration points (3×3×3) within a plate element are shown in Figure 2.3. The numerical integration is carried out in the following manner:

$$[k_T] = [\bar{k}] + [k_\sigma] = \frac{a}{2}\frac{b}{2}\frac{t}{2} \sum_{i=1}^{3}\sum_{j=1}^{3}\sum_{k=1}^{3} \left(\omega_i \omega_j \omega_k [B(\xi_i, \eta_j, Z_k)]^T \cdot \right.$$

$$\left.[\tilde{D}]\,[B(\xi_i, \eta_j, Z_k)]\right) + \frac{a}{2}\frac{b}{2}\frac{t}{2} \sum_{i=1}^{3}\sum_{j=1}^{3} \left(\omega_i \omega_j [G(\xi_i, \eta_j)]^T \cdot \right.$$

$$\left.[M] \cdot [G(\xi_i, \eta_j)]\right) \qquad (2.46)$$

Using the dimensionless coordinates system shown in Fig. 2.3, the location of integration points are given by the following:

$$\{\xi\}^T = \{\eta\}^T = \langle (0.5 - \sqrt{0.15}),\ 0.5,\ (0.5 + \sqrt{0.15}) \rangle \qquad (2.47)$$

and

$$\{Z\}^T = \langle -t\sqrt{0.15},\ 0,\ t\sqrt{0.15} \rangle \tag{2.48}$$

The weight factors for the 3 points integration scheme are given by

$$\{\omega\}^T = \langle \frac{5}{9},\ \frac{8}{9},\ \frac{5}{9} \rangle . \tag{2.49}$$

2.3 Constitutive Equation for the Plate Element

The inelastic behaviour of a material is distinguished from elastic behaviour in that, for the former, the stress-strain relationship varies according to the current state of stress experienced by the material. Therefore, an incremental stress-strain relation must be established. As will be shown, the relation in its simpliest form is analogous to the generalized Hooke's law for elastic materials with the difference that for plane elasticity matrix, [D] is replaced by the elasto-plastic "compliance" matrix $[D_{ep}]$. The detailed derivation of the elasto-plastic matrix has been presented by Yamada et al. [74] and Zienkiewicz et al. [75].

In the following subsection, the Prandtl-Reuss flow rule and the Von Mises [76] yield criterion are employed to derive the elasto-plastic compliance matrix in a very brief manner. In addition, the steel material of the box is assumed isotropic, linear elastic up to the yield limit, and linear strain-hardening thereafter.

2.3.1 Elastic-Plastic Compliance Matrix

The total strain increment $\{d\varepsilon\}$ is the sum of the incremental elastic and plastic components of strains, i.e.

$$\{d\varepsilon\} = \{d\varepsilon_e\} + \{d\varepsilon_p\} \tag{2.50}$$

where the elastic strain increment $\{d\varepsilon_e\}$ is given by

$$\{d\varepsilon_e\} = [D]^{-1} \{d\sigma\}. \tag{2.51}$$

The Prandtl-Ruess flow rule states that plastic strain increments can be expressed, using the normality principles, as

$$\{d\varepsilon_p\} = \lambda \{\frac{\partial F}{\partial \sigma}\} \tag{2.52}$$

where λ is a proportionality factor and F is the yield function defined as

$$F = F(\sigma_1, \sigma_2, \ldots, K) = F(\sigma, K) = 0 \tag{2.53}$$

in which K is a parameter representing strain hardening. The differential of F in 2.53 gives

$$dF = \frac{\partial F}{\partial \sigma_1} \cdot d\sigma_1 + \frac{\partial F}{\partial \sigma_2} \cdot d\sigma_2 + \ldots \frac{\partial F}{\partial K} \cdot dK = \{\frac{\partial F}{\partial \sigma}\} + A\lambda \tag{2.54}$$

After some algebraic manipulations, the parameter A is found to be equal to the strain hardening modulus H', i.e. the slope of the effective stress-strain curve deduced from unixial test as shown in Figure 2.4.

$$A = H' = \frac{d\bar{\sigma}}{d\bar{\varepsilon}_p} = d\bar{\sigma}/(\frac{d\bar{\sigma}}{E} - \frac{d\bar{\sigma}}{E_T}) = \frac{E \cdot E_T}{E - E_T} \tag{2.55}$$

In the equation above, E_T is the tangent modulus.

From Von Mises yield criterion, F in Equation 2.53 is defined as

$$F = (\sigma_{xx}^2 + \sigma_{yy}^2 - \sigma_{xx} \cdot \sigma_{yy} + 3\sigma_{xy}^2)^{1/2} - \sigma_y = \bar{\sigma} - \sigma_y \tag{2.56}$$

Now differentiate Equation 2.56 with respect to σ_i and substitute the following deviatoric stresses

$$\sigma_{xx}^1 = \sigma_{xx} - \frac{1}{3}(\sigma_{xx} + \sigma_{yy}) \tag{2.57a}$$

$$\sigma_{yy}^1 = \sigma_{yy} - \frac{1}{3}(\sigma_{xx} + \sigma_{yy}) \tag{2.57b}$$

$$\sigma_{xy}^1 = \sigma_{xy} \tag{2.57c}$$

to obtain the following

$$\{\frac{\partial F}{\partial \{\sigma\}}\}^T = < \frac{3\sigma^1_{xx}}{2\bar{\sigma}}, \frac{3\sigma^1_{yy}}{2\bar{\sigma}}, \frac{3\sigma^1_{xy}}{\bar{\sigma}} >. \tag{2.58}$$

The elasto-plastic stress-strain relationship sought is of the following form:

$$\{d\sigma\} = [D_{ep}]\ \{d\varepsilon\} \tag{2.59}$$

The substitutions of Equations 2.51 and 2.52 into 2.50, leads to

$$\{d\varepsilon\} = [D]^{-1}\ \{d\sigma\} + \lambda \{\frac{\partial F}{\partial \sigma}\} \tag{2.60a}$$

After, manipulation of Equations 2.52 and 2.53, and invoking Equations 2.55 and 2.58, the above equation becomes

$$\{d\dot{\varepsilon}\} = [D]^{-1}\ \{d\sigma\} + \frac{\{\frac{\partial F}{\partial \sigma}\}\ \{\frac{\partial F}{\partial \sigma}\}^T\ [D]\ \{d\varepsilon\}}{\{\frac{\partial F}{\partial \sigma}\}^T\ [D]\ \{\frac{\partial F}{\partial \sigma}\} + H'} \tag{2.60b}$$

Substituting Equation 2.60(b) into 2.59, one obtains the explicit form of the compliance matrix. This is where

$$[D_{ep}] = \begin{bmatrix} \left(\frac{E}{1-\nu^2} - \frac{S_1^2}{S}\right) & & \text{symm.} \\ \left(\frac{\nu E}{1-\nu^2} - \frac{S_1 S_2}{S}\right) & \left(\frac{E}{1-\nu^2} - \frac{S_2^2}{S}\right) & \\ \left(-\frac{S_1 S_2}{S}\right) & \left(-\frac{S_1 S_2}{S}\right) & \left(\frac{E}{2(1+\nu)} - \frac{S_3^2}{S}\right) \end{bmatrix} \qquad (2.61)$$

and

$$S = \frac{4}{9} H \bar{\sigma}^2 + S_1 \sigma^1_{xx} + S_2 \sigma^1_{yy} + 2S_3 \sigma^1_{xy} \qquad (2.62a)$$

$$S_1 = \frac{E}{1-\nu^2} (\sigma^1_{xx} + \nu\sigma^1_{yy}) \qquad (2.62b)$$

$$S_2 = \frac{E}{1-\nu^2} (\sigma^1_{yy} + \nu\sigma^1_{xx}) \qquad (2.62c)$$

$$S_3 = \frac{E}{1+\nu} (\sigma^1_{xy}) \qquad (2.62d)$$

Also, it is worth noting that for elastic-perfectly plastic material where $E_T = 0$, only the term involving H' will be dropped out but S remains nonzero. Thus the compliance matrix above is valid for both perfectly plastic and the strain hardening materials.

2.4 Eccentric Stiffener Element Formulation

2.4.1 Displacement Field

The eccentric stiffener element presented here is for symmetric stiffeners only, e.g. T-shaped or flat type. A detailed elastic formulation for this element is covered by Mirza [77]. It is now extended to include both material and geometric non-linearities. Figure 2.2(b) illustrates a simple beam-column element with two nodes and three degrees of freedom, u, w, and $\frac{\partial w}{\partial x}$ per node. This element is used to model the eccentric stiffener element. Note that the lateral bending and twisting of the stiffener have been ignored.

The displacements along the centroidal axis of the stiffener element are approximated by the following polynomials:

$$w^{sc} = a_1 + a_2 x + a_3 x^2 + a_4 x^3 \tag{2.63}$$

$$u^{sc} = a_5 + a_6 x + a_7 x^2 \tag{2.64}$$

The transverse displacements for the plate elements representing the skin of the box girder, and the stiffeners are assumed to be the same. However, the axial displacement for the stiffener must be matched with the in-plane displacement of the plate elements along the direction of the stiffeners. This compatibility condition is shown in Figure 2.5 and translates into the following equations

$$w^{st} = w^{sc} \tag{2.65}$$

$$u^{st} = u^{sc} - e \frac{\partial w^{sc}}{\partial x} \tag{2.66}$$

where "e" is the distance along the Z-axis from the centroid of the stiffener to the middle plane of the plate elements. Substituting Equations 2.63, and 2.64 into Equation 2.66, leads to

$$u^{st} = (a_5 - ea_2) + (a_6 + 2e\ a_5)\ x + (a_7 - 3e\ a_4)\ x^2 \tag{2.67}$$

Since the in-plane displacements for the plate elements are linear along x and y directions, this necessitates u^{st} in Equation 2.67 to be linear as well, therefore

$$a_7 = 3e\ a_4. \tag{2.68}$$

Back substitution of a_7 into Equations 2.63, 2.64, and 2.67 yields;

$$w^{sc} = a_1 + a_2\ x + a_3\ x^2 + a_4\ x^3 \tag{2.69}$$

$$u^{sc} = a_5 + a_6\ x + 3e\ a_4\ x^2 \tag{2.70}$$

$$u^{st} = (a_5 - e\ a_2) + (a_6 - 2e\ a_3)\ x \tag{2.71}$$

The equations above define the displacement fields for the eccentric

stiffener element along its centroidal axis (u^{sc}, w^{sc}), and at the mid-surface of the box plate element (u^{st}). Using degrees of freedom shown in Fig. 2.2, the following end conditions result;

$$\begin{aligned} u_1 &= u^{st}(0) \quad , \quad w_1 = w^{st}(0) \quad , \quad \theta_1 = \frac{\partial w^{st}}{\partial x}(0) \\ u_2 &= u^{st}(\ell) \quad , \quad w_2 = w^{st}(\ell) \quad , \quad \theta_2 = \frac{\partial w^{st}}{\partial x}(\ell) \end{aligned} \tag{2.72}$$

Substitution of the nodal coordinates of the stiffener element into Equations 2.69, and 2.71 and using Equation 2.72, the following transformation is obtained

$$\{\delta^s\} = [C]\ \{A\} \tag{2.73}$$

in which

$$\{\delta^s\}^T = < u_1,\ w_1,\ \theta_1,\ u_2,\ w_2,\ \theta_2 > \tag{2.74}$$

$$\{A\}^T = < a_1,\ a_2,\ a_3,\ a_4,\ a_5,\ a_6 > \tag{2.75}$$

$$[C] = \begin{bmatrix} 0 & -e & 0 & 0 & 1 & 0 \\ 1 & 0 & 0 & 0 & 0 & 0 \\ 0 & 1 & 0 & 0 & 0 & 0 \\ 0 & -e & -2e\ell & 0 & 1 & \ell \\ 1 & \ell & \ell^2 & \ell^3 & 0 & 0 \\ 0 & 1 & 2\ell & 3\ell^2 & 0 & 0 \end{bmatrix} \tag{2.76}$$

To find vector $\{A\}$ of the unknown coefficients in terms of the nodal D.O.F, matrix [C] must be inverted to obtain

$$\{A\} = [C]^{-1} \{\delta^s\}. \tag{2.77}$$

The coefficients $\{A\}$ from equation 2.77 can be substituted into Equations 2.69, and 2.71 in order to obtain the shape functions for the stiffener element. Using $\xi = \frac{x}{\ell}$, the finite element approximations for w^{sc} and u^{ac} take the following form;

$$w^{sc} = \sum_{i=1}^{4} N^s_{bi} \{\delta^s_{bi}\} \tag{2.78}$$

and

$$u^{sc} = \sum_{i=1}^{6} N^s_{pi} \{\delta^s_i\} \tag{2.79}$$

where N^s_{bi}, and N^s_{pi} are the shape functions for transverse and axial displacements, respectively. These are listed in Appendix - A.2

and

$$\{\delta^s_b\}^T = < w_1, \theta_1, w_2, \theta_2 > \tag{2.80}$$

with $\{\delta^s\}$ as the element nodal displacement vector defined in Equation 2.74.

2.4.2 Strain-Displacement Relationship

The strain in the stiffener element is given by:

$$\{\varepsilon_s\} = \frac{\partial u}{\partial x}^{sc} - z\frac{\partial^2 w}{\partial x^2}^{sc} + \frac{1}{2}\left(\frac{\partial w}{\partial x}^{sc}\right)^2 + \frac{\partial w_o}{\partial x}^{sc}\frac{\partial w}{\partial x}^{sc} \tag{2.81}$$

where the axes are defined in Figure 2.5. The linear term $\{\varepsilon_s^L\}$ and the nonlinear term $\{\varepsilon_s^{NL}\}$ can be separated as

$$\{\varepsilon_s\} = \{\varepsilon_s^L\} + \{\varepsilon_s^{NL}\} \tag{2.82}$$

where

$$\{\varepsilon_s^L\} = \frac{\partial u}{\partial x}^{sc} - z\frac{\partial^2 w}{\partial x^2}^{sc} \tag{2.83}$$

$$\{\varepsilon_s^{NL}\} = \frac{1}{2}\left(\frac{\partial w}{\partial x}^{sc}\right)^2 + \left(\frac{\partial w_o}{\partial x}^{sc}\frac{\partial w}{\partial x}^{sc}\right) \tag{2.84}$$

The linear strain matrix $[B_L^s]$ for the stiffener element can be obtained via Equation 2.83 as

$$\{\varepsilon_s^L\} = [L][N^s]\{\delta^s\} = [B_L^s]\{\delta^s\} \tag{2.85}$$

where

$$[B_L^s] = [\frac{\partial}{\partial x} - z \frac{\partial^2}{\partial x^2}] \begin{bmatrix} N_{p1}^s & N_{p2}^s & N_{p3}^s & N_{p4}^s & N_{p5}^s & N_{p6}^s \\ 0 & N_{b1}^s & N_{b2}^s & 0 & N_{b3}^s & N_{b4}^s \end{bmatrix} . \quad (2.86)$$

After carrying out the necessary differentiation in Equation 2.86, the linear strain matrix $[B_L^s]$ is given by

$$[B_L^s] = \begin{Bmatrix} 1/\ell \\ \frac{6z}{\ell^2}(1-2\xi) + \frac{6e}{\ell^2}(2\xi-1) \\ \frac{2z}{\ell}(2-3\xi) + \frac{2e}{\ell}(3\xi-2) \\ 1/\ell \\ -\frac{6z}{\ell^2}(1-2\xi) + \frac{6e}{\ell^2}(1-2\xi) \\ \frac{2z}{\ell}(1-3\xi) + \frac{2e}{\ell}(3\xi-1) \end{Bmatrix} . \quad (2.87)$$

Similar to the plate element, the nonlinear strain matrix $[B_{NL}^s]$ for the stiffener element can be obtained by considering the nonlinear strain terms $\{\varepsilon_{NL}^s\}$ in the following form;

$$\{\varepsilon_{NL}^s\} = \frac{1}{2} < S^s > \{Q^s\} + < S_o^s > \{Q_o^s\} \quad (2.88)$$

where

$$< S^s > = \frac{\partial w^{sc}}{\partial x} = \sum_{i=1}^{4} \frac{dN_{bi}^s}{dx} (\delta_{bi}^s) \quad (2.89)$$

$$< S^s_o > = \frac{\partial w_o}{\partial x} = \sum_{i=1}^{4} \frac{dN^s_{bi}}{dx} (\delta^s_{boi}) \tag{2.90}$$

$$\underset{1\times1}{\{Q^s\}} = \underset{1\times1}{\{\frac{\partial w}{\partial x}^{sc}\}} = \underset{1\times6}{[0 \quad \frac{dN^s_{b1}}{dx} \quad \frac{dN^s_{b2}}{dx} \quad 0 \quad \frac{dN^s_{b3}}{dx} \quad \frac{dN^s_{b4}}{dx}]} \quad \underset{6\times1}{\begin{Bmatrix} 0 \\ w_1 \\ \theta_1 \\ 0 \\ w_2 \\ \theta_2 \end{Bmatrix}} \tag{2.91}$$

and $\{\delta^s_{bo}\}$ is the initial nodal displacement vector for the stiffener element which accounts for the initial imperfections. Equation 2.91 can be rewritten as

$$\underset{1\times1}{\{Q^s\}} = \underset{1\times6}{[G^s]} \; \underset{6\times1}{\{\delta^s_{bi}\}} \tag{2.92}$$

Similar to the plate element, the incremental form of Equation 2.88 leads to

$$\underset{1\times1}{d\{\epsilon^s_{NL}\}} = \underset{1\times1}{[\underline{S}^s + \underline{S}^s_o]} \; \underset{1\times6}{[G^s]} \; \underset{6\times1}{d\{\delta^s\}}. \tag{2.93}$$

consequently,

$$[B^s_{NL}] = [\underline{S}^s + \underline{S}^s_o] \; [G^s]. \tag{2.94}$$

Hence, the total strain matrix $[B^S]$ is given by

$$\underset{6\times1}{[B^S]} = \underset{6\times1}{[B_L^S]} + \underset{6\times1}{[B_{NL}^S]} \tag{2.95}$$

2.4.3 Tangent Stiffness Matrix

The initial stress stiffness matrix $[k_\sigma^S]$ is given by

$$\underset{6\times6}{[k_\sigma^S]} = \int_V \underset{6\times1}{[G^S]}^T \underset{1\times1}{[\sigma_x^S]} \underset{1\times6}{[G^S]}\, dV \tag{2.96}$$

where $[\sigma_x^S]$ is the axial stress in the stiffener element. The matrix $[B^S]$, defined in Equation 2.95, is now used to derive the linear part and the initial displacement matrices, similar to Equation 2.42, as

$$\underset{6\times6}{[\bar{k}^S]} = [k_L^S] + [k_{NL}^S] = \int_V \underset{6\times1}{[\underline{B}_L^S + \underline{B}_{NL}^S]} \underset{1\times1}{[\tilde{E}]} \underset{1\times6}{[\underline{B}_L^S + \underline{B}_{NL}^S]}\, dV \tag{2.97}$$

where $[\tilde{E}]$ is the compliance matrix of the stiffener element and it depends only on the tangent modulus according to the stress level. If the stress within the element exceeds or equals the yield stress, the tangent modulus E_T is used in place of the elastic modulus E.

The total tangent stiffness matrix for the stiffener element is then given by

$$[k_T^S] = [k_\sigma^S] + [\bar{k}^S] = [k_\sigma^S] + [k_L^S] + [k_{NL}^S]. \qquad (2.98)$$

Similar to the plate element, all components of the tangent stiffness matrix are evaluated numerically. However, only a two dimensional integration scheme, with three integration points along the length and the depth, is employed for the stiffener element. The coordinate system and the numerical integration points are shown in Figure 2.6. The numerical integration is carried out in the following manner:

$$[k_T] = [\bar{k}^S] + [k_\sigma^S] = \frac{\ell}{2}\frac{D}{2} B \sum_{i=1}^{3}\sum_{j=1}^{3} \{\omega_i\ \omega_j\ [B^S(\xi_i, Z_j)]^T\ [\hat{E}]$$

$$[B^S(\xi_i, Z_j)]\} + \frac{\ell}{2}\frac{D}{2} B \sum_{j=1}^{3} \{\omega_i\ [G^S(\xi_i)]^T\ [\sigma_x^S]\ [G^S(\xi_i)]\} \qquad (2.99)$$

where ℓ, D, and B are the length, depth, and breadth of the element, respectively. The integration points used are as given below.

$$\{\xi\}^T = \langle (0.5 - \sqrt{0.15}),\ 0.5\ ,\ (0.5 + \sqrt{0.15}) \rangle$$

$$\{Z\}^T = \langle -(\frac{D}{2}\sqrt{0.6})\ ,\ 0\ ,\ (\frac{D}{2}\sqrt{0.6}) \rangle \qquad (2.100)$$

The following weight factors for the 3 points integration scheme have been used:

$$\{\omega\}^T = \langle \frac{5}{9} \quad , \quad \frac{8}{9} \quad , \frac{5}{9} \rangle \tag{2.101}$$

One of the highlights of the present model is generation of a Tee-section stiffener element as a combination of two eccentric beam elements with different eccentricities, one for the vertical flat and the other for the horizontal flat as shown in Figure 2.7.

2.5 Three-Dimensional Assemblage

The special elements employed for mutually perpendicular intersecting plates to model the skin of a box girder required all three rotations (about x, y and z) at the nodes only along the intersections. Therefore, all nodes (interior as well) are assigned three rotations (θ_x, θ_y and θ_z) along with u, v and w degrees of freedom. Note that θ_z at some nodes (in the local axes system), is not accounted for during the stiffness matrix derivation of the plate elements as mentioned before. To add θ_z term at some nodes, the corresponding diagonal term of the element stiffness matrix is taken as unity with the rest of the row and column as zeros. Of course, the corresponding row of the load vector will always be zero. Also note that there is a row and a column added to each θ_z degree of freedom. This increases the plate element stiffness matrix to 24 × 24.

Similarly for the tangent stiffness matrix of the stiffener element as defined by Equation 2.98, zeros have been inserted in appropriate locations to match the degrees of freedom of both the plate and the stiffener elements. As a result, the final tangent stiffness matrix of a stiffener element is of size 12 × 12.

If the directions of the element nodal point displacements $\{\delta_n\}^T = < u\ v\ w\ \theta_x\ \theta_y\ \theta_z >$ are not the same as the directions of the global nodal point displacement $\{\tilde{\delta}_n\}^T = < \tilde{u}\ \tilde{v}\ \tilde{w}\ \tilde{\theta}_x\ \tilde{\theta}_y\ \tilde{\theta}_z >$, a transformation of $\{\delta_n\}$ to $\{\tilde{\delta}_n\}$ can be performed by the following equations:

$$\{\delta_n\} = \begin{bmatrix} [\hat{T}]_{3\times3} & [\underline{0}] \\ [\underline{0}] & [\hat{T}]_{3\times3} \end{bmatrix} \{\tilde{\delta}_n\} = \underset{6\times6}{[\tilde{T}]}\ \{\tilde{\delta}_n\} \tag{2.102}$$

where [T] is a transformation matrix, and the entries in column j of the matrix [T] are the direction cosines of a unit vector corresponding to the j^{th} degree of freedom in $\{\tilde{\delta}_n\}$, when measured in the directions of $\{\delta_n\}$ degrees of freedom. Thus, the rectangular element tangent stiffness matrix $[k_T]$ and load vector $\{f\}$ in the global coordinate system, can be obtained as

$$[\tilde{k}_T] = [T]^T\ [k_T]\ [T] \tag{2.103}$$

$$\{\tilde{f}\} = [T]^T\ \{f\} \tag{2.104}$$

$$\text{where } \underset{24\times24}{[T]} = \begin{bmatrix} [\underline{T}] & [\underline{0}] & [\underline{0}] & [\underline{0}] \\ [\underline{0}] & [\underline{T}] & [\underline{0}] & [\underline{0}] \\ [\underline{0}] & [\underline{0}] & [\underline{T}] & [\underline{0}] \\ [\underline{0}] & [\underline{0}] & [\underline{0}] & [\underline{T}] \end{bmatrix}. \tag{2.105}$$

The relations given by Equations 2.103 and 2.104, are valid for the eccentric stiffener element except that [T] matrix is replaced by the following transformation matrix

$$[T^S]_{12\times12} = \begin{bmatrix} [\underline{T}] & [\underline{0}] \\ [\underline{0}] & [\underline{T}] \end{bmatrix}. \qquad (2.106)$$

2.6 Finite Element Modelling of the Diaphragm

To optimize the use of the central memory available, the half-bandwidth of the total stiffness matrix must be minimized. A simultaneous solution of both, the box's skin and the diaphragm would require a very large central memory, needless to say a very large bandwidth. As such, the diaphragms are modelled with plate elements and are handled in the analysis through substructuring.

The final stiffness matrix of a substructured diaphragm $[ST]_d$ can be obtained by a rearrangement of the global equilibrium equations for the diaphragm. This is accomplished by interchanging rows and columns so that all interior degrees of freedom appear first, followed by all exterior degrees of freedom as indicated by Equation 2.105 below.

$$\begin{bmatrix} [K_{II}]_{n_i\times n_i} & [K_{IB}]_{n_i\times n_b} \\ [K_{BI}]_{n_b\times n_i} & [K_{BB}]_{n_b\times n_b} \end{bmatrix} \begin{Bmatrix} \{\delta_I\}_{n_i\times 1} \\ \{\delta_B\}_{n_b\times 1} \end{Bmatrix} = \begin{Bmatrix} \{F_I\}_{n_i\times 1} \\ \{F_B\}_{n_b\times 1} \end{Bmatrix} \qquad (2.105)$$

The vector $\{\delta_I\}$ of the interior degrees of freedom is then, eliminated via static condensation process.

The elimination of $\{\delta_I\}$ in Equation 2.105 yields the condensed substructured equation for the diaphragm as shown;

$$[ST]_d \{\delta_B\}_d = \{F_B\}_d \tag{2.106}$$

where $[ST]_d$ is the condensed stiffness matrix of the diaphragm, and of size $n_b \times n_b$, while $\{F_B\}_d$ is the corresponding load vector and of size n_b. Both of $[ST]_d$ and $\{F_B\}_d$ are is given by

$$[ST]_d = [\, [K_{BB}] - [K_{IB}]^T [K_{II}]^{-1} [K_{BI}] \,] \tag{2.107}$$

$$\{F_B\}_d = \{F_B\} - [K_{IB}]^T [K_{II}]^{-1} \{F_I\} . \tag{2.108}$$

After assemblage of $[ST]_d$ and $\{F_B\}_d$ and solving for nodal displacements, $\{\delta_B\}_d$ will be obtained, and $\{\delta_I\}_d$ is obtained using the following relationship:

$$\{\delta_I\}_d = [K_{II}]^{-1} [\{F_I\} - [K_{IB}] \{\delta_B\}_d] \tag{2.109}$$

The nonlinear solution of the governing finite element equations and handling of diaphraghm substructuring will be discussed in the next Chapter.

2.7 Load Vector due to Residual Stresses

The plate components of a box girder and the associated stiffeners will very likely be subject to some non-uniform initial stress distribution existing in self-equilibrium. These initial stresses within each element then contribute to the equilibrium equations through the following load vector [70],

$$\{P_o\} = \int_V [B_L]^T \{\sigma_o\} \, dV \tag{2.110}$$

where $\{\sigma_o\}$ is the initial stress vector due to residual stresses.

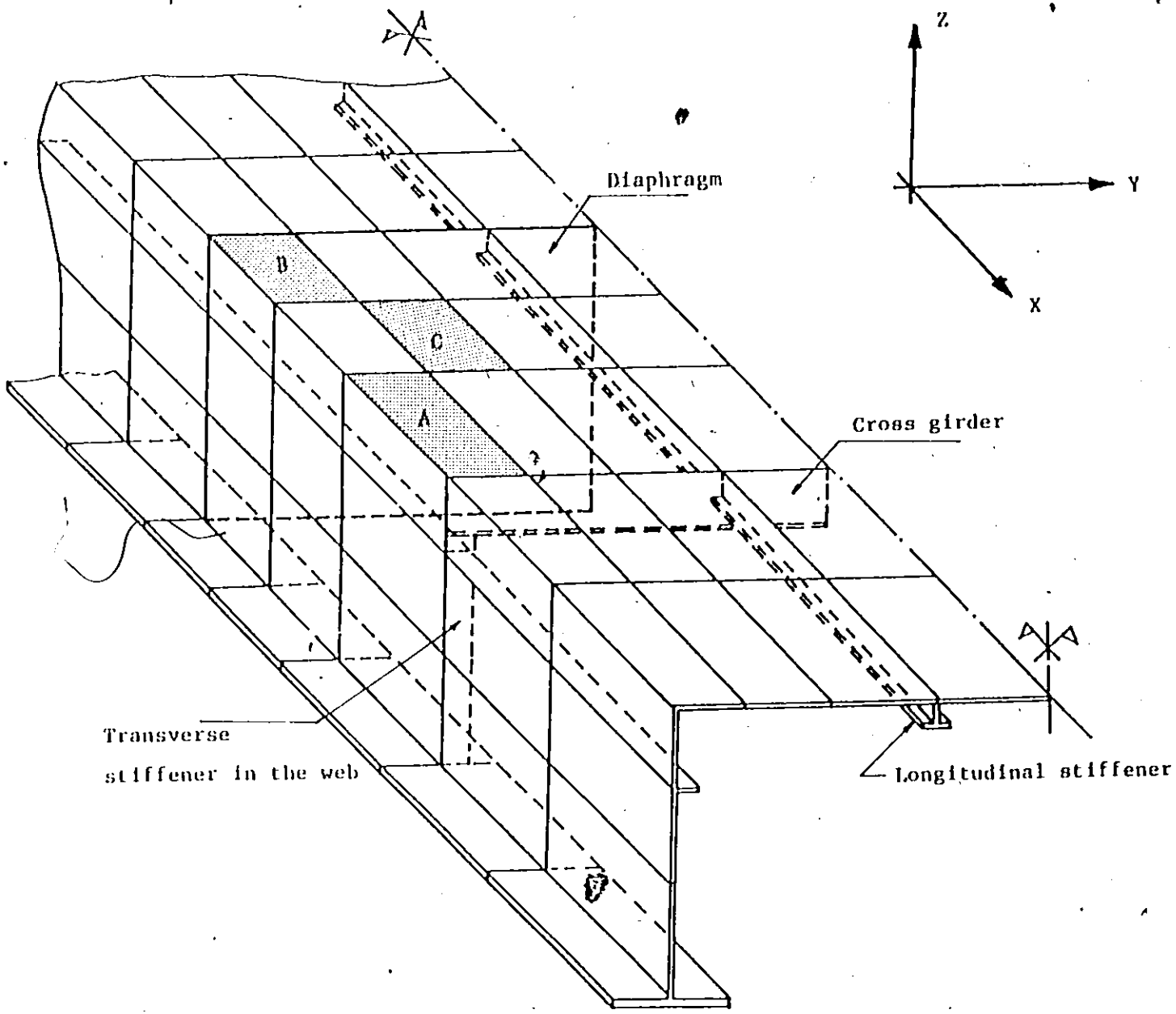

Figure 2.1 : Symmetric half of a box girder and different elements employed in the finite element modelling

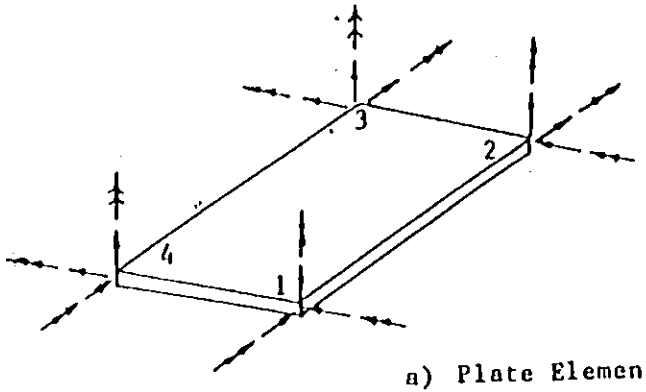

a) Plate Element (A).

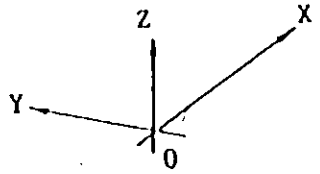

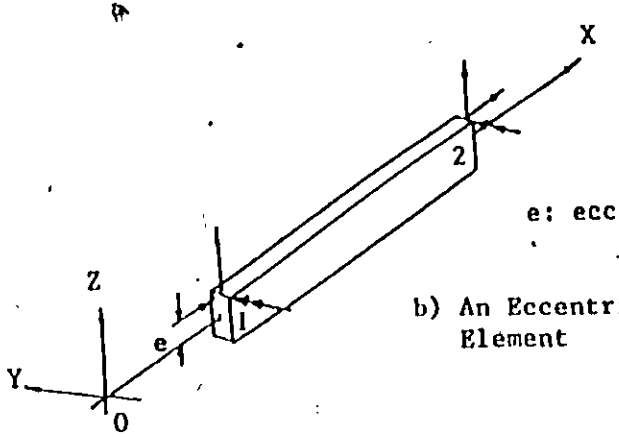

e: eccentricity.

b) An Eccentric Stiffener Element

θ_z : in-plane rotational DOF

$\tilde{\theta}_z$: suppressed DOF

Element Type	Nodes 1	2	3	4
A	θ_z	θ_z	$\tilde{\theta}_z$	$\tilde{\theta}_z$
B	θ_z	θ_z	$\tilde{\theta}_z$	θ_z
C	$\tilde{\theta}_z$	$\tilde{\theta}_z$	$\tilde{\theta}_z$	$\tilde{\theta}_z$

Figure 2.2 : Different Elements Adopted in the Finite Element Modelling

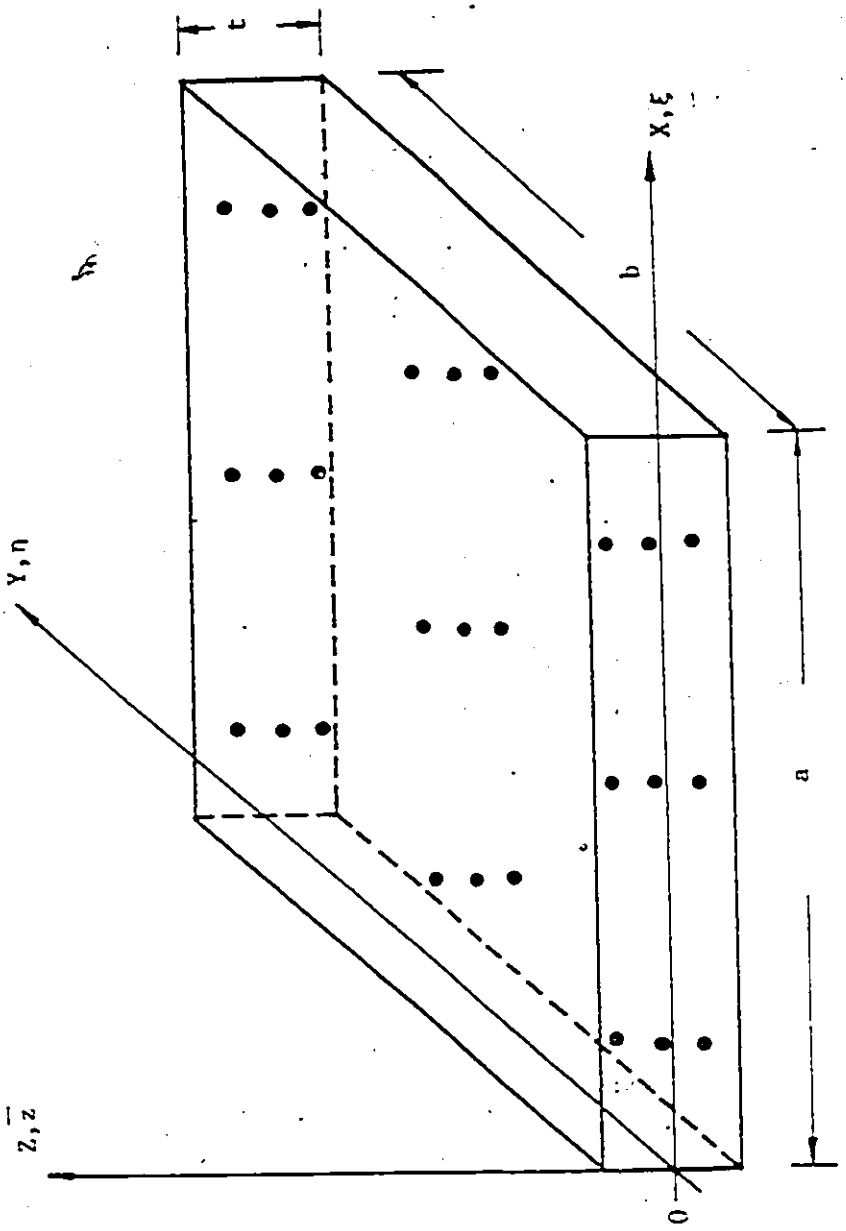

Figure 2.3 : Distribution of Integration Points Within a Plate Element

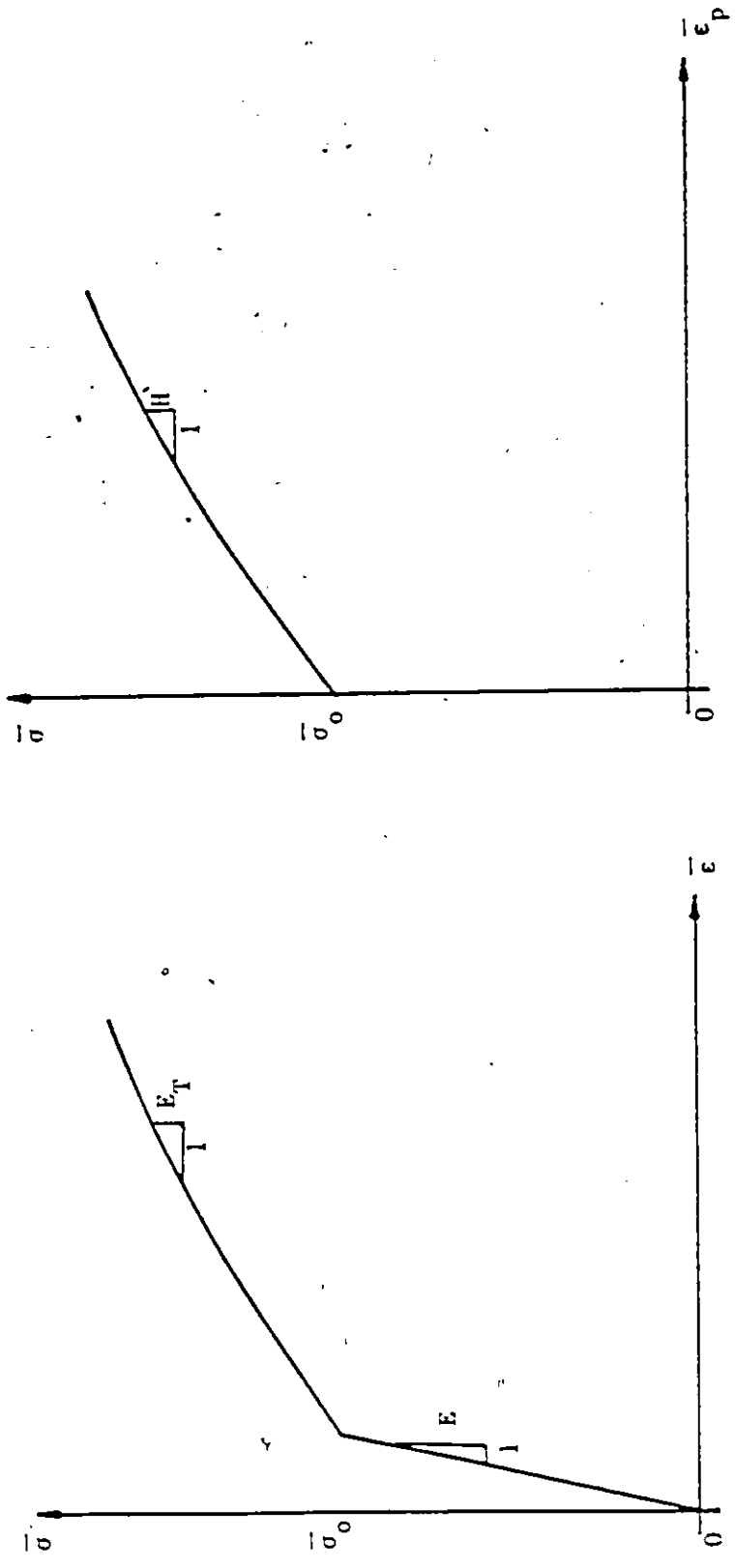

Figure 2.4 : Effective stress-effective strain relations

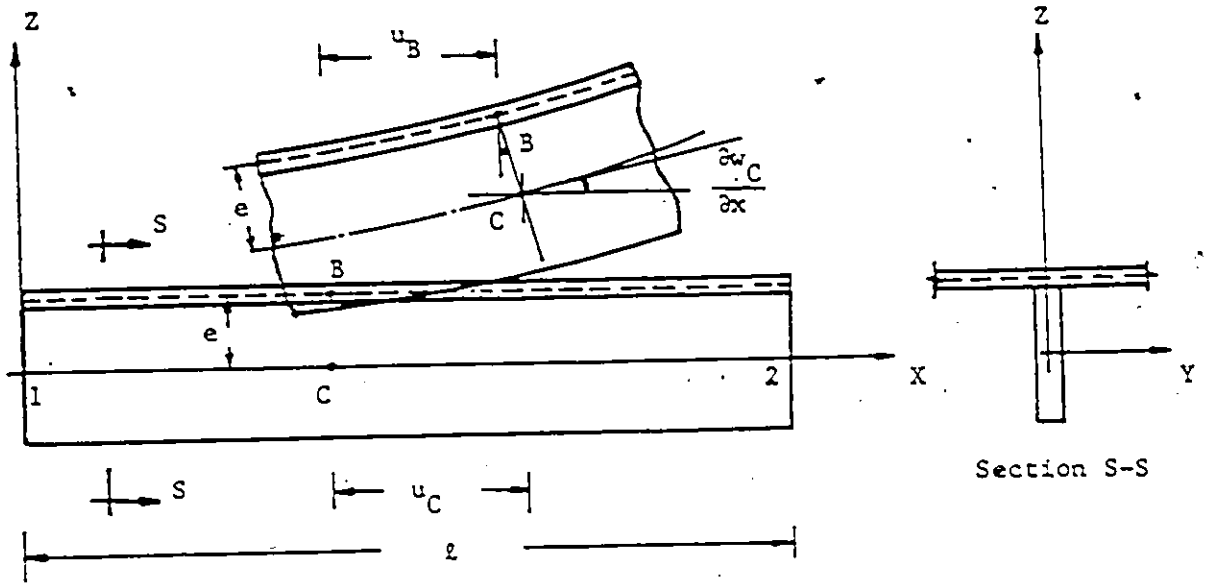

Figure 2.5 : Compatibility of the Stiffener and the Plate

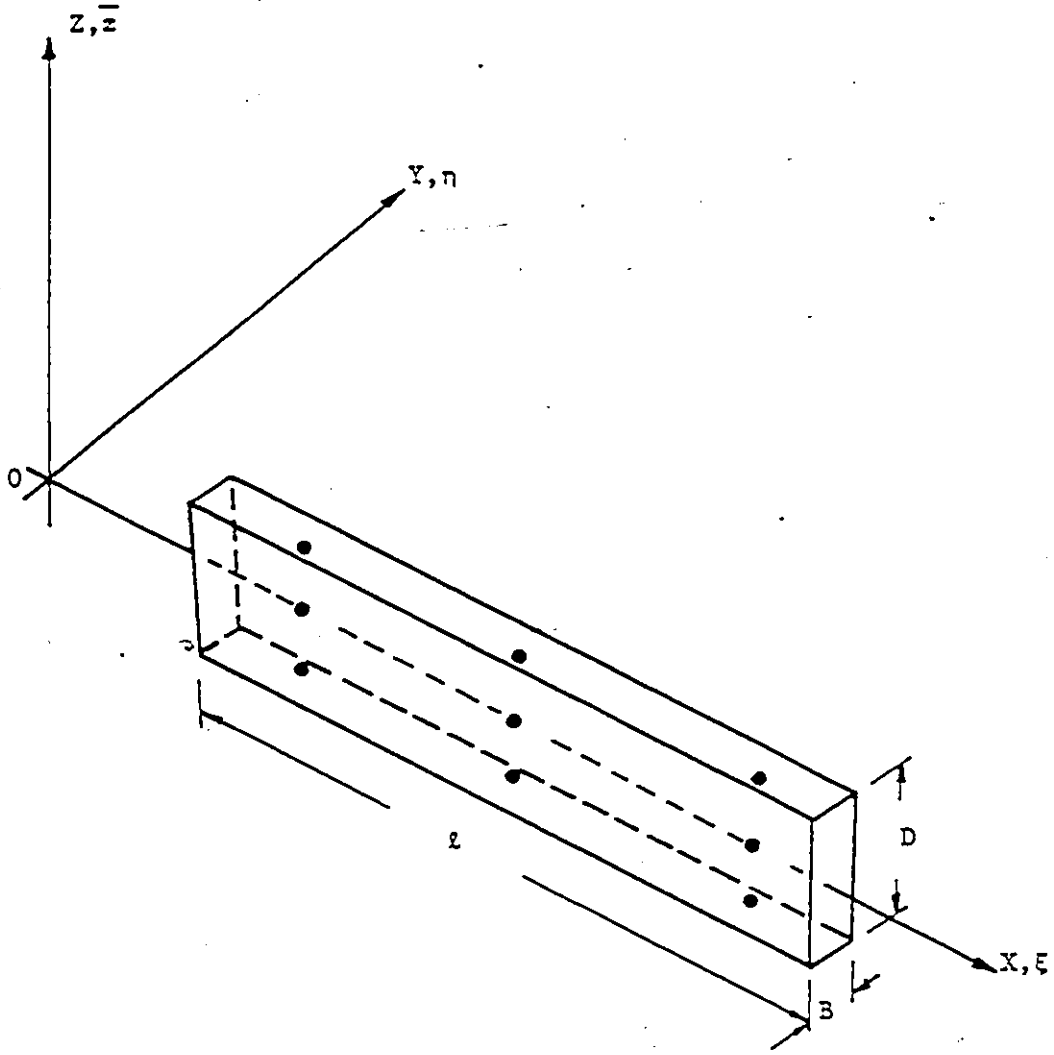

Figure 2.6 : Distribution of Integration Points
Within a Stiffener Element

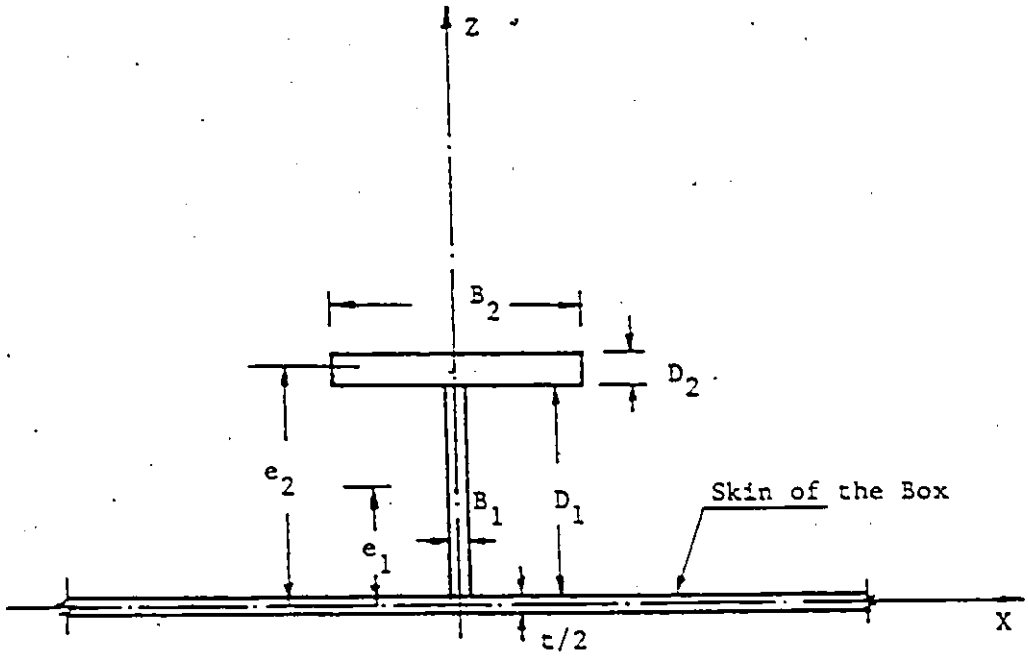

Figure 2.7 : Finite Element Idealization of T-Section Eccentric Stiffener Element

CHAPTER THREE

NONLINEAR FINITE ELEMENT ANALYSIS AND VERIFICATION

3.1.1 Nonlinear Finit Element Analysis

For non-linear analysis, the principle of virtual work and the incremental load method are employed to obtain the discretized equations of equilibrium. These equations for the n^{th} load increment, can be written in the following form [70]:

$$\{\psi_n\} = \int_V [B]^T \{\sigma_n\} \, dV - \{F_n\} = \{0\} \tag{3.1}$$

where $\{F_n\}$ represents the consistent load vector due to the applied loads on the structure, and $\{\psi_n\}$ is the unbalanced force vector called the residual force vector due to lack of equilibrium. In order to minimize these residual forces $\{\psi_n\}$ and prevent drifting of the solution, iterations are carried out within each load increment. Hence, during the n^{th} load increment and m^{th} iteration, the residual forces are computed in the following manner:

$$\{\psi_n^m\} = \int_V [B_n^m]^T \{\sigma_n^m\}\, dV - \{F_n\}. \qquad (3.2)$$

When applying the Newton-Raphson method, the iterative equation becomes

$$\{\psi_n^{m+1}\} = \{\psi_n^m\} + [K_T\ (\underline{\delta}_n^m,\ \underline{\sigma}_n^m)]\ \{\Delta\delta_n^m\} = \{\underline{0}\} \qquad (3.3)$$

in which $[K_T\ (\underline{\delta}_n^m,\ \underline{\sigma}_n^m)]$ is the tangential stiffness matrix which depends on the level of displacements $\underline{\delta}_n^m$ and level of stresses $\underline{\sigma}_n^m$ due to geometric and material nonlinearities, respectively. This matrix is established by assembling the individual stiffness matrices of all elements and the substructured components (diaphragms) comprising the entire structure. It is formulated using the numerical integration with twenty seven integration points in each rectangular element for the state of stresses $\underline{\sigma}_n^m$ and displacement $\underline{\delta}_n^m$, and only nine integration points for the stiffener element.

The elasto-plastic compliance matrix is evaluated at every integration point at which the effective stress has exceeded the yield stress. The updated element tangential stiffness matrix $[k_T^e\ (\underline{\delta}_n^m,\ \underline{\sigma}_n^m)]$ is evaluated for the rectangular elements and the stiffener elements using Equation 2.46 and 2.98, respectively.

After obtaining the residual load using Equation 3.2, the incremental displacements can be computed from

$$\{\Delta\delta_n^m\} = -[K_T(\underline{\delta}_n^m, \underline{\sigma}_n^m)]^{-1} \{\psi_n^m\} \tag{3.4}$$

and the incremental strains and stresses at any point within an element are then given by

$$\{\Delta\varepsilon_{ne}^m\} = [B_{ne}^m] \{\Delta\delta_{ne}^m\} \tag{3.5}$$

$$\{\Delta\sigma_{ne}^m\} = [\tilde{D}_{ne}^m] \{\Delta\delta_{ne}^m\} \tag{3.6}$$

where $\{\Delta\delta_{ne}^m\}$, $\{\Delta\varepsilon_{ne}^m\}$ and $\{\Delta\sigma_{ne}^m\}$ are the element incremental nodal displacements, incremental strains and stresses for the element at a given point, respectively. Both, updated strain matrix $[B_{ne}^m]$ and elastic or elasto-plastic compliance matrix $[\tilde{D}_{ne}^m]$, must be evaluated at each integration point within an element. The proper matrix $[\tilde{D}_{ne}^m]$, elastic or elasto-plastic, is used according to the stress level $\underline{\sigma}_n^m$.

The Newton-Raphson method, described above, is illustrated graphically in Figure 3.1 for a single degree of freedom system. Its extension to a multi-degrees of freedom system is natural.

3.1.2 Algorithm for Incremental Method

A description of the steps followed in the finite element computer program is presented here.

I. After the m^{th} Newton-Raphson iteration has converged for the

$(n-1)^{th}$ load increment within a specified tolerance, let $\{\psi^m_{n-1}\}$ be the resulting residual load. The n^{th} load increment is then applied and the displacement increments are then given by

$$[K_T(\underline{\delta}^0_n, \underline{\sigma}^0_n)]\ \{\Delta\delta^0_n\} = -\{\psi^0_n\} + \{\Delta F_n\} \tag{3.7}$$

where $\{\Delta F_n\}$ is the n^{th} load increment and $\{\psi^0_n\} = \{\psi^m_{n-1}\}$.

II. The global nodal displacement vector is then updated

$$\{\delta^1_n\} = \{\delta^0_n\} + \{\Delta\delta^0_n\}. \tag{3.8}$$

III. From $\{\Delta\delta^0_n\}$, the incremental element nodal displacements $\{\Delta\delta^0_{ne}\}$ are extracted for each element (plate or stiffener element) as the case may be.

IV. For each element, the local incremental and total nodal displacement vectors $\{\Delta\delta^1_{ne}\}$, and $\{\delta^1_{ne}\}$, are computed using the transformation presented in Section 2.5.

a) Plate elements

For each plate element, either in a web or a flange of the box girder, the following steps are performed:

1. Compute the incremental strains and stresses;

$$\{\Delta\varepsilon^0_{ne}\} = [B^0_{ne}]\ \{\Delta\delta^0_{ne}\} \tag{3.9}$$

$$\{\Delta\sigma^0_{ne}\} = [D^0_{ne}]\ \{\Delta\varepsilon^0_{ne}\} \tag{3.10}$$

where $[D^0_{ne}]$ is either the elasticity matrix [D] or the elasto-plastic matrix $[D_{ep}]$.

2. Update the stresses and strains;

$$\{\varepsilon^1_{ne}\} = \{\varepsilon^0_{ne}\} + \{\Delta\varepsilon^0_{ne}\} \tag{3.11}$$

$$\{\sigma^1_{ne}\} = \{\sigma^0_{ne}\} + \{\Delta\sigma^0_{ne}\}. \tag{3.12}$$

3. Compute the effective stress $\bar{\sigma}$ in Equation 2.56 to check whether yielding has occurred at a particular integration point. If the effective stress is smaller than, or equal to the yield limit, the elasticity matrix in Equation 2.32 is used. If it is greater than the yield stress, the elasto-plastic compliance matrix $[D_{ep}]$ in Equation 2.61 is used.

4. Compute the new element stiffness matrix $[\bar{k}\ (\delta^1_{ne},\ \delta_{oe})]$ in the local coordinate system using Equation 2.42 with the updated matrix $[B^1_{ne}\ (\delta^1_{ne},\ \delta_{oe},\ \xi,\ \eta,\ z)]$ and the compliance matrix $[\tilde{D}^1_{ne}]$ based on the information in step 3.

5. Compute the initial stress stiffness matrix $[k_\sigma(\sigma^1_{ne})]$, again in the local coordinate system, according to Equation 2.41. Then obtain $[k_T]$ as

$$[k_T] = [\bar{k}(\delta^1_{ne}, \delta_{oe})] + [k_\sigma(\sigma^1_{ne})]. \tag{3.13}$$

6. Compute the internal load vector for the element in the local coordinate system.

$$\{R^1_{ne}\} = \int_V [B^1_{ne}]^T \{\sigma^1_{ne}\}\, dV \tag{3.14}$$

7. Assemble the global tangential stiffness matrix $[K_T]$ and the global internal load vector $\{R^1_n\}$ after proper transformations have been performed.

b) Stiffener elements

For each stiffener element, the following steps are performed:

1. The incremental strains and stresses are calculated and then updated analogous to Equations 3.9 to 3.12 for the plate element except here it is a beam-column element.

2. Check for the compliance matrix at each integration point by comparing the axial stress σ^1_{ne} with the yield stress σ_y. As such,

$$\text{if } \sigma_{ne}^{1} > \sigma_y \qquad \tilde{E}_n^1 = E_T \text{ (tangent modulus)} \tag{3.15}$$

$$\text{if } \sigma_{ne}^{1} < \sigma_y \qquad \tilde{E}_n^1 = E \text{ (elastic modulus)} \tag{3.16}$$

3. Compute the new element tangential stiffness matrix in the local coordinate system $[k_T^s (\underline{\delta}_{ne}^1, \underline{\sigma}_{ne}^1)]$ via Equation 2.98 and transform it to the global coordinate system.

4. Compute the element internal load vector $\{R_{ne}^{s1}\}$ in the global coordinate system as

$$\{R_{ne}^{s1}\} = \int_{V^s} [T^s]^T [B_n^{s1}(\delta_{ne}^1, \delta_{oe}, \xi, z)]^T \{\sigma_{ne}^1\} dV^s \tag{3.17}$$

where $[T^s]$ is the transformation matrix defined by Equation 2.106.

5. Set up the global stiffness matrix $[K_T^s (\underline{\delta}_{ne}^1, \underline{\sigma}_{ne}^1)]$ and the global internal load vector $\{R_n^{s1}\}$.

c) Diaphragm

As mentioned before, the diaphragm is handled through substructuring. In the nonlinear analysis, the following steps are followed:

1. Extract the incremental nodal displacements $\{\Delta\delta_{Bn}^1\}$ of the nodes at the intersection of the box girder and the diaphragm

periphery.

2. Obtain the incremental displacements for the interior nodes $\{\Delta\delta^1_{In}\}$ via Equation 2.109.

3. Update the diaphragm global nodal displacement;

$$\{\delta^1_n\}_d = \{\delta^0_n\}_d + \{\Delta\delta^0_n\}_d \tag{3.18}$$

where $\{\Delta\delta^0_n\}_d$ is the union of $\{\Delta\delta^0_{Bn}\}$ and $\{\Delta\delta^0_{In}\}$.

4. For each plate element within the diaphragm, repeat steps 1 to 6 as was done for the plate elements in (a).

5. Compute the global condensed tangential stiffness matrix for the diaphragm $[ST\ (\underline{\delta}^1_n,\ \underline{\sigma}^1_n)]_d$ as explained in Section 2.6, and the associated internal load vector $\{R^1_{Bn}\}$.

V. The global tangential stiffness matrices and internal load vectors from (a), (b) and (c) above are then combined to obtain the total tangential stiffness matrix $[K_T\ (\underline{\delta}^1_n,\ \underline{\sigma}^1_n)]$ and the internal load vector $\{R^1_n\}$ for the entire box girder.

VI. Calculate the residual load vector for the entire system.

$$\{\psi^2_n\} = \{R^1_n\} - \{F^1_n\} \tag{3.19}$$

VII. Solve the following equation for the next incremental displacement vector $\{\Delta\delta_n^2\}$.

$$[K_T\ (\underline{\delta}_n^1,\ \underline{\sigma}_n^1)]\ \{\Delta\delta_n^2\} = -\ \{\psi_n^2\}. \tag{3.21}$$

VIII. Repeat steps II to VI until the incremental solution has converged within a specified percentage tolerance γ which is calculated in the following manner.

$$\gamma = 100 \times \frac{\text{Det}\ [K_T\ (\underline{\delta}_n^m,\ \underline{\sigma}_n^m)] - \text{Det}\ [K_T\ (\underline{\delta}_n^{m-1},\ \underline{\sigma}_n^{m-1})]}{\text{Det}\ [\ K_T\ (\underline{\delta}_n^{m-1},\ \underline{\sigma}_n^{m-1})]} \tag{3.21}$$

IX. If the percentage tolerance is within the prescribed value, apply the next load increment and repeat steps I to VIII.

The interative procedure outlined above is commenced by performing an elastic analysis under the applied loads. The size of the first load increment is usually chosen so that linear elastic response is assured. If the geometric nonlinearity is accounted for in the problem under consideration, equilibrium check is performed before applying the second load increment and the residual forces are then added to this load increment (see Fig. 3.1). However, if only the material nonlinearity is considered, the first load increment is scaled up to the yield load. The scaling factor is determined such that $\bar{\sigma}$ at the most stressed point is equal to the yield stress σ_y. Of course, the same scaling factor is then applied to the calculated displacements, strains

and stresses. Additional load increments of variable magnitude are then applied until the stiffness of the structure under consideration deteriorates or reduces significantly in comparison with its initial stiffness. These load increments are taken as a percentage of the initial applied load increment, or the yield load. Generally, large increments are considered where the behaviour of the structure is linear elastic. However, in the plastic range, small increments are used and reduced progressively to be very small near failure.

The computer algorithm outlined in this section requires a complete re-analysis of the system for every iteration since the Newton-Raphson method has been employed. Although the N-R requires the regeneration of the tangent stiffness matrix at each iteration, the extra computing time is repaid by rapid convergence and better accuracy.

3.2 Program Verifications

Prior to application of the finite element model presented to stiffened steel box girders, a number of numerical examples were carried out to verify the finite element formulation presented in Chapter 2. Examples of beams, plates and three-dimensional plate assemblage structures were tested and the results are presented in this Section.

These examples were chosen so that different loading patterns, various boundary conditions, and plate assemblage could be tested individually. The numerical results obtained were compared with those

available in the literature. Before describing the test examples above, it is pointed out here that the results obtained in the elastic range for simply supported and clamped square plates under uniformly distributed load, with 2 × 2 and 4 × 4 grids, were found to be the same as those reported by Zienkiewicz [70]. Again in the elastic range, simply supported stocky, square hollow section beams, with grid sizes of 2 × 2 × 4 and 4 × 4 × 8 were also analyzed under mid-span concentrated loads. The deflections obtained from the present finite element model compared well with the beam theory deflection, which also included the shear deformation.

3.2.1 Examples of Beam-Columns

a) Fully Encastré Beam Subjected to a Central Point Load

Campbell and Charlton [78] reported the results of a series of tests on fully encastré mild steel beams subjected to a central point load, with ends prevented from moving-in. They also carried out an elasto-plastic analysis on this beam. This example was chosen to check the combined effect of material and geometric nonlinearities, and also because of the availability of other analytical results in the literature [47].

Taking symmetry into account, only a half-span was analyzed using an irregular mesh with a finer mesh division near the centre and the ends. This is to ensure more effective modelling for the highly stressed zones. The material properties and the beam geometry used are

The computed load-central displacement curve is compared with both the experimental and the previous analytical results (see Fig. 3.2). Good agreement between the predicted response from the present model with the experimental and analytical results can be observed up to a load level of 0.54 kN. Thereafter, the difference is evident, especially with the experimental curve.

Campbell and Charlton [78] commented on this surprising observation in that initial plastic flow should have occurred in tension faces of the section where bending moment is maximum at a load of 0.31 kN (56% of the primary collapse load 0.54 kN). However, they noted that there was no indication of such behaviour either from the characteristic increase in deflection rate or cracking of the resin coating on the beam. They added that the experiments showed the presence of a higher yield stress in the outer fibers which might have accounted for the abrupt transition from elastic to plastic behaviour.

The discrepancy between the present finite element modelling, and that of Crisfield [47], is due to the difference in handling the material nonlinearity. While the present formulation uses the Von Mises yield criterion; Crisfield used Iliyushin's yield criterion as a function of stress resultants within an element. In addition, the present model uses numerical integration as explained in Chapter 2; while Crisfield used the layered approach for evaluating the element stiffness matrix. In the post elastic range, the deviation from the experimental results is believed to be due to the tangent modulus used as $E_T = E/400$.

b) Uniaxially Compressed Column

The finite element model was also verified through its application to a single-span strut analyzed by Crisfield [47]. A strut with a rectangular cross section of 30 × 10 mm and length 600 mm is considered under axial load. The column has a slenderness ratio L/r of 70, and a sinusoidal initial imperfection with an amplitude of L/1000. Again, due to symmetry, only one half of the strut is considered with four elements of equal length. Load versus central deflection and load versus end shortening from the present model are shown in Figures 3.3(a) and 3.3(b), respectively. Fig. 3.3(a) indicates that the deflection of the column at collapse is small in comparison to its dimensions. In addition, collapse of the column is encountered just after the first yield. This is due to a sudden overall loss of stiffness. For purpose of comparison, results due to Crisfield [47] are given. Only a minor discrepancy can be observed from Figure 3.3. Perhaps, these are due to the differences in the formulation of the beam elements mentioned before, and the number of load increments applied to reach the same deflection.

c) Uniaxially Compressed Beam-Column with T-Section

Another beam-column example, simulates the failure of closely stiffened steel panels through a column with T-section. In the present example a two-span beam-column is analyzed. The dimensions used are the same as those employed by Chatterjee and Dowling [79], in which the web area and the flange area are equal. See Figure 3.4 (a) for details.

The slenderness ratio of the column L/r is 100. Imperfection is represented by a single half sine wave over each span with an amplitude of L/750 as proposed in Reference [79]. Mild steel with yield stress of 240 N/mm^2, modulus of elasticity of 206000 N/mm^2 and tangent modulus $E_T = E/400$, has been used for the beam-column considered. An axial force is applied at the centroid of the cross section.

This example was also analyzed by Moan and Soreide [80] and Crisfield [47]. In the present modelling, two beam elements were added together, each with a specific eccentricity from the centroid of the beam, to form the T-section. While Moan and Soreide divided the span into ten beam elements, the present analysis used eight elements only. This was also true for the analysis reported by Crisfield. In the present analysis, stress ratios at first yield and at ultimate load are found to be 0.75 and 0.85, respectively. Load versus mid-span deflection and load versus end shortening obtained are then compared with other numerical results in Fig. 3.4.

The earlier prediction of yield by Moan and Soreide is probably due to the larger number of elements used in their idealisation. The collapse load from the present study and the first yielding are higher than the other results, which may be due to using three integration points through the depth of the beam in the present study, while the other investigators used five or more layers.

3.2.2 Examples of Plates

a) Elasto-Plastic Modelling of a Square Plate

The verification of bending part of the rectangular element is carried through an elasto-plastic analysis of a thin plate and compared with the results obtained by Stanton and Schmit [81]. The square plate is simply supported. Its dimensions are 10 × 10 × 0.5 in. and is subjected to a transverse uniformly distributed load. The material properties for the plate are shown in Figure 3.5 (a). Owing to double symmetry, only one quarter of the plate, with a 3 × 3 grid, was analyzed.

Fig. 3.5 (a) indicates very good agreement for the uniform pressure versus the central deflection response. The slight discrepancy between the two solutions is due to the difference in the formulation of the plate bending elements used. Stanton and Schmit employed bicubic Hermit displacement functions. In addition, bicubic spline constraints are introduced that produce interelement curvature continuity. Overall, the element used in [81] is stiffer than that used in the present analysis. The progression of the plastic zones within a quarter of the plate for four stages of loading is shown in Figure 3.5 (b). The yielding is observed to commence at the centre of the plate and to progress towards the corner. This type of plastic behaviour is as expected for simply supported plate.

b) Imperfect Simply Supported Plate

The elastic post-buckling behaviour of a simply supported plate subjected to a uniform in-plane compression was studied previously by Yamaki [82] using the Fourier series approach and by Crisfield [46] using the finite element method. Yamaki's classical solution is based on using a double Fourier series with four coefficients to solve Marguerre's fundamental equations [69].

The geometry and the material properties are shown in Figure 3.6. It should be noted that the edges of the plate parallel to the loading are free to pull-in. In order to initiate lateral deflection, imperfections are introduced as single half-sine waves in both directions with maximum magnitude of ten percent of the thickness of the plate. Mathematically, it can be written as

$$w_o = (0.1\ t) \cdot \sin \frac{\pi x}{L} \cdot \sin \frac{\pi y}{L} \qquad (3.22)$$

where L is the dimension of the square plate and t is the thickness. Figure 3.6 shows Yamaki's average stress versus plate central deflection curve, that due to Crisfield [46], and the one obtained from the present analysis. A very good comparison can be observed.

c) Buckling of Simply Supported Imperfect Plate

The elasto-plastic-large deformation behaviour of a simply sup-

ported steel plate of aspect ratio (a/b = 0.875), width-to-thickness ratio (b/t = 55), and subjected to uniaxial in-plane loads is investigated. The sides of the plate parallel to the loading were kept free to move. The initial imperfection involves only a single half wave with amplitude $\bar{w}_o$ = b/1000 which is introduced through the nodal coordinates using a sinusoidal curve. The result, was observed to be in very good agreement with these reported by Crisfield [46], as shown in Figure 3.7.

d) Buckling of Simply Supported Imperfect Plate With Residual Stresses

The imperfect steel plate tested in the previous example is considered again to investigate the effect of residual stresses on its strength. Dwight and Maxham [18] have proposed a rectangular tension block distribution for the residual stresses which are due to welding balanced by uniform compressive stresses within the central portion of the plate panel. The resulting stress distribution is shown in Figure 3.8. Unfortunately, the present plate element used in the present study as well as Crisfield's analysis [46], can only handle a continuous stress field with a linear variation across the element. Crisfield replaced the tension block by linear distribution as shown by dashed lines in Figure 3.8. In the present study, the finite element grid is adjusted so that one element fitted the tension block and three elements are used in the central portion of the plate panel and subjected to compression.

The relation between the applied average stress and plate central deflection, as analysed by Crisfield, and that obtained from the present modelling is shown in Figure 3.9. The collapse load obtained from the present analysis is slightly higher than that reported by Crisfield. This difference is expected since in Crisfield's case a modified stress pattern is adopted which leads to more compressive stresses in the central portion of the panel. This renders a more flexible plate than that considered in the present analysis.

3.2.3 Examples of Three-Dimensional Plate Assemblage Structures

a) Square Hollow Section T-Joint Under Punch Moment

The verification of the finite element model for three-dimensional assemblage of plate elements is carried through analysis of an unequal width single chord square hollow section T-joint as tested by Brady [83]. The joint (as shown in Figure 3.10) was composed of a 10 x 10 x 0.375 in. chord and a 6 x 6 x 0.188 in. branch with a measured yield stress of 59.6 ksi. It is intended not only to compare the present 3-D assemblage modelling with experiments [83], but also to compare its performance with the previously reported elasto-plastic 2-D model by Mirza et al. [84]. In the previous model, the top flange of the chord was treated as a thin plate supported by coupled springs, accounting for the remaining hollow section through the transverse stiffness of frames of unit width. They took the plate thickness within the branch inclusion as one thousands times the chord's thickness which allowed the inclusion to move rigidly.

In the present modelling, the chord is represented by three-dimensional assemblage of plate elements. For direct comparison, the rigid inclusion inside the branch member at the connection with the chord is maintained. The branch moment is transferred to the chord via loads along the preiphery of the rigid inclusion. Since the main purpose is the investigation of the localized behaviour of the joint, it is deemed appropriate to introduce a roller support along the web-bottom flange junction of the chord. The boundary conditions maintained are exactly the same as those used by Mirza et al. [84].

The finite element grid for one-quarter of the joint employed in the modelling is shown in Figure 3.11. The material is modelled as an elasto-plastic with the following properties: modulus of elasticity E = 29000 ksi, tangent modulus E_T = 0.025 E, and Possion's ratio = 0.3.

The computed moment-rotation curves are compared with both experimental and previous analytical results and are shown in Figure 3.12. When the geometric nonlinearity is considered, excellent agreement can be observed up to 250 k-in branch moment between the present analysis and the experimental results. It appears that when rotation of the joint is large, the small deflection theory is not adequate and rendered a much more flexible joint.

b) Square Hollow Section T-Joint Under Punch Shear

A single chord T-joint under punching shear was investigated

using the present finite element model. This example also verified the assumption of rigid inclusion that was adopted in the previous example by modelling the branch member by the rectangular elements. In the process, it also demonstrated the application of the substructuring algorithm that was incorporated in the finite element model. Branch axial force was applied directly to the branch member. The finite element discretization of one quarter of the joint is shown in Figure 3.13. The present model predictions were to be verified by comparison with the experimental results of the specimen L-5 tested by Petal et al. [85]. The following material properties were used: modulus of elasticity $E = 29 \times 10^6$ psi, yield stress $\bar{\sigma}_y = 36 \times 10^3$ psi, and tangent modulus $E_T = 0.023E$.

Both small and large displacement elasto-plastic analyses were carried out. The load-displacement curves, along with the experimental results by Patel et al., are shown in Figure 3.14. Good agreement can be observed between the experimental results and the large deflection curve. It is clear that the elasto-plastic response indicates the inadequency of small deflection theory in predicting the response of the joint. Furthermore, in the near elastic range, the discrepancy can be explained due to the presence of the residual stresses in the actual joint tested by Patel et al. and these were not modelled in the numerical analyses performed.

c) Unstiffened Thin-Walled Steel Box Beam

There are only very limited experimental or analytical results available in the literature for the strength of unstiffened steel box girders. In Ref. [55], four test results were reported for small model specimens that were designed and tested to predict their strengths. In the results presented here, model III in ref. [55] was considered. This specimen failed due to full plastification of the cross section. Because no buckling had taken place in the experiments and stocky nature of the cross section, only the material nonlinearity was considered in the numerical modelling. Owing to the lack of information about the yield stress of the steel used, two values of 33000 and 40000 psi were considered. The material was modelled as an elasto-plastic with some strain hardening along with the following propetties: modulus of elasticity $E = 29 \times 10^6$ psi, tangent modulus $E_T = 0.002\ E$, and Possion's ratio $\nu = 0.3$.

The dimensions of the box girder model are shown in Fig. 3.15. Two central loads are applied directly above the mid-span at the web-top flange junctions. Due to double symmetry, only one quarter of the beam is considered. The finite element grid used is shown in Fig. 3.15.

The yield load is determined by searching for the most highly stressed point throughout the girder and scaling this point up or down so that the equivalent stress $\bar{\sigma}$ just reaches the yield stress σ_y. After that, load increments were applied up to the ultimate load and main-

tained between ten to five percent of the yield load determined as outlined above. Again, good agreement for the load-mid-span deflection between the anlytical and the experimental results can be observed for the yield stress value of 33000 psi in Fig. 3.15. It is also obvious that the responses are different only in the inelastic range for the two values of the yield stress considered, as was expected. Once again, the response from the numerical model is stiffer in the elastic range due to neglecting the residual stresses. Figure 3.16 shows progressions of the yield zones at different load levels. These appear to be very reasonable and consistent with the experimental evidence of failure that is mainly due to plastication.

3.3 Closure

It was necessary to first check the individual components of the algorithm because of the complexity of the finite element model that was developed based on the formulation presented in the previous Chapter. This has been done successfully through extensive comparisons with the existing results in the literature. Different examples of beams, plates, and three-dimensional plate assemblage problems were analysed with good to excellent agreements with other reported analytical, or experimental results found in the literature.

Next, the nonlinear finite element model is applied to the stiffened steel box girder to investigate its behaviour and to predict its ultimate strength including the effects of imperfections. This is the topic of the next Chapter.

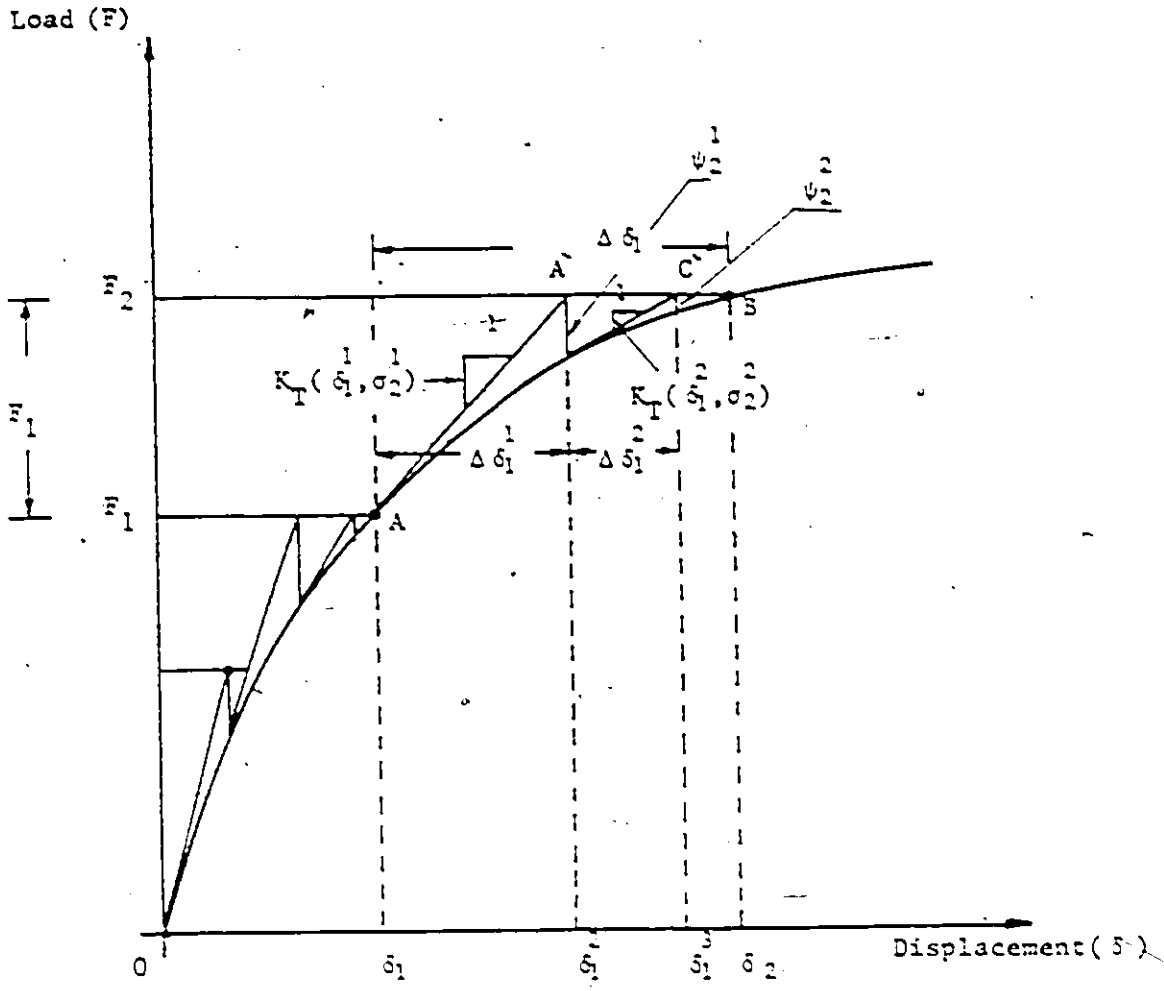

Figure 3.1 : Newton-Raphson iterative method

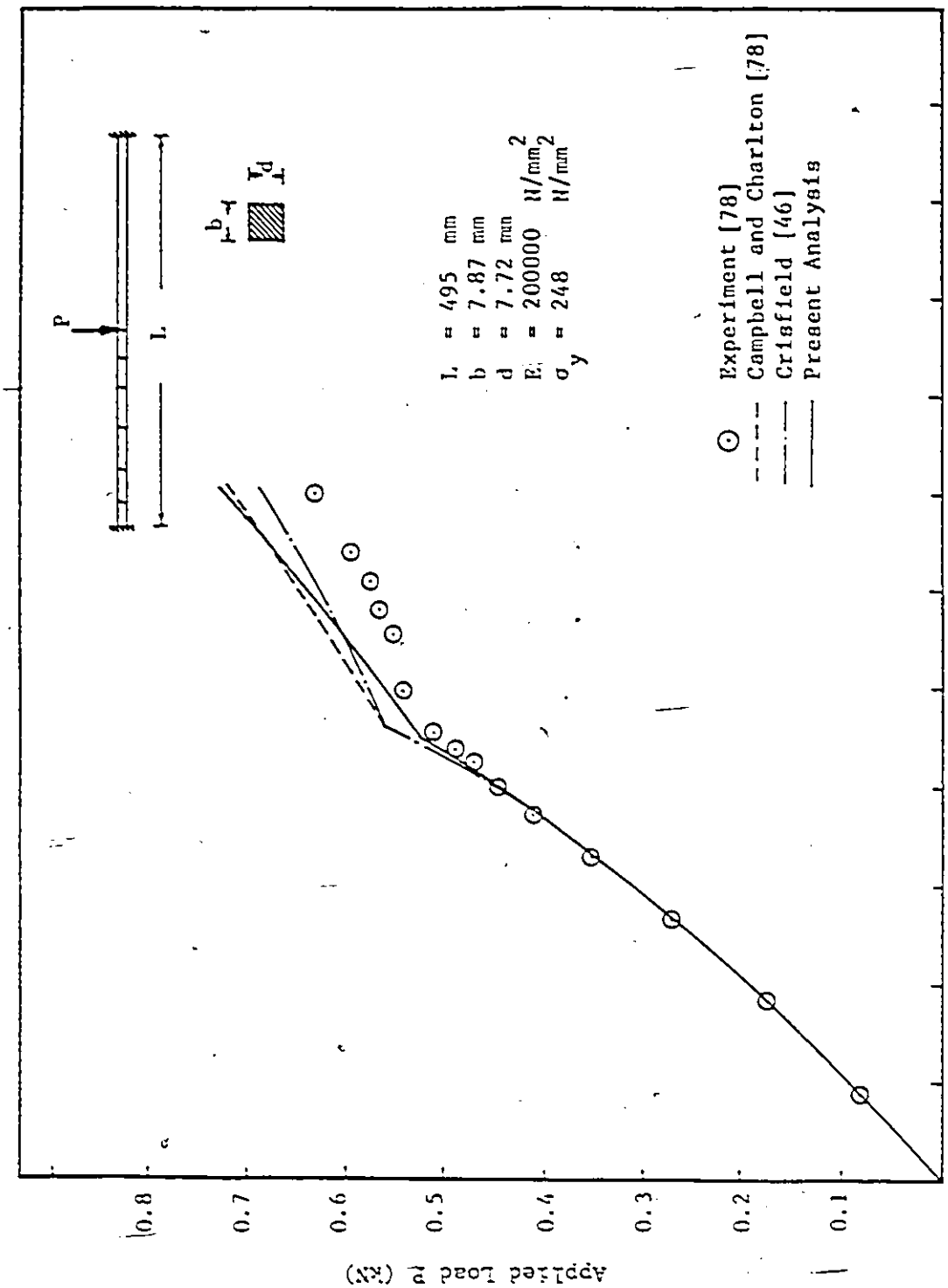

Figure 3.2 : Load-Central Deflection for Fully Encastre' Beam

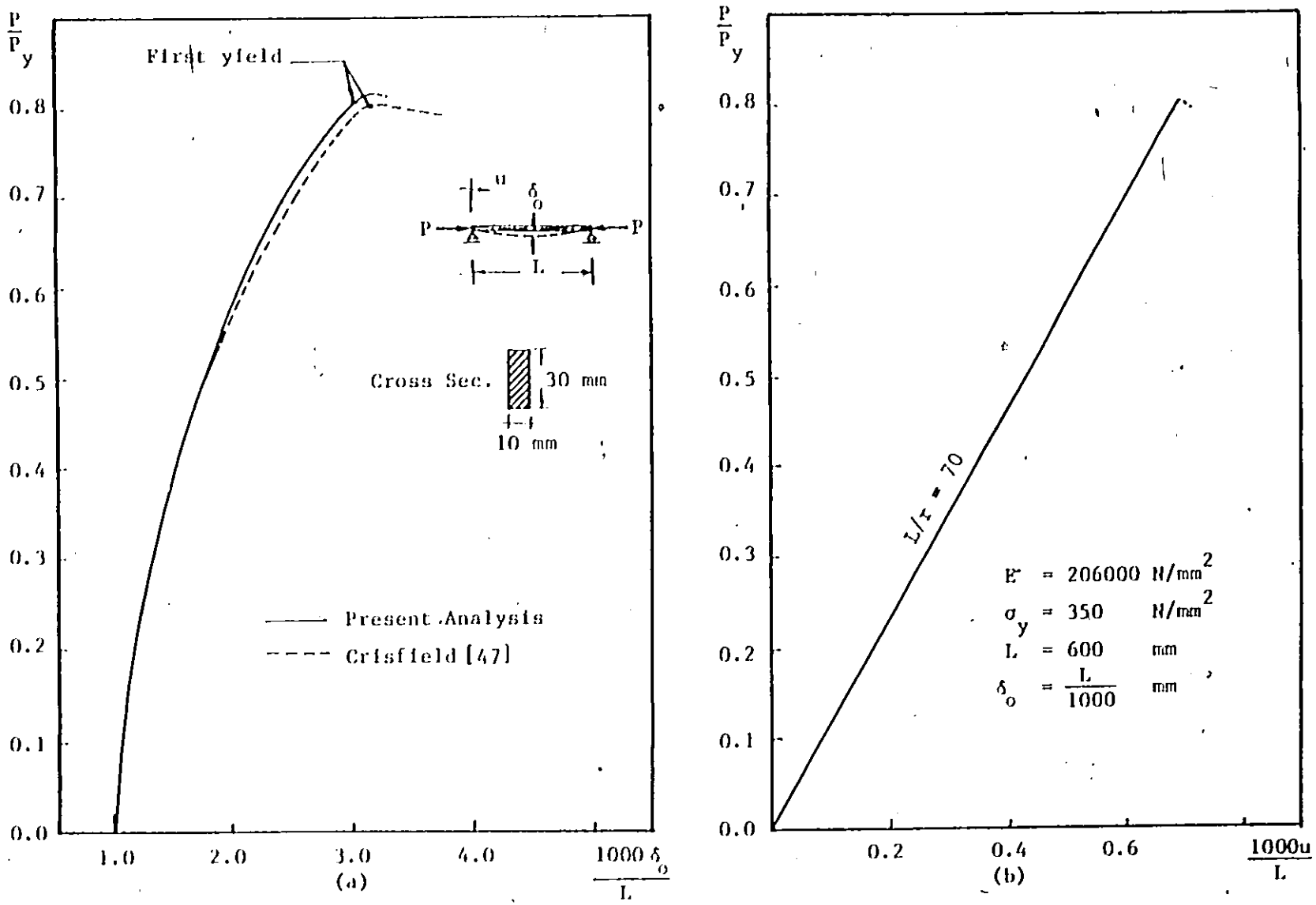

Figure 3.3 : Results of Single-Span Beam-Column Under Axial Loading

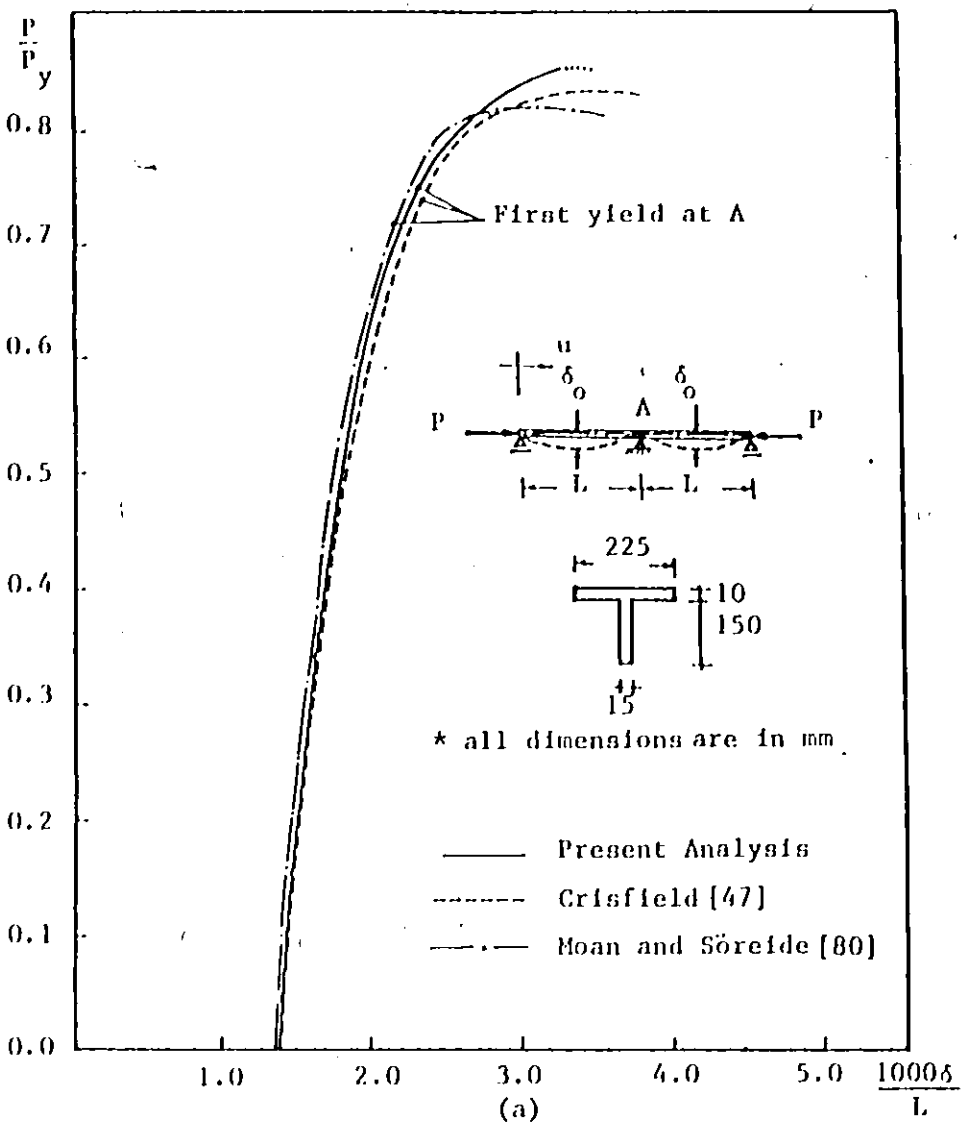

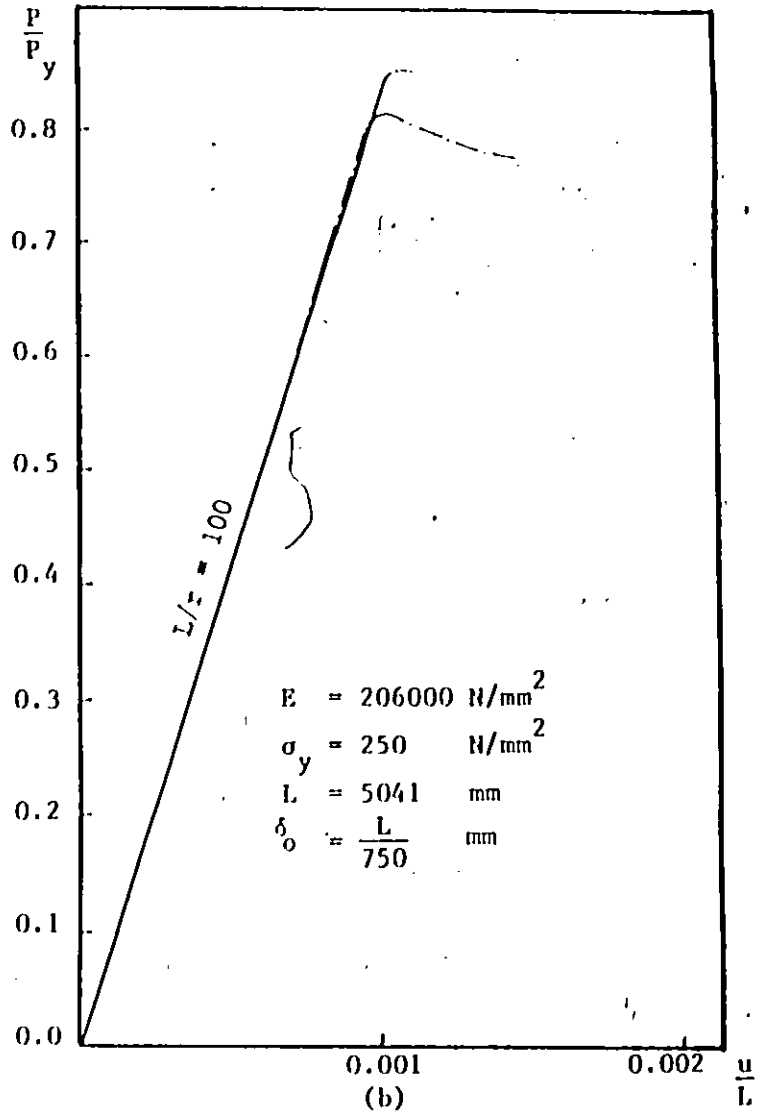

Figure 3.4 : Predictions of Two-Span Beam-Column Under Axial Loading

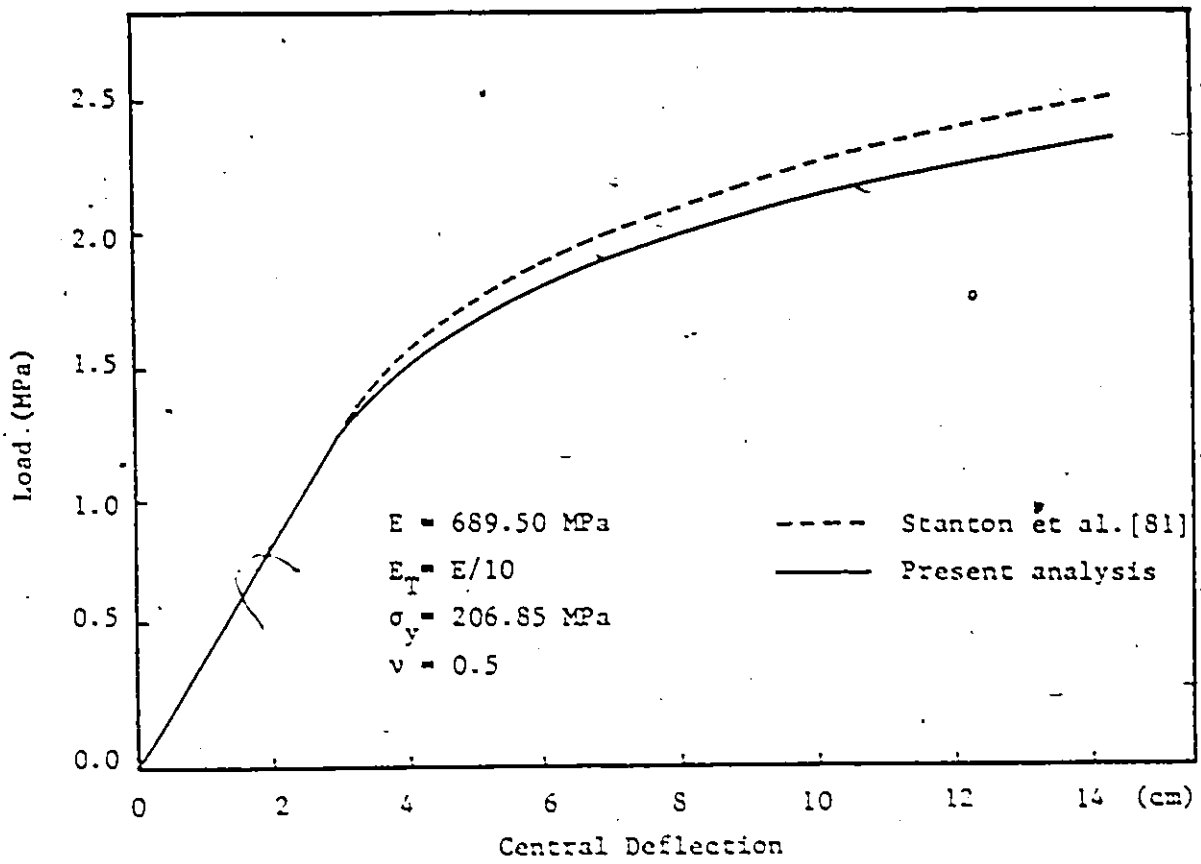

a) Load-Deflection Curve

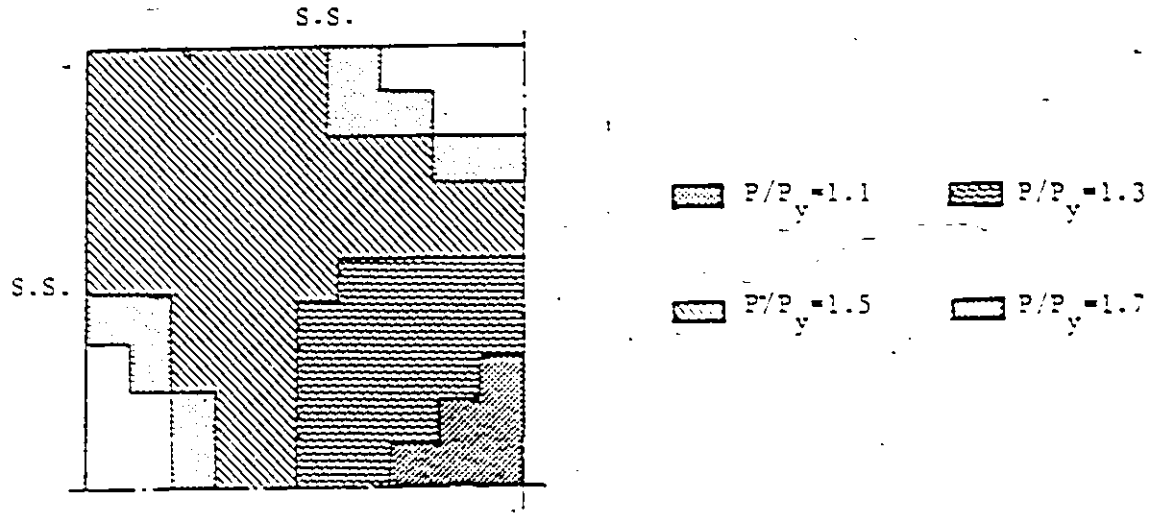

(b) Progression of Full Plastic Regions

Figure 3.5 : Post-Elastic Prediction of Simply Supported Square Plate

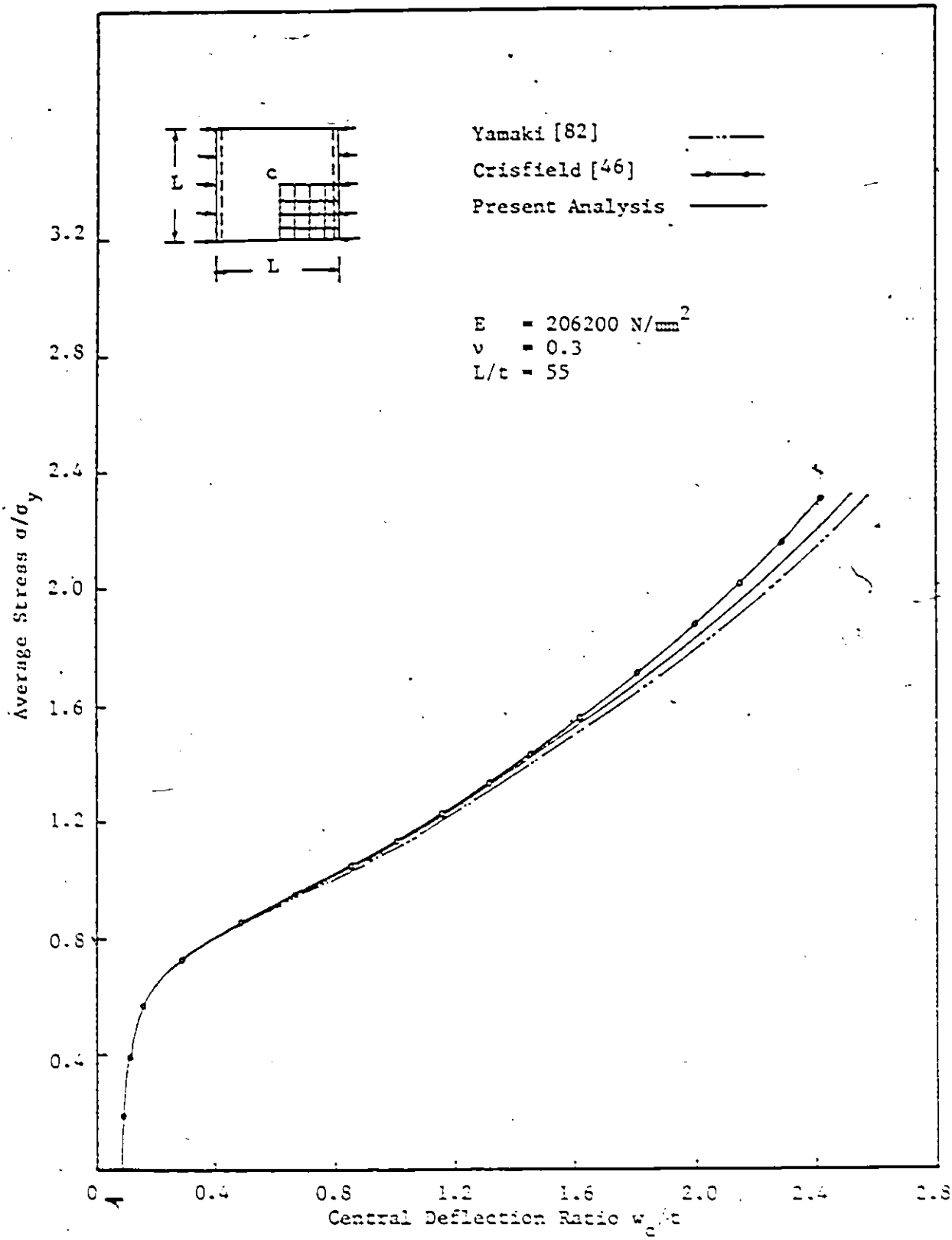

Figure 3.6 : Response of Imperfect Elastic Plate under In-Plane Load

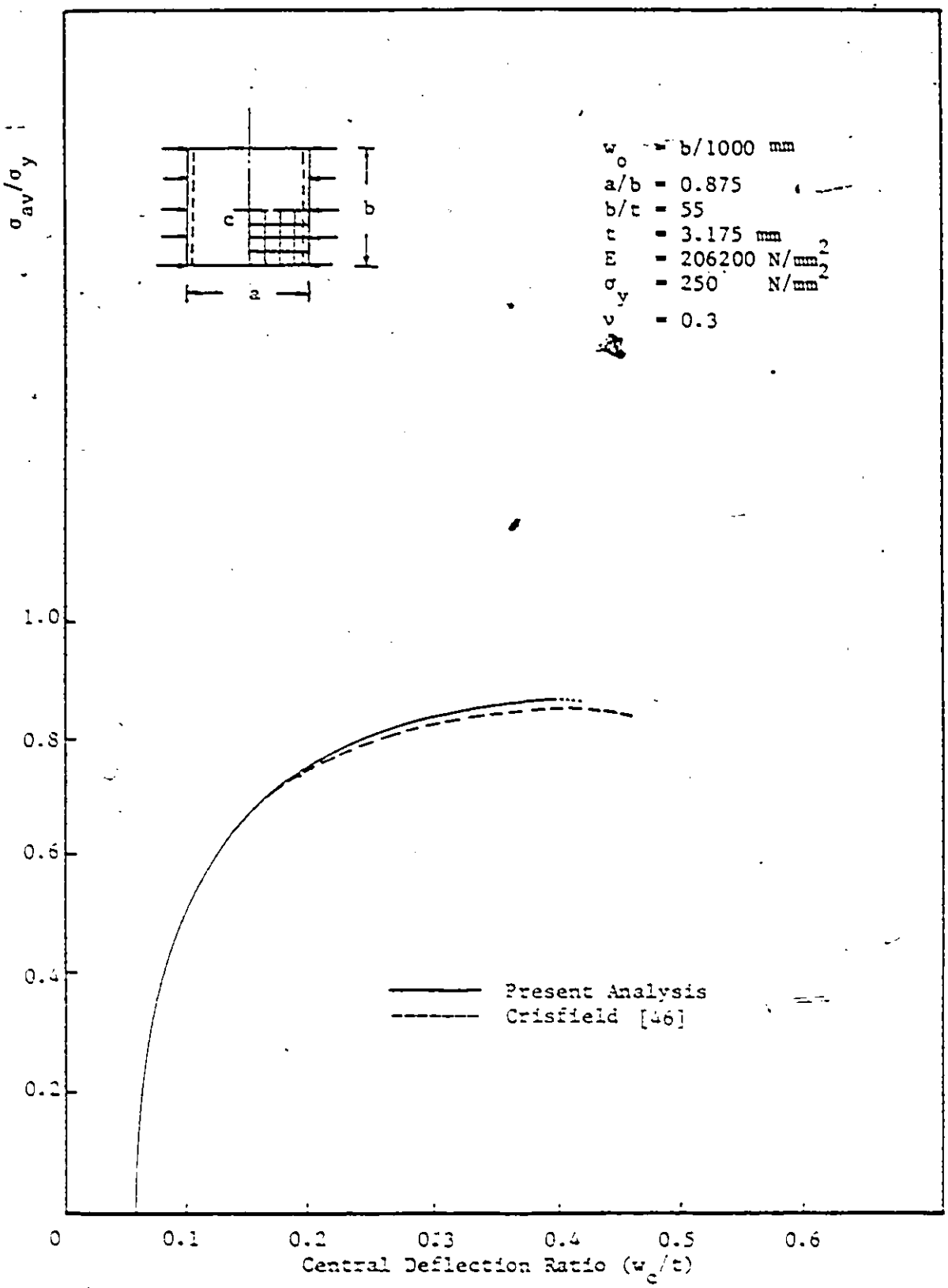

Figure 3.7 : Elasto-Plastic Response of Imperfect Plate Panel in Direct Compression

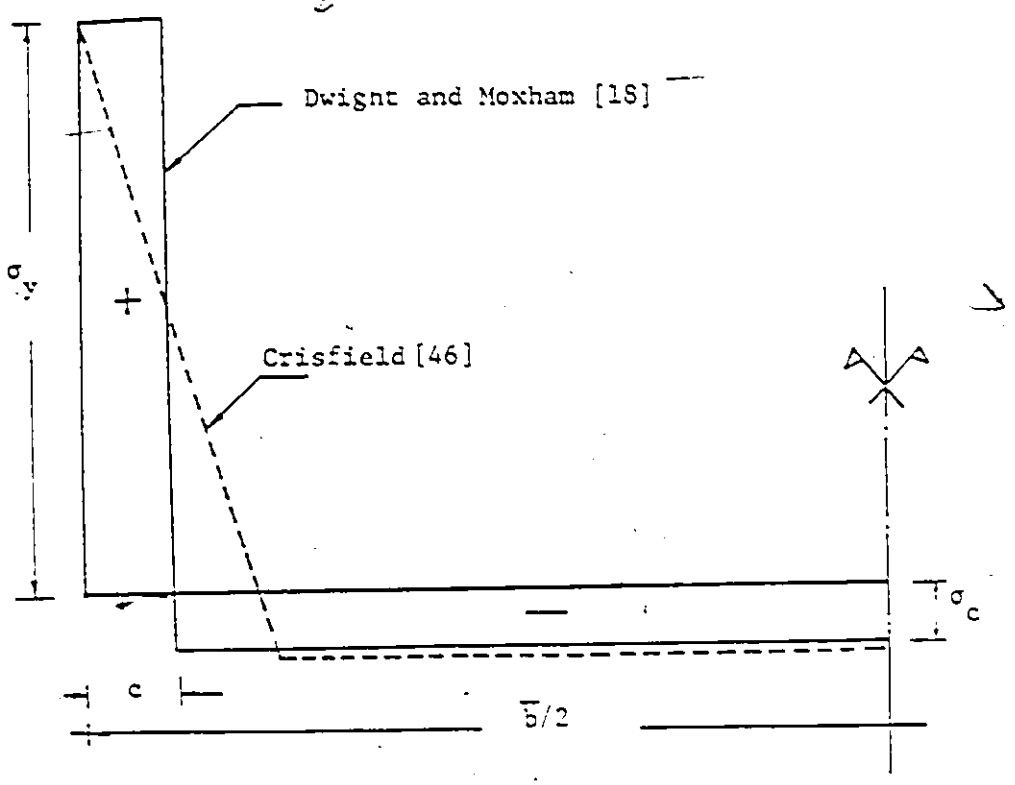

Figure 3.8 : Possible Residual Stress Distribution due to Welding

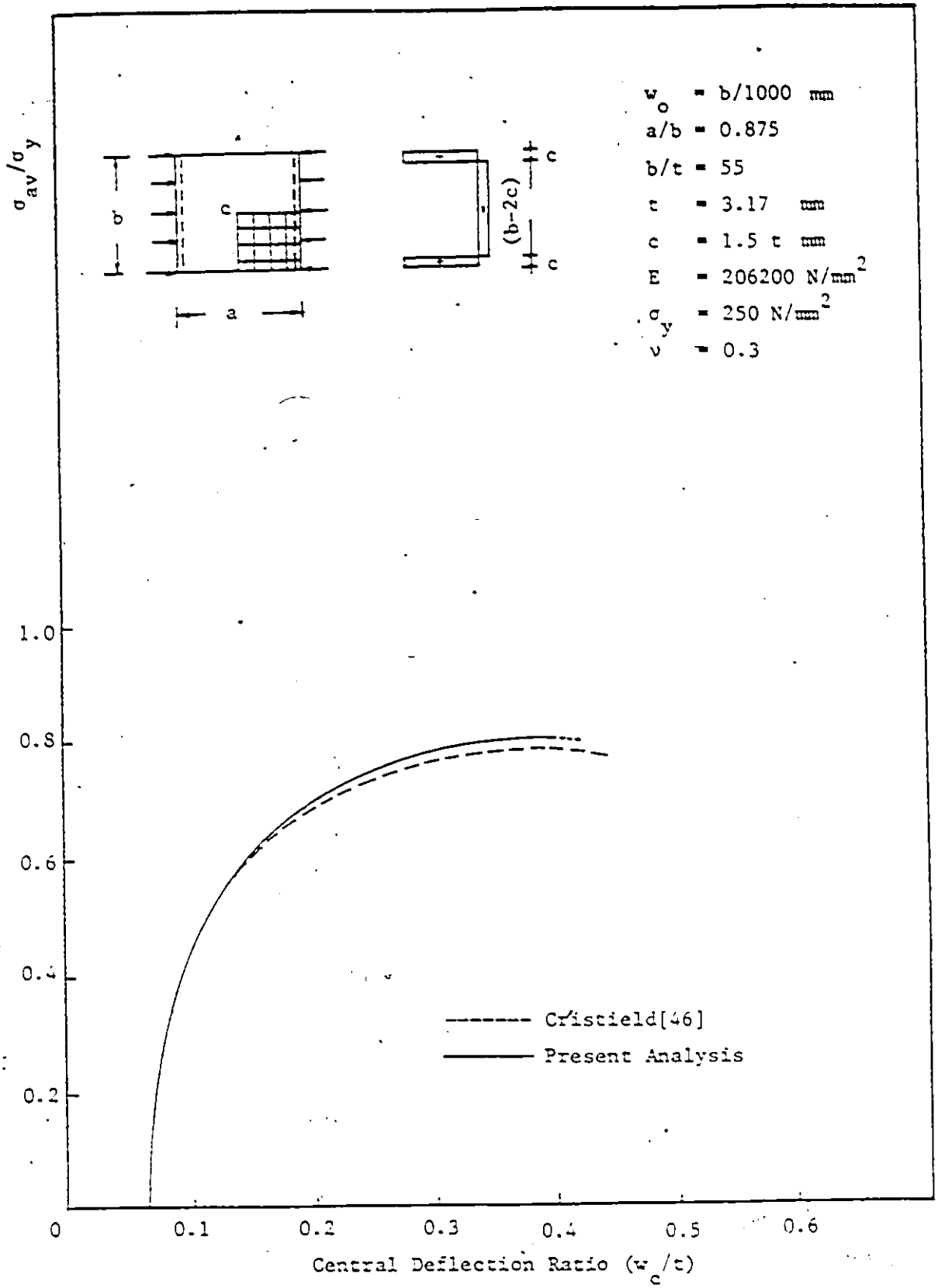

Figure 3.9 : Response of Uniformly Compressed Plate Panel With Residual Stresses

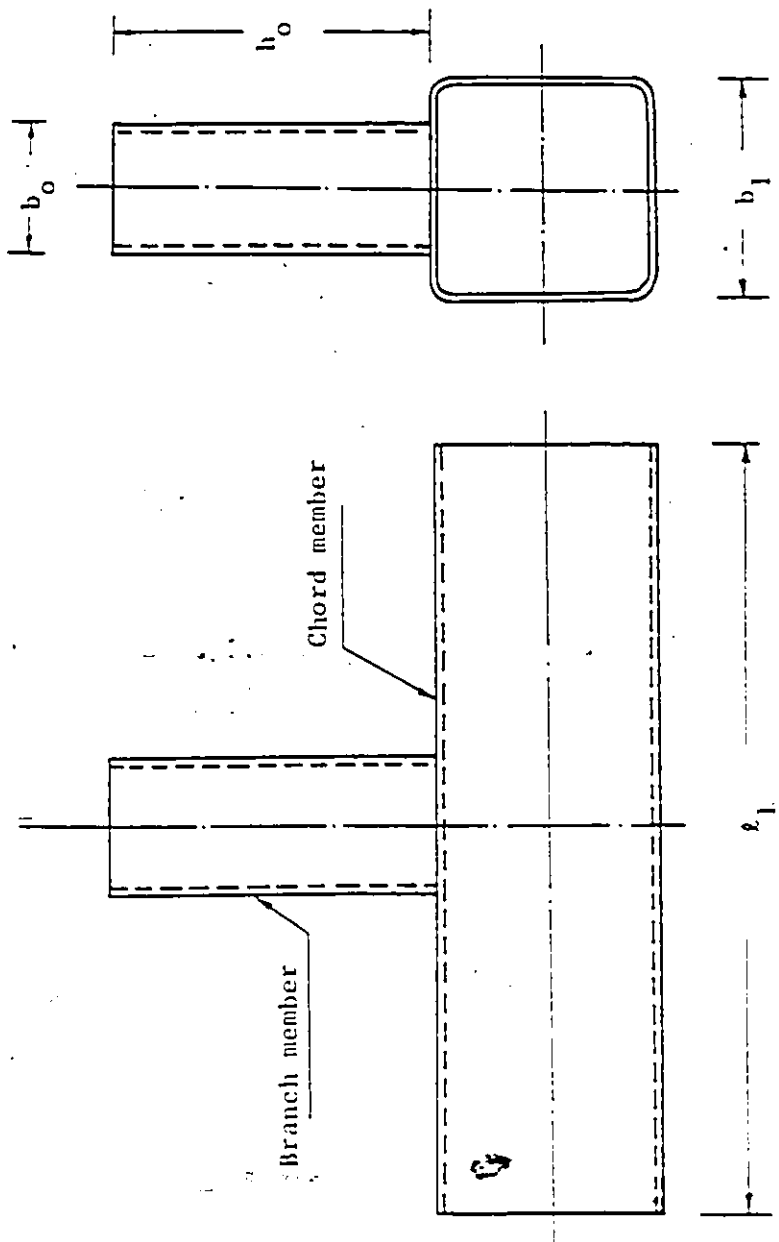

Figure 3.10 : Sketch of Typical Unequal Width Hollow Section T-joint

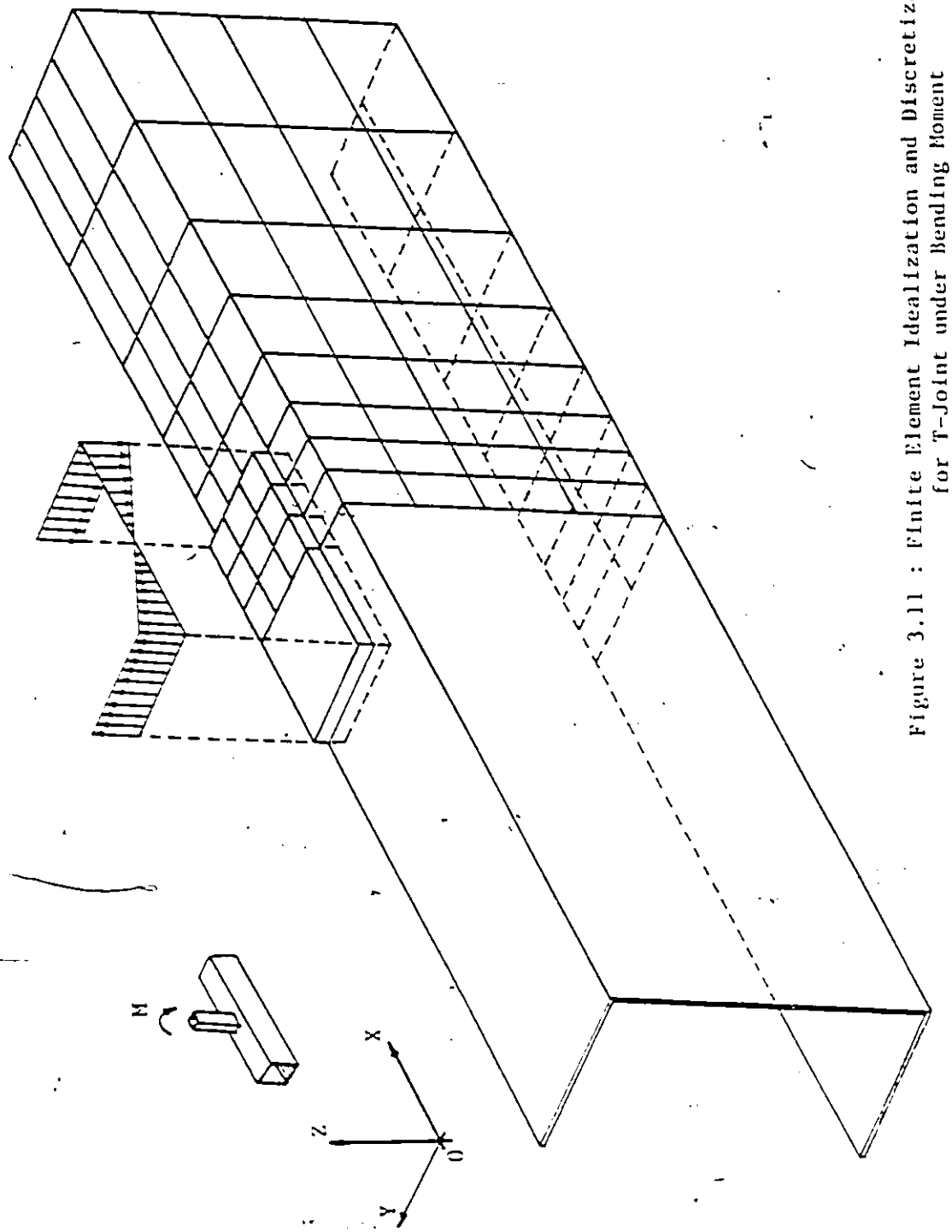

Figure 3.11 : Finite Element Idealization and Discretization for T-Joint under Bending Moment

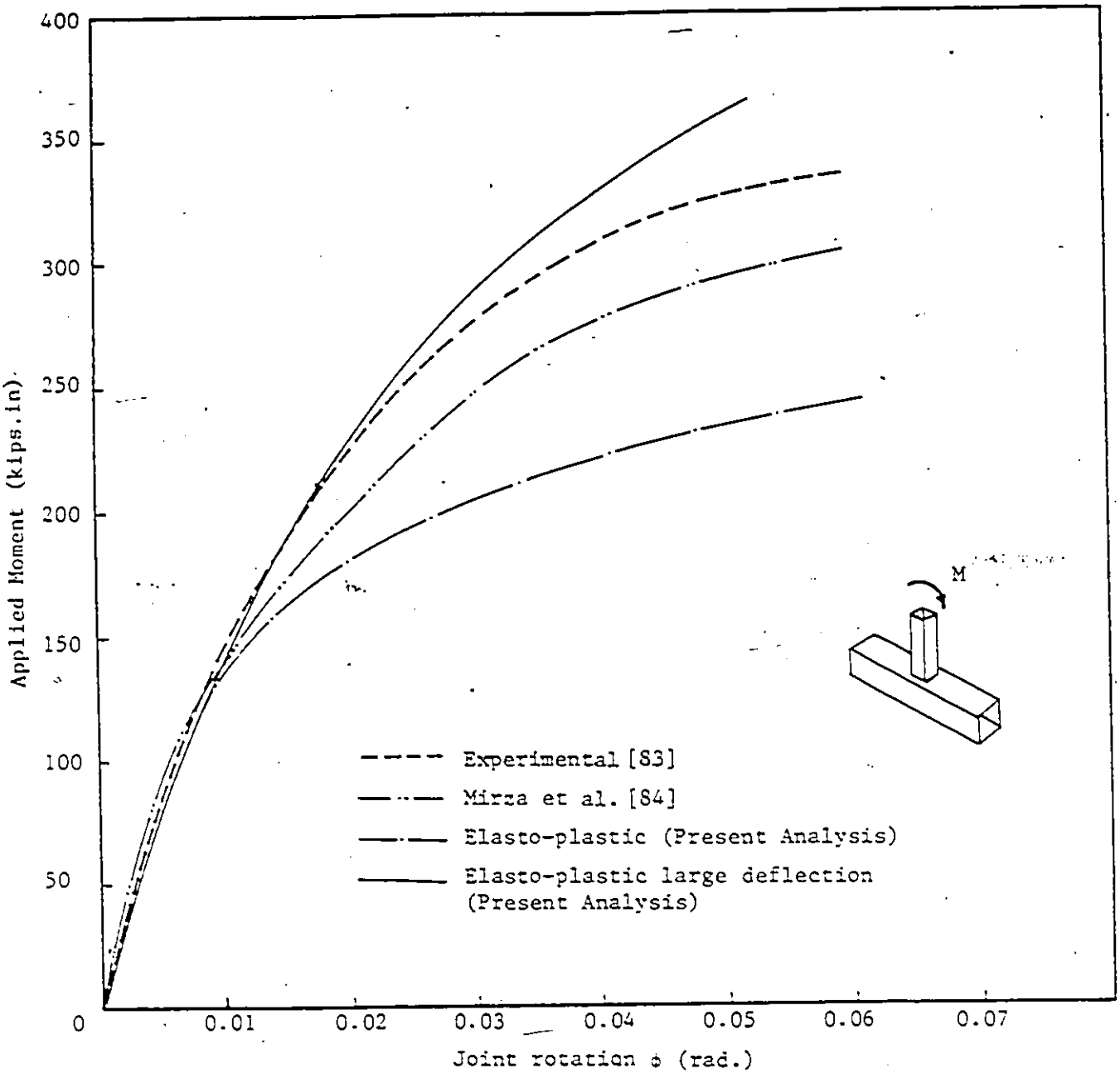

Figure 3.12 : Moment Rotation of Single Chord T-joint

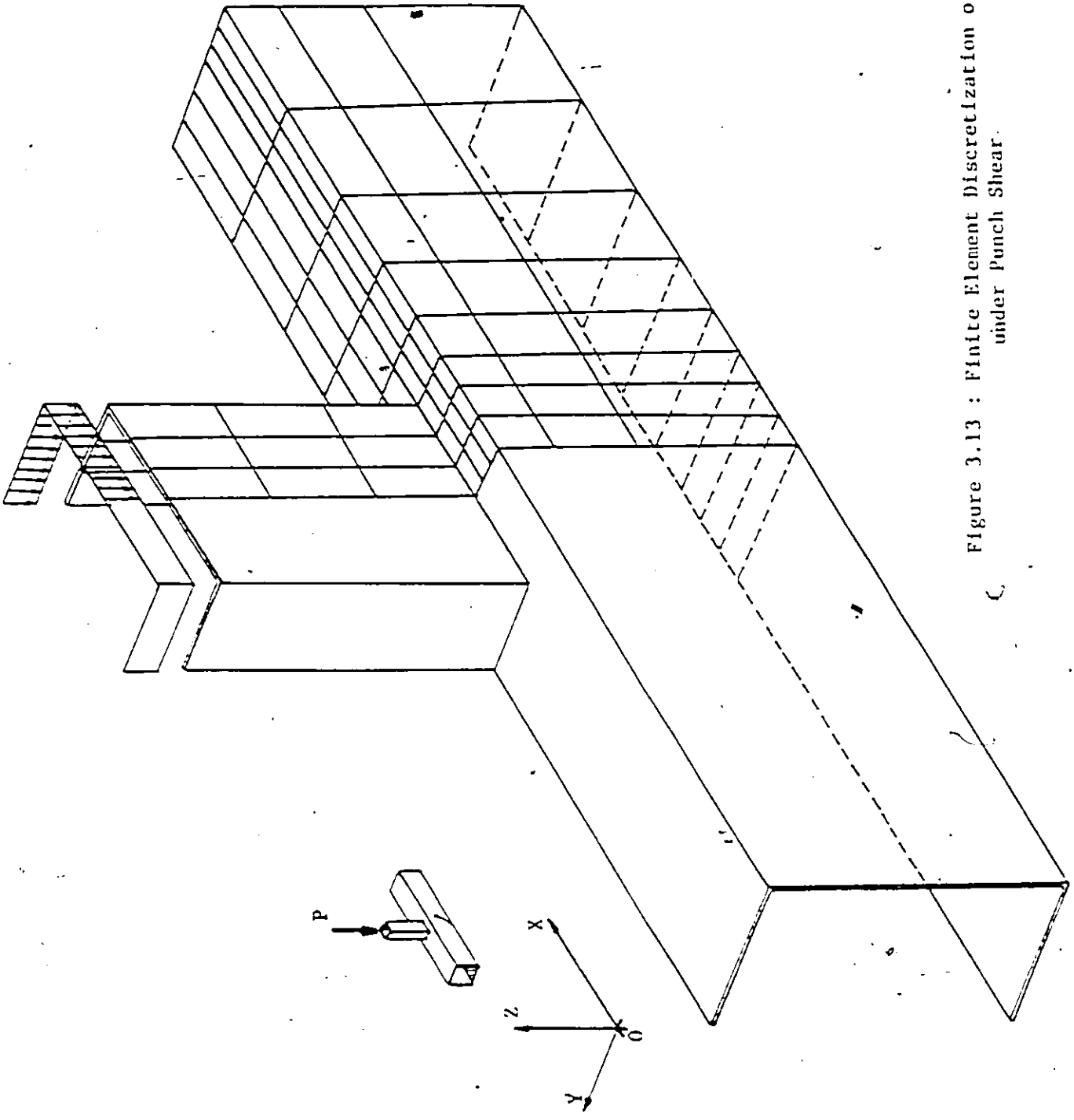

Figure 3.13 : Finite Element Discretization of T-Joint under Punch Shear

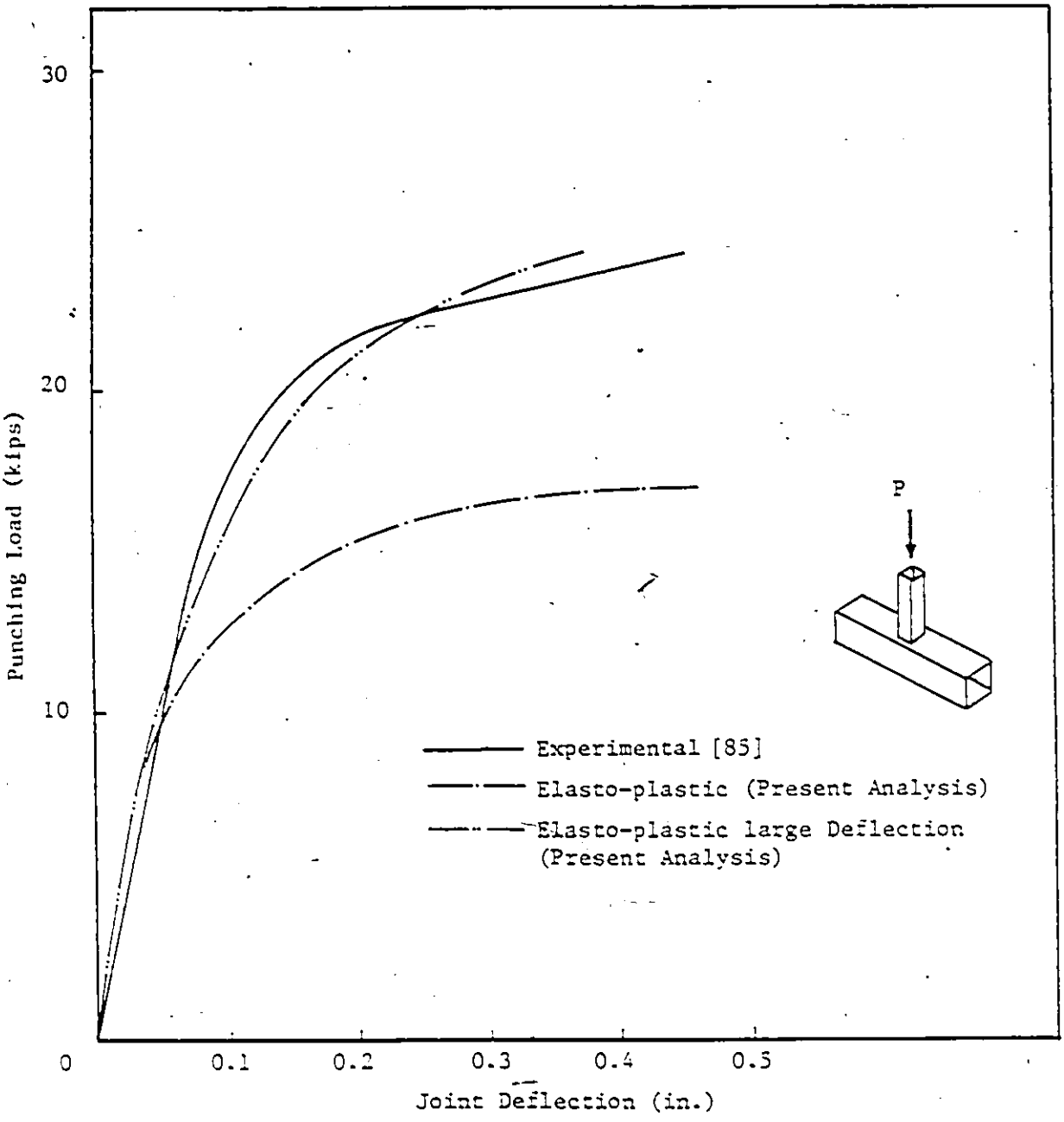

Figure 3.14 : Load Deflection of Single Chord T-joint Under Punching Shear

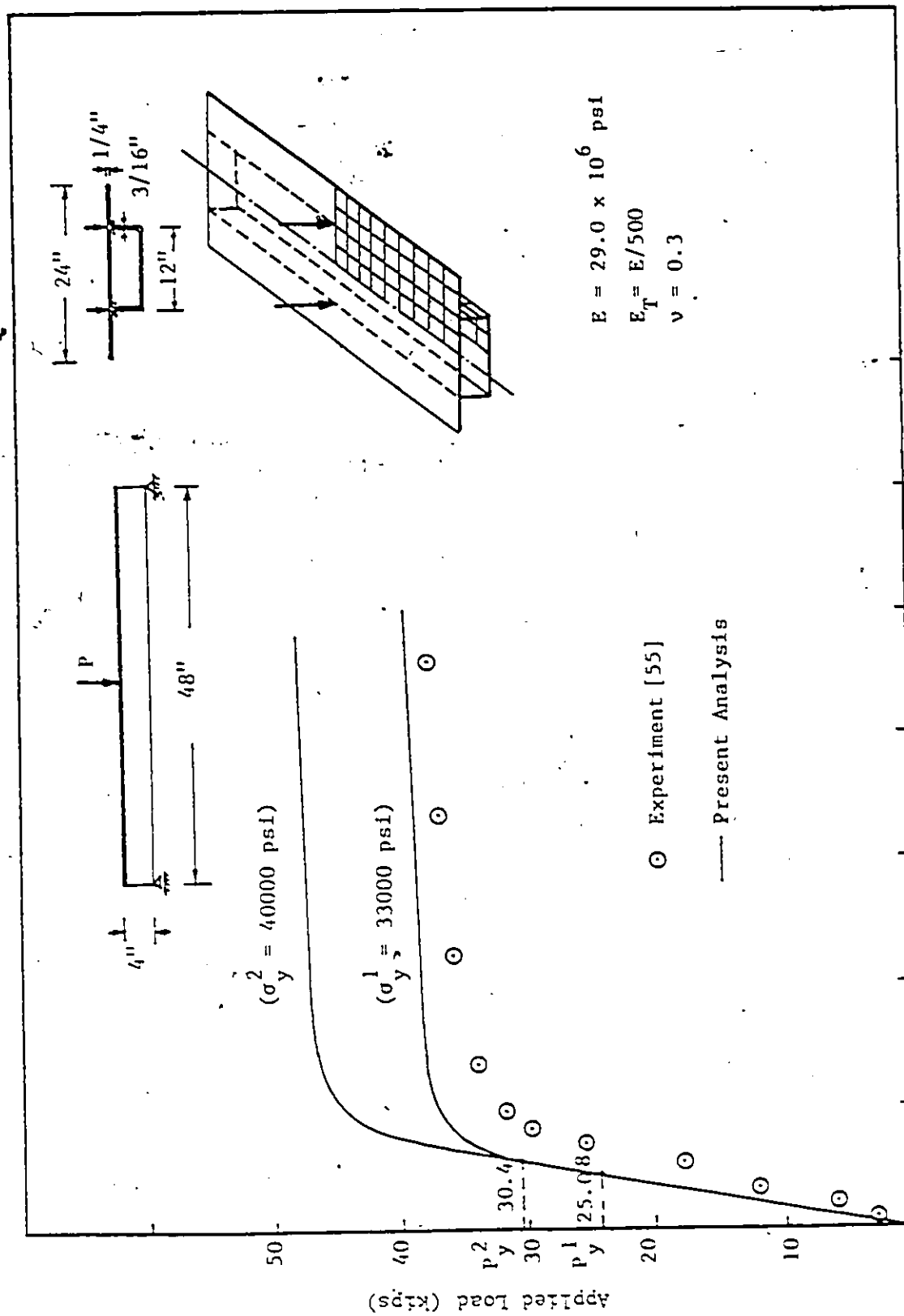

Figure 3.15 : Load-Deflection of Simply Supported Box Beam

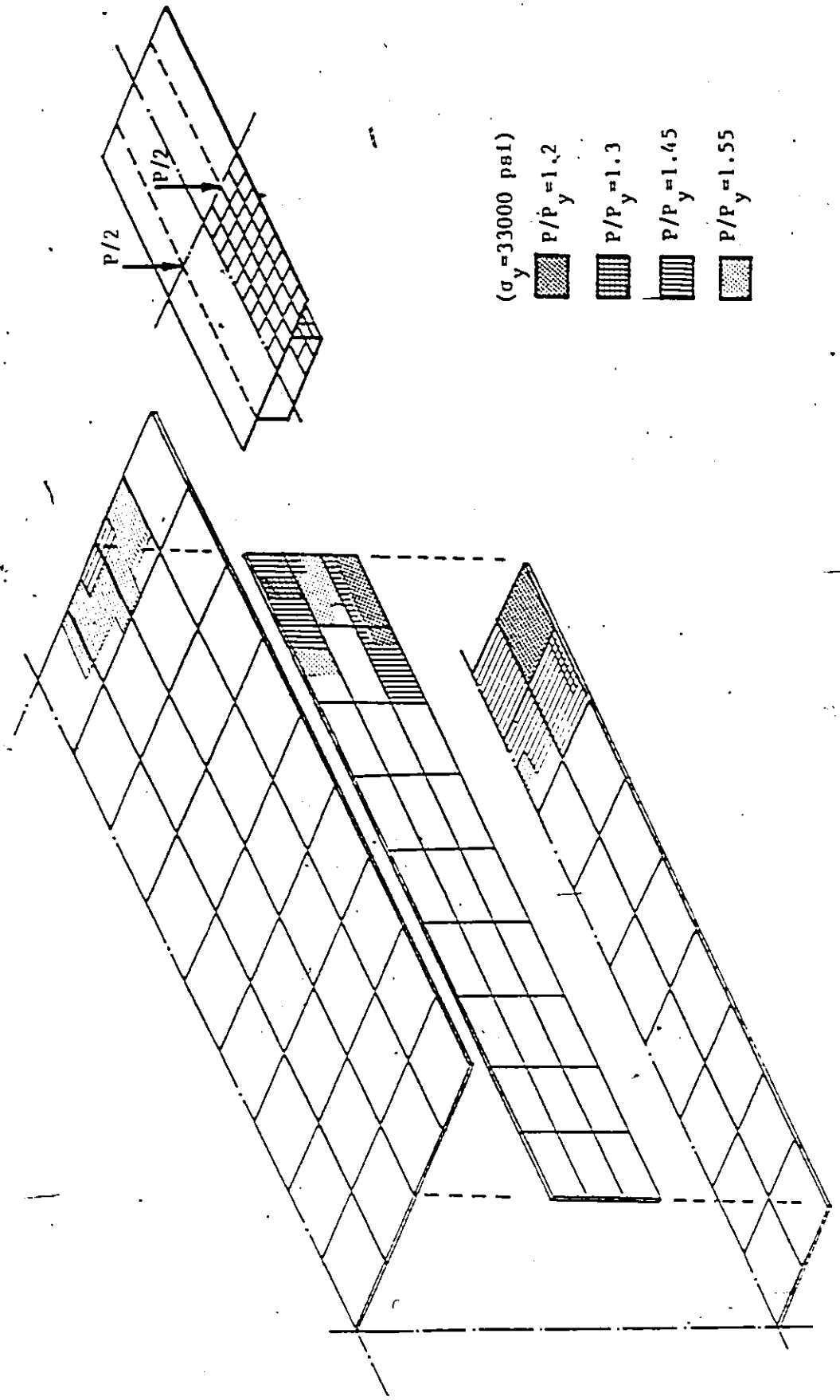

Figure 3.16 : Plastic Zones at Different Load Levels

CHAPTER FOUR

ANALYSIS OF STIFFENED BOX GIRDER

4.1 Introduction

4.1.1 General

The response of the stiffened steel box girder finite element model formulated in Chapter 2 is the subject of investigation in this Chapter. It is important to establish whether the model is capable of giving reasonable predictions of the strength and behavioural characteristics of these complex structures for several cases of assumed fabrication states. Since the compression flange of the box girder is generally the most critical component as earlier described, the present study focuses on the overall collapse of the box precipitated by buckling of that component.

The analysis will include the effect of geometric initial imperfections and residual stresses due to welding on the behaviour of stiffened steel box girders. The effects of two types of geometric initial imperfection commonly encountered in code provisions pertaining to tolerance recommendations were investigated. These include out-of-

plane deviations of plate panels and out-of-straightness of stiffeners. In addition, the effects of residual stresses due to welding are considered for a prescribed stress distribution across the compression flange.

Another topic of controversy which is considered to be important in the strength of box girders is the so-called "shear lag" effect. A minor focus of the study has addressed this question through a study of the influence of moment gradient compared with that of constant moment.

To demonstrate the significance of the aforementioned factors on the behaviour, the finite element model is applied to a symmetrical overhanging stiffened steel box girder model recently tested at McMaster University, and portrayed schematically in Figure 4.1. That experimental model was constructed to shed light on the response of a typical pier girder of the Hunt Club Bridge in Ottawa, subjected to heavy concentrated loads. Theoretical and experimental ultimate capacities are compared, thus providing a basis for evaluating the adequacy of the theoretical model developed in this thesis.

4.1.2 Experimental Model Characteristics

There is a considerable diversity of tolerance levels that exist in specifying plate panel out-of-planeness in standards of practice among countries of the industrialized world [68]. This controversy is due to uncertainty regarding the extent to which the capacity is affected by these imperfections. Moreover, no Canadian bridge code

appears to have addressed the question of a tolerance for out-of-planeness of plate panels. Consequently, Korol and Thimmhardy [65] decided to carry out two experimental tests to investigate the strength reduction of a stiffened steel box girder due to initial imperfections.

They tested to collapse a symmetrical overhanging rectangular stiffened steel box girder, measuring 14.0 m in span, 1.2 m in height and 1.8 m in width. The webs and flanges of the box consisted of thin plates with plate width-to-thickness ratios in a range commonly used in Canada. The model was to simulate the highly stressed region existing over the supports of a continuous bridge structure.

Their physical model was a quarter scale of the prototype. Such a scale was chosen for two reasons. First, there is the problem of hydraulic jacking capacity and support force limitations in the laboratory. Second, there is the need to represent as accurately as possible the effects of residual stresses that would occur during fabrication of the prototype.

The compression flange of the model consisted of a steel plate with a number of equally spaced longitudinal T-stiffeners and more widely spaced and deep transverse T-stiffeners. The compression domain of the web was stiffened by two appropriately spaced longitudinal stiffeners having angle cross sections, while the entire web was provided with equally spaced vertical T-stiffeners. The full width tension

flange in the prototype was replaced by equivalent area tension flange plates attached to each web.

In addition, the model included full width solid plate bearing diaphragms which were stiffened transversely by compact flat stiffeners located at the twin bearing supports. Another three solid plate diaphragms were located at mid-span and at the free ends of the cantilevers.

Figure 4.2 shows dimensions of the principal components comprising the box girder model. The structural parameters relevant to these components are summarized in Table 4.1. It can be seen that the panel slenderness (width-to-thickness) ratio for the flange was 45, and ranged from approximately 48 to 144 for the web plate panels.

The material used in the various components was generally Grade CSA G40.21-M350W, although tensile tests were conducted to establish their actual yield stresses and post elastic responses.

The resulting out-of-plane distortions and welding residual stresses within the model are caused principally from the normal process of manufacturing, and in particular by the welding of components. Of primary interest in this study is the influence due to the welding of the stiffeners to the compression flange plate. The common type of geometrical imperfection associated with the resulting plate panels that are formed is the so-called "hungry horse" shape type [68] as shown in Figure 4.3(a), while out-of-straightness is associated with the

longitudinal stiffeners. The pattern of residual stresses created due to the weld shrinkage is similar to that shown in Figures 1.2 and 4.3(b).

Two different levels of imperfection were created within each cantilever of the model, with a view to assessing the effect of the magnitude of imperfections on load sustaining capacity. The welding processes within the two cantilever sections were the same, except the size of the continuous fillet welds used to attach the stiffeners to the flange plate which differed. For one cantilever, the weldment was 2.5 mm in thickness, while it ranged from approximately 3.0 to 3.5 mm in the other cantilever.

Two simulated concentrated loads were applied to each tip of a cantilever part in turn as shown in Figure 4.4. Due to this loading configuration, box panels either in the cantilever portion or in the central region between supports could then be subjected to shearing force and bending moment. From simple structural analysis, it is obvious that the most stressed box panels are those adjoining the diaphragm on either side of the upward force resisting support. Also, from the standpoint of moment gradient the more highly stressed of the two panels lies in the central region between supports.

As mentioned earlier, part of this work considers the weakening effects of welding residual stresses on initially distorted stiffened steel box girders; thus simulating the initial conditions experienced by girders over intermediate supports in a continuous bridge structure. Since the compression flange is the most critical component, it was

desirable to cause collapse of the whole box by initiating plate buckling of the compression flange close to the support in each cantilever portion separately. Torsional buckling of a longitudinal stiffener was deemed unlikely to govern collapse since its T-shape tends to inhibit instability.

Additional longitudinal stiffeners were attached to the highly stressed box panels within the compression flange in the central region between supports to avoid its precipitating failure of the girders. This precaution thus permitted testing the cantilevers in turn. Also, to avoid interaction between the bearing diaphragm and the compression flange of the adjacent box panels, the former was stiffened by stocky compact flat stiffeners over the bearing supports.

4.1.3 Analytical Model Characteristics

Because constructing and monitoring the tests of such a large scale model is especially expensive, additional experiments could not be contemplated. Consequently, confidence in an analytical model whose predictions are in accord with tests must be tempered. However, as indicated in Chapter 3 a very close agreement was achieved for other types of problems having well accepted analytical approaches. It was decided then to apply the present analytical model developed in Chapter 2 to several cases to further insights into the effect of geometric imperfections and residual stresses on the strength reduction of "perfect" box girders.

The analytical models to be considered, replicate in most details the physical model mentioned above and are summarized in Table 4.1. Because the present beam element formulation did not include a stiffener having an angle as its cross section, the web stiffeners in the physical model were replaced by equivalent flat stiffeners as shown in Figure 4.6. For simplicity and economy, the stiffened full width bearing diaphragm in the physical model was replaced by a stocky unstiffened full width solid plate diaphragm. Also, the twin bearing supports under the diaphragm were replaced by a full width line support in the analytical model. In cases where the diaphragm is excluded, each web was provided with transversely stocky stiffeners over the support to distribute the concentration of shearing force over its whole depth.

To minimize the amount of computer storage and time requirements for the numerical computations involved, simulated loads were applied to the free ends of the box simultaneously, as shown in Figure 4.5. This loading and support arrangement allowed the girder to have double symmetry. In such circumstances only one quarter of the model needed to be considered in the analysis.

4.2 Idealization and Discretization

In the present finite element model, the compression flange, webs, and diaphragms were discretized by membrane-bending elements, while the tension flanges were modelled by beam elements. With regard to flat stiffener components, these were simulated by eccentric beam

elements, while a T-section stiffener was idealized by superimposing two eccentric beam elements as explained in Chapter 2.

In three-dimensional plate assemblage structures, refining the mesh of any component is associated with an increase in the number of elements in the other components, which automatically increases the computing cost. A reasonable number of elements has been arbitrarily chosen within each component to achieve a moderate aspect ratio for the elements. Thus, the total size of the problem could be handled by the main frame computer available. For the one-quarter portion of the model that needed to be considered, eighteen elements along the half length were chosen. This number was deemed to be sufficient to provide reasonable accuracy. Ten elements in total, were adopted transversely for the web and half width of the compression flange. Figures 4.8, and 4.9 show different meshes adopted in the present study.

The assumed properties of steel for the analytical model are as follows: modulus of elasticity = 210000 N/mm^2, tangent modulus E_T = 0.001 E, yield stress = 350 N/mm^2, and Poisson's ratio = 0.3.

4.3 Imperfections

4.3.1 Geometrical Imperfections

To investigate the degree to which the collapse strength of

steel plated structures is sensitive to the magnitude and modes of geometric imperfections, different states of idealized imperfection were assumed within the compression flange of the box to be analyzed. The types considered were as follows: the plate mode, the stiffener mode, and the superimposed mode. Out-of-straightness about an axis parallel to its neutral axis, was the type of imperfection considered for the stiffener.

Because the compression flange of the box was provided with longitudinal T-section stiffeners which are commonly used in Canadian-built bridges, their buckling due to a torsional mode would rarely occur. Consequently, such an imperfection mode was excluded.

The compression flange of the analytical model is provided by geometric imperfection modes with an oscillating pattern. The superimposed mode within the collapsed box panel can be expressed as

$$w_o = \bar{w}_o^{st} \sin\left(\frac{\pi x}{L^p}\right) \sin\left(\frac{\pi y}{W^p}\right) + \bar{w}_o^{p\ell} \sin\left(\frac{3\pi x}{L^p}\right) \sin\left(\frac{5\pi y}{W^p}\right) \qquad (4.1)$$

where the first term represents an overall stiffener mode, while the second denotes the plate buckling mode. The system of axes x, and y are defined in Figure 4.7, while L^p and W^p are the length and width of the considered box panel, respectively. Also, $\bar{w}_o^{st}$ and $\bar{w}_o^{p\ell}$ represent the amplitudes of these modes. The permitted values of these are generally related to the corresponding span, i.e. L^p and $\bar{b}$ respectively. The permitted out-of-straightness of stiffeners is specified in several

bridge standards in the world but vary widely from $\frac{L^p}{500}$ to $\frac{L^p}{1200}$} [68]. Similarly, acceptable out-of-plane deviations of plates vary in the range $\frac{\bar{b}}{300}$ to $\frac{\bar{b}}{150}$, where $\bar{b}$ has been defined previously as the plate width (spacing between stiffeners). In fact, it has been suggested that in the Canadian context, a tolerance limit of $\bar{b}/150$ might be acceptable [65].

In the present analysis, two levels of out-of-straightness, and out-of-plane deviations were adopted representing a specified tolerance limit and the one proposed [32]. For the plate mode, $\bar{w}_o^{p\ell}$ was chosen as $\bar{b}/200$ and $\bar{b}/150$, while for the stiffener mode, $\bar{w}_o^{st}$ was chosen as $\frac{L^p}{750}$ and $\frac{L^p}{500}$.

4.3.2 Residual Stresses

In the United Kingdom, bridge designers are provided with formulae for computing the approximate shrinkage forces of welds used in attaching stiffeners to plate components [14]. Two alternative ways of allowing for the weld induced stresses are provided. The first way is to calculate an additional residual deflection which is equivalent to the residual stress and hence ignore this stress subsequently. A second approach is to treat the residual stress as an additional applied stress. When applying the first method, the effective residual deflection of the panel should be taken as:

$$\bar{w}_o^* = \sqrt{\bar{w}_o^2 + 8(\ell_b)^2 \sigma_c/\pi^2 E} \qquad (4.2)$$

where σ_c is the residual compressive stress in the middle portion of the plate panel. The displacements $\bar{w}_o^*$ and $\bar{w}_o$ denote the amplitude of the effective (equivalent) deflection and the real (initial) deflection, respectively, both of which are compatible with the critical buckling mode of the panel. The symbol (ℓ_b) denotes the half-wave length of this buckling mode.

In this study, the residual stresses have been considered as initial stresses confined to the plate panels and to the stiffeners of the compression flange. The residual stress pattern within the plate panels between stiffeners is adopted according to the Dwight and Moxham [18] idealization shown earlier in Figure 3.8. The idealized compressive residual stress (σ_c) in the middle portion of the plate panels induced by weld shrinkage in the heat affected zone has been computed with an empirically derived formula originally proposed by Dwight and White [86]. This compressive stress is a function of the ratio of the weld area to that of the plate-stiffener combination assumed affected by the weld. Mathematically, this formula is expressed as

$$\sigma_c = 0.2\ \bar{\beta}\ \Sigma\ A_w/\Sigma(\bar{b}t+A_s) \qquad (4.3)$$

where $\bar{\beta}$ is a constant that depends on the welding process; it ranges

from 40070 to 70130 N/mm^2[87]. A_s and A_w are the areas of stiffener's cross section and weld respectively. For the dimensions of the model, the computed σ_c value was determined as 21 N/mm^2. An average value of $\bar{\beta}$ = 55000 N/mm^2 was assumed in this case. In the present analysis, the residual stress pattern over the depth of the eccentric stiffeners was idealized following Nordsve's approach [50] to satisfy both force and moment equilibrium requirements within the domain of the model (see Figure 4.3(b)).

4.4 General Description of the Simulated Numerical Tests

A majority of the present analytical simulated tests was carried out to investigate the effect of imperfections on the collapse of the box girder panel closest to the support and subjected to both shearing force and bending moment.

One simulation was performed as a bench mark case and involved the collapse of a box panel subjected to bending moment only. The strength of such a panel could be related to those involving similar panels (i.e. having the same geometry) but subjected to shear and moment. The effects of shear lag on the structural performance of the box girder could then be ascertained. Because the analytical models were loaded symmetrically as shown in Figure 4.5, the middle zone between supports was thus subjected to pure moment. The cantilevers, meanwhile, were subjected to a combination of moment and shear.

For all except one loading case (pure moment of box panels between supports), it was necessary to force a collapse of the box panel of the cantilever section nearest the support by hypothetically providing special reinforcement between supports. Therefore, to cause the collapse of box panel (4) shown in Figure 4.7, box panels (1), (2), and (3) required reinforcing. To initiate failure of the box panel (1), panels (2), (3), and (4) had to be stiffened.

The simulated reinforcement required to achieve buckling of a particular box panel in the analytical model was carried out somewhat differently than was done for the physical model. For example, in the physical model, additional stiffeners were added to the compression flange. However, in the analytical model, the thickness of the compression and tension flange was increased in such a way as to avoid any shift in the centroid of the box cross section. By doing so, it was possible to avoid any unforeseen complicating effect in the behaviour of the box.

In the analytical simulations where the diaphragm was included, the diaphragm's thickness was increased up to 40 mm to assure that it would behave elastically until the whole box would reach its ultimate load. Consequently, no interaction would be expected to take place between the diaphragm and adjacent components.

4.5 Commentary on the Analytical Tests and their Results

Numerical simulation tests were conducted employing somewhat

different rectangular element meshes to obtain the one that would provide the most satisfactory results. Of course, the constraints of computer time and storage were considered of prime importance. The grid identified as mesh (3) in Figure 4.9 satisfied these objectives and is the one for which most of the theoretical results involving a collapse of the critical box panel subjected to bending and shearing forces is reported. Similarly, mesh (4) was used for the case where the collapsed box panel resists bending moment only. Figures 4.8, and 4.9 show the pattern of discretization of those two meshes together with other meshes investigated, also deemed to be satisfactory. Note that only one-quarter of the structure (shown upside down for clarity) needed to be considered in the analysis of the double cantilever beam, and was therefore used to predict ultimate load states.

Twelve simulated tests were conducted with a classification made into three categories, as shown in Table 4.2. In Category A, a diaphragm over each of the supports was included which possessed both in-plane and bending actions. Different meshes shown in Figures 4.8 and 4.9 were used to investigate the sensitivity of the collapse load to the number of elements contained in the most highly stressed panel. Four simulated tests were performed to identify the best mesh able to predict failure loads, stresses and collapse modes considering computational constraints.

Since it was found that accurate modelling of the diaphragms made a negligible difference on the response of the structure to the applied loading and support condition, they were replaced by stocky

transverse stiffeners attached to the web at support in Categories B and C. More attention was devoted to investigate the effect of imperfections on the strength of the compression flange of the box girder for combined shear and moment. In total, seven simulations were performed with this assumption. One simulated test in Category C was carried out on a perfect box girder, where the collapsed box panel was subjected to a simple pure moment. This case served to provide a basis for investigating the effect of moment gradient and consequent shear lag on the strength of the perfect box obtained in other cases. Collapsed panels in Categories A, B and C required artificial reinforcement of the adjacent panels as shown in Figures 4.7(a) and 4.7(b), respectively.

The results obtained from the twelve finite element simulated tests will be discussed in subsections presented below. Results are given of predicted deflections, stresses, the development of plastification and collapse loads. Special attention is given to the effect of imperfections in the Category B load tests.

4.5.1 A-Group Simulations

This group consists of four simulated tests identified as A1, A2, A3 and A4. Full diaphragm properties were included in analysis A1 to A3. Imperfections have been excluded in this group, since the intention was to establish the sensitivity of the ultimate load to the number of elements considered in the most highly stressed panel. The meshes (1), (2), and (3) were used in test runs A1, A2, and A3, respectively.

The yield loads and ultimate loads obtained from the runs A1 to A3, ranged from 842 to 848 kN, and from 1648 to 1674 kN, respectively. The results indicate a negligible difference for the corresponding load limits.

Meanwhile, the tip deflection versus load relationships for the three simulated tests were found to be virtually identical. Overall behaviour indicates essentially linear behaviour very near to the ultimate load. It is of interest to compare the tip load deflection case with the experimental and the simple beam theory results. Hence, in Figure 4.10, the finite element solution for simulation A3 is plotted with these other curves. Note that the adjusted finite element solution, was obtained by converting from the double overhanging girder stiffness case to that which applied in the experiments (Figure 4.4). This shows excellent correlation with tests in the linear part of the loading path.

In all cases, the failure mode was predicted to be plate buckling and occurred in the box panel of the cantilever portion nearest the support, (i.e. box panel No. (4) in Figure 4.7(a)). Also, the mid-plane stress distributions of the middle section of the critical box panel in A1 to A3 were traced for different load levels as shown in Figure 4.11. The stress distributions illustrate the classical shear lag effect for all cases of the A-grouping. It is noted from test A3 the existence of pockets (lagging) in the stress distribution between stiffeners near collapse.

At points within the diaphragm, in-plane principal stresses at the load level P/P_{ult} = 0.1 were traced in Figure 4.12 for test A3. The compressive stresses are represented by arrows while tensile stresses are denoted by slashes. It can be seen that the elements adjacent to the web must resist very high compressive stresses while the lower elements at the flange-diaphragm junction are subjected to tensile stresses.

In fact, the portion of the diaphragm at the lower corner is the most highly stressed region within the domain of the box. This would suggest that there are very high stresses at the junction of all three components (diaphragm, web, and flange) which was thought to have contributed to the failure of the West Gate Bridge, in Melbourne, Australia in 1970.

It was decided to exclude the diaphragm in test A4 to assess its effect on the strength of the box under the same loading configuration and support condition as were A1 to A3. The predicted yield load and ultimate load obtained from test A4 were found to be 840 kN, and 1620 kN, respectively. These results confirm the negligible effects that the physical properties of the diaphragm have on the response of the present model. This is to be expected because the twin bearings were replaced by a full width line support, and the webs were stiffened by stocky transverse stiffeners over the supports.

For cross sections I, II, and III defined in Figure 4.7(a), the mid-plane axial stresses and the out-of-plane deflection profiles are

plotted in Figures 4.13, 4.14, and 4.15, respectively. It can be seen the buckling modes depicted in Figure 4.13(a), 4.14(a) and 4.15(a), are classical. The flange sub-panels between stiffeners buckled transversely into five half waves and longitudinally into three half waves, i.e. into almost square panels. In addition, it was observed that the amplitudes of these half waves diminish gradually as the distance from the support increases. The influence of elastic shear lag on the stress distribution of these three sections is evident from Figures 4.13(b) to 4.15(b). Clearly, there is a more pronounced effect in the proximity of the support than at more distant cross section locations.

The pattern of deformation at collapse and the progression of plasticity for the simulated test A4 is presented in Figure 4.16. The patterns obtained for tests A1 to A3 were similar. It is evident that plasticity penetrated the web-flange junction elements to a considerable degree, particularly near the support; to a lesser extent it is observed to have also spread to the corresponding tension flange elements. Such an observation was indeed obtained in the physical experiments undertaken on the model structure [65].

4.5.2 B-Group Simulations

The mesh used in this group of simulated tests is the same as was employed in test A4. The collapsed panel in this group of simulations was again subjected to both shear and bending moment. However, in this group the effects of initial imperfections and residual stresses

confined to the compression flange is investigated. Seven runs in this series, B1 to B7, were undertaken.

In tests B1 and B2, initial imperfections were considered in the form of sinusoidal plate modes having different amplitudes $\frac{\bar{b}}{200}$ and $\frac{\bar{b}}{150}$, respectively. For test B1, the ultimate load obtained was 1600 kN, whereas for B2 it was only slightly less, 1584 kN. For these two simulations, the out-of-plane deflections of the bottom (compression) flange at Sections I, II, and III were plotted for different load levels as shown in Figures 4.17 and 4.19, respectively. Figures 4.18, and 4.20, show the mid-plane axial stresses versus load levels at the mid-section of the collapsed box panel for both tests.

The existence of pockets (lagging) in the axial stress distribution between stiffeners is pronounced in these two cases, while there is no evidence of the effect of shear lag over the entire bottom flange width. Provided that buckling is precluded before the initiation of yielding, it is evident that the unequal stress distributions between the stiffeners will have the effect of causing plastification at the boundaries of the plate panel adjacent to the stiffener. This is especially true near the supports of the box girder as shown in Figure 4.21.

In tests B3 and B4, initial imperfections were considered in the form of an upwards sinusoidal stiffener mode in the box panel (4) with an oscillating pattern thereafter. Two different levels were prescribed

as $L^P/750$, and $L^P/500$, respectively. The collapse obtained was found to be 1580 kN for B3, and 1550 kN for B4.

The out-of-plane deflections of the compression flange of the collapsed panel are plotted at different load levels in Figures 4.22 and 4.24 respectively. Both simulations indicate that final collapse is associated with a plate buckling mode. Comparisons between plate imperfection mode cases B1 and B2, and the stiffener imperfection cases B3 and B4 indicate that the latter have a greater influence in deteriorating the ultimate strength of the box girder than do the former.

Figures 4.23 and 4.25, show the mid-plane axial stress distribution at section II for different load levels for tests B3, and B4, respectively. They indicate an absence of elastic shear lag effect since the stress distribution is about constant across the section; however, there is a girdle on one side of the line of symmetry in the first plate panel, which was shown in one of the experimental tests at Imperial College [58] for which there appears to be no simple explanation.

For test B4, the spread of plasticity at collapse is shown in Figure 4.26, the pattern of which is very similar to that for test B3. It may be inferred that the absence of the plate imperfection mode results in a more restricted spread of plasticity than B1 and B2 at collapse. It is evident that the centre of the collapsed box panel remains elastic for B3 and B4.

The plate and the stiffener imperfection modes with magnitudes of $\bar{b}/150$, and $L^p/500$, respectively, are superimposed in simulation test B5. In this instance the failure load was found to be 1520 kN. Transverse deflections of the bottom flange at Sections I, II, and III were plotted for different load levels in Figure 4.27. It is evident from these figures, that both modes (plate and stiffener) are propagated simultaneously with increasing the applied load. Moreover, it is observed in Figure 4.28 that a very pronounced girdle is predicted in the axial stress distribution at section-II in the second plate panel. Unfortunately, there is no simple explanation yet for this type of stress distribution. In addition, Figure 4.29 shows the spread of partial yielding over the width of the whole box panel.

In test B6, residual stresses due to the welding of longitudinal stiffeners in the compression flange was accounted for. Other imperfections were excluded in this case. The collapse load was found to be 1520 kN. Out-of-plane displacement of the compression flange at sections I, II, and III, are presented for different load configurations in Figure 4.30. A slight elastic shear lag effect is evident for the axial stress distribution at section-II, from Figure 4.31. The deformation and progression of plasticity is shown in Figure 4.32.

It was the objective of test B7 to determine the effect of superimposing the geometric imperfection modes of plate panels and longitudinal stiffeners presumed for B5, and residual stresses assumed in B6. The ultimate load obtained from this test was the lowest obtained of any of the runs, 1470 kN. Transverse deflections of the

bottom flange for different levels of load are shown in Figure 4.33. A similarity is noted between the response obtained for test B7 and that for test B5. In addition, mid-plane axial stresses at section-II, shown in Figure 4.34, reveal considerable similarity between tests B7 and B6. An exception, however, is the existence of a girdle in the second plate panel of B7, similar to the one depicted in test B5. Deformations and the spread of plasticity are shown in Figure 4.35.

4.5.3 C-Group Simulations

The compression flange box panel examined in the previous simulations under combined moment and shearing force was tested under pure moment in test C1. For reasons of economy only one simulation was conducted in this group. The critical panel in this case lies in the zone of the box girder between supports as shown in Figure 4.7(b); reinforcement in panels (2), (3), and (4) was postulated to force collapse of panel (1). The box panel was presumed to be free of imperfections and residual stresses.

The collapse load obtained from the simulated test C1 was 1610 kN, with failure caused by buckling of plate panels comprising the compression flange of the box panel section. The out-of-plane deflections at sections I, II, and III for various loads are given in Figure 4.36. The dashed lines were drawn to reference the stiffener locations and the webs. These results suggest almost no interaction existed between the stiffeners and the bottom flange plate panels up to collapse.

The mid-plane axial stress distribution at section-II clearly indicates, (Figure 4.37), an absence of a shear lag effect, as expected. The longitudinal stress distribution throughout the web depth for increasing loads is plotted in Figure 4.38; it is evidently linear in accordance with Navier's theory. The pattern of deformation and the extent to which plasticity has penetrated the box at collapse is shown in Figure 4.39.

As expected, the most stressed parts are the tension and compression flanges comprising the box girder part between supports, and the web-flange junction. The simulation did not show any significant difference in ultimate load of the box girder with or without shear lag, which confirms the findings of the Imperial College team [58], viz., that shear lag has a minimal effect on the strength reduction of stiffened steel box girders.

Referring to the physical model tested at McMaster University, a comparison between the collapse load obtained from the present finite element model and other theoretical approaches is shown in Table 4.3. There is evidently very good agreement between experimental collapse load and that predicted by the analytical model, which indicates the adequecy of the present model in predicting the strength of a stiffened steel box girder.

4.6 Discussion

The finite element model developed in this study has been found

to be an excellent vehicle for predicting the collapse behaviour of stiffened steel box girders. With the three-dimensional assemblage of all components comprising the box girder, a realistic simulation of such a structure can be made. Substantial savings in computer storage was achieved by modelling the diaphragm through the substructuring technique and employing a skyline solver. While it was only demonstrated on box girders having a rectangular configuration, the modelling is also capable of analysing a variety of 3-D thin-walled structures.

From the demonstrated results, it may be concluded that the finite element model gives excellent predictions for the strength and collapse mode of the box girder. On the other hand, the results obtained were based on the assumption that imperfections are considered only within the compression flange.

In addition, the geometrical imperfections are assumed to be with the same magnitude in all sub-panels comprising the compression flange. Moreover, the imperfection modes were presumed to be similar to that corresponding to the buckling modes. In actual fact, the imperfections within the physical model are random and exist in all components of the box.

It should also be noted that in the analytical model only residual stresses developed by welding of longitudinal stiffeners were included. In the physical model, such stresses were also generated from the action of welding transverse stiffeners, diaphragms and webs to the flange plates.

It may be noted that a comparison between the analytical and physical model might reasonably be based on simulation B7 which includes both geometrical and structural imperfections.

Table 4.1: Components of the Physical Model and Relevent Characteristics

Main Component	Subcomponent	Size	Relevant Characteristic ratios
Web	Web plate	1200 × 5	$h_w^L/t_w = 144^{**}$ $h_w^S/t_w = 48^{*}$
	Longitudinal stiffener	∠ 45 × 45 × 5	$\ell/r = (80)$
	Transverse stiffener	MT 75 × 4.22 [T-sec.]	$\ell/r = (26)$
Flanges	Compression flange plate	1800 × 8	$\bar{b}/t = 45$
	Tension flange plate	330 × 25	-
	Longitudinal stiffener	MT 75 × 4.22 [T-sec.]	$\ell/r = (40)$
	Transverse stiffener (x-girder)	1/2 MT 200 × 9.7 [T-sec.]	$\ell/r = (33)$
Diaphragm	Full width plate diaphragm	1800 × 1200 × 8	
	Additional vert. flat stiffeners were added to the diaphragm		

** Largest height to thickness ratio.

* Smallest height to thickness ratio.

( ) Slenderness ratio.

Table 4.2: Features of Different Test Categories

Group	Test No.	Mesh used	Diaphragm is included	Collapse due to shear & Mom.	Collapse due to pure Mom.	Perfect box	Geometric Initial Imper.	Residual Stress	Collapsed box panel
A	A1	1	✓	✓	–	✓	–	–	4
	A2	2	✓	✓	–	✓	–	–	4
	A3	3	✓	✓	–	✓	–	–	4
	A4	3	–	✓	–	✓	–	–	4
B	B1	3	–	✓	–	–	$\bar{b}/200$	–	4
	B2	3	–	✓	–	–	$\bar{b}/150$	–	4
	B3	3	–	✓	–	–	$L^p/750$	–	4
	B4	3	–	✓	–	–	$L^p/500$	–	4
	B5	3	–	✓	–	–	$\bar{b}/150$ & $L^p/500$	–	4
	B6	3	–	✓	–	–	–	✓	4
	B7	3	–	✓	–	–	$\bar{b}/150$ & $L^p/500$	✓	4
C	C1	4	–	–	✓	✓	–	–	1

Table 4.3: Comparison between Present F.E. Model Predictions and other Results

Method	Approach	$(P_{ult})^{th}$ kN	$\frac{P_{(ult)}{}^{th}}{*(P_{ult})^{exp}}$
Present F.E. Model	Discrete approach	1470	0.98
Leige [Jetteur-Massonet]	Orthotropic Plate approach	1302	0.868
Cambridge [Little]	Strut approach	1296	0.864
Manchester [Horne]	Strut approach	1305	0.87
Merrison rule	Strut approach	1413	0.94

*The collapse load for the experimental test at McMaster University is 1500 kN.

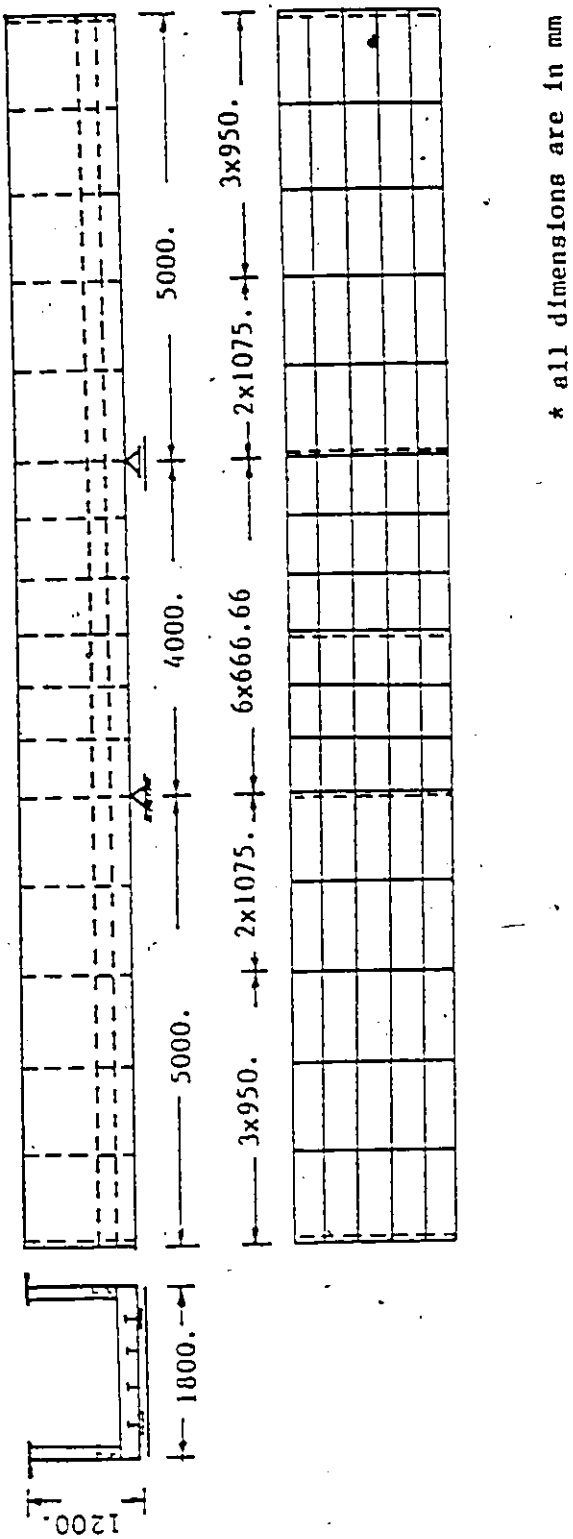

* all dimensions are in mm

Figure 4.1 : General Layout of Box Girder Model

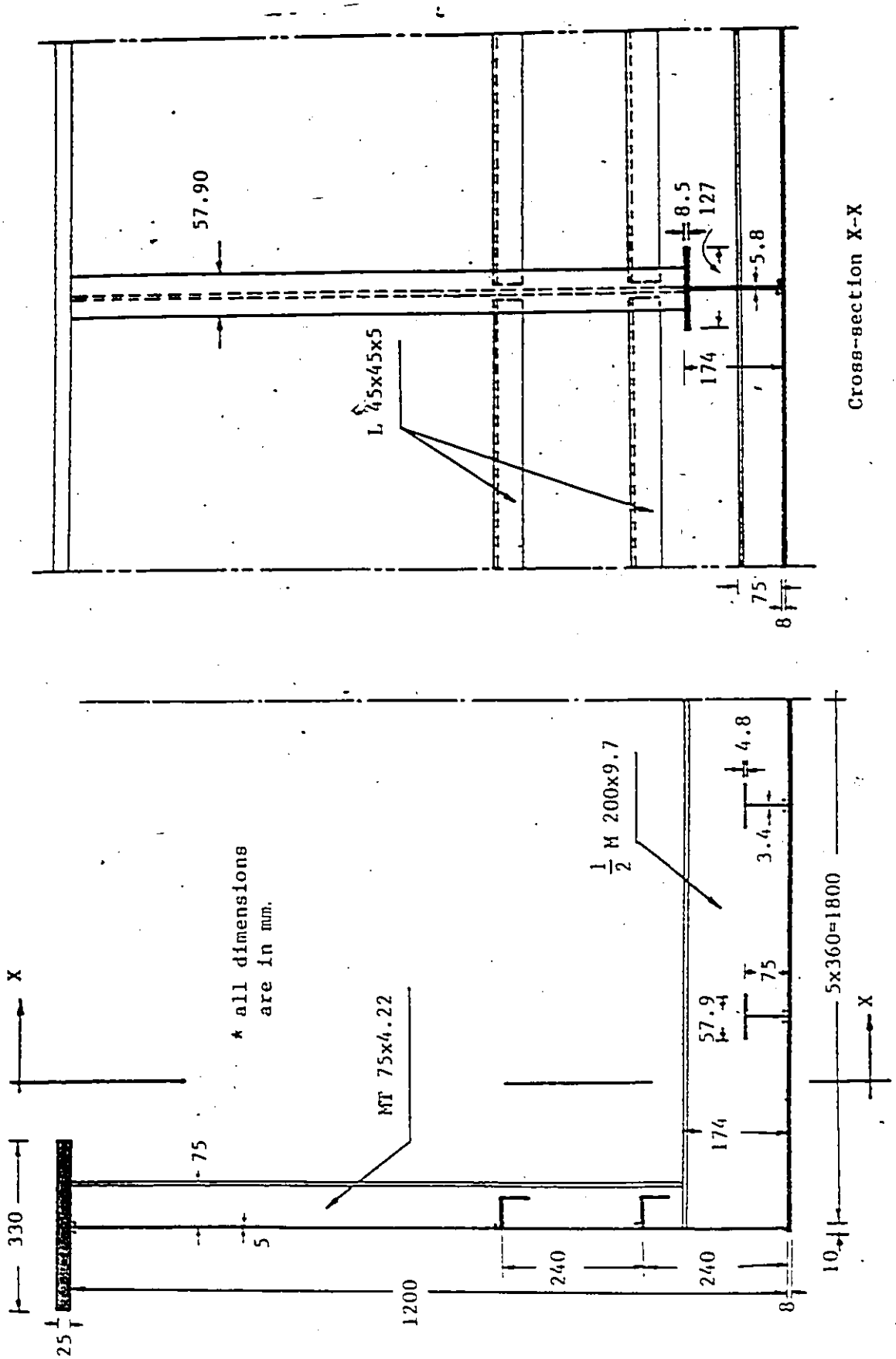

Figure 4.2 : Details and Dimensions of Box Girder Components

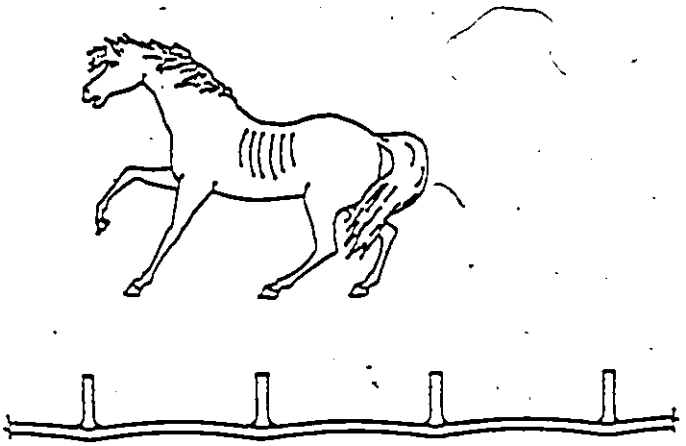

a) Cross Section of Plating Showing 'Hungry Horse' Shape

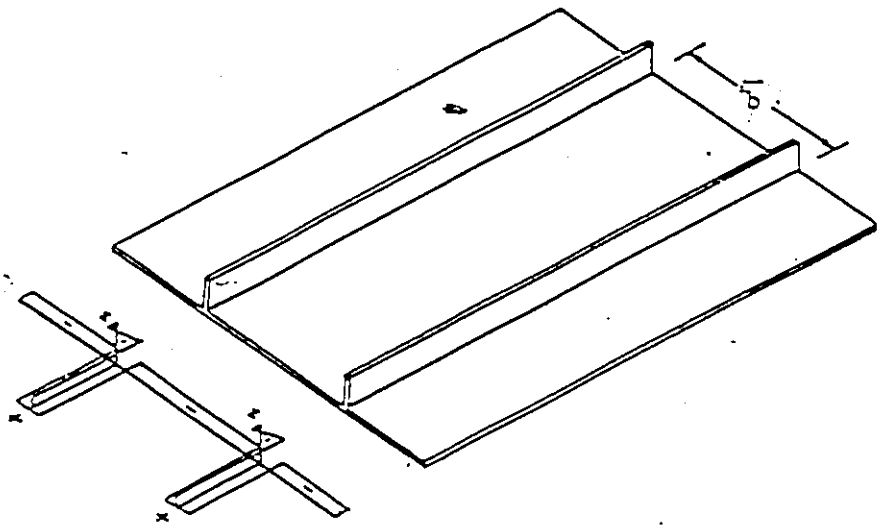

b) Idealized Equilibrated Residual Stress Distribution

Figure 4.3 : Typical Initial Imperfections in Stiffened Panel

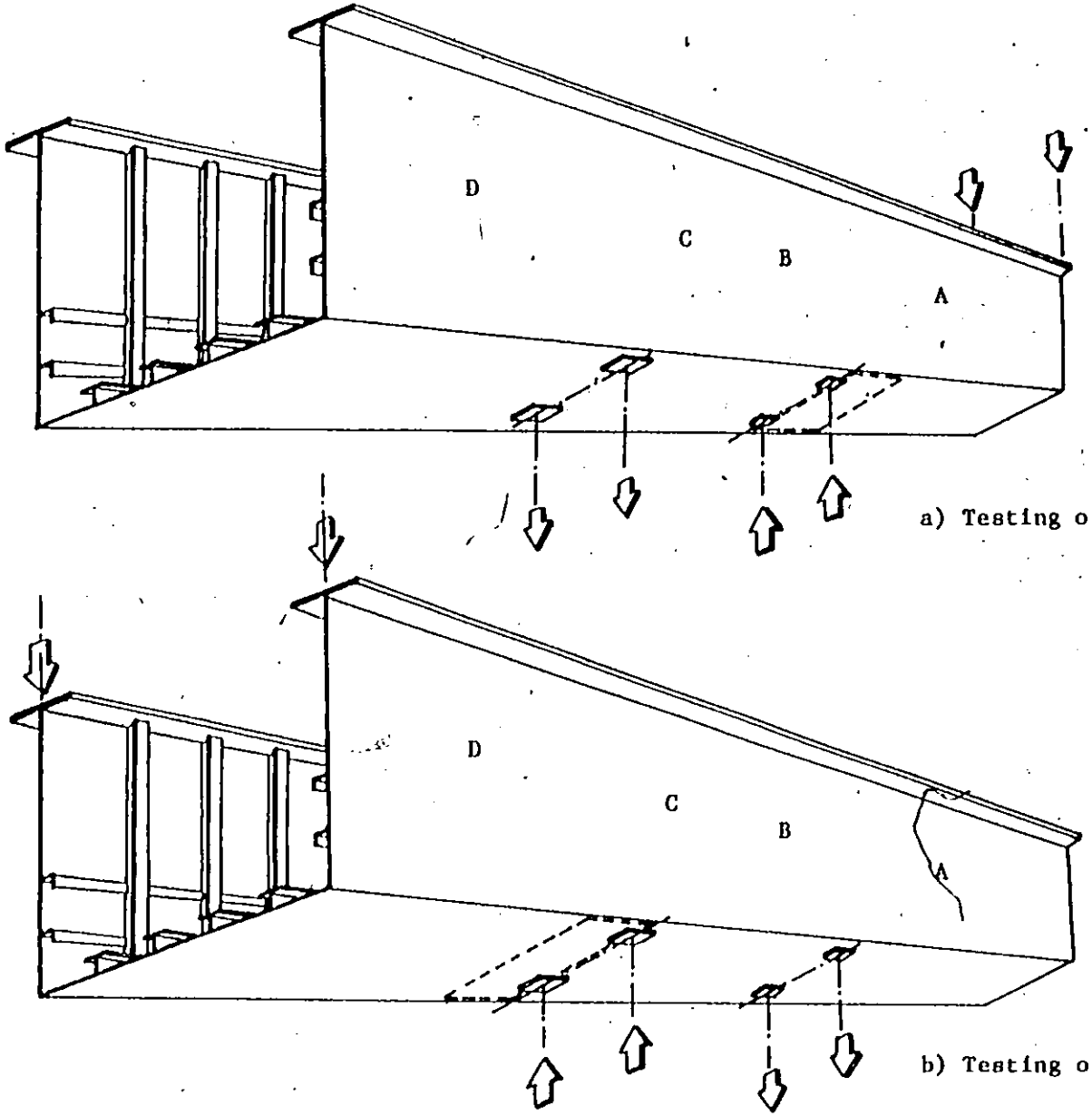

Figure 4.4 : Loading System for Experiments

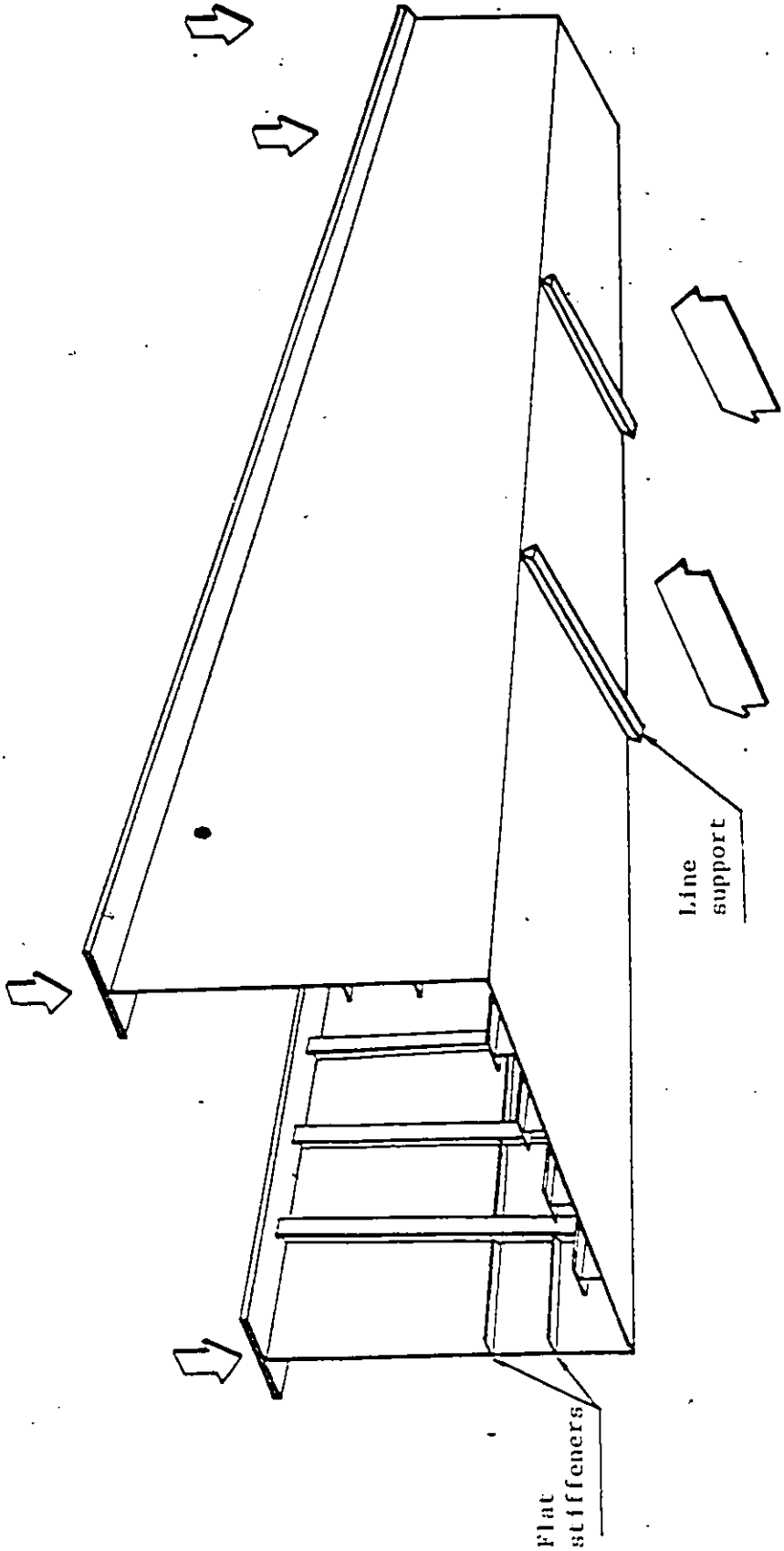

Figure 4.5 : Loads Applied to Analytical Model

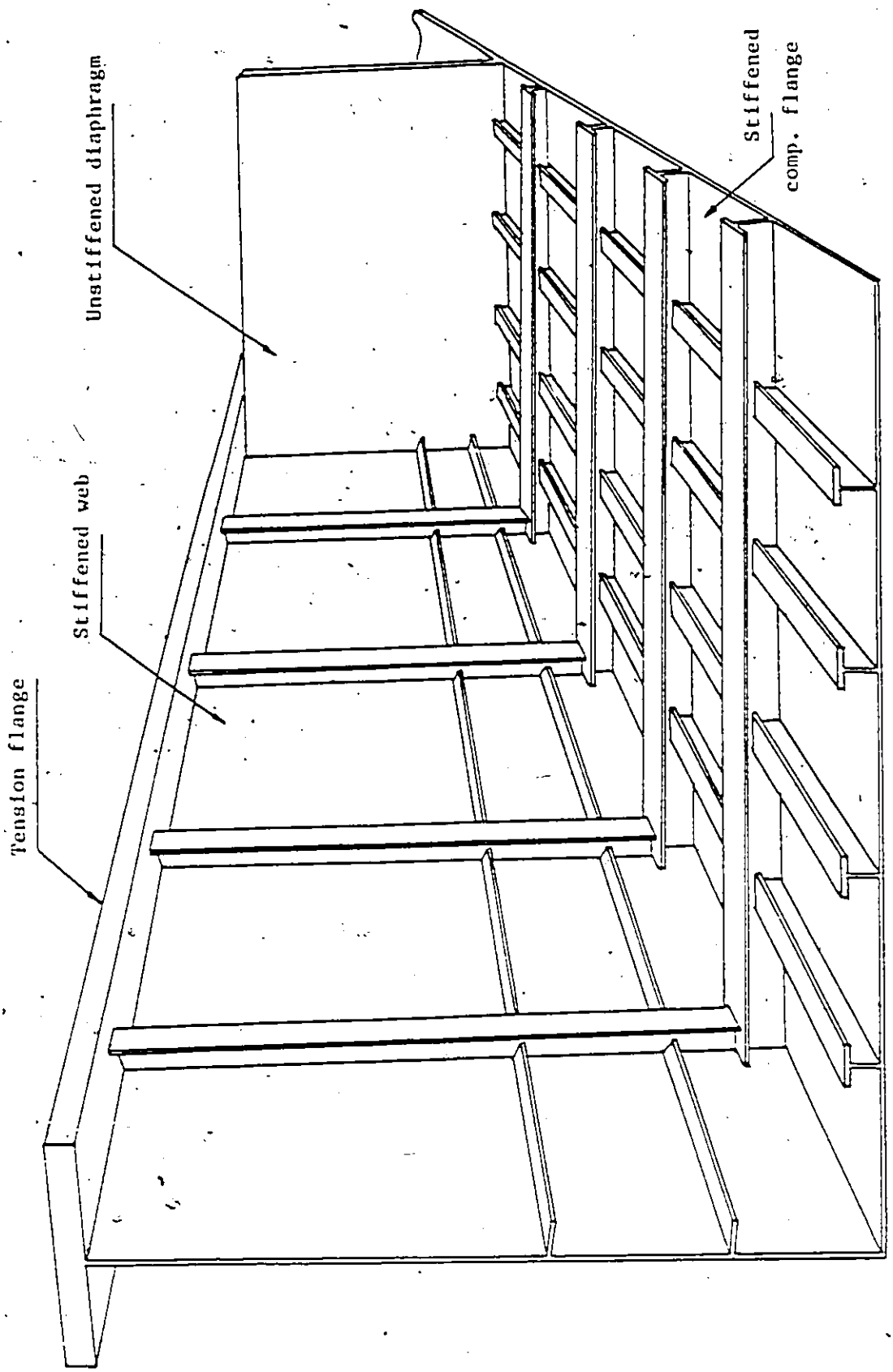

Figure 4.6 : Sketch of Stiffener Arrangement of Analytical Model

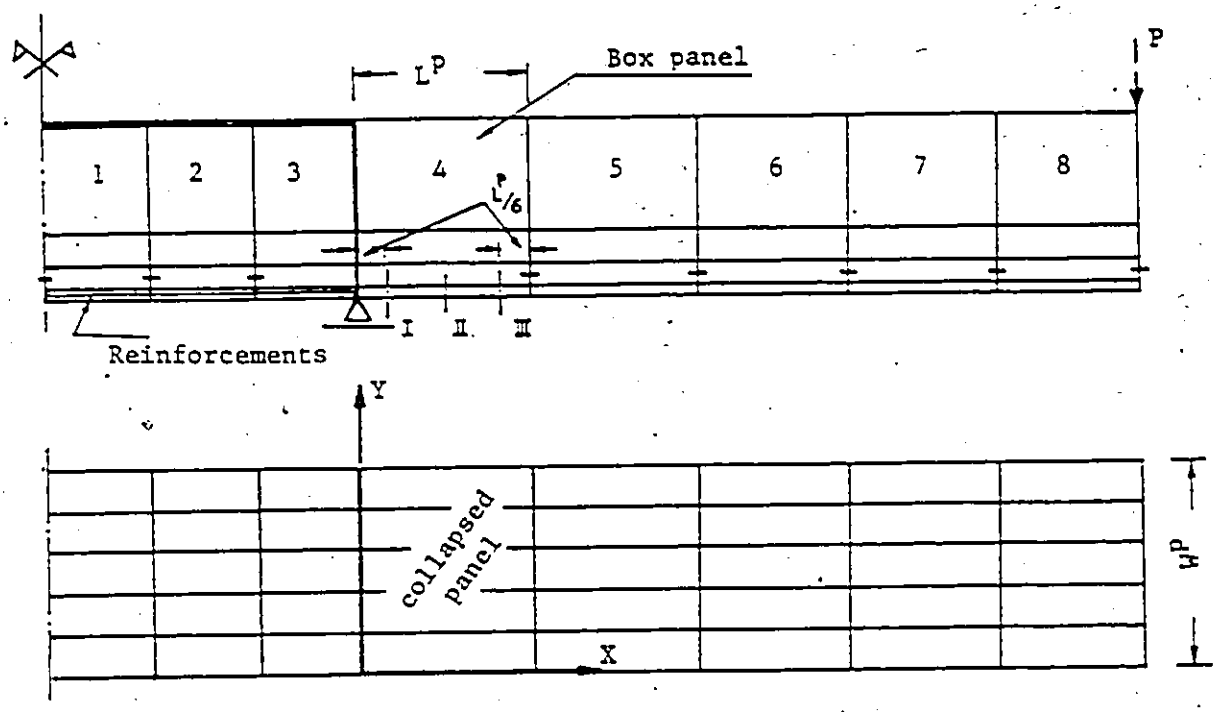

a) Reinforcements required to cause collapse of box panel 4

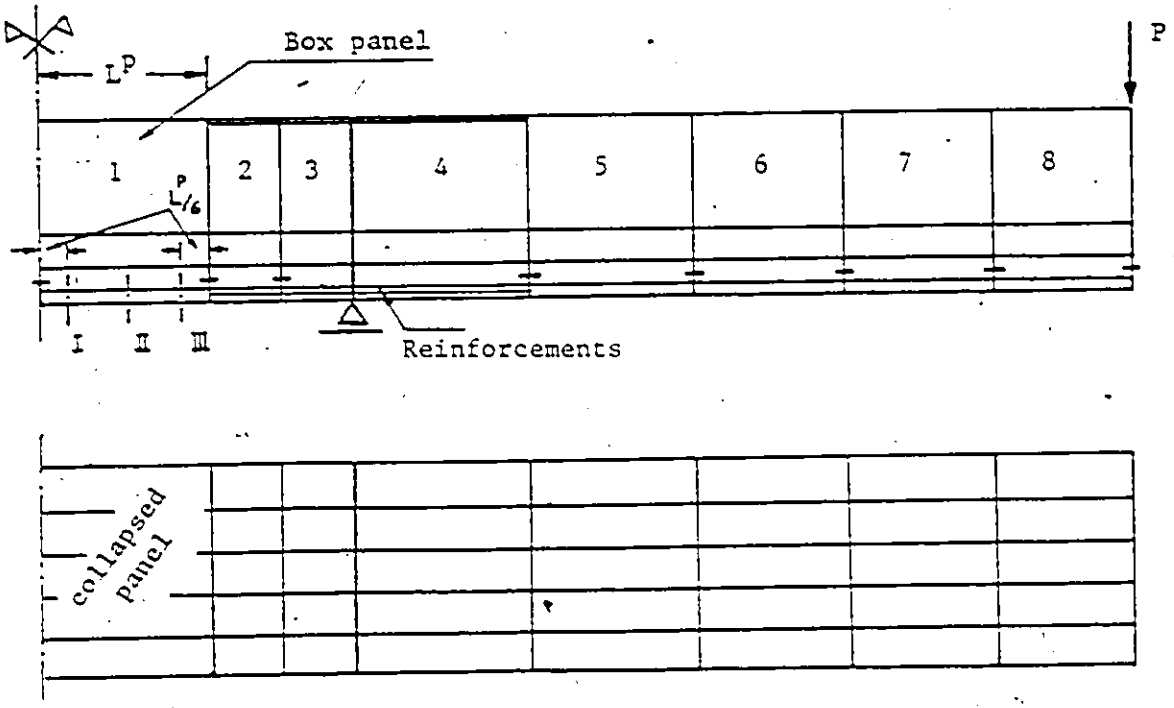

b) Reinforcements required to cause collapse of box panel 1

Figure 4.7 : Critical Box Panels and Hypothetical Stiffening

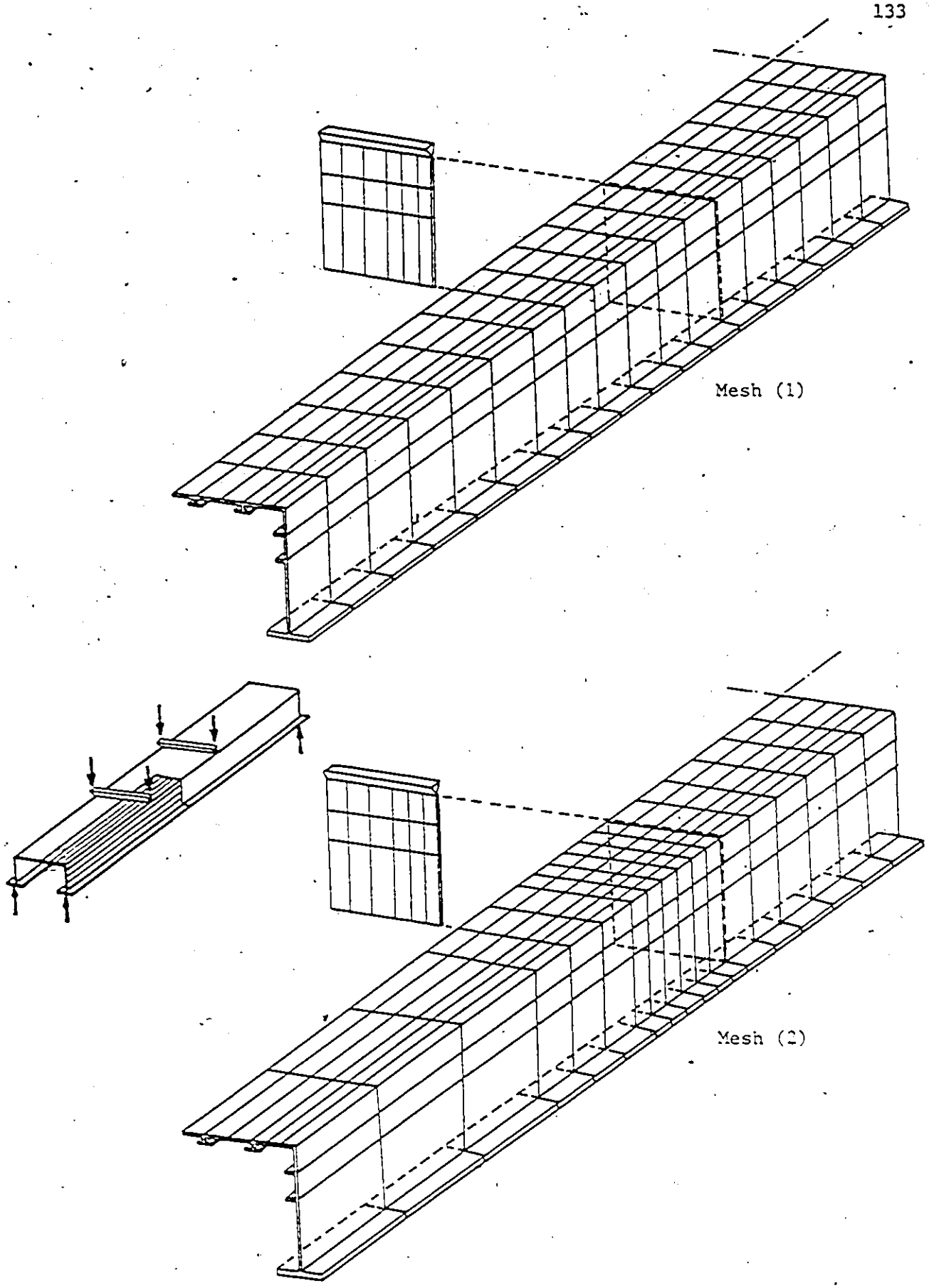

Figure 4.8 : Finite Element Mesh Patterns (1) and (2)

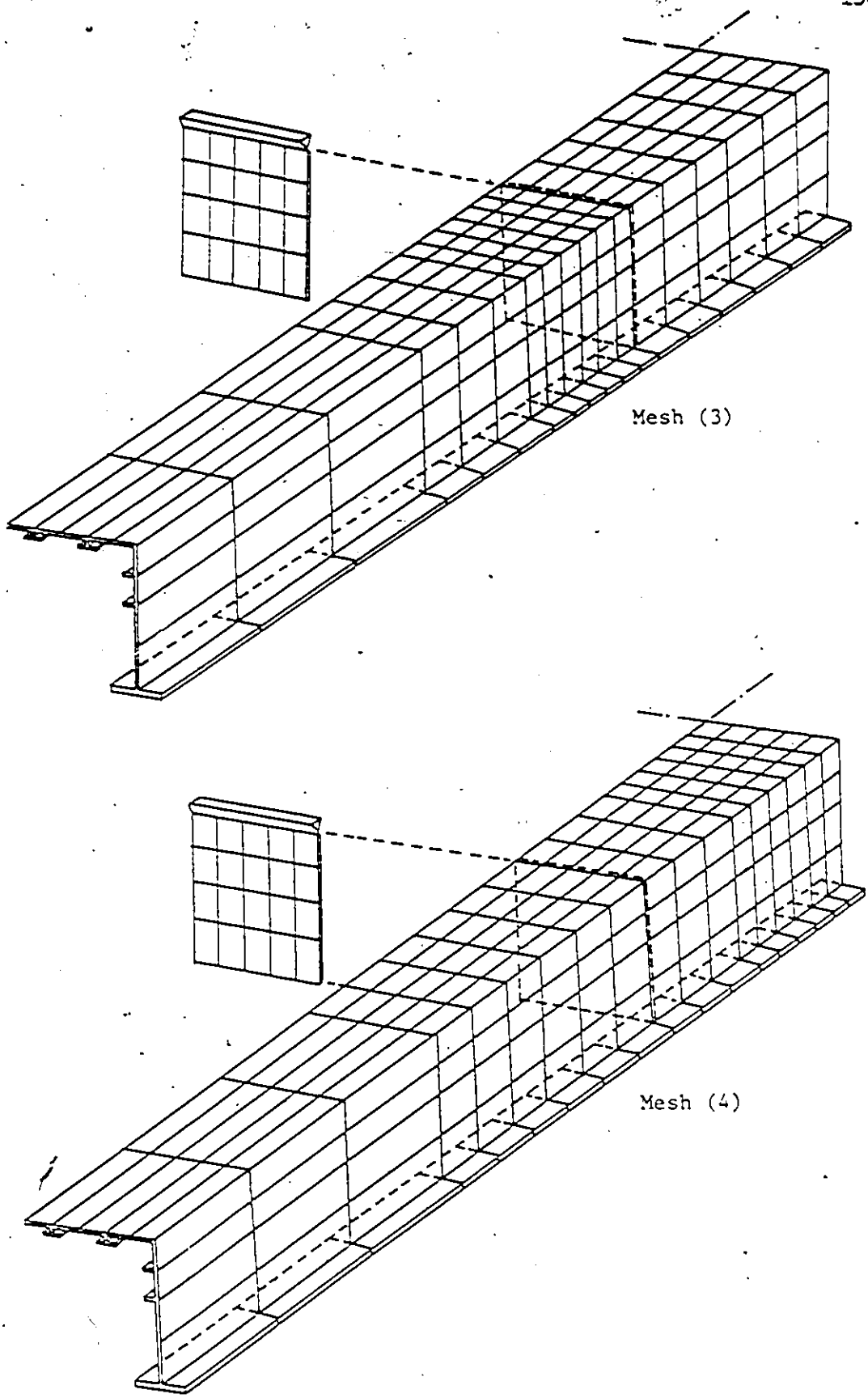

Figure 4.9 : Finite Element Mesh Patterns (3) and (4)

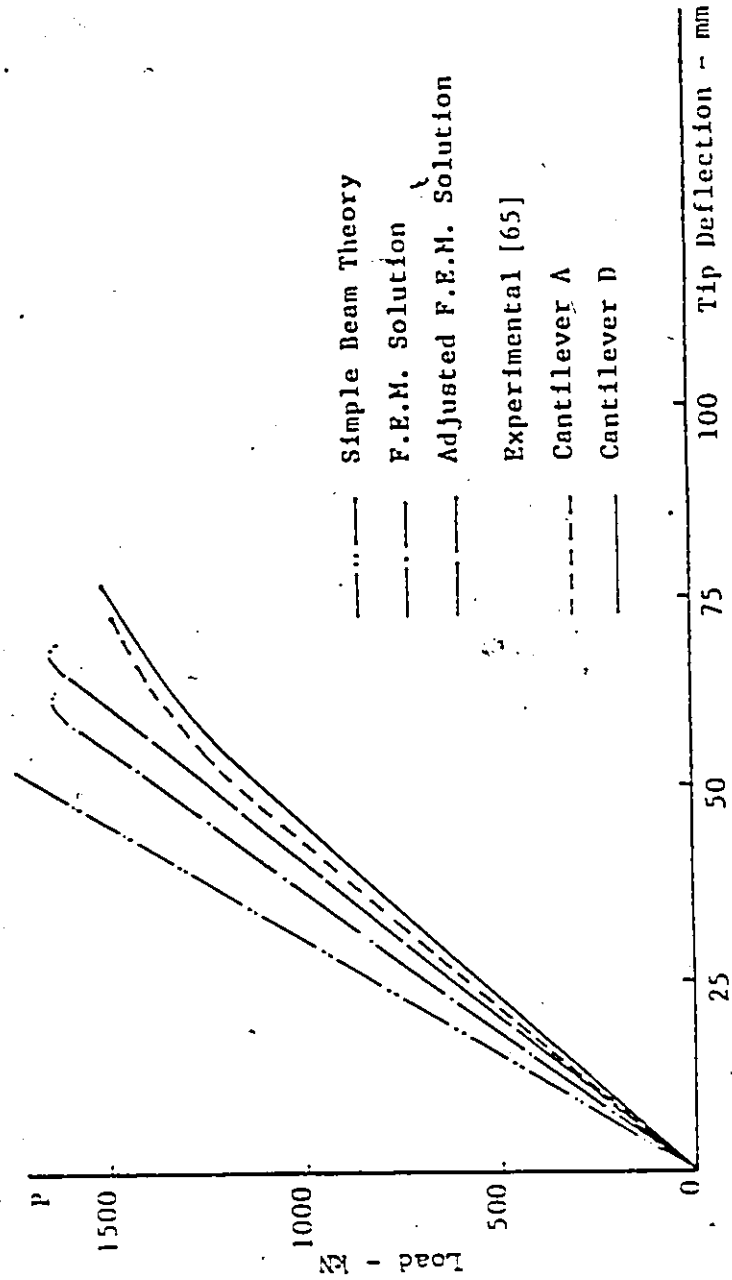

Figure 4.10 : Load-Tip Deflection Curves

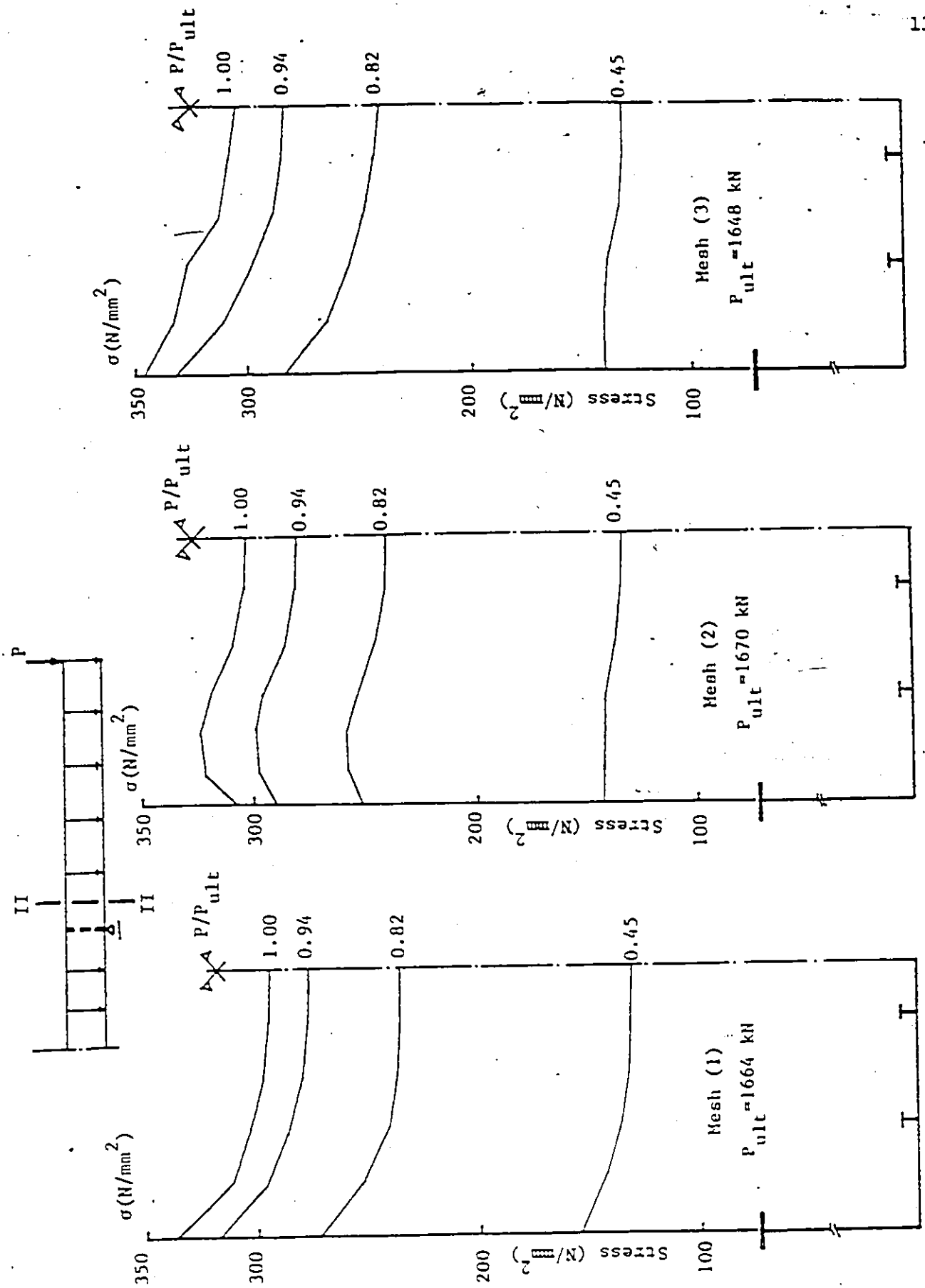

Figure 4.11 : Mid-Plane Axial Stresses at Section-II for Tests A1 to A3

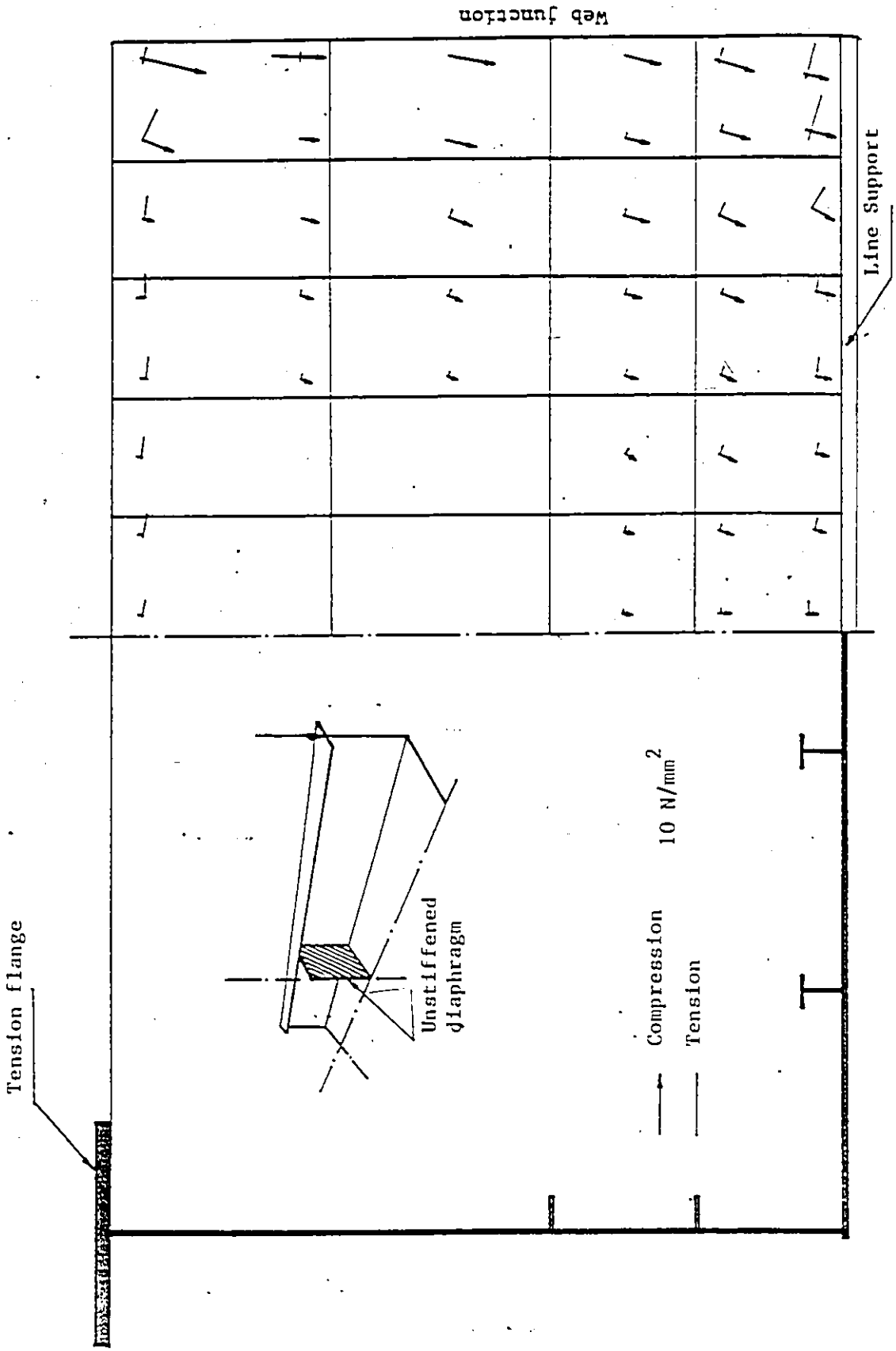

Figure 4.12 : Principal Stresses in Unstiffened Diaphragm for Simulation A3

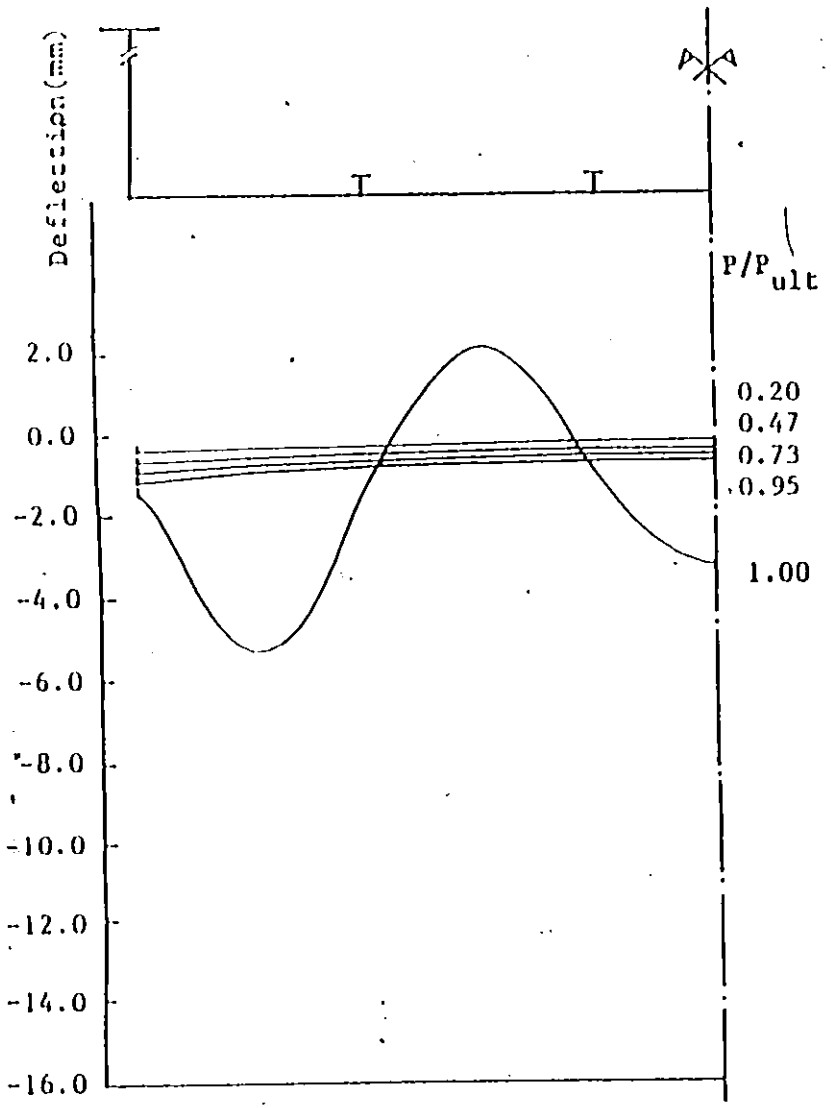

a) Bottom Flange Deflections

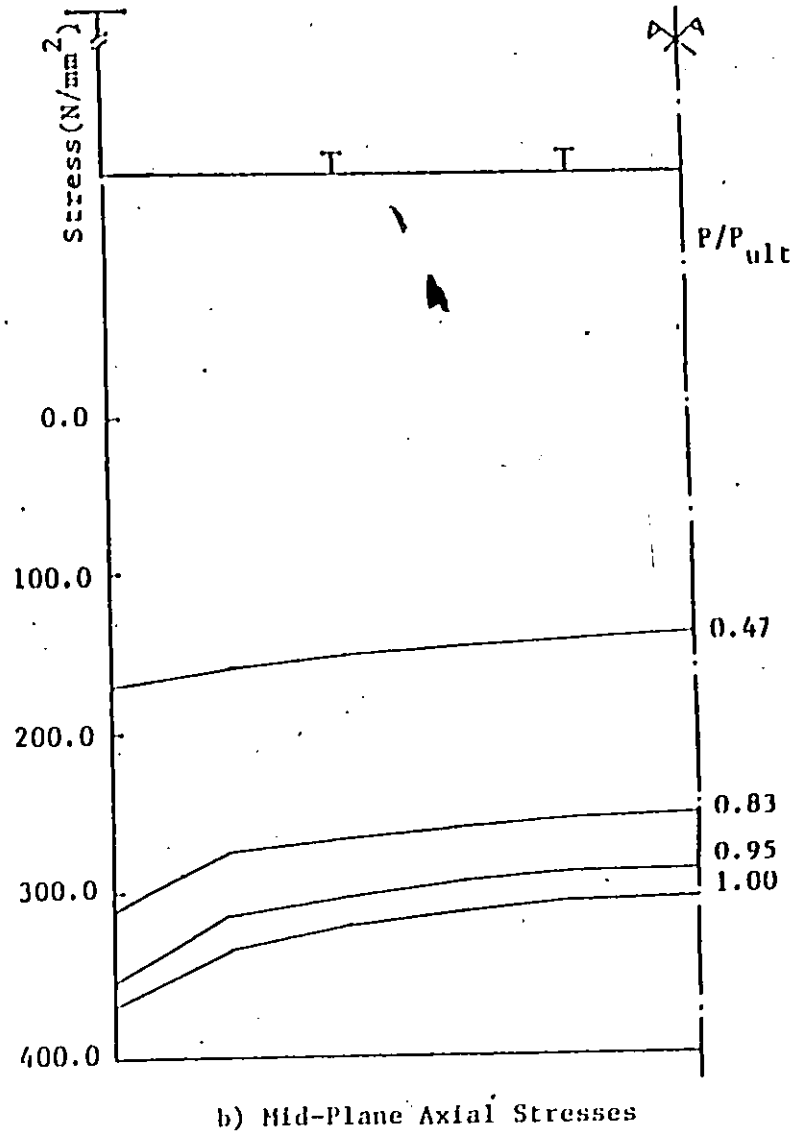

b) Mid-Plane Axial Stresses

Figure 4.13 : Analytical Predictions for Simulation A4 at Section I

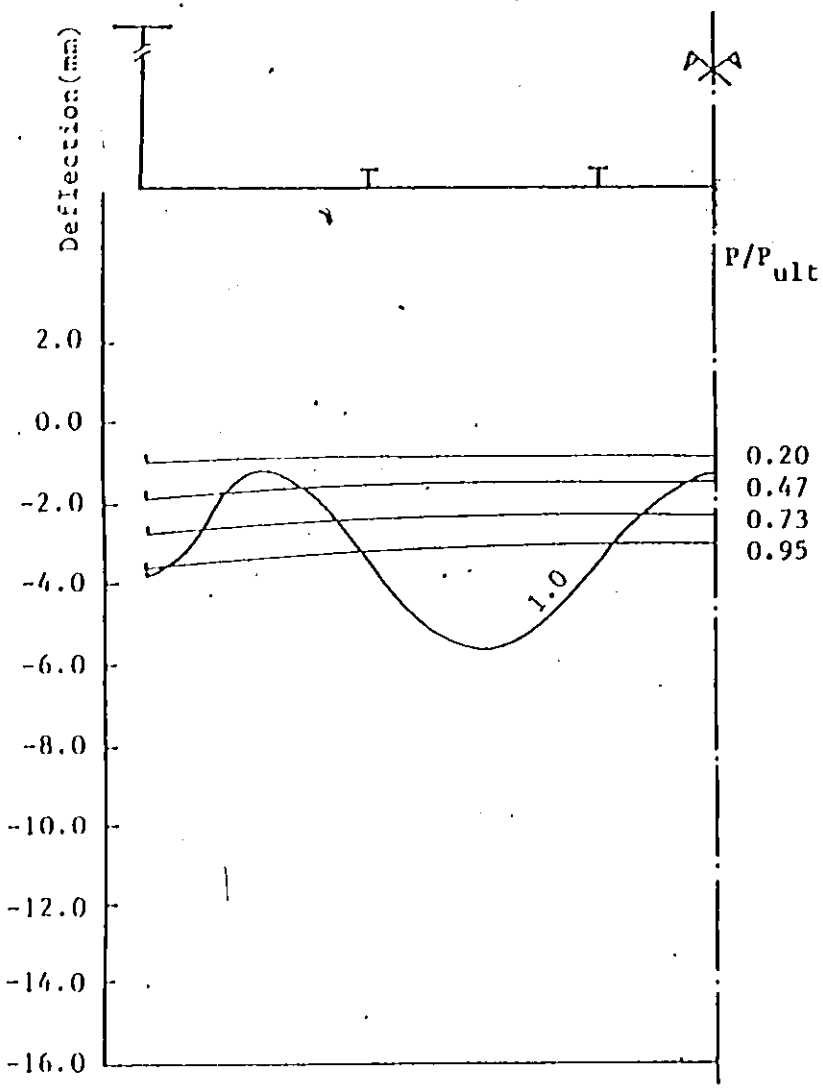

a) Bottom Flange Deflections

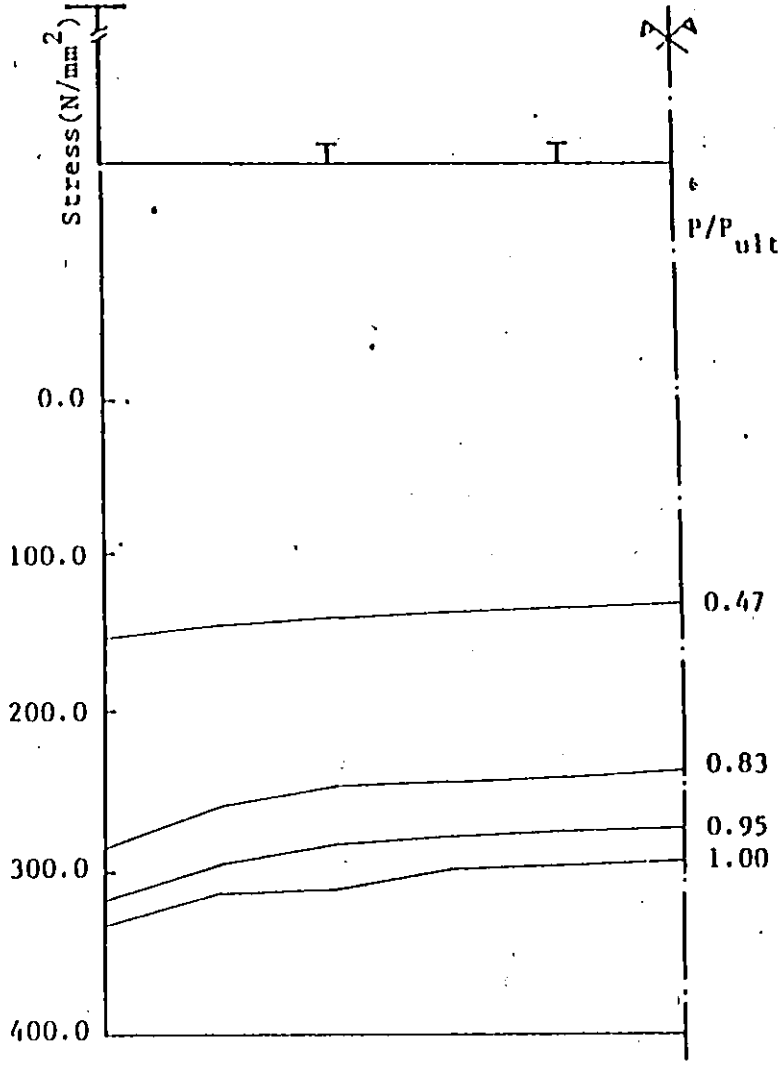

b) Mid-Plane Axial Stresses

Figure 4.14 : Analytical Predictions for Simulation A4 at Section II

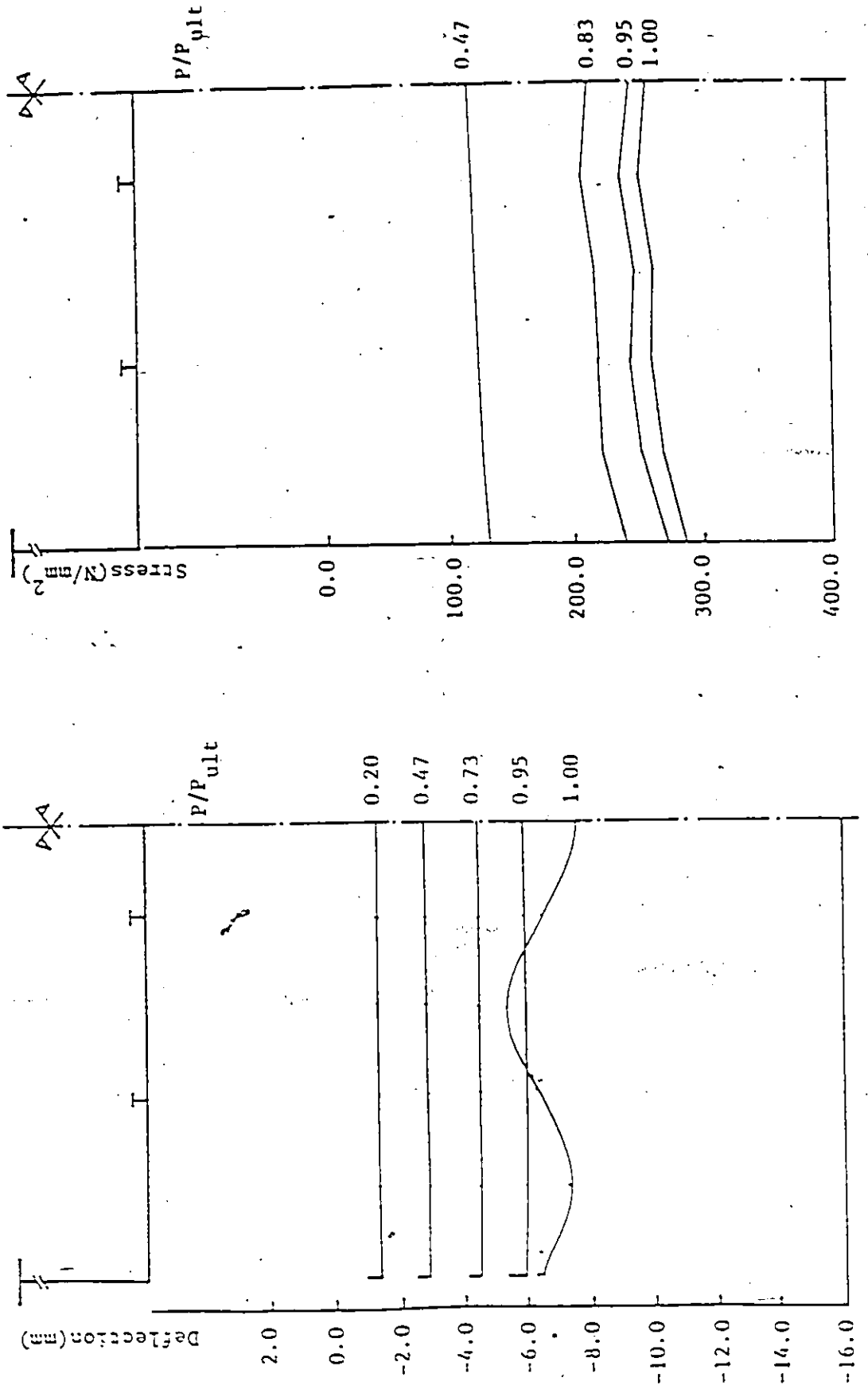

a) Bottom Flange Deflections

b) Mid-Plane Axial Stresses

Figure 4.15 : Analytical Predictions for Simulation A4 at Section III

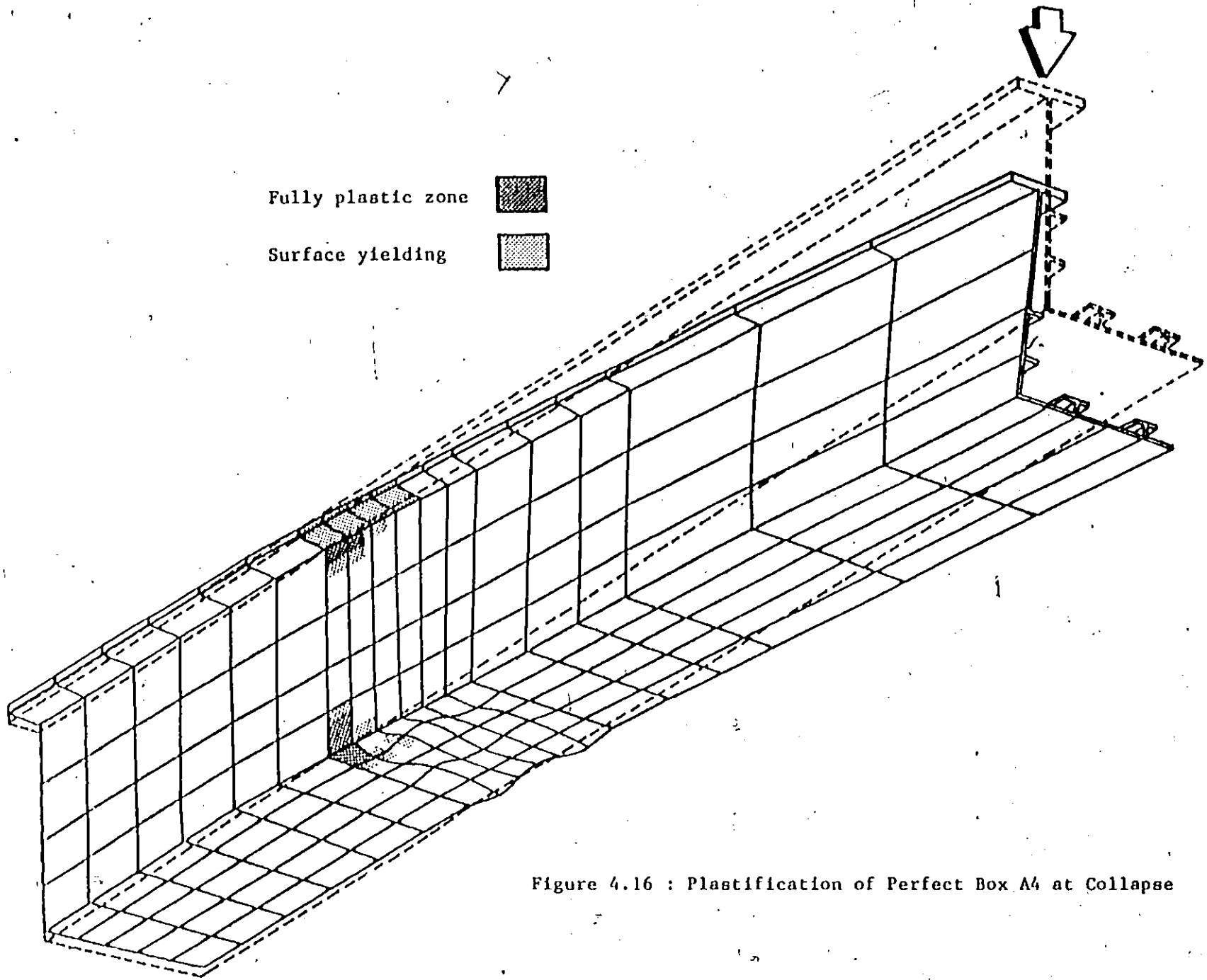

Figure 4.16 : Plastification of Perfect Box A4 at Collapse

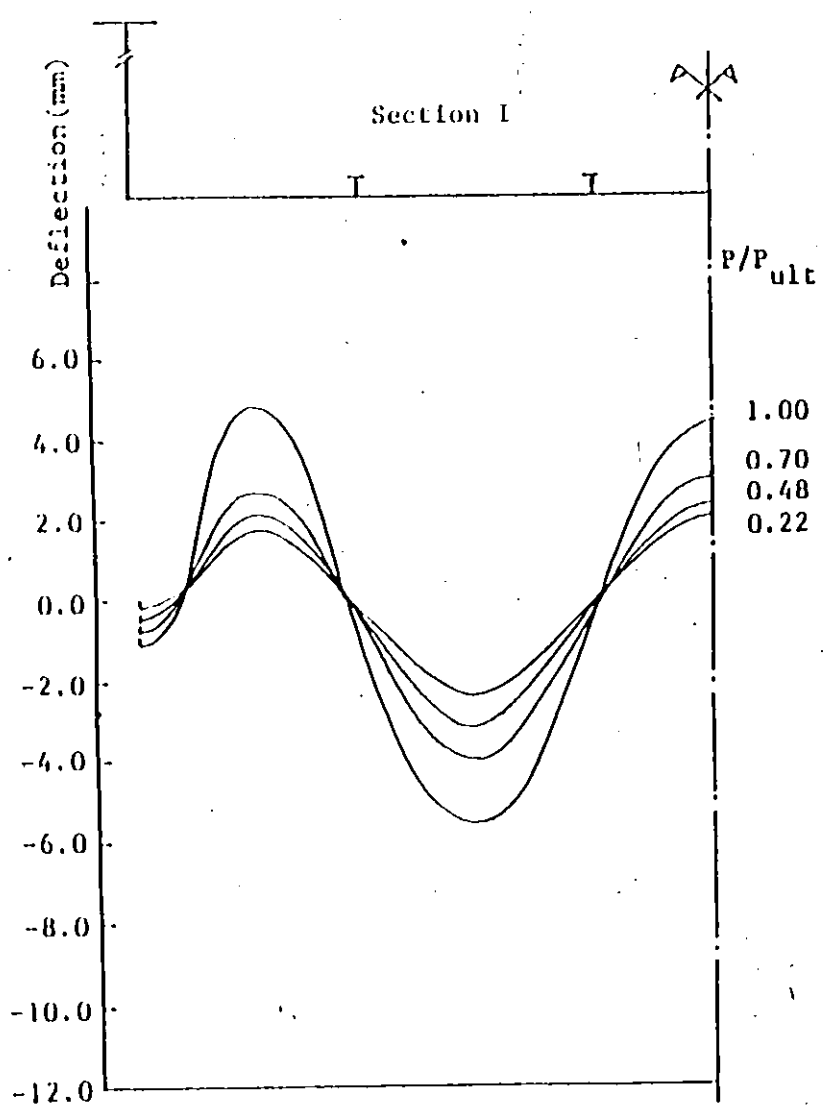
Section I
Deflection (mm)
P/P ult
6.0
4.0
2.0
0.0
-2.0
-4.0
-6.0
-8.0
-10.0
-12.0
1.00
0.70
0.48
0.22

a)

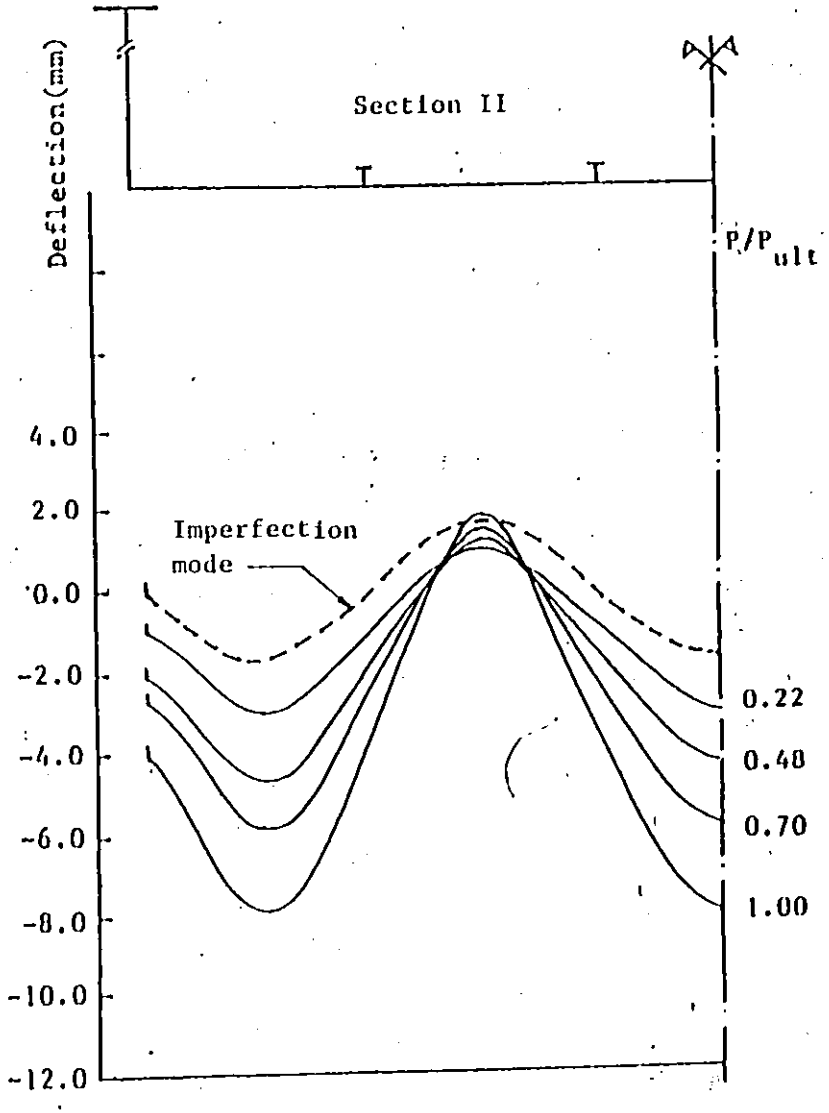
Section II
Deflection (mm)
P/P ult
4.0
2.0
0.0
-2.0
-4.0
-6.0
-8.0
-10.0
-12.0
Imperfection mode
0.22
0.48
0.70
1.00

b)

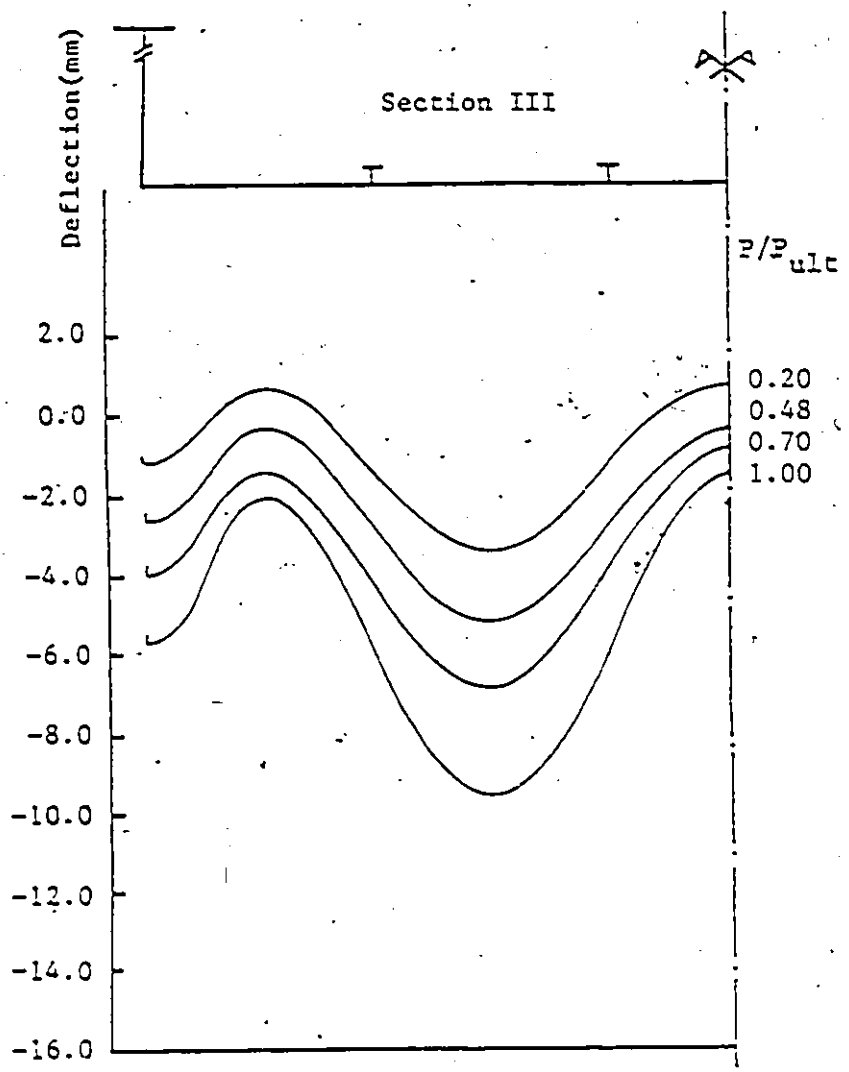

c)

Figure 4.17 : Bottom Flange Deflections at Different Sections for Simulation B1

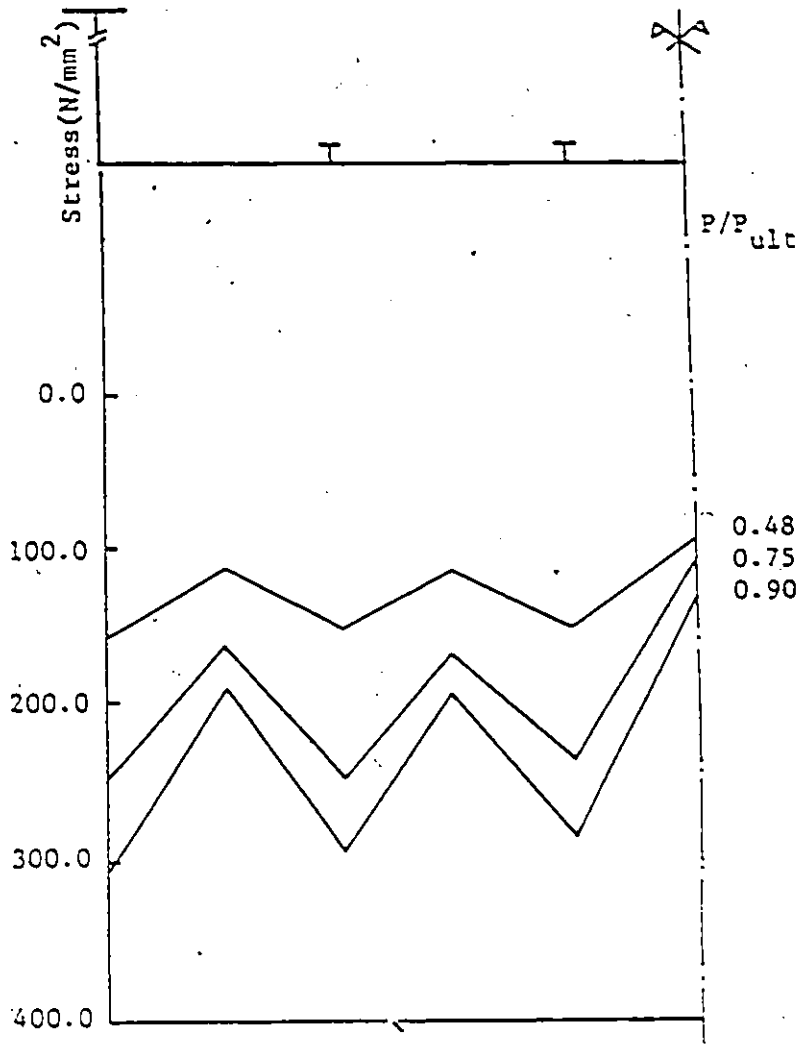

Figure 4.18 : Mid-Plane Axial Stresses at Section II for B1

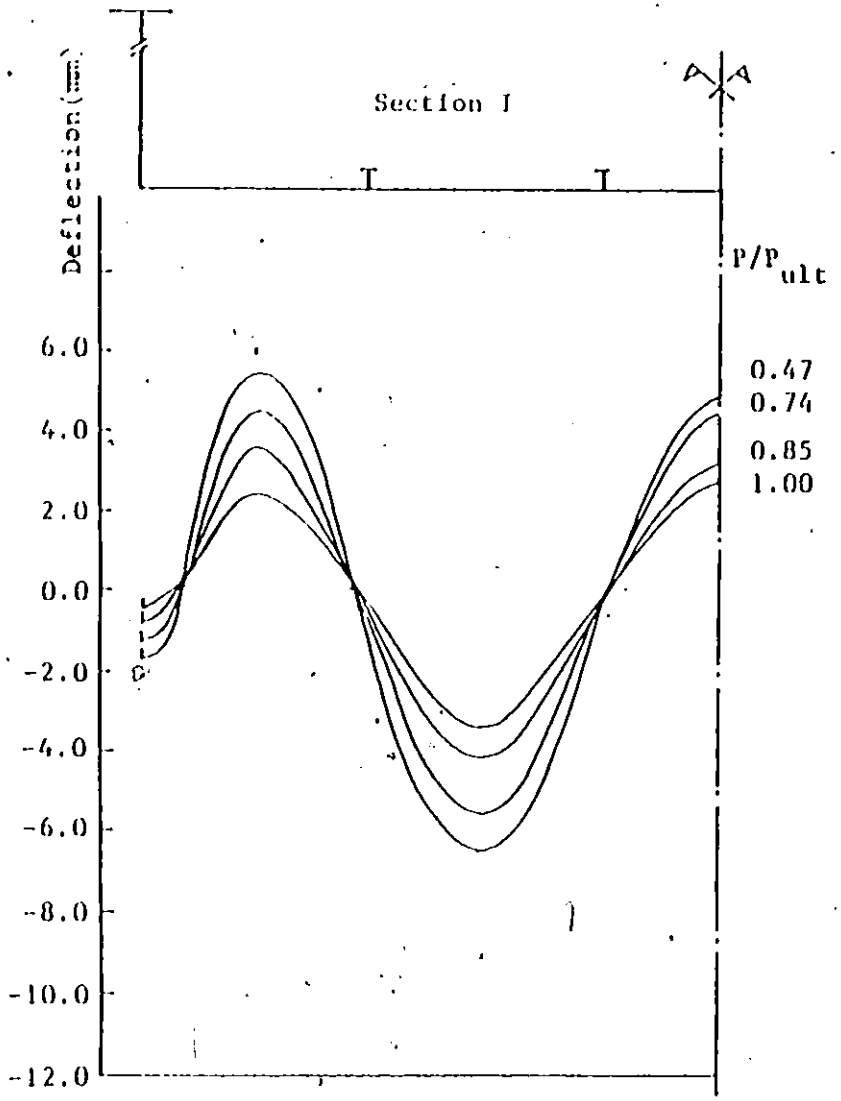
Section I
Deflection (mm)
P/P ult
6.0
4.0
2.0
0.0
-2.0
-4.0
-6.0
-8.0
-10.0
-12.0
0.47
0.74
0.85
1.00

a)

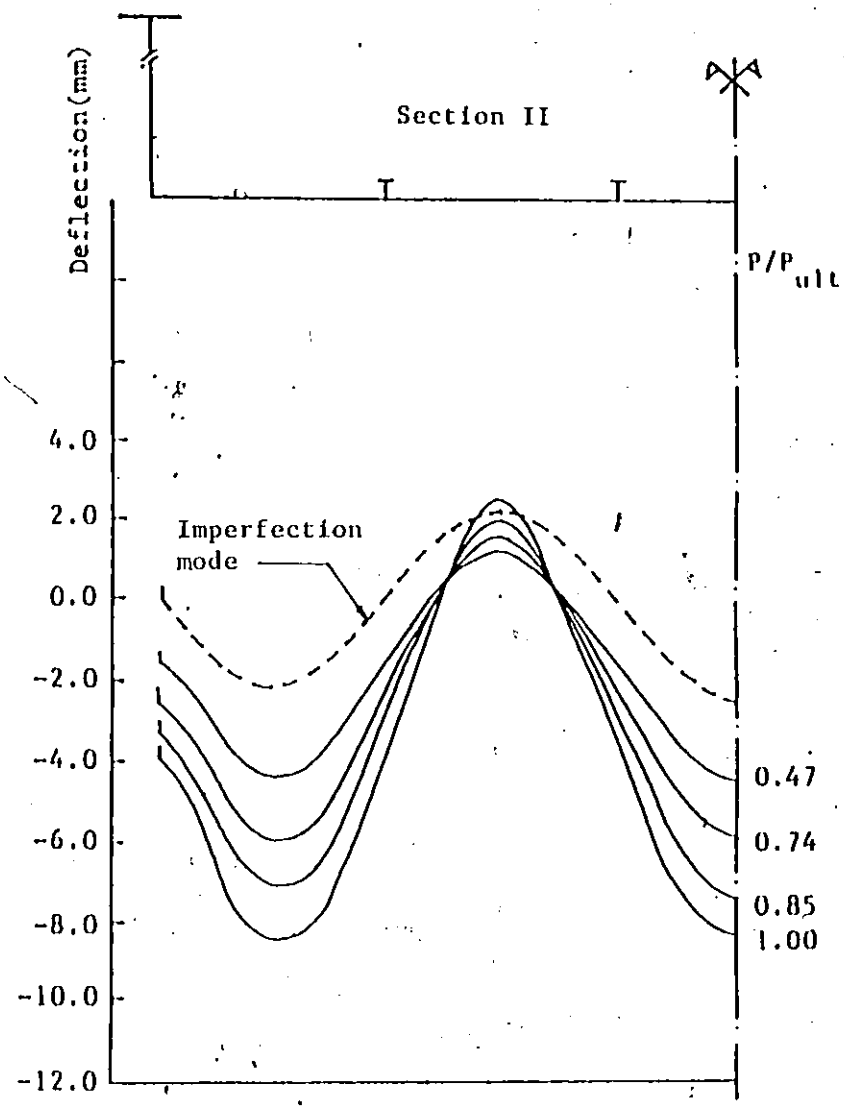
Section II
Deflection (mm)
P/P ult
4.0
2.0
0.0
-2.0
-4.0
-6.0
-8.0
-10.0
-12.0
Imperfection mode
0.47
0.74
0.85
1.00

b)

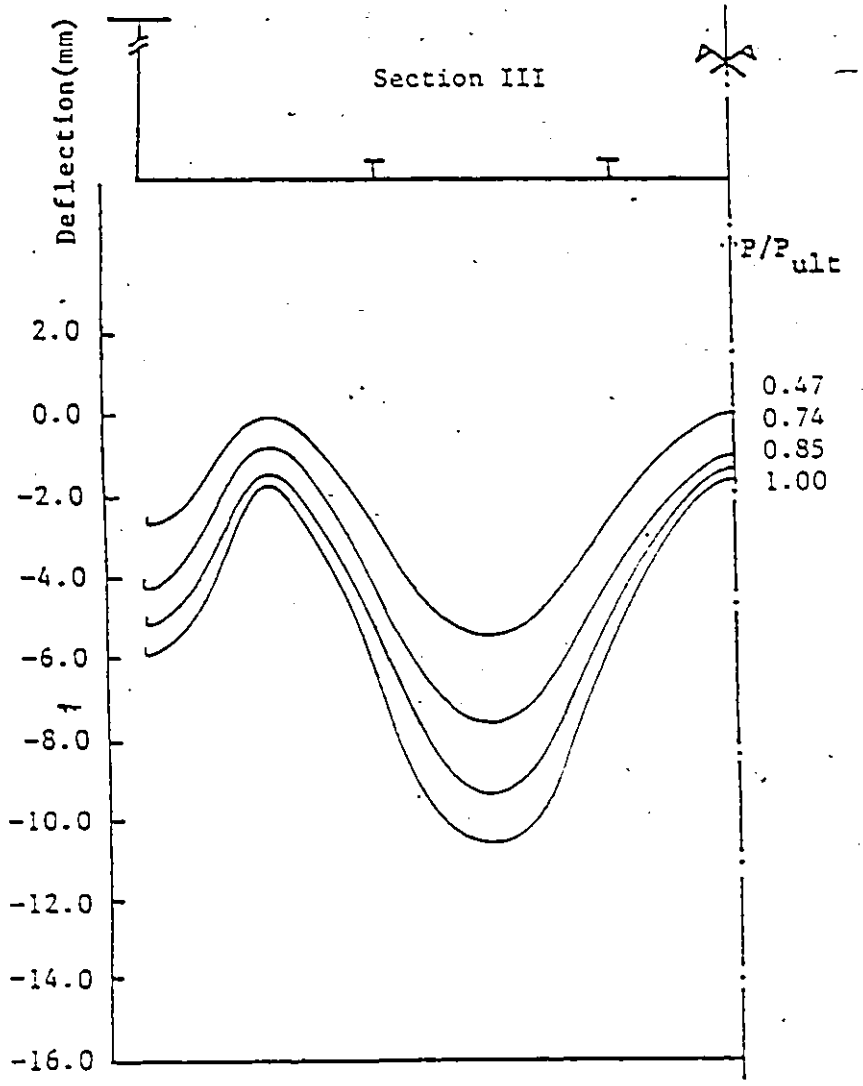

c)

Figure 4.19 : Bottom Flange Deflections at Different Sections for Simulation B2

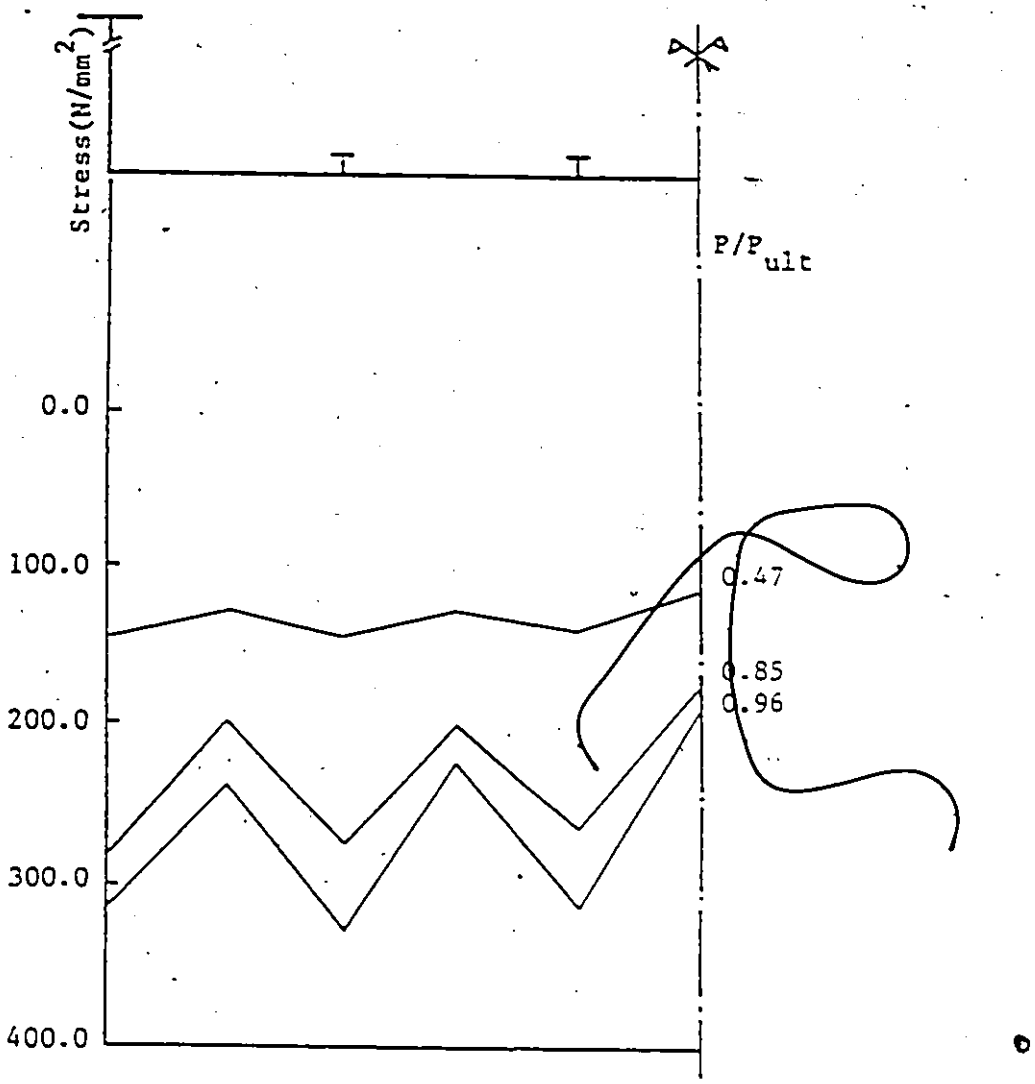

Figure 4.20 : Mid-Plane Axial Stresses at Section II for B2

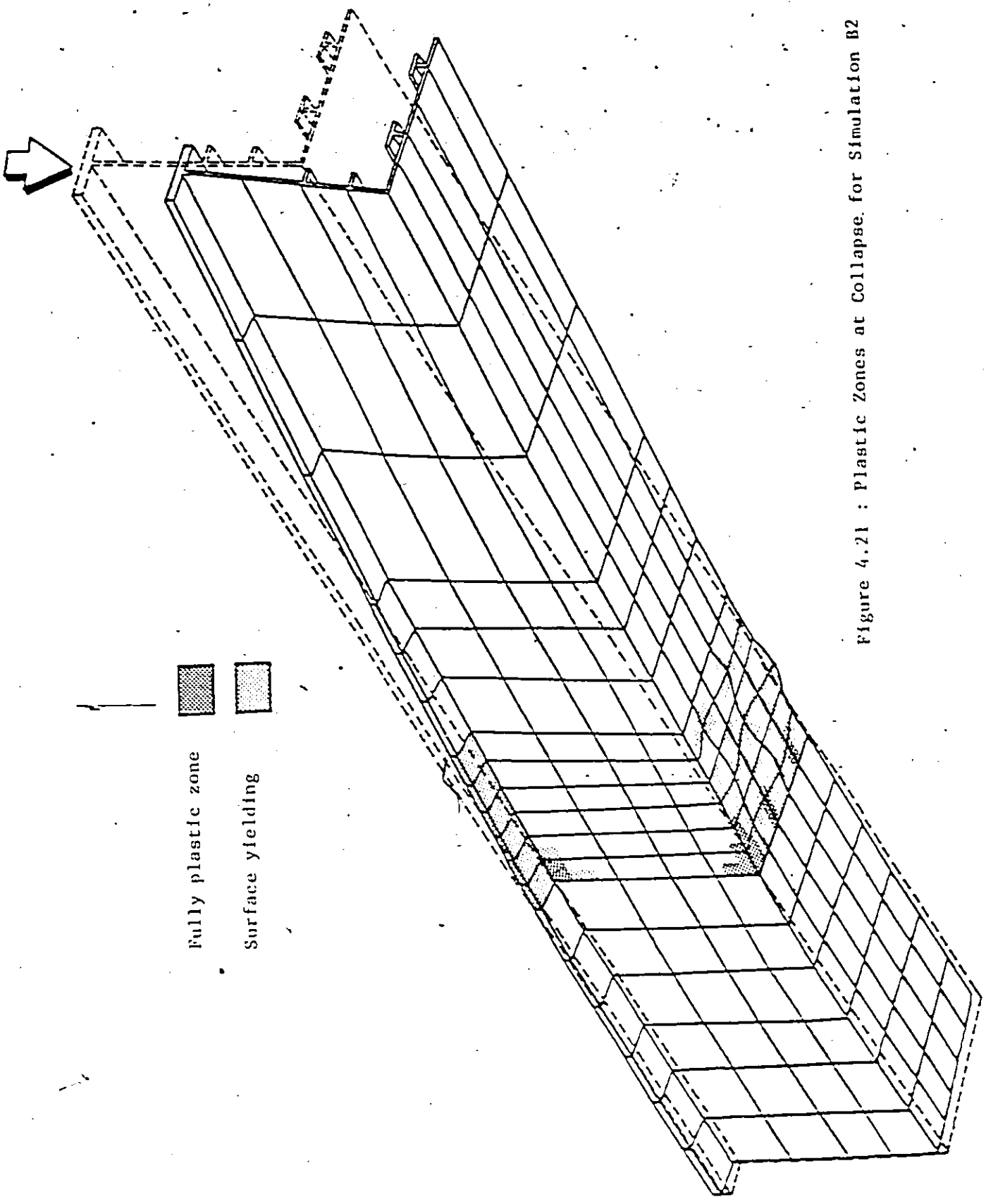

Figure 4.21 : Plastic Zones at Collapse for Simulation B2

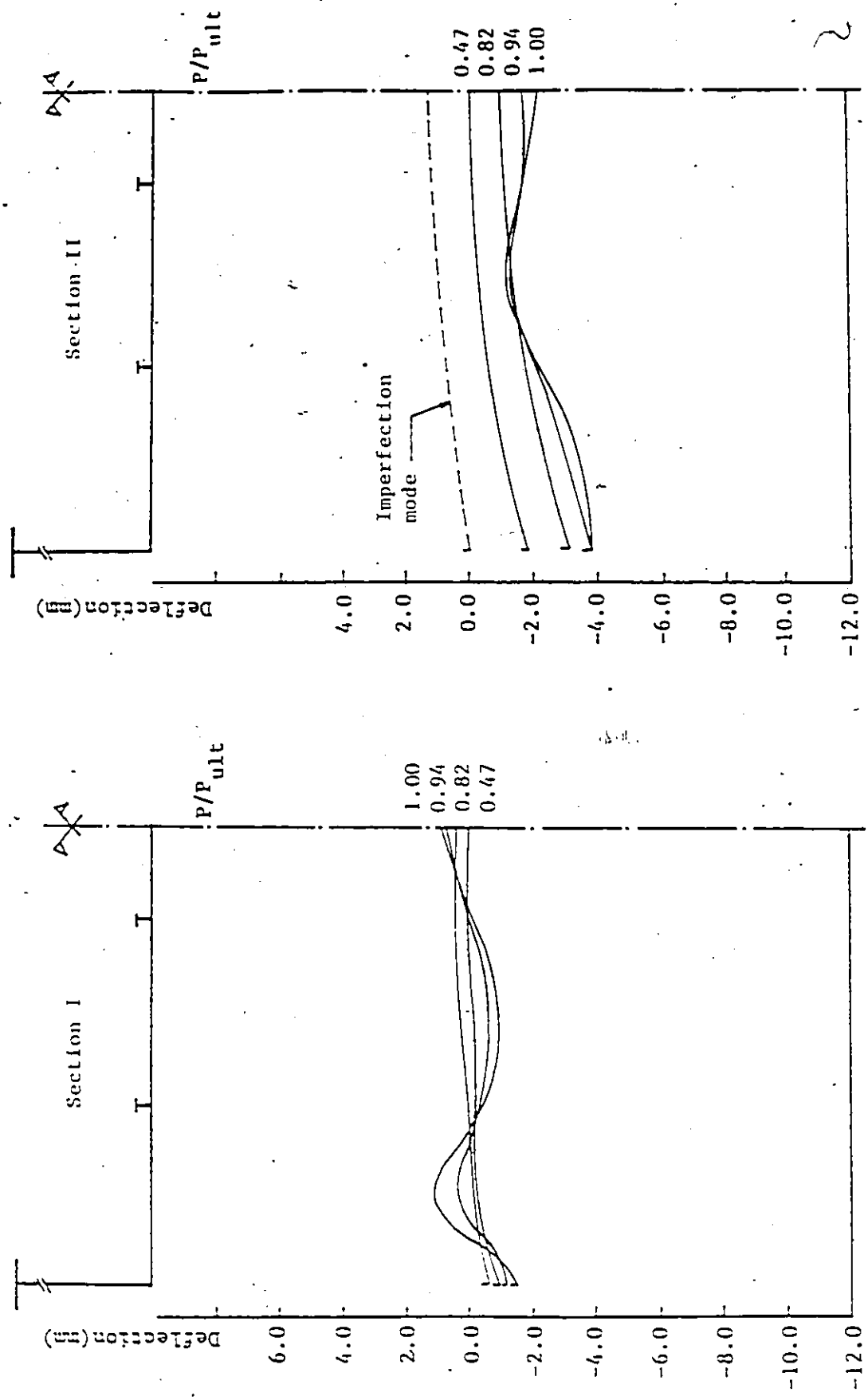
Section II
P/P ult
0.47
0.82
0.94
1.00
Imperfection mode
Deflection (mm)
4.0
2.0
0.0
-2.0
-4.0
-6.0
-8.0
-10.0
-12.0
b)
Section I
P/P ult
1.00
0.94
0.82
0.47
Deflection (mm)
6.0
4.0
2.0
0.0
-2.0
-4.0
-6.0
-8.0
-10.0
-12.0
a)

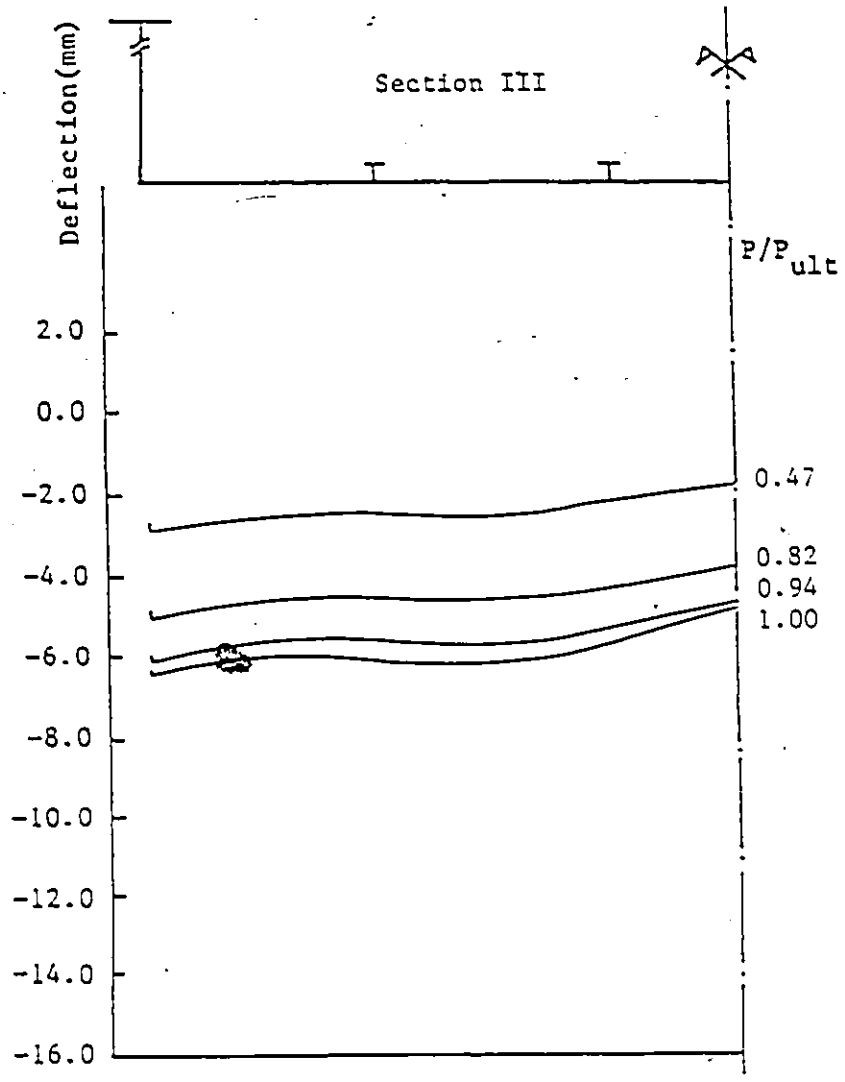

c)

Figure 4.22 : Bottom Flange Deflections at Different Sections for Simulation B3

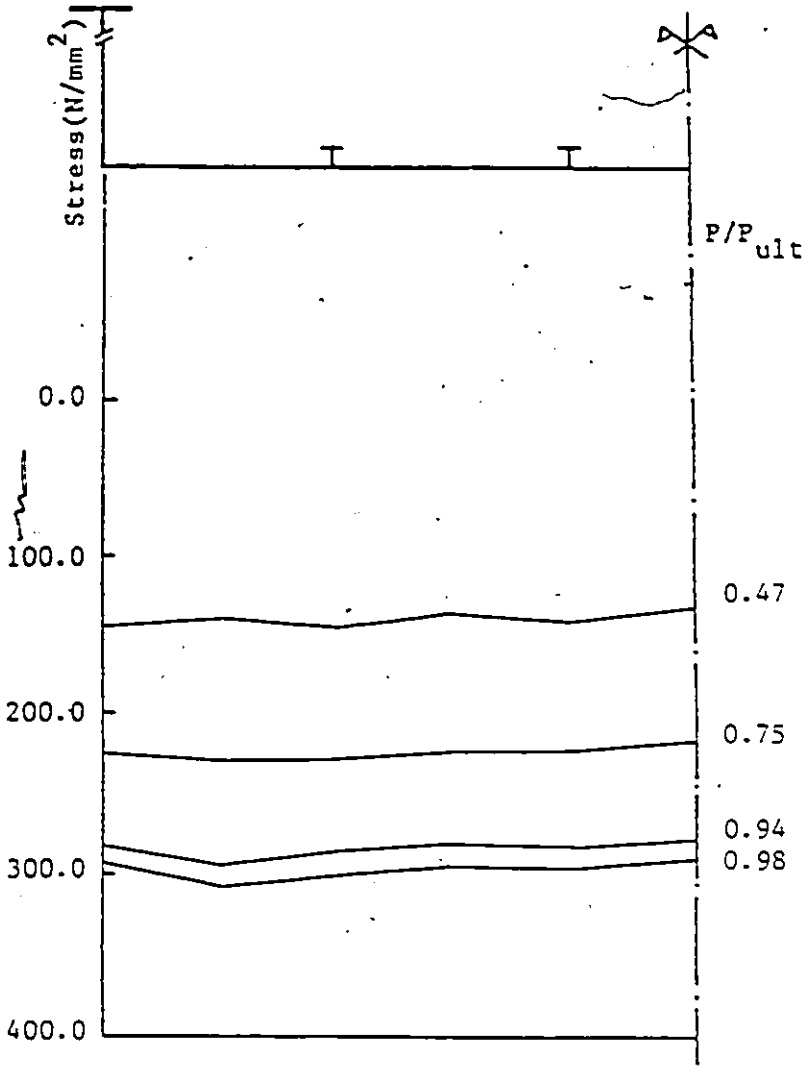

Figure 4.23 : Mid-Plane Axial Stresses at Section II for B3

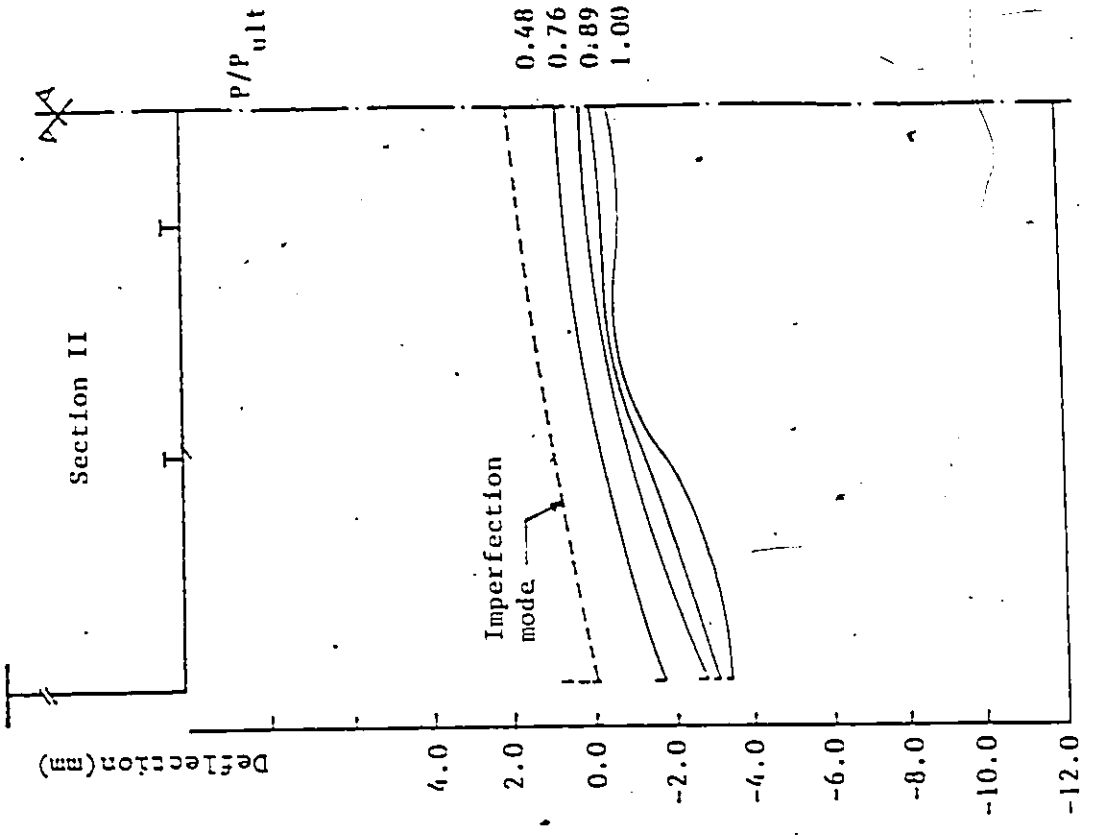
Section II
A
A
P/P ult
0.48
0.76
0.89
1.00
Imperfection mode
Deflection (mm)
4.0
2.0
0.0
-2.0
-4.0
-6.0
-8.0
-10.0
-12.0

b)

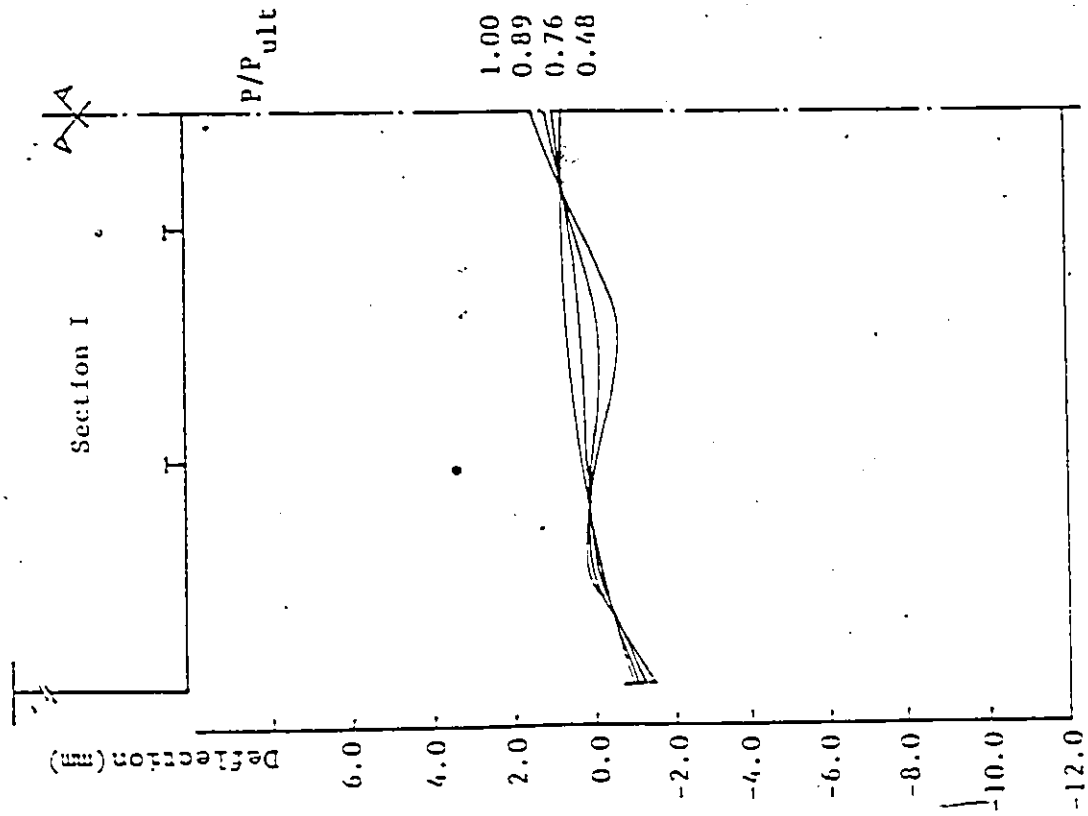
Section I
A
A
P/P ult
1.00
0.89
0.76
0.48
Deflection (mm)
6.0
4.0
2.0
0.0
-2.0
-4.0
-6.0
-8.0
-10.0
-12.0

a)

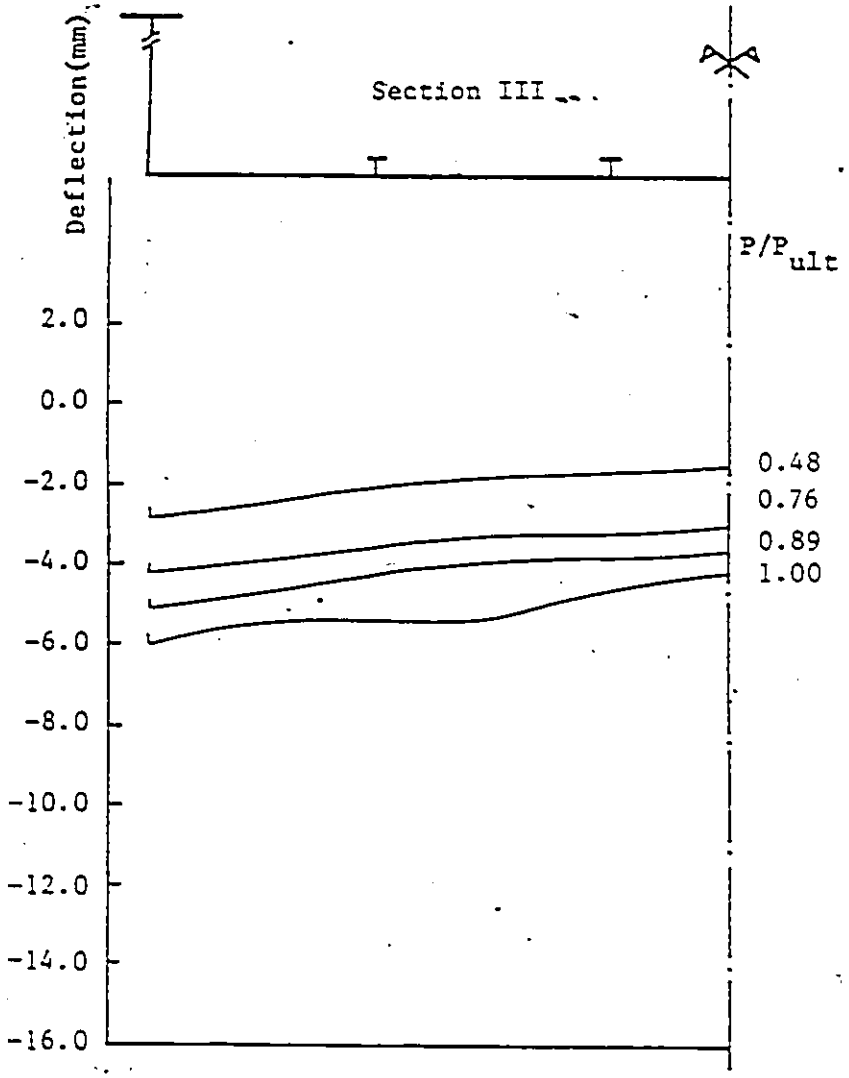

c)

Figure 4.24 : Bottom Flange Deflections at Different Sections for Simulation B4

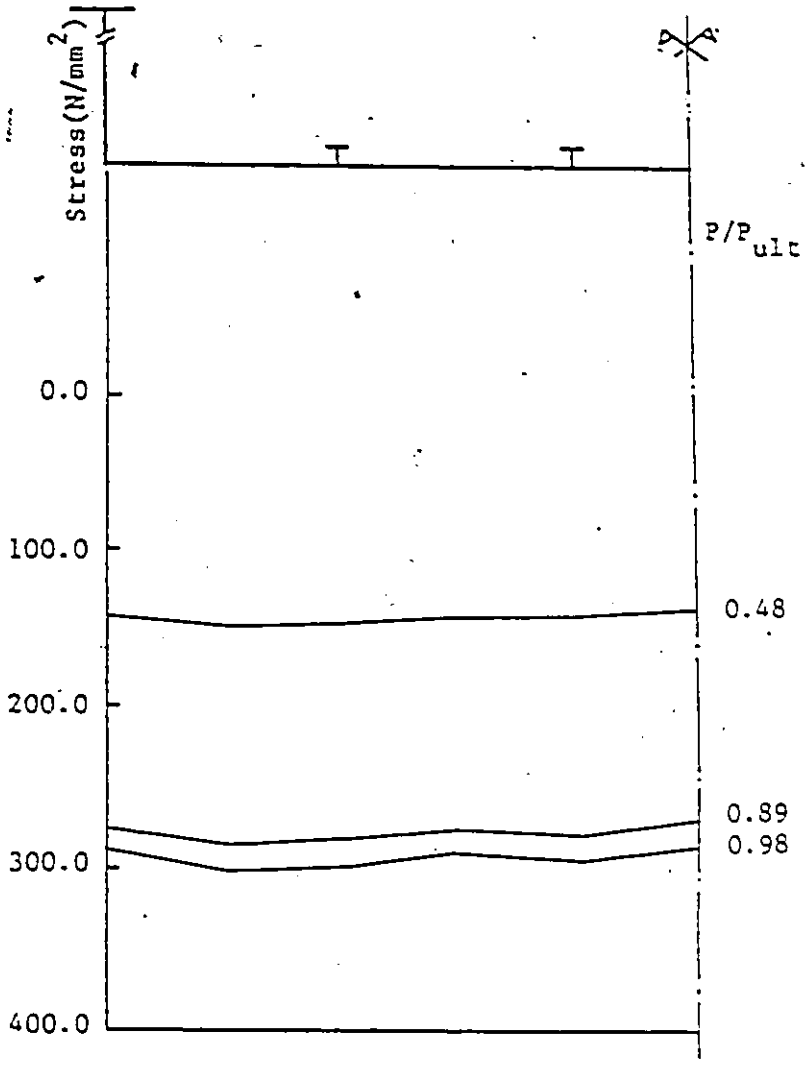

Figure 4.25 : Mid-Plane Axial Stresses at Section II for B4

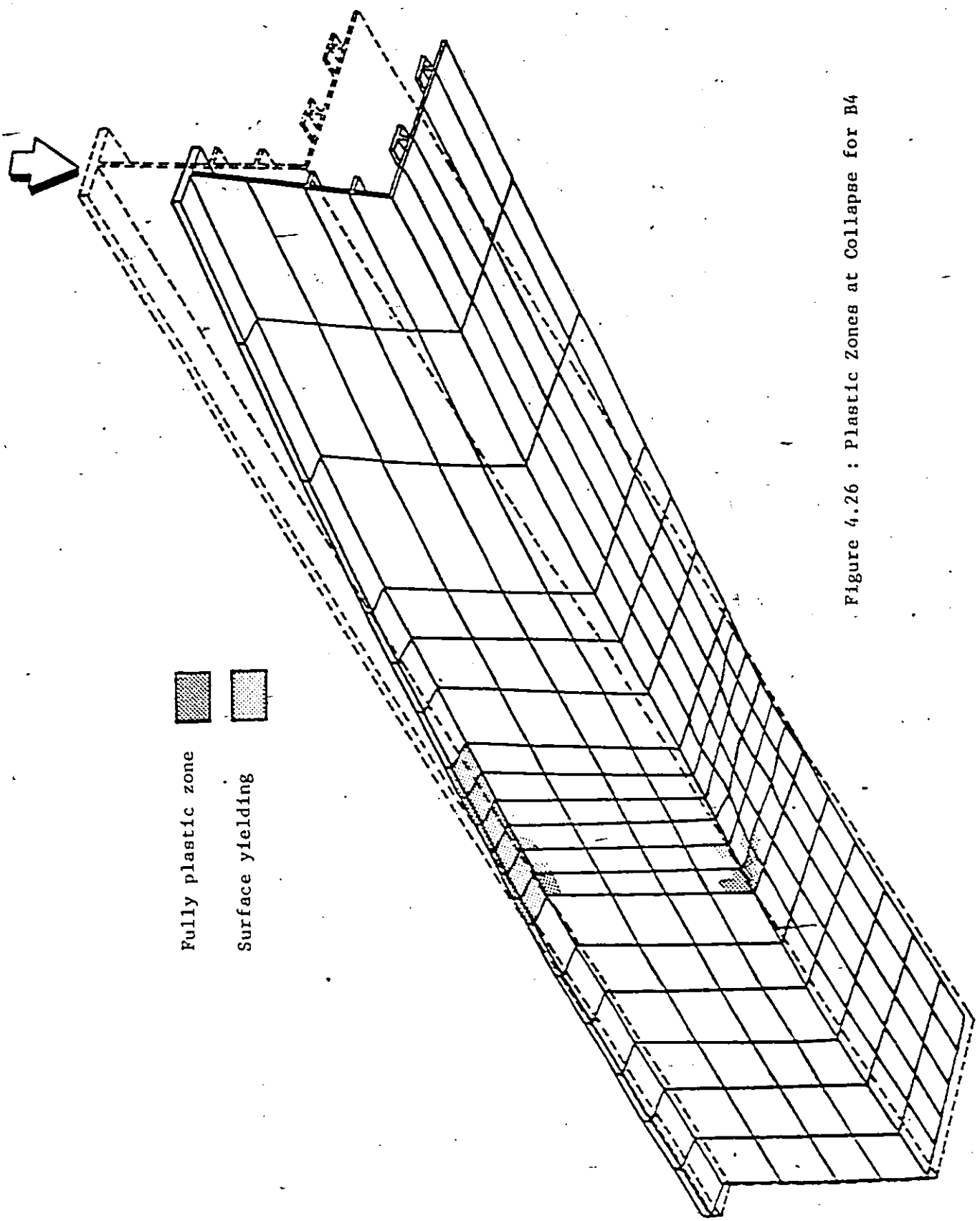

Figure 4.26 : Plastic Zones at Collapse for B4

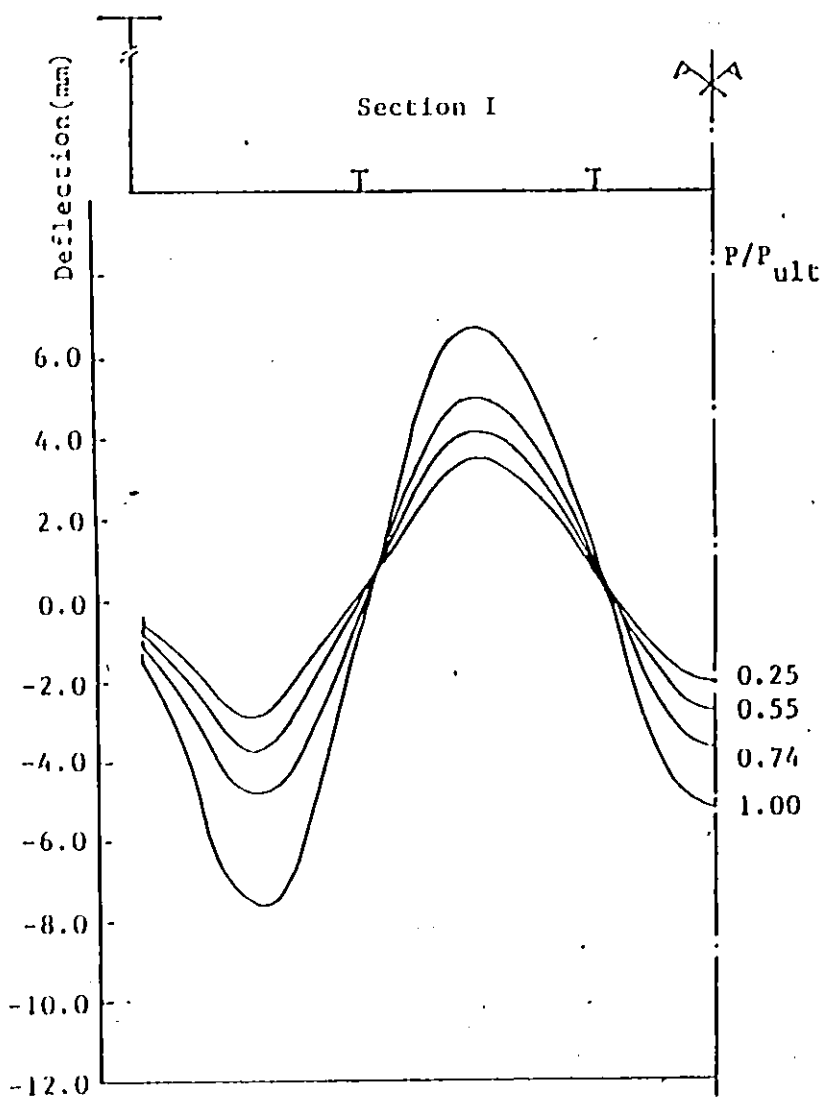
Section I
Deflection(mm)
P/P ult
6.0
4.0
2.0
0.0
-2.0
-4.0
-6.0
-8.0
-10.0
-12.0
0.25
0.55
0.74
1.00

a)

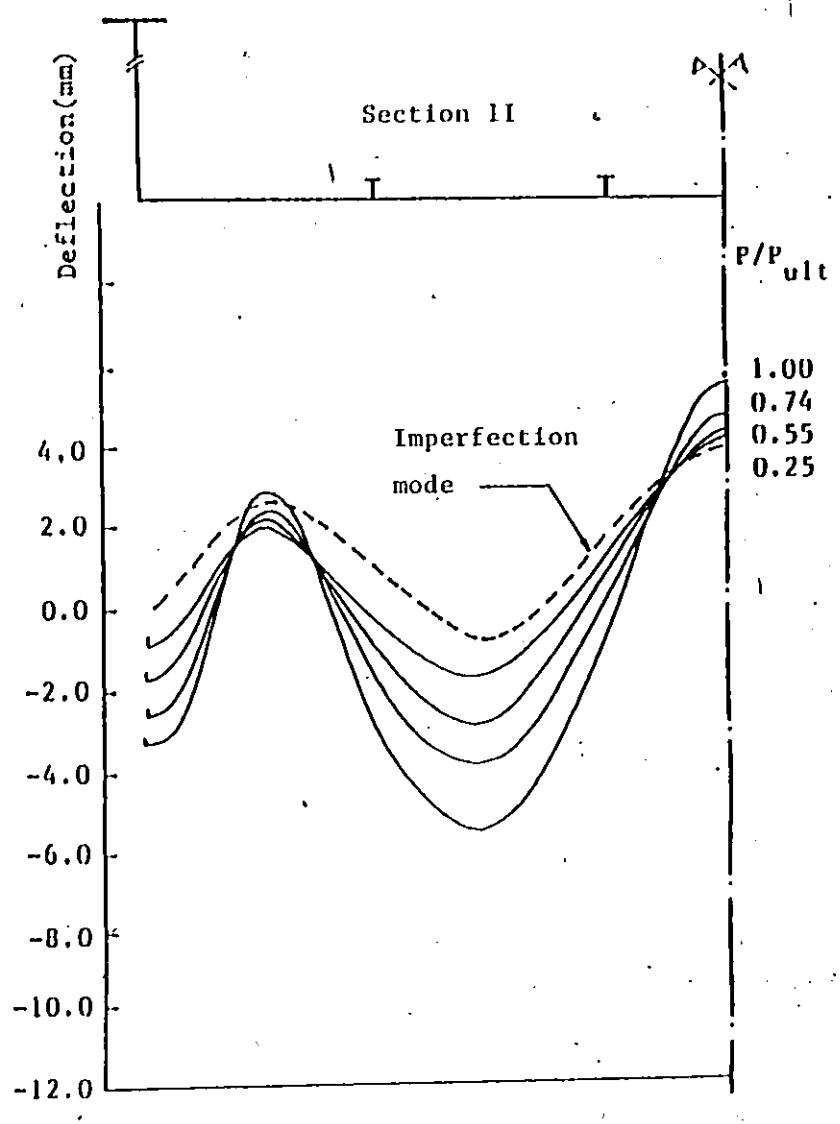
Section II
Deflection(mm)
P/P ult
4.0
2.0
0.0
-2.0
-4.0
-6.0
-8.0
-10.0
-12.0
1.00
0.74
0.55
0.25
Imperfection
mode

b)

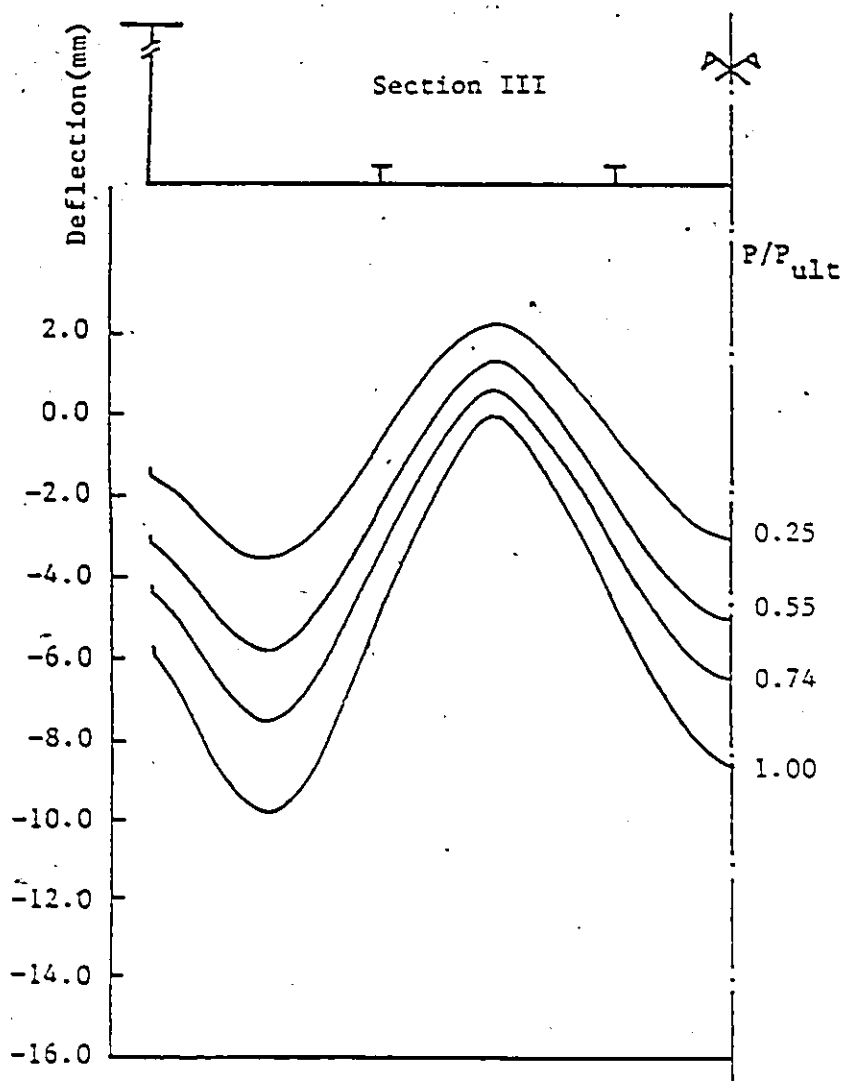

c)

Figure 4.27 : Bottom Flange Deflections at Different Sections for Simulation B5

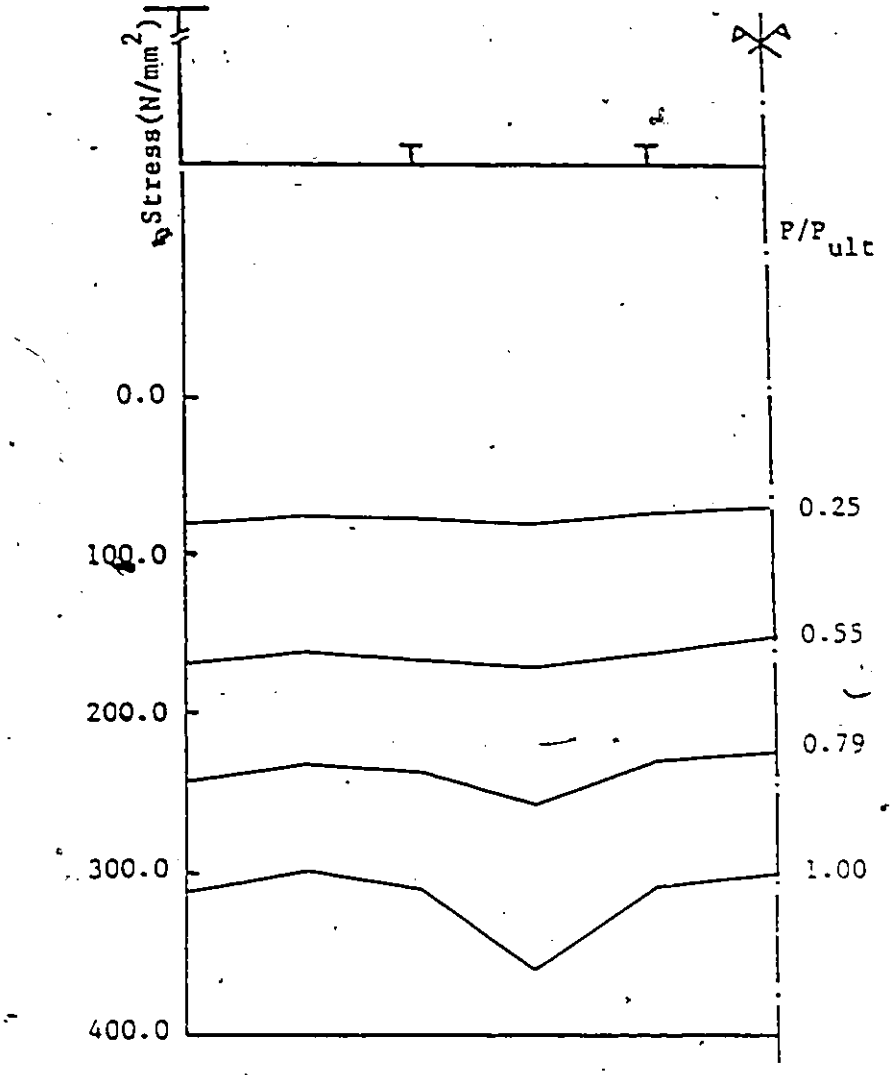

Figure 4.28 : Mid-Plane Axial Stresses at Section II for B5

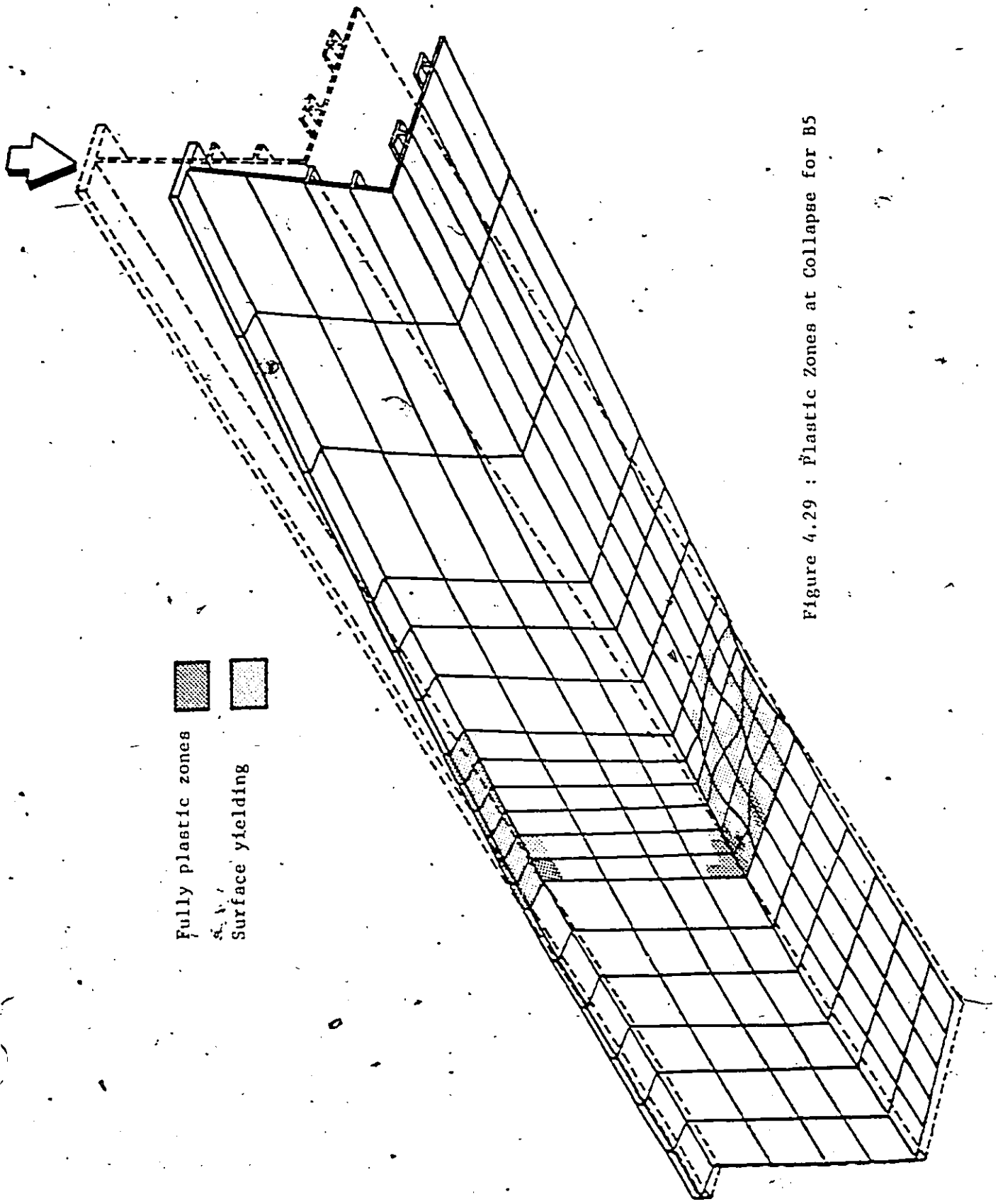

Figure 4.29 : Plastic Zones at Collapse for B5

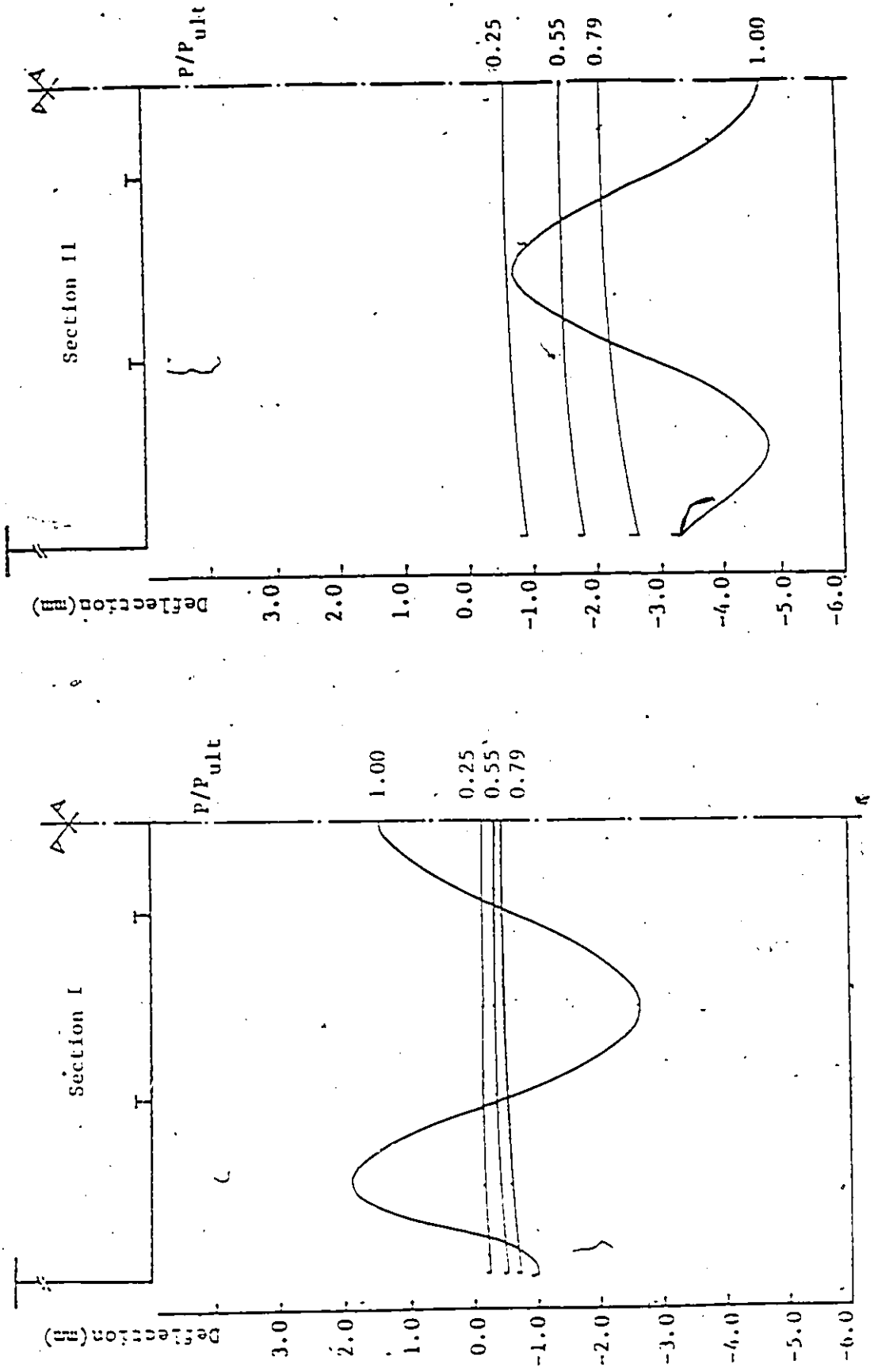
Section II
P/P_ult
0.25
0.55
0.79
1.00
Deflection (in)
3.0
2.0
1.0
0.0
-1.0
-2.0
-3.0
-4.0
-5.0
-6.0
b)
Section I
P/P_ult
1.00
0.25
0.55
0.79
Deflection (in)
3.0
2.0
1.0
0.0
-1.0
-2.0
-3.0
-4.0
-5.0
-6.0
a)

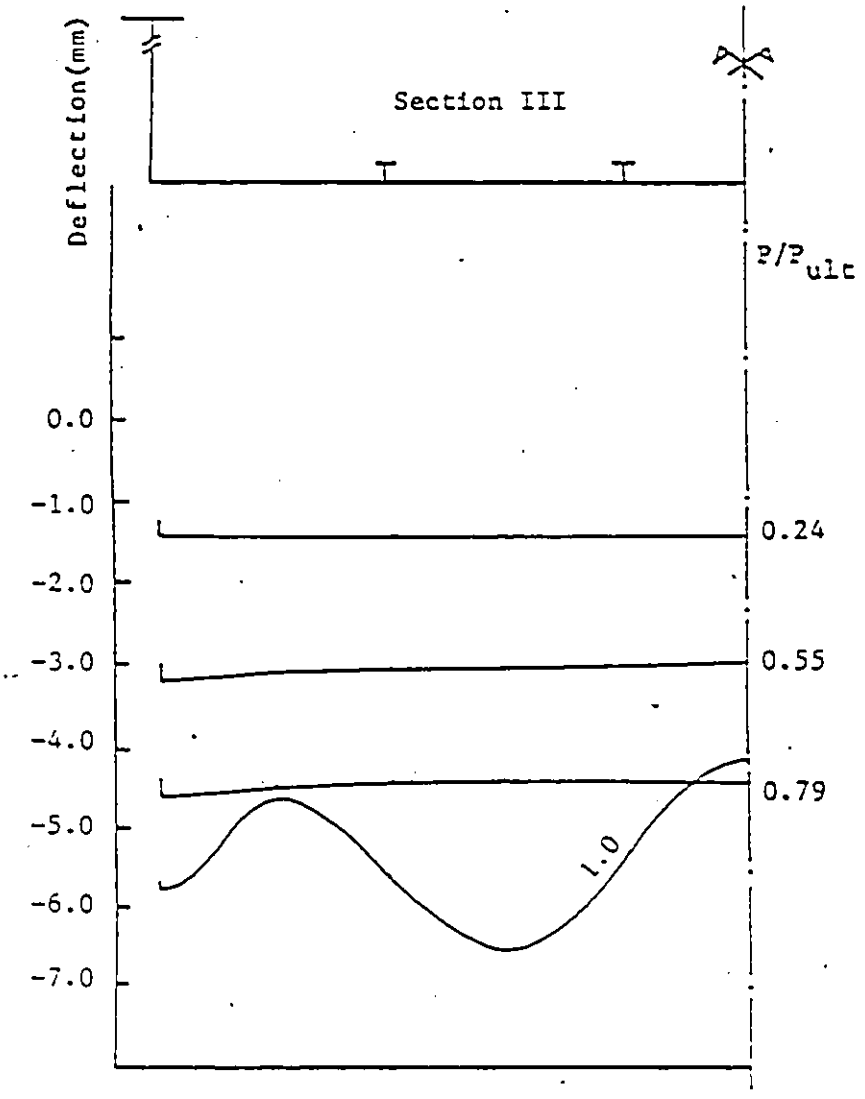

c)

Figure 4.30 : Bottom Flange Deflections at Different Sections for Simulation B6

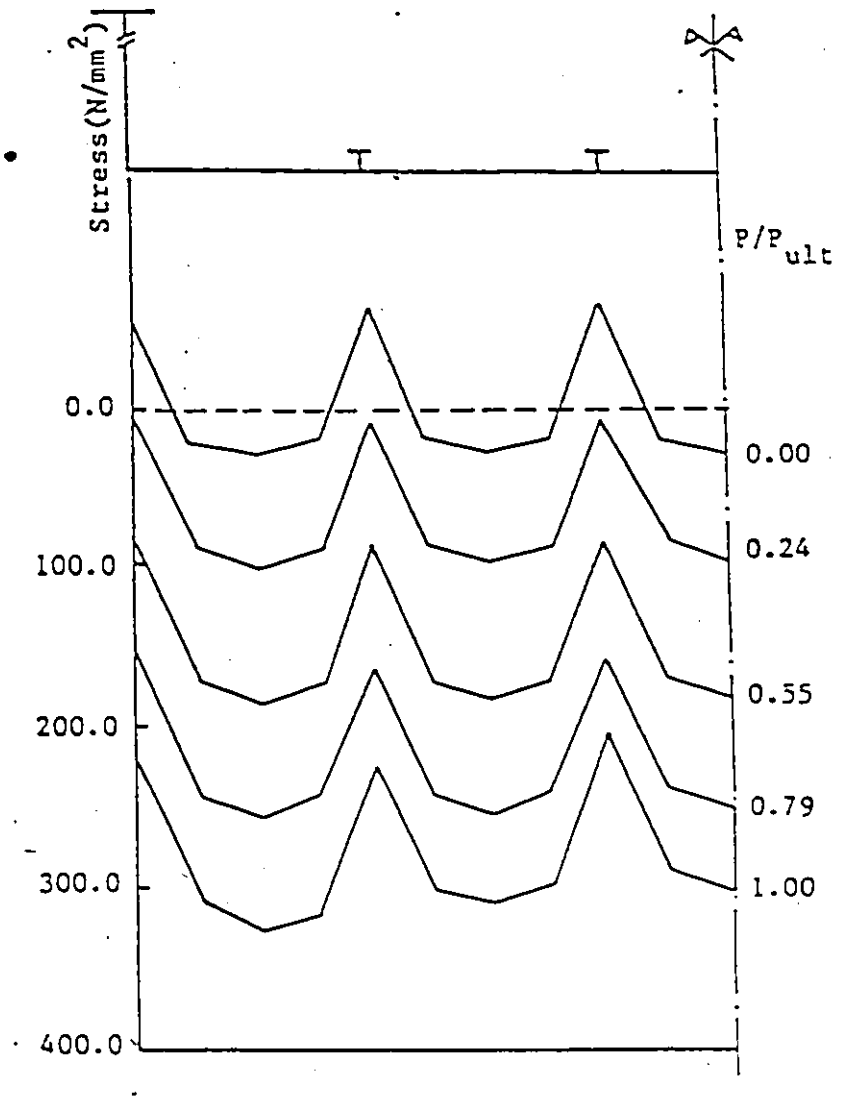

Figure 4.31 : Mid-Plane Axial Stresses at Section II for B6

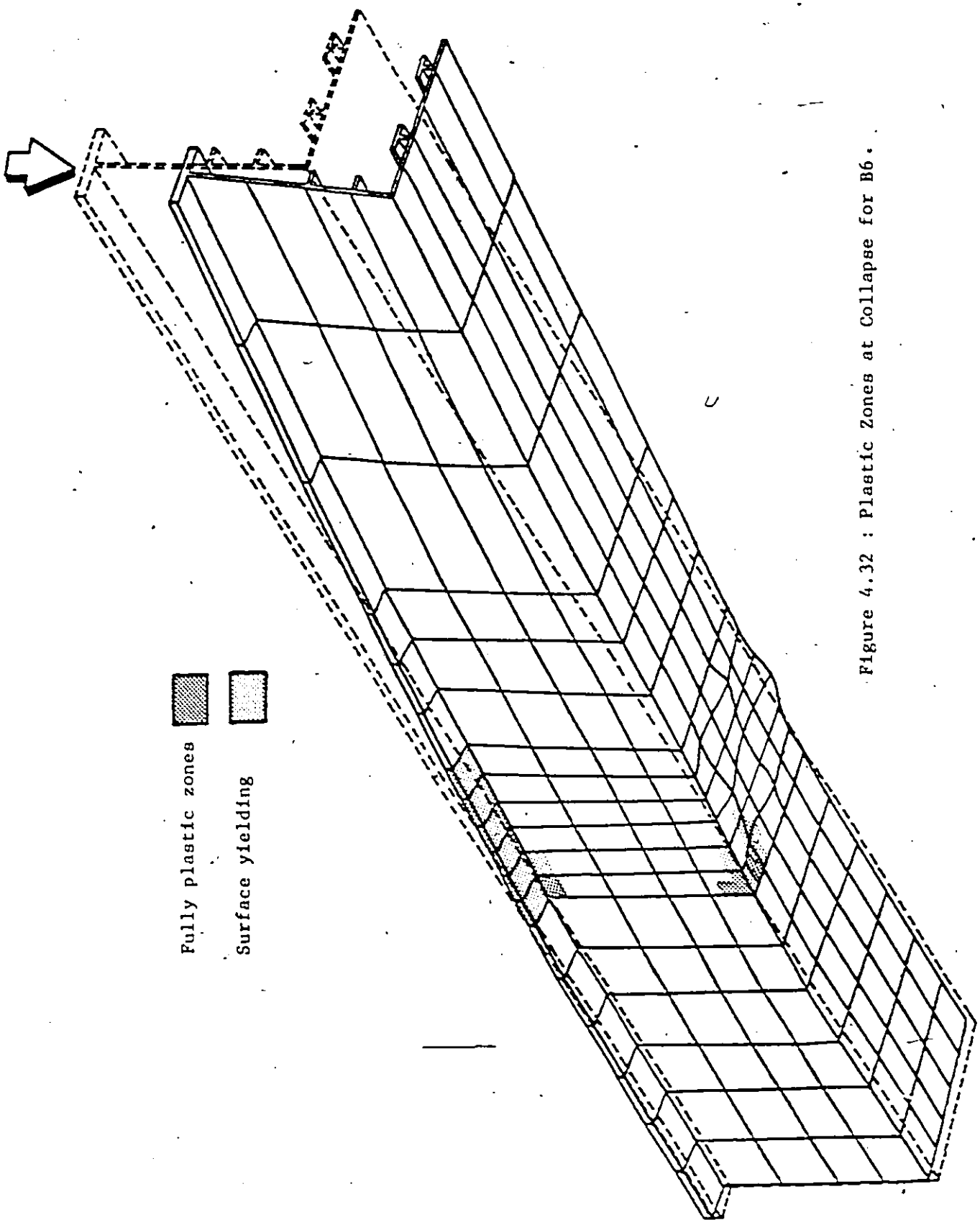

Figure 4.32 : Plastic Zones at Collapse for B6.

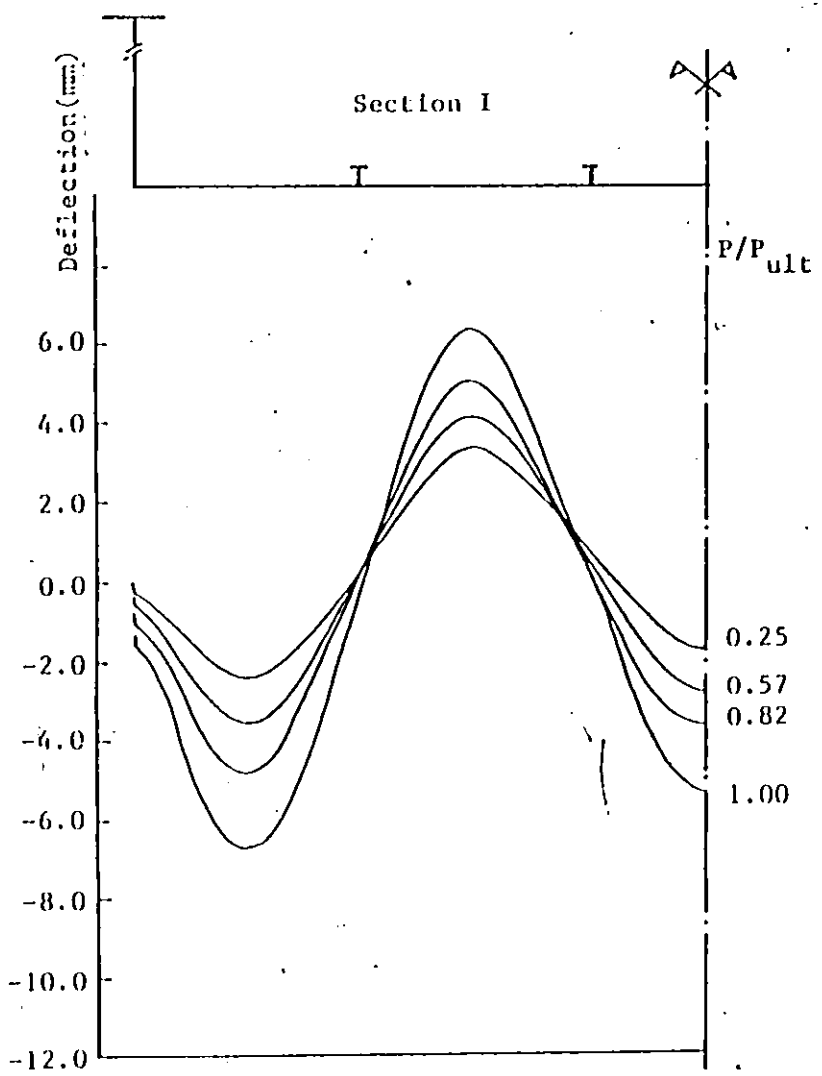
Section I
Deflection(mm)
P/P ult
6.0
4.0
2.0
0.0
-2.0
-4.0
-6.0
-8.0
-10.0
-12.0
0.25
0.57
0.82
1.00

a)

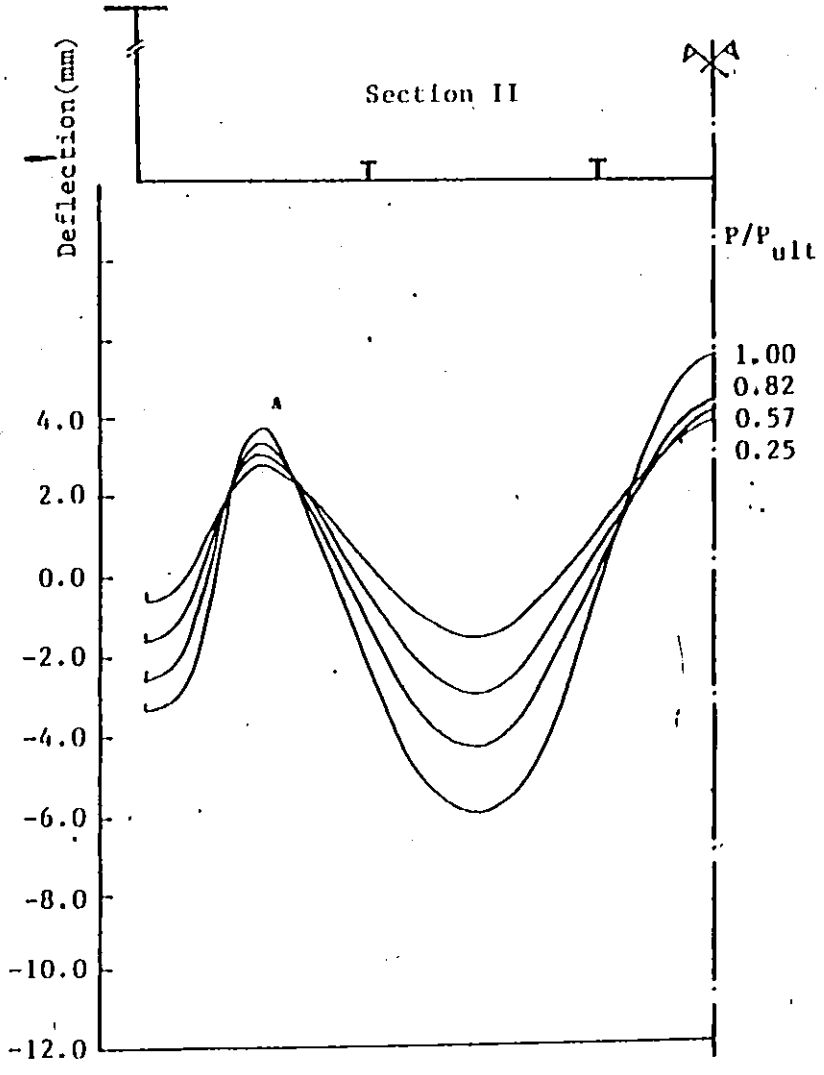
Section II
Deflection(mm)
P/P ult
4.0
2.0
0.0
-2.0
-4.0
-6.0
-8.0
-10.0
-12.0
1.00
0.82
0.57
0.25

b)

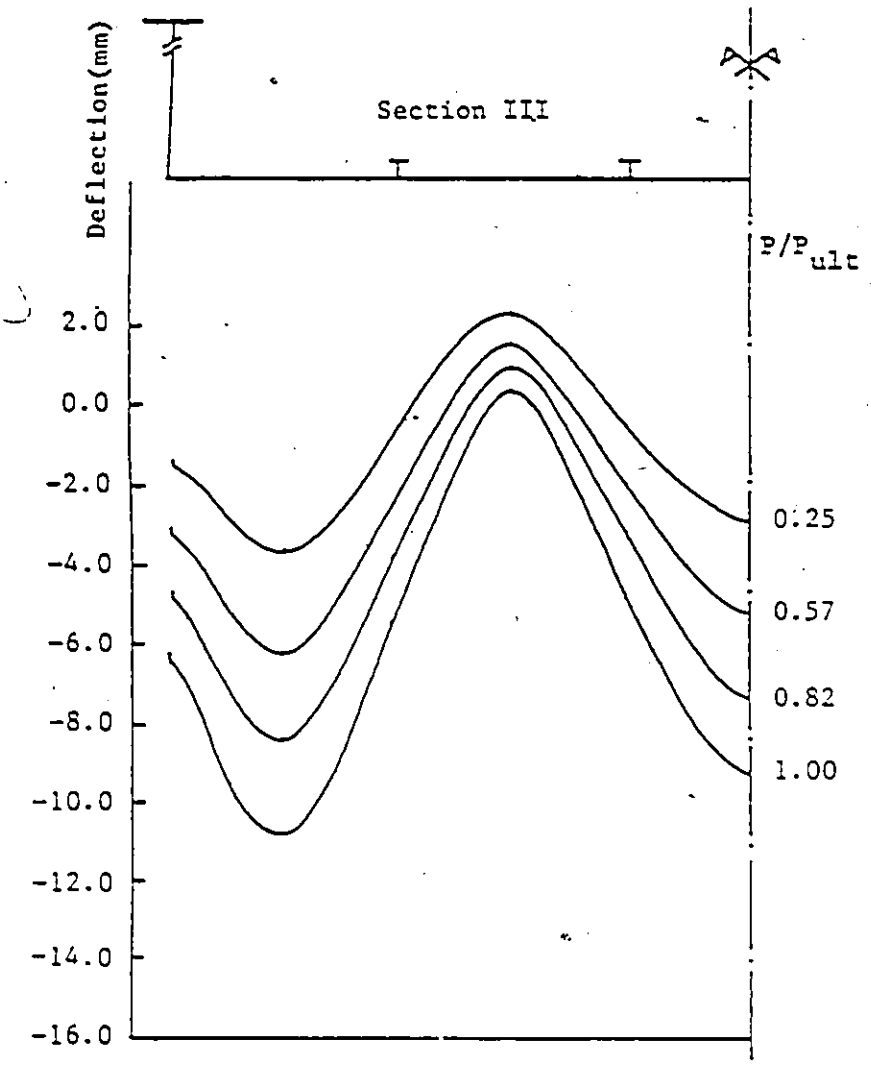

c)

Figure 4.33 : Bottom Flange Deflections at Different Sections for Simulation B7

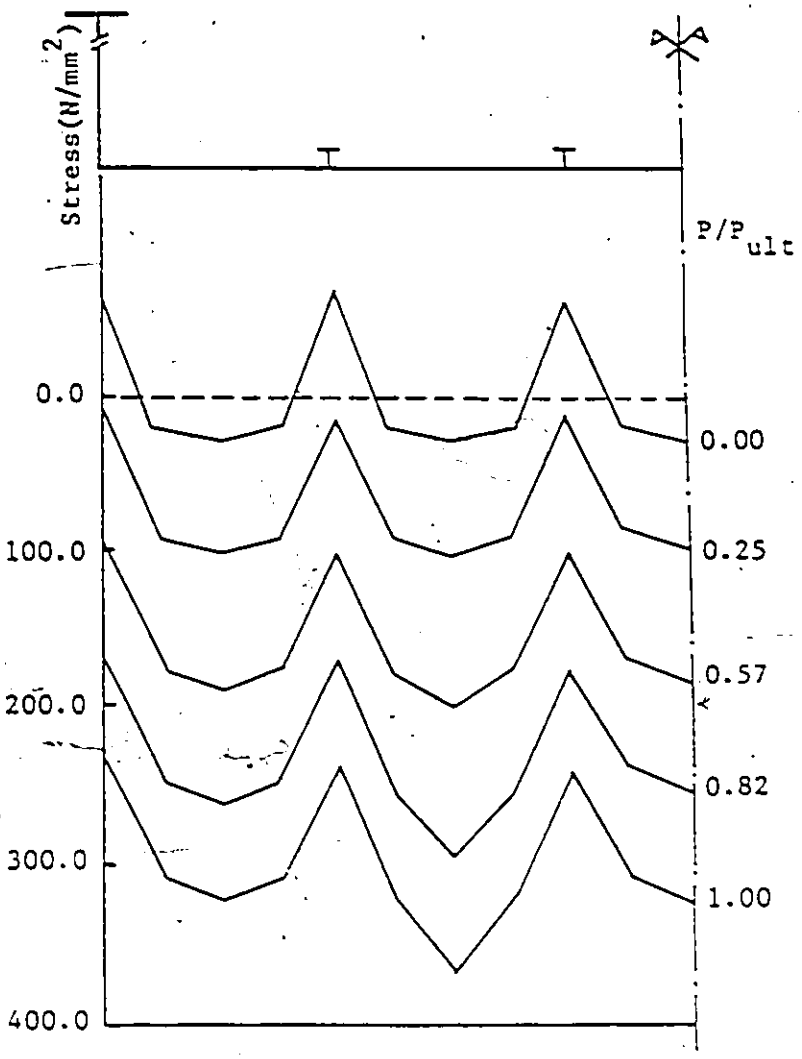

Figure 4.34 : Mid-Plane Axial Stresses at Section II for B7

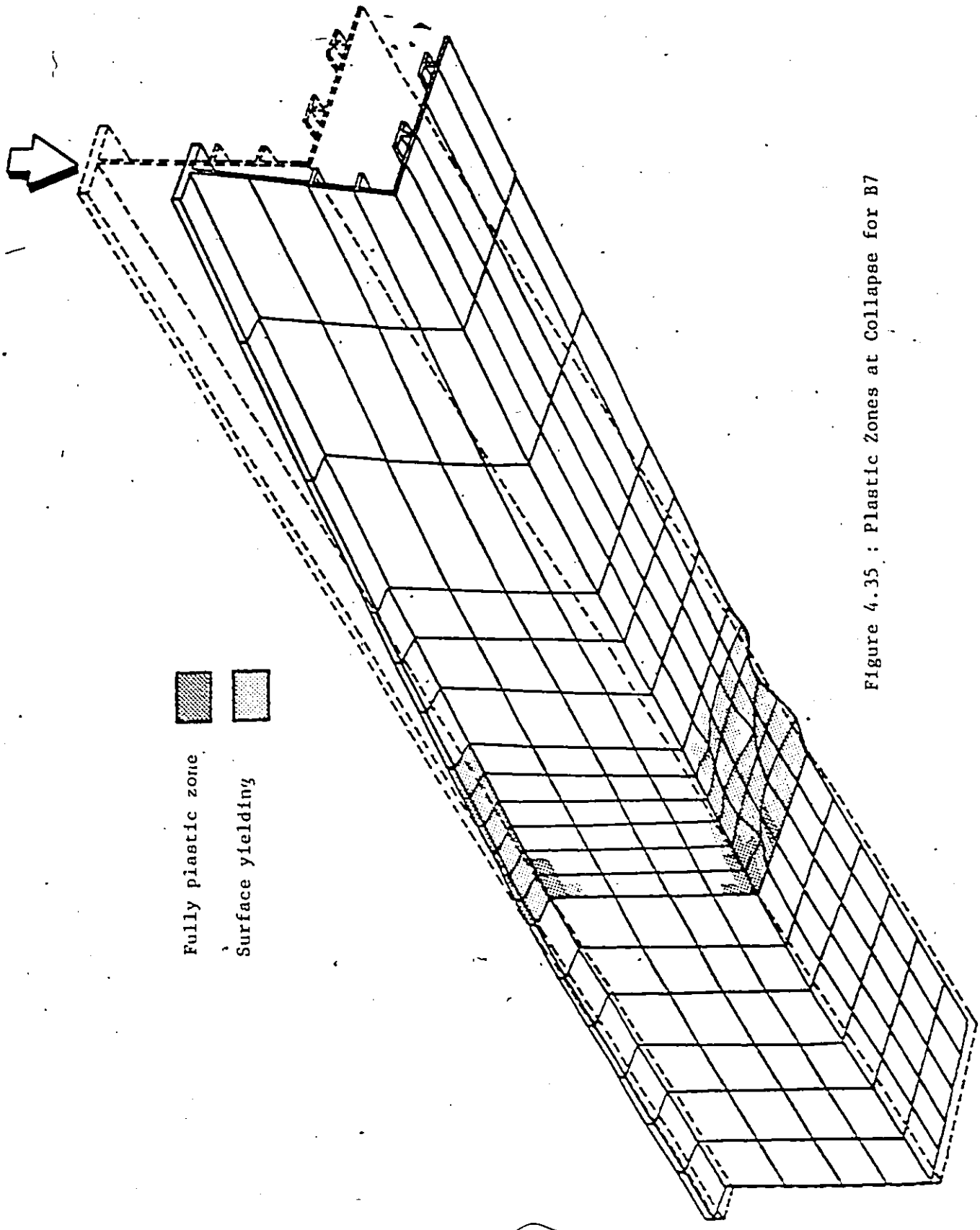

Figure 4.35 : Plastic Zones at Collapse for B7

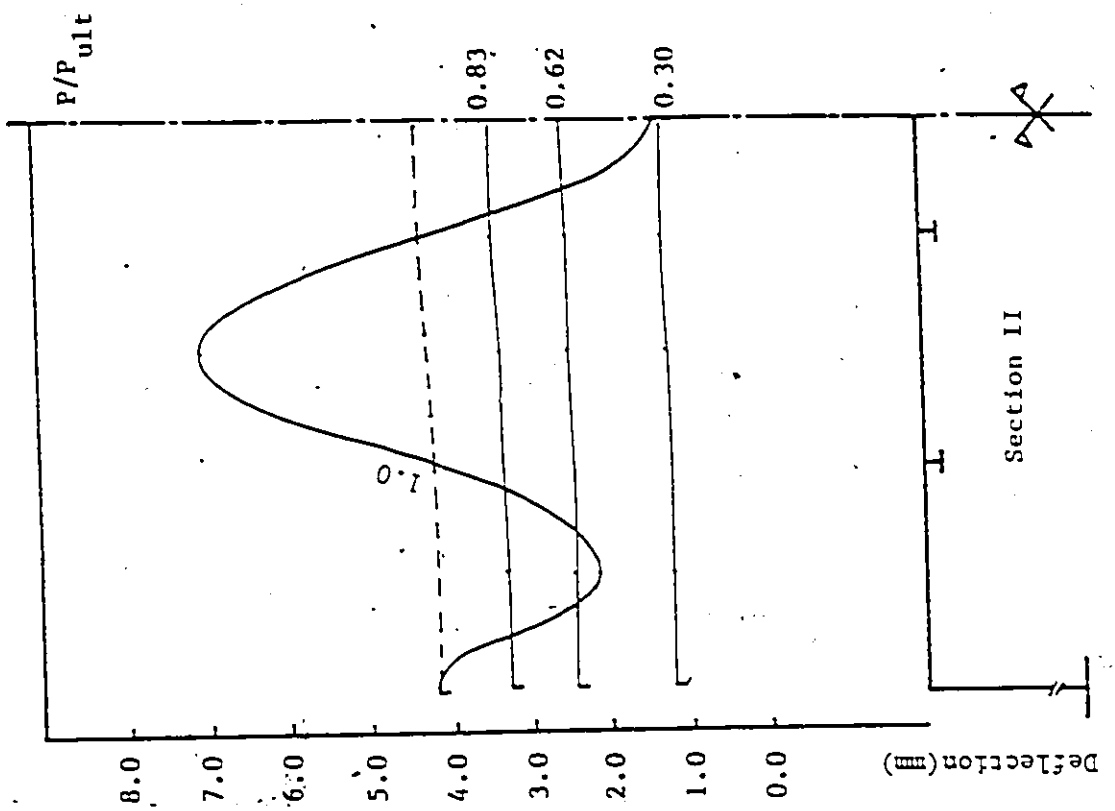
P/P ult
0.83
0.62
0.30
1.0
Section II
Deflection(mm)
8.0
7.0
6.0
5.0
4.0
3.0
2.0
1.0
0.0

b)

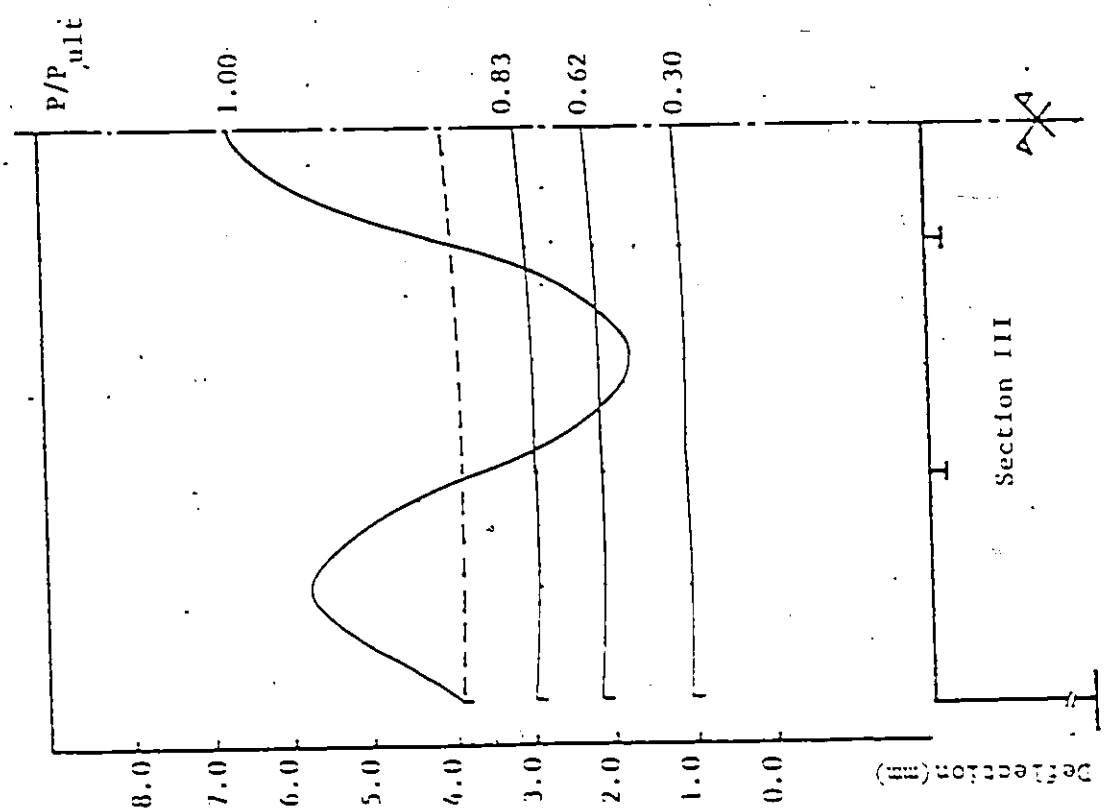
P/P ult
1.00
0.83
0.62
0.30
Section III
Deflection(mm)
8.0
7.0
6.0
5.0
4.0
3.0
2.0
1.0
0.0

a)

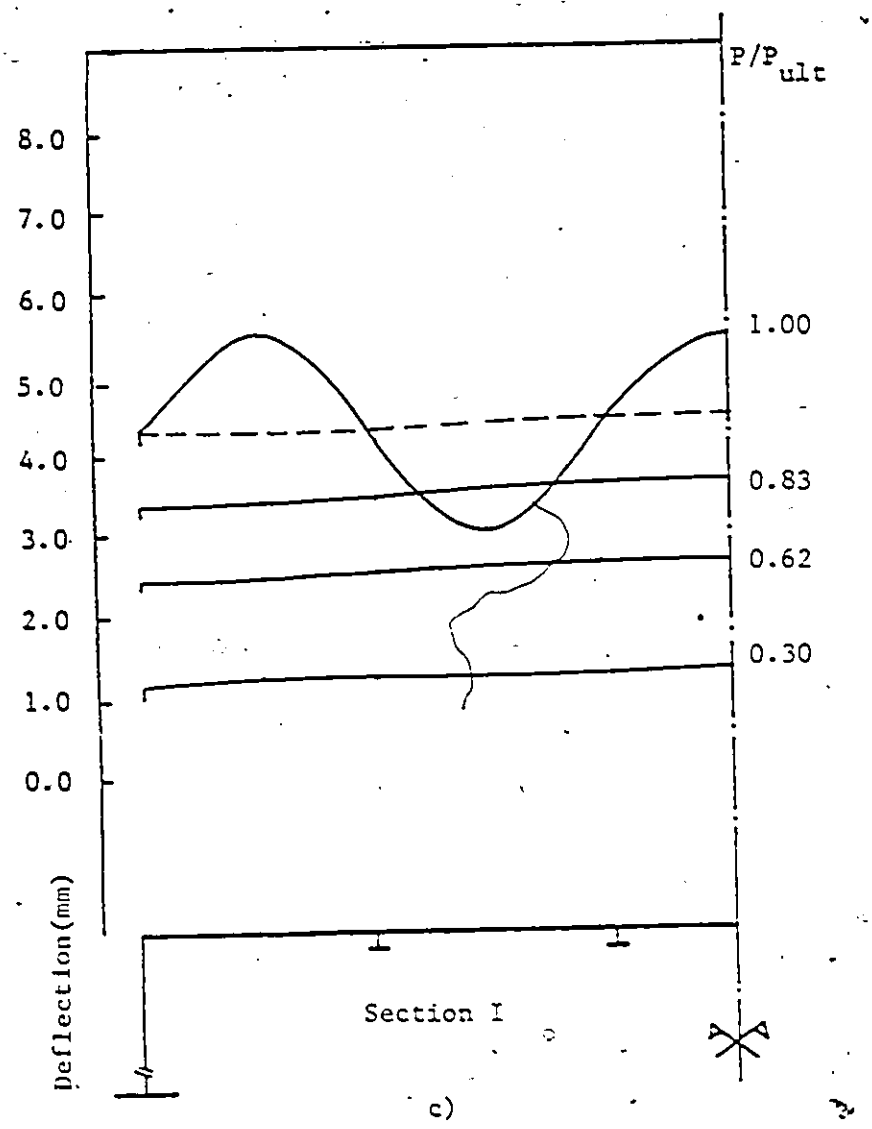

Figure 4.36 : Bottom Flange Deflections at Different Sections for Simulation C1

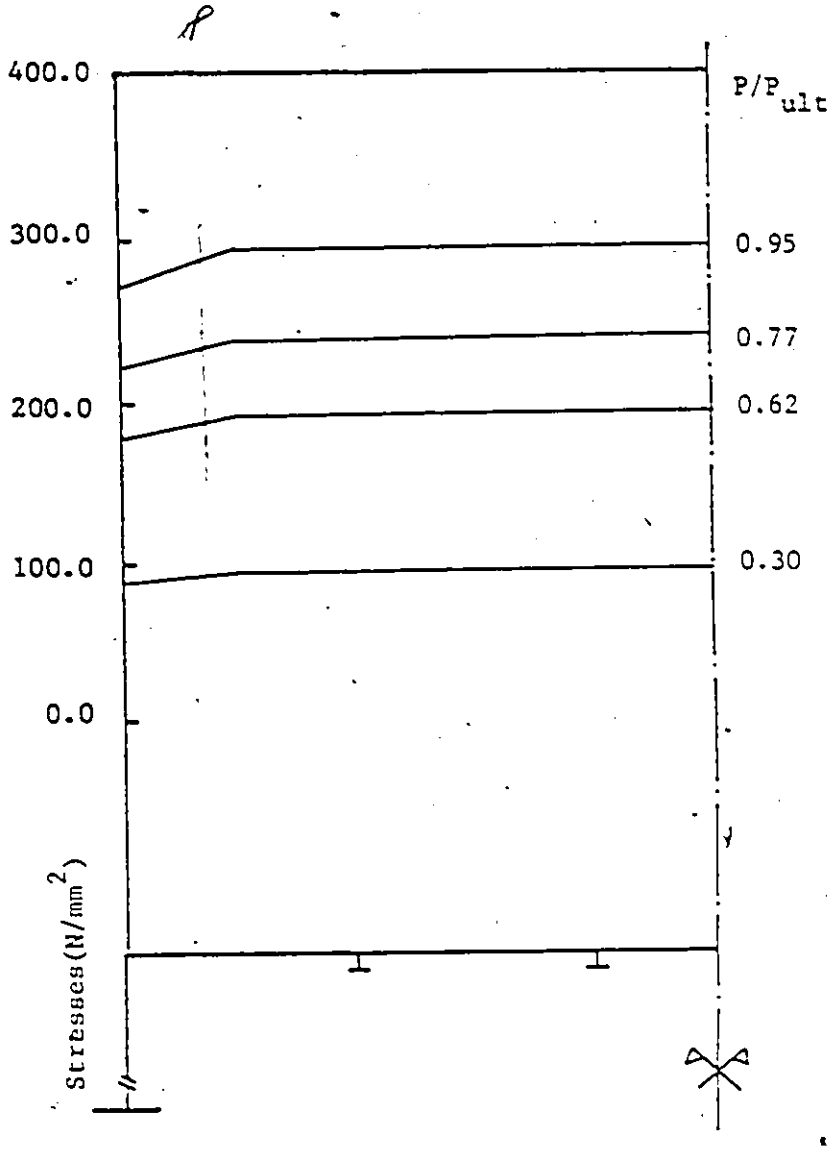

Figure 4.37 : Mid-Plane Axial Stresses at Section II for C1

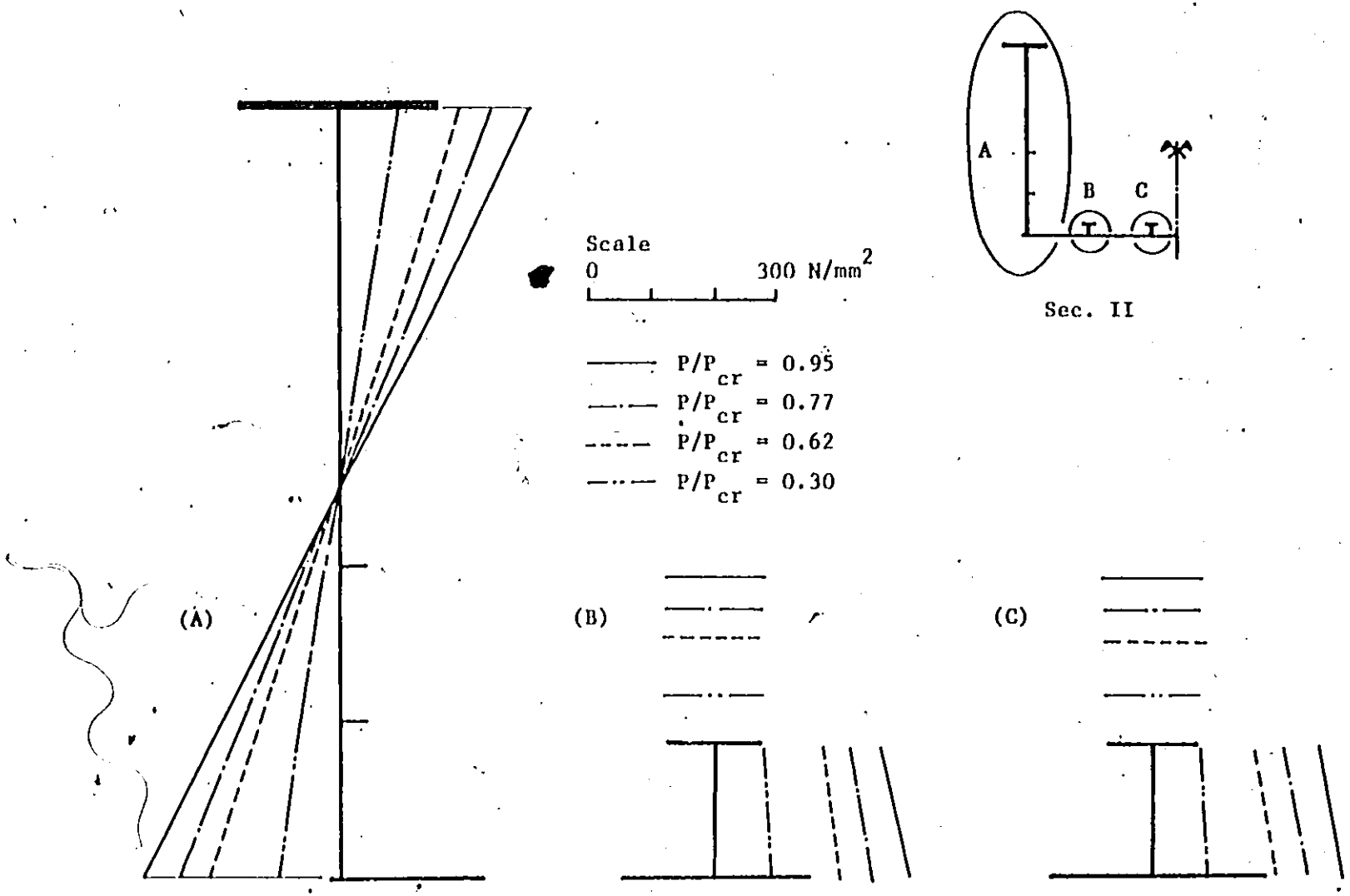

Figure 4.38 : Longitudinal Stress Distribution at Section II for Simulation C1

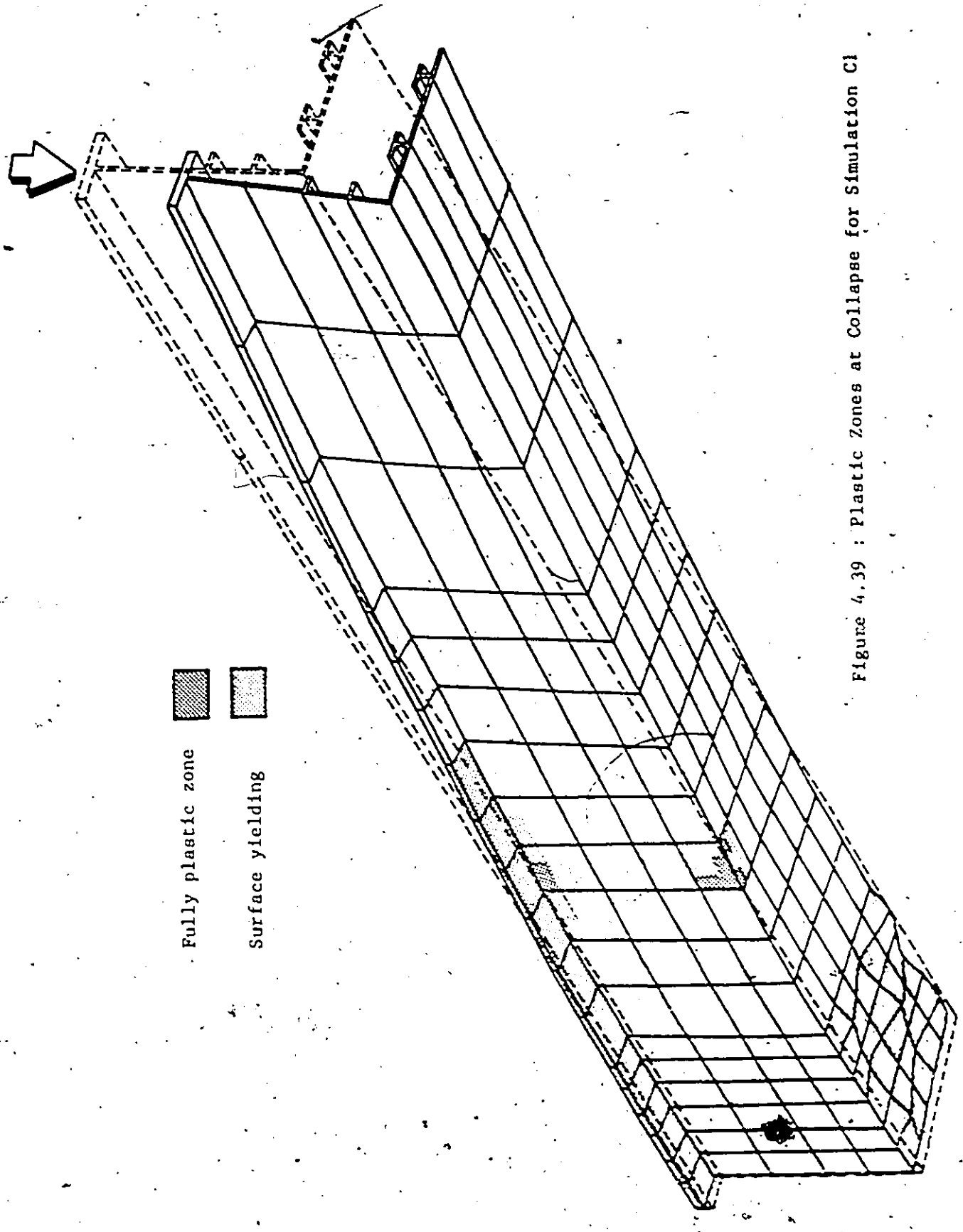

Figure 4.39 : Plastic Zones at Collapse for Simulation C1

CHAPTER FIVE

CONCLUSION

5.1 Summary and Conclusions

In this thesis the major objective has been to formulate an efficient and realistic analytical model to predict the strength of stiffened steel box girders that are employed in continuous bridge structures. An important accomplishment of the work has been to overcome the limitations inherent in previously reported simulations. As such, all of the stiffened components (i.e. flanges, webs and diaphragms) have been integrated, thus forming a realistic model for a typical box girder. Furthermore, both geometric imperfections and residual stresses are included to account for inherent flaws due to the processes of fabrication. While the model has been specifically developed for a constant depth stiffened steel box of rectangular cross section subjected to static loading, a more general configuration of the structure can be simulated with only minor modifications.

The present analytical model is based on a finite element displacement approach. This method can efficiently accommodate complex

structures with a variety of loadings and boundary conditions. The finite element model has been formulated through a three-dimensional assemblage of nonconforming rectangular plate elements for the flanges, webs and diaphragms. The rectangular elements, which are employed, incorporate both in-plane and out-of-plane actions. These elements utilize special provisions for displacement continuity along junctions between components of the box. In addition, eccentric beam-column elements are incorporated to represent the stiffeners. Diaphragms are handled in the analysis through a substructuring technique. This approach helps to reduce the size of the overall global stiffness matrix and hence renders a more efficient numerical scheme.

The model includes both material and geometric nonlinearities to account for inelastic response and large deflection, and to predict localized and overall behaviour of a box girder up to the ultimate capacity. In this regard, the box material is presumed to be isotropic; its plastic behaviour is described by the Von Mises yield criterion and the associated plastic flow rule. The stress-strain relationships have been idealized by bilinear behaviour to account for varying degrees of strain hardening. On the other hand, geometric nonlinearity is accomplished through nonlinear strain-displacement relationships that include second order terms. A total Lagrangian formulation is employed throughout the analysis, together with the Newton-Raphson incremental procedure.

The finite element model presented in this study has been verified through a comparison with predictions of other analytical

approaches, as well as experimental results available in the literature. The model verification included analyses of the following problems:

a) The elasto-plastic large deflection of beams and inelastic buckling of struts;

b) elasto-plastic, inelastic buckling and post-buckling of imperfect plate panels with, and without, residual stresses due to welding;

c) three dimensional assemblage and substructuring of a single chord T-joint and an unstiffened steel box beam.

Experimental results that covered the previously mentioned problems and which were used for validation of the present model included: a fully encastre' beam; a single chord T-joint under either punching shear or moment and an unstiffened steel box girder. Comparisons show very good agreement between the present model and the experimental and analytical results cited from the literature. However, in some cases, discrepancies did exist. The reasons for such discrepancies are explained.

Of paramount interest is the application of the model to investigate the behaviour of stiffened steel box girders. It is claimed to exhibit its superiority among other models previously reported for the following reasons:

a) all of a box girder's components are included in a unified manner to represent their interactions;

b) both flat and Tee type stiffeners are accommodated;

c) initial geometric imperfections and locked-in residual stresses, which are due to welding, are taken into account.

Analytical predictions for behaviour and strength of the box were carried out on simulated girders of an experimental model. It was built to represent a scaled-down version of a pier girder of a recently constructed bridge in Ontario. Theoretical solutions were generated, both to compare the results with the experiments undertaken and to assess the sensitivity of the box girder's strength to geometric and structural imperfections. As such, a series of finite element simulations were conducted for the perfect box and for imperfect girders to assess the importance of out-of-planeness of plate panels, out-of-straightness of stiffeners, residual stresses and an imperfection mode combination. These cases are important because the imperfections identified correspond to tolerance levels that have been proposed for possible application to North American-built girders.

The effect of moment gradient on the strength reduction of a box girder was investigated through one simulation test. For economy, diaphragms are only considered in three tests and replaced by stocky transverse stiffeners within the web in the remaining runs. It should be noted that the loading configurations and support conditions used in

the present simulation cases did not allow for the webs and diaphragm to influence appreciably the strength of the box. On the other hand, more interaction between components is expected when different load configurations and support conditions are used.

Comparison with experimental data demonstrates clearly the effectiveness of the newly developed model in giving excellent prediction of box strength. It is shown that the estimates for load carrying capacity are in far better agreement, than those obtained using previous approaches as reported in the literature. Based on the limited number of simulations that were performed, it appears reasonable to conclude that:

1) A rigorous finite element model that can accurately predict the response of a straight rectangular stiffened steel box girder under static loading has been developed. The model includes all the components that comprise a real stiffened steel box girder, and accounts for geometrical and structural imperfections;

2) a comparison between the predicted and experimental ultimate loads was found to be in excellent agreement, with the difference being in the order of 3%. It has, therefore, been ascertained that the model holds considerable promise for analysis and should be extended to future research in the field of box girder structures;

3) initial imperfections in the form of a longitudinal stiffener out-of-straightness has more influence than the plate mode in

reducing the strength of the box for similar amplitudes. A superimposed mode has a greater influence on the strength reduction than do modes considered separately;

4) relaxing a proposed tolerance level for compression flange plate panels from $\bar{b}/200$ to $\bar{b}/150$ might be justified. A difference of only 3% was found for the girder studied;

5) the effect of all imperfections (plate panel, longitudinal stiffener and residual stresses) for which possible tolerance amplitudes have been used in the present analysis (i.e. $\bar{b}/150$ and $L^p/500$), suggests that a reduction in strength of about 1-2% from that of an idealized girder is likely. Further investigations need to be done before more general conclusions can be drawn in this regard;

6) the influence of shear lag on the strength of a box girder that is proportioned in accordance with typical Canadian practice suggests an insignificant effect of shear lag on the strength;

It should be noted that many phenomenological aspects such as distortion of the box cross section, interaction between components, progress of yielding at junctions etc., can only be analysed satisfactorily by complete model representation. In addition, the model developed could be applied to a much wider range of problems involving geometric and/or material nonlinearities.

5.2 Suggestions for Future Research

The model developed in this dissertation, applied to box girder structures, has laid the foundation for some promising directions for further research in the general area of thin walled structures. A number of research areas are suggested to broaden the scope of applications of the finite element model developed in this study. These are:

1) the development of a sub-program to generate stiffness matrices of a triangular plate bending element so that box girders having trapezoidal cross section (i.e. with trapezoidal diaphragms) can be investigated;

2) modification of the beam element so that lateral buckling of flat plate stiffeners can also be investigated;

3) modification of the solution algorithm in such a way that unloading paths of equilibrium can be traced successfully.

Of particular interest to practicing engineers is an enhancement of knowledge about the behaviour and strength of box girders. Consequently, further research in the following topics are suggested:

1) the investigation of the effects of initial imperfections within all the components of the box girder on strength reduction. In particular, random imperfections with varying levels and modes need

to be investigated before definitive conclusions can be drawn about their influence on strength;

2) the effects of imperfections on European designed girders would be useful, particularly as more experimental data and analytical results have been based on such structures (that tend to minimize weight). It might be expected that these structures are more sensitive to imperfections (and hence the more urgent need for tolerance requirements in such codes of practice);

3) the undertaking of a systematic parametric study on box girders to investigate the influence of stiffener spacing and their rigidities for the compression flange;

4) a carrying out of more simulations to investigate and predict the behaviour and strength of box girders having different geometries, support conditions and loading configurations.

Appendix A

A.1 Shape Functions for the Rectangular Plate Element

A.1.1 Shape Functions for Bending Action

If $w = N_{b1}\, w_1 + N_{b2}\, \theta_{x1} + N_{b3}\, \theta_{y1} + \ldots N_{12}\, \theta_{y4}$, then

$N_{b1} = 1 - \xi\,\eta - (3-2\xi)\,\xi^2\,(1-\eta) - (1-\xi)\,(3-2\eta)\,\eta^2$

$N_{b2} = (1-\xi)\,\eta\,(1-\eta)^2 b$

$N_{b3} = -\,\xi\,(1-\xi)^2\,(1-\eta)a$

$N_{b4} = (3-2\xi)\,\xi^2\,(1-\eta) + \xi\,\eta\,(1-\eta)\,(1-2\eta)$

$N_{b5} = \xi\,\eta\,(1-\eta)^2 b$

$N_{b6} = (1-\xi)\,\xi^2\,(1-\eta)a$

$N_{b7} = (3-2\xi)\,\xi^2\eta - \xi^2\eta - \xi\,\eta\,(1-\eta)\,(1-2\eta)$

$N_{b8} = -\xi\,(1-\eta)\,\eta^2 b$

$N_{b9} = (1-\xi)\,\xi^2\eta\,a$

$N_{b10} = (1-\xi)\,(3-2\eta)\,\eta^2 + \xi\,(1-\xi)\,(1-2\xi)\eta$

$N_{b11} = -\,(1-\xi)\,(1-\eta)\,\eta^2\,b$

$N_{b12} = -\xi\,(1-\xi)^2\,\eta\,a$

A.1.2 Shape Functions For In-Plane Action

a) Element Type A

If $u = N_{p1}\, u_1 + N_{p2}\, u_2 + N_{p3}\, u_3 + N_{p4}\, u_4$, then

$N_{p1} = (1-\xi)\,(1-\eta)$

$N_{p2} = \xi(1-\eta)$

$N_{p3} = \xi\eta$

$N_{p4} = (1-\xi)\eta$

Also, if

$v = N_{p1}\, v_1 + N_{p2}\, \theta_{z1} + N_{p3}\, v_2 + N_{p4}\, \theta_{z2} + N_{p5}\, v_3 + N_{p6}\, v_4$, then

$N_{p1} = (1-\eta)\,(1-3\xi^2 + 2\xi^3)$

$N_{p2} = (1-\eta)\,(1-2\xi + \xi^2)\,\xi\, a$

$N_{p3} = (1-\eta)\,(3-2\xi)\,\xi^2$

$N_{p4} = (1-\eta)\,(\xi-1)\,\xi^2\, a$

$N_{p5} = \xi\,\eta$

$N_{p6} = (1-\xi)\,\eta$

b) Element Type B

If $u = N_{p1}\, u_1 + N_{p2}\, \theta_{z2} + N_{p3}\, u_2 + N_{p4}\, u_3 + N_{p5}\, u_4 + N_{p6}\, \theta_{z4}$, then

$N_{p1} = (1-\xi)\,(1-3\eta^2 + 2\eta^3)$

$N_{p2} = (1-\xi)\,(1-2\eta + \eta^2)\,\eta\, b$

$N_{p3} = (1-\eta)\,\xi$

$N_{p4} = \xi\,\eta$

$N_{p5} = (1-\xi)\,(3-2\eta)\,\eta^2$

$N_{p6} = (1-\xi)\,(\eta-1)\,\eta^2 b$

Also, if $v = N_{p1}\, v_1 + N_{p2}\, \theta_{z1} + N_{p3}\, v_2 + N_{p4}\, \theta_{z2} + N_{p5}\, v_3 + N_{p6}\, v_4$, then N_{p1} to N_{p6} are the same as for element type A.

c) Element Type C

If $u = N_{p1}\, u_1 + N_{p2}\, u_2 + u_{p3}\, u_3 + N_{p4}\, u_4$, and

if $v = N_{p1}\, v_1 + N_{p2}\, v_2 + N_{p3}\, v_3 + N_{p4}\, v_4$, then

$N_{p1} = (1-\xi)\,(1-\eta)$

$N_{p2} = \xi\,(1-\eta)$

$N_{p3} = \xi\,\eta$

$N_{p4} = (1-\xi)\,\eta$

A.2 Shape Functions for the Eccentric Stiffener Element

A.2.1 Shape Functions for Bending Action

If $w = N^s_{b1}\, w_1 + N^s_{b2}\, \theta_{y1} + N^s_{b3}\, w_2 + N^s_{b4}\, \theta_{y2}$, then

$N^s_{b1} = (1 - 3\xi^2 + 2\xi^3)$

$N^s_{b2} = \xi\,(1 - 2\xi + \xi^2)\,\ell$

$N^s_{b3} = \xi^2\,(3 - 2\xi)$

$N^s_{b4} = \xi^2\,(\xi - 1)\,\ell$

A.2.2 Shape Functions for In-plane Action

If $u = N^s_{p1}\, u_1 + N^s_{p2}\, w_1 + N^s_{p3}\, \theta_{y1} + N^s_{p4}\, u_2 + N^s_{p5}\, w_2 + N^s_{p6}\, \theta_{y2}$, then

$N^s_{p1} = (1 - \xi)$

$N^s_{p2} = \frac{6e}{\ell}\,(\xi^2 - \xi)$

$N^s_{p3} = e\,(1 - 4\xi + 3\xi^2)$

$N^s_{p4} = \xi$

$N^s_{p5} = \frac{6e}{\ell}\,(\xi - \xi^2)$

$N^s_{p6} = e\,(3\xi^2 - 2\xi)$

REFERENCES

[1] Billington, C.J., Ghavami, K., and Dowling, P.J., "Parametric Study of Cross-Sectional Distortion Due to Eccentric loading", CESLIC Report BG16, Imperial College, London, England, September 1972.

[2] Gent, A.R., and Shebini, V.K., "Parametric Study Report on Torsional Warping", CESLIC Report, Imperial College, London, England, June 1972.

[3] Moffatt, K.R., and Dowling P.J., "Parametric Study on the Shear Lag Phenomenon in Steel Box Girder Bridges", CESLIC Report BG17, Imperial College, London, England, September 1972.

[4] Moolani, F.M., and Dowling, P.J., "Tests to Study The Effect of Shear Lag on the Collapse of Steel Box Girders", CESLIC Report BG34, Imperial College, London, England, 1974.

[5] Ballio, G., and Mazzolani, F.M., "Theory and Design of Steel Structure", Chapman and Hall, New York, 1983.

[6] Heckel, R., "The Fourth Danube Bridge in Vienna, Damage and Repair", International Conference on Development in Bridge Design and Construction, University College, Cardiff, Crosby Lockwood and Son Ltd., London, 1971. pp. 588-598.

[7] Anonymous, "Cantilever Box Girder Bridge Collapse During Construction", Engineering News Record, June [redacted] 1970. p.9.

[8] Maquoi, R., and Massonnet, C., "Lecons a tirer des accidents survenus a quatre grands ponts métalliques en caisson", Annales des Travaux Publics de Belgique, 2, 1972, pp. 69-84.

[9] Chatterjee, S., "Design of Stiffened Compression Flanges in Box and Plate Girders", The Design of Steel Bridges, Granada Edn. 1980, pp. 281-305.

[10] Dowling, P.J., Chatterjee, S., Frieze, P.A., and Moolani, F.M., "Experimental and Predicted Collapse Behaviour of Rectangular Steel Box Girders", Steel Box Girder Bridges, ICE, London 1973, pp. 77-95.

[11] Murray, N.W., "Buckling of Stiffened Panels loaded Axially and in Bending", The Structural Engineer, 51, 1973.

[12] Rubin, H., "Das Tragverhalten langsversteifter, Vorverformter Rechteck-platten unter Axialbelastung nach der nichtlinearen Beultheorie", Schriftenreihe H.I. Karlsruhe, 1976.

[13] Bilsten, W., "Anwendung der nichtlinearen Beultheorie aut vervormfte mit diskreten Langssteifen verstarkte Rechteck platten under Langsbelastung", Publ. Inst. fur Statik und Stahlbau, T.H. Darmstadt, 1974.

[14] Department of the Environment, Merrison Committee, "Inquiry into the Basis of Design and Method of Erection of Steel Box Girder Bridges-Interim Report", HMSO, London, 1973.

[15] Chatterjee, S., and Dowling, P.J., "The Design of Box Girder Compression Flanges", Proc. of Int. Conference on Steel Plated Structures, Imperial College, London, 1976.

[16] Murray, N.W. "Analysis and Design of Stiffened Plates for Collapse Load", The Structural Engineer, Vol. 53, No. 3, March 1975, pp. 153-158.

[17] Horne, M.R., and Narayanan, R., "Ultimate Capacity of Longitudinally Stiffened Plates Used in Box-Girders", Proc. ICE. Part 2, 61, June 1976, pp. 253-280.

[18] Dwight, J.B., and Moxham, K.E., "Welded Steel Plates in Compression", The Structural Engineer, February 1969.

[19] Rockey, K.C., Evans, H.R., and Porter, D.M., "Ultimate Load Capacity of Stiffened Webs Subjected to Shear and Bending", Proc. Int. Conf., ICE, London, 13-14, February 1973, pp. 45-61.

[20] Evans, H.R., Porter, D.M., and Rockey, K.C., "Ultimate Load Behaviour of Plate and Box Girder Webs", Proc. of Int. Conf. on Steel Plated Strucutures", Imperial College, London, 1976.

[21] Rockey, K.C., and El-Gaaly, M.A., "Stability of Load Bearing Trapezoidal Diaphragms", IABSE publication 32-11, p. 155, 1972.

[22] Dowling, P.J., Lee, J.A., and Dean, J.A., "The Behaviour up to Collapse of Load Bearing Diaphragms in Rectangular and Trapezoidal Stiffened Steel Box Girders", Proc. Int. Conf., ICE, London, 13-14 February, 1973, pp. 95-117.

[23] Yilamz, C., "Ultimate Strength of Box Girders by Finite Element Method", Ph.D. Dissertation, Lehigh University, 1975.

[24] Puthli, R.S., Crisfield, M.A., and Supple, W.J., "Interactive Collapse of Plate Assemblages in Relation to the Strength of Box Girders", 2nd Int. Colloq. on Stability of steel structures, Liege, 1977, pp. 427-432.

[25] Jetteur Ph., Maquoi, R., and Massonnet, C., "Simulation of the Behaviour of Stiffened Box Girder with and without Shear Lag", Thin-walled Structures, 1, 1983, pp. 211-237.

[26] Dwight, J.B., Proc. Conf. on Developments in Bridge Design and Construction, Cardiff Univ., 1971. Crosby Lockwood, London.

[27] The Institution of Civil Engineers. Informal Meeting on Steel Box-Girder Bridges, London, April 1972.

[28] Dowling, P.J., "Strength of Steel Box-Girder Bridges", Journal of the Structural Divison, ASCE, Vol. 101, No. ST9, Proc. Paper 11550, Sept. 1975, pp. 1929-1946.

[29] Chatterjee, S., Summary of the Measurment of Imperfection, Dct. of Commission 8 - W.G.3 of ECCS, 1978.

[30] Karnikova, I., and Skaloud, M., "Initial Imperfections Measurement on a Number of Newly Built Steel Box Girder Bridges in Czechoslovakia", Int. Doct. of TG., "Tolerances in Steel Plated Structures", May 1979.

[31] Ellis, L.G., "A Statistical Appraisal of the Measured Deformations in Several Steel Box Girder Bridges", Paper of a conference organized by the Institute of Mechanical Engineer, London, 1976.

[32] Korol, R.M., and Thimmhardy, E.G., "Geometric Imperfections of Steel Box Girder Bridges in Canada", 3rd Int. Colloquium on stability of metal structures, May 1983.

[33] Vlasov, B.Z., "Torsion ket stabilité des tiges a'parois minces et a profil ouvert", Ind. de la Constr., 1937.

[34] Vlasov, B.Z., "Thin-walled Elastic Beams", National Science Foundation, Washington, D.C., 1961.

[35] Timoshenko, S., "Theory of Bending, Torsion and Buckling of Thin-Walled Member of Open Section", Jnl. Franklin Inst., 1945.

[36] Timoshenko, S.P., and Gene, J.M., "Theory of Elastic Stability", McGraw Hill Book Co. Inc., N.Y., 1961.

[37] Karman, V., and Christensen, "Methods of Analysis for Torsion with Variable Twist", Jnl. Aeornaut. Sci., 1944, 11, No. 2.

[38] Capurso, M., "Sul calcolo delle travi di parete sottile in presenza di forze distorsioni", Notes 1, 2, 3, 4, 5, Ric. Sci., 1953, 29, (2A).

[39] Faulkner, D., "A Review of Effective Plating for Use in the Analysis of Stiffened Plating in Bending and Compression",

Journal of Ship Research, Vol. 19, No. 1, March 1975, pp. 1-17.

[40] Little, G.H., "Stiffened Steel Compression Panels - Theoretical Failure Analysis", The Structural Engineer, 54, No. 12, December 1976.

[41] Horne, M.R., and Narayanan, R., "An Approximate Method for the Design of Stiffened Steel Compression Panels, University of Manchester, Simon Eng. Lab., February 1975.

[42] Smith, C.S., "Compressive Strength of Welded Steel Ship Grillages", RINA Spring Meeting, 1975.

[43] Massonnet, C., and Maquoi, R., "New Theory and Tests on the Ultimate Strength of Stiffened Box Girders", paper 9, Steel Box Girder Bridges, Institution of Civil Engineers, London, England, 1973.

[44] Jetteur, Ph., "A New Design Method for Stiffened Compression Flange of Box Girders", Thin-walled Structure, 1, 1983, pp. 189-210.

[45] Moolani, F.M., and Dowling, P.J., "Ultimate Load Behaviour of Stiffened Plates in Compression", An Int. Symposium, Crosby Lockwood Staples, London, 1977.

[46] Crisfield, M.A., "Large-Deflection, Elasto-Plastic Buckling Analysis of Plates Using Finite Elements". Transport and Road Research lab. Report No. LR 593, 1973.

[47] Crisfield, M.A., "Large-Deflection, Elasto-Plastic Buckling Analysis of Eccentrically Stiffened Plates Using Finite Elements", TRRL Laboratory Report 725, Crowthorne, Berkshire, 1976.

[48] Soreide, T.H., Bergan, P.J., and Moan, T., "Ultimate Collapse Behaviour of Stiffened Plates Using Alternative Finite Element Formulations", Steel Plated Structures, Crosby Lockwood Staples, London, 1977.

[49] Soreide, T.H., Moan, T., and Nordsve, N.T., "On the Behaviour and Design of Stiffened Plates in Ultimate Limit State", J. Ship Res. 22, 1978.

[50] Nordsve, N.T., and Moan, T., "Numerical Collapse Analysis of Compression Members", Computer and Structures Vol. 12, pp. 521-531.

[51] Fujita, Y., Yoshida, K., and Takazawa, M., "On the Strength of Stiffened Plate Structures", 2nd Int. Colloquium Stability Steel Structures, ECCS, Washington, 1977.

[52] Ueda, Y., and Yao, T., "Ultimate Strength of Square Plates Subjected to Compression", JSNA, Japan, Vol., 137, June 1975, pp. 210-221.

[53] Grave Smith, T.R., "The Post-Buckled Behaviour of a Thin-Walled Box Beam in Pure Bending", Int. J. of Mechanical Sciences, 14, No. 1, November 1972.

[54] Lee, H.P., "Non-Linear Finite Element Analysis of Thin-Walled Members", Doctoral Dissertation, McGill University, 1977.

[55] Dennis H. Parr, and Samuel P. Maggard, "Ultimate Design of Hollow Thin-Walled Box Girders", J. of Structural Div., ST7, ASCE, July 1972

[56] Corrado, J.A. "Ultimate Strength of Single-Span Rectangular Box Girders", Ph.D. Dissertation, Lehigh University, 1971.

[57] Corrado, J.A., and Yen, B.T., "Failure Tests of Rectangular Model Steel Box Girders", Journal of the Structural Division, ASCE, Vol. 99, No. ST7, July 1973.

[58] Dowling, P.J., Moolani, F.M., and Frieze, P.A., "The Effect of Shear Lag on the Ultimate Strength of Box Girders", Proc. Conf. on Steel Plated structures, pp. 108-41, Crosby Lockwood Staples, London 1977.

[59] Roderick, K.C., and Skaloud, M., "The Behaviour of Small-Scale Box-Girders of Stiffened Plate Construction", Aust. Welding Res., Dec. 77, 15-29, 1972.

[60] Dubas, P., "Tests about Post-Critical Behaviour of Stiffened Box Girders", Proc. of Colloquium of Design of Plate and Box Girders for Ultimate Strength, Int. Assn. Bridge and Struct. Eng., 1972.

[61] Steinhardt, O., "Recent Revisions to German Standard DIN 4114 in steel Box-girder Bridges", pp. 203-208, Clowes and Sons, London, 1973.

[62] Steinhardt, O., "Berechnungsmodelle für ausgesteifte Kastentrager", Deutscher Ausschus fur Stalbau, 3, 1975, pp. 27-35.

[63] Mikami, I., Dogaki, M., and Yonezawa, H., "Ultimate Load Tests on Multi-Stiffened Steel Box Girders", Technology Reports of Kansai University, Osaka, Japan, 1980.

[64] Tupula, Y.F., "Buckling Behaviour of Steel Box-Girder Bridges", Ph.D. Dissertation, Concordia University, 1981.

[65] Korol, R.M., and Thimmhardy, E.G., "An Investigation of the Effects of Geometric Imperfections and Residual Stresses on

the Strength of Steel Box Girders", report submitted to D.P.W., Canada, 1985.

[66] Korol, R.M., and Thimmhardy, E.G., "An Investigation of the Effects of Geometirc Imperfections", to be published in Int. Conf. on Short and Medium Span Bridges, Ottawa, August 1986.

[67] El Aghoury, M., Mirza, F.A., and Korol, R.M., "Finite Element Modelling of Steel Box Girders", to be published in Int. Conf. on Short and Medium Span Bridges, Ottawa, August 1986.

[68] Massonnet, Ch., "Tolerances in Steel Plated Structures", International Association of Bridge and Structural Engineering Surveys, S-14/80, Periodica, 1980, pp. 49-76.

[69] Marguerre, K., Die Mittragende Breite der Gedruckten Platte. Buckling Strength of Metal Structures (Edited by F. Bleich), pp. 462-473. McGraw-Hill, New York, 1952.

[70] Zienkiewicz, O.C., "The Finite Element Method in Engineering Science", McGraw Hill Book Company, London (third Edition), 1977.

[71] Abu Gazeleh, B.N., "Analysis of Plate Type Structures", Ph.D. Thesis, University of California, Berkeley, January 1966.

[72] Taig, J.C., and Kerr, R.I., "Some Problems in the Discrete Element Representation of Aircraft Structures", Matrix Method of Structural Analysis. Edited by B. Fraeijs de Veubeke, Pergamon Press, 1964, pp. 267-316.

[73] Crook, R.D., "Concepts and Application of Finite Element Analysis", John Wiley and Sons Inc. (2nd Edition), 1981.

[74] Yamada, Y., Yishimura, N. and Sakurai, T., "Plastic Stress-Strain Matrix and its Application for the Solution of Elasto-Plastic Problems by the Finite Element Method", Int. J. Mech. Sci., Vol. 10, 1968, pp. 343-354.

[75] Zienkiewicz, O.C., Valliappen, S. and King, I.P., "Elasto-Plastic Solutions of Engineering Problems. Initial Stress, Finite Element Approach", Int. J. Num. Meth. Eng., Vol. 1, 1968, pp. 75-100.

[76] Von Mises, R., "Merchanik der Plastischem Fomanderung Von Kristallen", Zeitschrift fur Angewandte Mathematik and Mechanik, Vol. 8, 1928, pp. 161-185.

[77] Mirza, F.A., "Course Notes CE 713", McMaster University, 1982.

[78] Campbell, T.I., and Charlton, T.M., "Finite Deformation of a Fully Fixed Beam Comprise of a Non-Linear Material", Int. J. of Mech. Sci., Vol. 15, No. 5, 1973, pp. 415-428.

[79] Chatterjee, S., and Dowling, P.J., "Proposed Design Rules for Longitudinal Stiffeners in Compression Flange of Box Girders", Imperial College of Science and Technology. CESLIC Report BG40, 1975.

[80] Moan, T., and Soreide, T., "Analysis of Stiffened Plates Considering Non-Linear Material and Geometric Behaviour using Finite Elements", World Congress on Finite Element Method in Structural Mechanics, ed. J. Robinson, Bournemouth, 1975.

[81] Stanton, E.L., and Schmit, L.A., "A Discrete Element Stress and Displacement Analysis of Elasto-Plastic Plates", AIAA Journal, Vol. 8, No. 7, pp. 1245, 1970.

[82] Yamaki, N., "Post-Buckling Behaviour of Rectangular Plates with Small Initial Curvature Loaded in Edge Compression", Journal of Applied Mech. 26, 3, Sept. 1959, pp. 407-414.

[83] Brady, F.J., "An Experimental Investigation of Unequal Width HSS Moment Connections for Vierendeel Trusses", M. Eng. Thesis, McMaster University, 1974.

[84] Mirza, F.A., Shehata, A.A., and Korol, R.M., "Elasto-Plastic Finite Element Analysis of Double Chord Rectangular Hollow Section T-Joints", Computer and Structures, Vol. 19, No. 5/6, 1984, pp. 829-838.

[85] Patel, N.M., Graff, W.J., and White, A., "Punching Shear Characteristics of RHS Joints", ASCE National Structural Engineering Meeting, San Francisco, April 1975.

[86] Dwight, J.B., and White, J.D., "Prediction of Weld Shrinkage in Plate Structures", Stability of Steel Structures, Preliminary Report, ECCS, Liege, 1977, pp. 31-7.

[87] Young, B.W., and Dwight, J.B., "Residual Stresses and their Effects on the Moment - Curvature Properties of Structural Steel Sections", CIRIA TN32, December 1971.